

ABSTRACT

Title of Document: STUDY OF THE FEASIBILITY OF
CONTROLLING THE LENGTH SCALE OF THE
PHASE SEPARATION OF ORGANIC
MOLECULAR MIXTURES ON Si(111)
SUBSTRATES

Miriam Cezza, Doctor of Philosophy, 2014

Directed By: Professor Raymond J. Phaneuf,
Department of Materials Science and Engineering

We present investigations on the arrangements of phase separating small organic molecules in mixtures subsequent to deposition from liquid solution. This phenomenon may have technological applications in efficient organic solar cells. The spontaneous formation of a morphology during phase separation from a solvent-based, bimolecular solution onto a substrate depends on several parameters, including relative molecular concentrations, individual molecules/solvent/substrate interactions, solvent evaporation rate, and annealing conditions. Our molecular mixtures consist of tetranitro zinc-phthalocyanine (tn-ZnPc) and [6,6]-phenyl-C₆₁-butyric acid methyl ester (PCBM) in chloroform, deposited on native oxide-covered Si(111) substrates. We investigate the role that solvent evaporation rate during deposition, solvent vapor annealing (SVA) and thermal annealing play on the morphology formation of molecular domains. We find that slow enough rates of solvent evaporation, along with SVA action, lead to ordered PCBM structures. Most of tn-ZnPc molecules aggregate in rod-shaped clusters of size ~ 100 nm while in liquid solution, even at diluted concentrations, but some remain solvated, and

form a wetting layer on the Si(111) surfaces, affecting the morphology of PCBM deposited through mixture solutions. We find that PCBM aggregates vertically diffuse upon heating in spin-coated samples, while tn-ZnPc clusters and wetting layer are not affected.

Investigations of different relative concentrations of individual molecules in mixtures show that the concentration of tn-ZnPc strongly affects the crystallization process of PCBM: for a 1:1 ratio PCBM crystallization is suppressed, while changing the amount of tn-ZnPc, PCBM crystals form.

While PCBM domains display several different morphologies, tn-ZnPc cluster morphology is not affected by changes in the deposition conditions or by post-deposition treatments. Overall we find that, under the conditions studied here, PCBM molecules undergo heterogeneous nucleation at the substrate, while tn-ZnPc molecules predominantly precipitate.

This combination of donor/acceptor molecules deposited through the methods described here, show a slight tendency toward vertical growth of molecular domains for deposition onto a periodic array of cavities patterned onto a substrate. No significant effects are observed in presence of H-terminated surfaces.

Finally, our studies on evaporation of resting droplets shed light on individual molecules/solvent interactions, leading to a better understanding of the variation in domain coverages across the substrate.

STUDY OF THE FEASIBILITY OF CONTROLLING THE LENGTH SCALE OF THE
PHASE SEPARATION OF ORGANIC MOLECULAR MIXTURES ON Si(111)
SUBSTRATES

By

Miriam Cezza

Dissertation submitted to the Faculty of the Graduate School of the
University of Maryland, College Park, in partial fulfillment
of the requirements for the degree of
Doctor of Philosophy
2014

Advisory Committee:
Professor Raymond J. Phaneuf, Chair
Professor Manfred R. Wuttig
Professor Lourdes G. Salamanca-Riba
Professor Robert M. Briber
Professor Janice Reutt-Robey

© Copyright by
Miriam Cezza
2014

Dedication

To my family

Acknowledgements

I wish to deeply thank my advisor, Prof. Raymond Phaneuf, whom enabled this exciting and shaping experience. His guidance and support accompanied me since the first day, and his incredible love for science inspired me to always be a better scientist. I am very grateful for have had the opportunity of meeting important scientists and persons from whom I learned an enormous wealth of knowledge, professionalism and humanity.

The realization of this thesis would have not be possible without the important contribution of many collaborators, to whom I am very grateful: Prof. Hung-Chih Kan, Dr. Tsung-Cheng Lin, Dr. Chuan-Fu Lin, and Dr. Shy-Hauh Guo for collaborations on force curve analysis and AFM discussions, Dr. Karen Gaskell for XPS and Raman spectroscopy discussions, Dr. Peter Zavalij for the XRD results, Prof. Mikhail Anisimov and Elena Jouravleva for the DLS results, Dr. Gianluca Accorsi for the UV-Vis spectra, and Dr. Aldo Ponce and Prof. Janice Reutt-Robey for discussions on FTIR and ATR-FTIR spectroscopy.

I would like to thank the entire staff of the FabLab and NISPLab of the Maryland NanoCenter, and Scott Taylor from the Optical Instrumentation Facility for useful trainings and technical support.

I am very grateful to the undergraduate students that during these past four years have worked in our lab and shared valuable scientific insights. I would like to thank Colin Qualters, for the thermal annealing and the patterned samples experiments, Jessica Genta for the preliminary experiments, Kyle Elliot and George Stackhouse, whose work around the lab was very much appreciated.

Special thanks go to my “group-mate”, Amy Marquardt, for sharing with me good and bad times, for her incessant encouragements and valuable conversations.

I am very grateful to the all administrative staff of the Department of Materials Science and Engineering at the University of Maryland: their kindness and humanity have always made me feel like in a big warm family.

Also, I would like to thank all my colleagues and friends that significantly supported me during these years: Dr. Qian Shao, Romaine Isaacs, Wonseok Hwang, Karthik Sridhara, Dr. Gilad Kusne, Dr. Umberto Cannella, Dr. Claudia Ojeda Aristizabal, Dr. Fiorangela La Forgia, Dr. Elisabetta Lambertini, Dr. Devid Sabatini, and Dr. Silvia Protopapa.

I am deeply thankful for Neal, who has always been by my side and has always filled my days with joy and serenity; and to all his wonderful family that made me live unforgettable moments of happiness.

Finally, the most important thanks go to my parents, my sisters and my brother: their immense love has always been an active element in my life, and it is thanks to them that the realization of all my successes is made possible.

Table of Contents

Dedication	ii
Acknowledgements.....	iii
Table of Contents	v
List of Tables	viii
List of Figures	x
Chapter 1 – Introduction	1
1.1 Motivation	1
1.2 Objective	3
1.3 Background	4
Chapter 2 – Materials and Experimental Methods	11
2.1 Approach	11
2.2 Materials and Methods	14
Chapter 3 – Phase Separation and Crystallization on Unpatterned Substrates	22
3.1 Deposition onto Unpatterned Si(111) Substrates	22
3.1.1 Deposition Method by Spin-Coating	23
3.1.1.1 Spin-Coating Deposition of PCBM only	23
3.1.1.2 Spin-Coating Deposition of tn-ZnPc only.....	24
3.1.1.3 Spin-Coating Deposition of PCBM/tn-ZnPc (1:1) Mixtures	25
3.1.1.4 Conclusions for Spin-Coating Deposition Results.....	30
3.1.2 Deposition Method by Drop-Casting.....	31
3.1.2.1 Drop-Casting Deposition of PCBM only	31
3.1.2.2 Drop-Casting Deposition of tn-ZnPc only	35
3.1.2.3 Drop-Casting Deposition of PCBM/tn-ZnPc (1:1) Mixtures.....	37
3.1.2.4 Conclusions for Drop-Casting Deposition Results	38
3.1.3 Deposition Method by Immersion	39
3.1.3.1 Immersion in PCBM/chloroform Solution.....	39
3.1.3.2 Immersion in tn-ZnPc/chloroform Solution.....	42
3.1.3.2.1 Effect of Substrate Orientation	44

3.1.3.3	Immersion in (1:1) PCBM/tn-ZnPc Mixed Solution	45
3.1.3.4	Conclusions for Deposition via Immersion Results	53
3.2	Effect of Temperature-Annealing on Spin-Coated Samples	54
3.3	Stoichiometries (1:2) and (2:1) of tn-ZnPc/PCBM Mixtures	59
3.3.1	(1:2) tn-ZnPc/PCBM Mixtures	59
3.3.1.1	Drop-casting of (1:2) tn-ZnPc/PCBM Mixture Solutions	59
3.3.1.2	Immersion in (1:2) tn-ZnPc/PCBM Mixture Solutions	64
3.3.2	(2:1) tn-ZnPc/PCBM Mixtures	66
3.3.2.1	Drop-casting of (2:1) tn-ZnPc/PCBM Mixture Solutions	66
3.3.2.2	Immersion in (2:1) tn-ZnPc/PCBM Mixture Solutions	69
3.3.3	Conclusions for the Results of Stoichiometries (1:2) and (2:1) tn-ZnPc/PCBM Mixtures	71
3.4	Dynamic Light Scattering Analysis	73
3.5	Force-Curves Results	78
3.5.1	Force-Curves Measured with Spherical AFM Probe	83
3.5.2	Force-Curves Measured with Conical AFM Probe	88
3.5.3	Conclusions for Force-Curves Results	91
3.6	Summary and Conclusions	91
Chapter 4 – Results of Depositions on Patterned Substrates and on Surface Tension		
	Modified Patterned Substrates	95
4.1	Native Oxide-Covered Patterned Si(111) Substrates	95
4.1.1	Depositions on Large Scale Patterns on Si(111)	99
4.1.2	Depositions on Small Scale Patterns on Si(111)	105
4.2	H-terminated Patterned Si(111) Substrates	111
4.3	Conclusions for Native Oxide-Covered and H-terminated Patterned Substrates. . .	116
Chapter 5 – Vibrational Spectroscopy		
5.1	Raman Scattering Spectroscopy	118
5.2	FTIR and ATR-FTIR Spectroscopy	124
5.2.1	FTIR and ATR-FTIR Spectra from Powders	127
5.2.2	Polarized ATR-FTIR of Deposited Molecules	132

Chapter 6 – Evaporation of a Sessile Droplet of Chloroform Resting on an Isothermal Si(111) Substrate.....	138
6.1 Theoretical Basis	138
6.2 Experiments and Discussions.....	143
Chapter 7 – Summary and Conclusions.....	153
Chapter 8 – Future Work	156
Appendix A – Arrangement of Molecular Domains across the Substrate for (1:2) and (2:1) tn-ZnPc/PCBM Mixtures	158
Appendix B – XRD Patterns of Powders Materials.....	162
Appendix C – Optical Characterization – Charge Transfer Complexes.....	175
Appendix D – Determination of the Young’s Modulus of tn-ZnPc and the Thickness of the tn-ZnPc Wetting Layer.....	179
Bibliography	188

List of Tables

Chapter 2

Table 2-1. Values of the evaporation rates of chloroform of the initial and final regimes for the drop-casting, immersion in open cylinder, and nearly-closed cylinder. 21

Chapter 3

Table 3-1. Hydrodynamic radius of particles present in the tn-ZnPc solutions at different concentrations. 76

Table 3-2. Hydrodynamic radius of particles present in the mixture solutions at different concentrations. 77

Chapter 4

Table 4-1. Values of diameters, spacing and depth of the largest and medium dimension cells on the diagonal of the small scale pattern before and after deposition via spin-coating of the (1:1) tn-ZnPc/PCBM mixture. 108

Table 4-2. Values of diameters, spacing and depth of the largest and smallest dimension cells on the diagonal of the small scale pattern before and after deposition via drop-casting of the (2:1) tn-ZnPc/PCBM mixture..... 110

Table 4-3. Values of diameters, spacing and depth of the largest and smallest dimension cells on the diagonal of the small scale pattern before and after deposition via spin-coating of the (1:1) tn-ZnPc/PCBM mixture on H-terminated surfaces. 113

Table 4-4. Values of diameters, spacing and depth of the largest and medium dimension cells on the diagonal of the small scale pattern before and after deposition via drop-casting of the (2:1) tn-ZnPc/PCBM mixture on H-terminated surfaces. 115

Chapter 5

Table 5-1. Raman frequencies and group assignments of tn-ZnPc molecules. 121

Table 5-2. Characteristic FTIR absorption frequencies and group assignments of tn-ZnPc molecules. vw: very weak, w: weak, m: medium, s: strong, vs: very strong, sh: shoulder. 129

Table 5-3. Characteristic FTIR absorption frequencies and group assignments of PCBM molecules. w: weak, m: medium, s: strong, vs: very strong, sh: shoulder..... 130

Table 5-4. Percentage of increasing of the intensity of the peaks in the s-polarized spectra of PCBM. 134

Table 5-5. Percentage of increasing of the intensity of the peaks in the s-polarized spectra of tn-ZnPc and the mixture. 136

Chapter 6

Table 6-1. Values of the evaporation rates of the initial and final regimes for the solution under investigations. 148

Table 6-2. Overall values of the evaporation rate for the solutions under investigations. 148

Table 6-3. Estimation of the initial contact angle. 151

Appendix B

Table B-1. Miller indices (h , k , l), d spacing, 2θ angles and fitted intensities of PCBM. 174

List of Figures

Chapter 1

- Figure 1-1. Phase diagram showing the binodal and spinodal curves. 5
- Figure 1-2. Schematic of the nucleus forming on the substrate wall and forming the contact angle. 6
- Figure 1-3. Activation barrier (ΔG) as function of the nucleus radius for the three different nucleation processes (in liquid, on a substrate, and in a cavity). 7
- Figure 1-4. Schematic of the photocurrent generation process occurring in an OSC. EQE is the external quantum efficiency. 8
- Figure 1-5. Schematic of the effect of the high crystallinity on the diffusion of excitons. 9
- Figure 1-6. Schematic of the optimal geometry of the active layer in an organic solar cell. 10

Chapter 2

- Figure 2-1. Tetranitro zinc phthalocyanine (tn-ZnPc) and phenyl-C₆₁-butyric acid methyl ester (PCBM) molecules. 15
- Figure 2-2. Schematic representation of the three methods of deposition used in this work. Last image shows the variation of the method of deposition by immersion, in order to reach even lower evaporation rates. 19
- Figure 2-3. Mass change of chloroform as a function of time, for the drop-casting, immersion in open container, and immersion in nearly-closed container. 20

Chapter 3

- Figure 3-1. Height-contrast AFM images of the PCBM molecules deposited via spin-coating through single component solution and from the mixture with tn-ZnPc at (a, e) 500 rpm, (b, f) 1000 rpm, (c, g) 2000 rpm and (d, h) 3000 rpm, respectively. Height-contrast AFM images of the tn-ZnPc molecules deposited via spin-coating through single component solution and from the mixture with PCBM at (i, m) 500 rpm, (j, n) 1000 rpm, (k, o) 2000 rpm and (l, p) 3000 rpm, respectively. 28

Figure 3-2. Projected area coverage, calculated in percentage for the PCBM and tn-ZnPc clusters domains deposited through single component solution and from the mixture with the other component at different spin rates (left). Ratio of the coverage of the PCBM phase deposited from single component solution and from the mixture, showing the asymptotical trend (right)..... 29

Figure 3-3. Width (left) and height (right) of tn-ZnPc rods deposited by spin-coating at different spin rates from single component solution and from the mixture..... 29

Figure 3-4. Adhesive forces measured on the silicon dioxide of Si(111) surfaces and on the flat regions between rods of tn-ZnPc deposited through spin-coating..... 30

Figure 3-5. Photograph of a Si(111) substrate onto which PCBM molecules have been deposited via drop-casting. 31

Figure 3-6. Optical images of the PCBM deposited through drop-casting onto Si(111) surface, from the edge of the sample (a), to the intermediate region where the blanket-like phase starts to form (b) to the center of the sample where the blanket-like phase is predominant (c). Images (d) and (e) are the height-contrast AFM image of one circular depletion zone appearing in the blanket-like phase and the phase-contrast AFM image of the magnification of the crystal visible at the center, respectively. 33

Figure 3-7. Schematics of the different flows occurring inside the droplet in presence of the stagnation point on the free surface of the droplet.²⁷ Highly soluble molecules are transported towards the center of the droplet, while less soluble molecules are transported towards the center of the droplet..... 34

Figure 3-8. Schematic coverage maps of PCBM (a) and tn-ZnPc (b) after drop-casting deposition. The darker regions denote higher concentration of material..... 35

Figure 3-9. Photograph of a Si(111) substrate onto which tn-ZnPc molecules have been deposited via drop-casting. 36

Figure 3-10. SEM image (a) and optical image (b) of the tn-ZnPc deposited through drop-casting onto Si(111) surface. Image (b) shows a portion of a “coffee-ring”. 36

Figure 3-11. Photograph of a Si(111) substrate onto which the mixture in ratio 1:1 has been deposited via drop-casting..... 37

Figure 3-12. SEM images (a) and height- and phase-contrast AFM images (b, c) of drop-casted mixture of tn-ZnPc and PCBM in ratio 1:1.	38
Figure 3-13. Optical images (a-c) and SEM cross-section image (insert) of the PCBM crystal phase observable at evaporation rate of 0.00347 mL/min (immersion in open cylindrical container) followed by SVA, promoting the crystallization of PCBM molecules in hexagons. SEM cross-section image (d) of the stacking of hexagons at the surface.	40
Figure 3-14. Deposition of PCBM via immersion in PCBM/chloroform solution in a quasi-closed cylindrical container (evaporation rate of 0.0017mL/min). Pyramidal growth of PCBM molecules activated by the initial single hexagon that acts as nucleation site (a, b). Dendritic and cellular growth at the base of the pyramid (c).	41
Figure 3-15. EDS spectrum measured at hexagons of PCBM formed on silicon substrate via immersion in PCBM/chloroform solutions.	42
Figure 3-16. SEM images of tn-ZnPc rod-like clusters deposited from single component solution through vertical substrate orientation immersion in solution at 0.00347 mL/min (open container) (a) and 0.0017 mL/min (nearly-closed container) (b).	43
Figure 3-17. EDS spectrum measured at an agglomeration of tn-ZnPc rods on silicon substrate during immersion in tn-ZnPc/chloroform solutions.	44
Figure 3-18. SEM images of the structures resulting from deposition of a (1:1) tn-ZnPc/PCBM mixture via immersion with vertical substrate orientation in open container (0.00347 mL/min). Plates do not show a clear hexagonal shape (a). Areas with low and high density of rods (b). Stacking of plates in low rods density areas (c), and dendritic growth in high rods density areas (d).	46
Figure 3-19. Optical image of the structures resulting from deposition of a (1:1) tn-ZnPc/PCBM mixture deposited via immersion with vertical substrate orientation in open container (0.00347 mL/min). The horizontal strips of agglomeration of rods are observed.	47
Figure 3-20. EDS spectrum measured at an agglomeration of tn-ZnPc rods on the silicon substrate during immersion in a (1:1) tn-ZnPc/PCBM mixture solution.	47
Figure 3-21. EDS spectrum measured at PCBM dendrites formed on a silicon substrate during immersion in a (1:1) tn-ZnPc/PCBM mixture solution.	48

Figure 3-22. EDS spectrum measured at quasi-hexagonal plates of PCBM formed on a silicon substrate during immersion in a (1:1) tn-ZnPc/PCBM mixture solution.	49
Figure 3-23. Optical images of the structures resulting from deposition of a (1:1) tn-ZnPc/PCBM mixture deposited via immersion with a vertical substrate orientation at the rate of 0.0017 mL/min of (a) an area with high density of tn-ZnPc rods and (b) an area with low density of rods.	50
Figure 3-24. Optical microscopy images of the structures resulting from deposition of PCBM via immersion, with a vertical substrate orientation at the rate of 0.0017 mL/min showing (a) stacking of hexagons and (b) dendrites.	51
Figure 3-25. Optical image of the structures resulting from deposition of a (1:1) tn-ZnPc/PCBM mixture deposited via immersion with horizontal substrate orientation in nearly-closed container (0.0017 mL/min). Portion of an irregular “coffee-ring”	52
Figure 3-26. Optical images of the structures resulting from deposition of a (1:1) tn-ZnPc/PCBM mixture deposited via immersion with horizontal substrate orientation at the rate of 0.0017 mL/min. Areas with low density of rods show dendritic growth (a), and areas with high density of rods show stacking of plates (b).	53
Figure 3-27. Radius of gyration of tn-ZnPc rods, in the single component sample (left) and in the mixture in ratio 1:1 with the PCBM (right).	56
Figure 3-28. Diameter (left) and height (right) of the PCBM spherical caps in the pure PCBM samples at different temperatures.	57
Figure 3-29. Diameter (left) and height (right) of the PCBM spherical caps in the mixture samples at different temperatures.	58
Figure 3-30. Results of drop-casting of a solution of a (1:2) tn-ZnPc/PCBM mixture. Optical image of the sample (above). The inset in (a) is an AFM topography map (height scale 20 nm). The inset in (c) is an AFM phase map (data scale 20°).	61
Figure 3-31. Phase-contrast AFM images of a section where the blanket phase of PCBM starts to breaks down into spherical cap clusters.	62

Figure 3-32. SEM images of a "pinning object" formed via drop-casting of a (1:2) tn-ZnPc/PCBM mixture solution, shown in top view (left) and with the SEM stage tilted at 40° (right). The images at the bottom are magnifications of the images above. 63

Figure 3-33. Optical images of structures which form during deposition via immersion in a solution of a (1:2) tn-ZnPc/PCBM mixture; deposition was in a nearly-closed container, with a vertical orientation of the substrate. (a) Image recorded in an area with low density of tn-ZnPc rods; (b) image recorded in an area with high density of rods. 65

Figure 3-34. Optical images of structures which form during deposition via immersion in a solution of a (1:2) tn-ZnPc/PCBM mixture; deposition was in a nearly-closed container, with a horizontal orientation of the substrate. (a) Image recorded in an area with low density of tn-ZnPc rods; (b) image recorded in an area with high density of rods. 66

Figure 3-35. Optical images of structures which form during deposition via drop casting of a solution of a (2:1) tn-ZnPc/PCBM mixture. 67

Figure 3-36. SEM images of the "pinning object" resulting from drop-casting deposition from a solution of a (2:1) tn-ZnPc/PCBM mixture taken with the SEM stage tilted at 40°. The image at the right is magnifications of the contact area. 68

Figure 3-37. AFM topography images of structures resulting from drop casting deposition from a solution of a (2:1) tn-ZnPc/PCBM mixture measured (a) near the center of the sample, (c) within in a PCBM-rich arc, and (d) within a tn-ZnPc-rich arc. Panel (b) shows a phase-AFM image of a magnificated region of panel (a), as indicated by the square. ... 69

Figure 3-38. Optical images of structures which form during deposition via immersion in a solution of a (2:1) tn-ZnPc/PCBM mixture; deposition was in a nearly-closed container, with a vertical orientation of the substrate. (a) Image recorded in an area with low density of rods; (b) image recorded in an area with high density of rods. 70

Figure 3-39. Optical images of structures which form during deposition via immersion in a solution of a (2:1) tn-ZnPc/PCBM mixture; deposition was in a nearly-closed container, with a horizontal orientation of the substrate. (a) Image recorded in an area with low density of rods; (b) image recorded in an area with high density of rods. 71

Figure 3-40. Absence of the detectable autocorrelation function of PCBM/chloroform solution at 2.5 mM 75

Figure 3-41. Autocorrelation functions (left) and hydrodynamic radius of particles (right) of tn-ZnPc/chloroform solutions.....	76
Figure 3-42. Autocorrelation functions (left) and hydrodynamic radius of particles (right) of Mix/chloroform solutions.	77
Figure 3-43. Schematics of the dipoles of tn-ZnPc (left) and PCBM (right) molecules (in the negative-to-positive charge convention).	81
Figure 3-44. Schematics of native oxide and hydrocarbons present on Si(111) surfaces.	82
Figure 3-45. Objects under examination on spin-coated samples in force curves analysis.	83
Figure 3-46. Comparison between retracted force-curves measured with spherical AFM tip on bare Si(111) and areas between tn-ZnPc rods on sample spin-coated with pure tn-ZnPc solution (left), and on PCBM spherical caps and tn-ZnPc rods present in the mixture-coated sample, on PCBM spherical caps present on PCBM-coated sample and on the tn-ZnPc rods present on the tn-ZnPc-coated sample (right).	85
Figure 3-47. Adhesion forces measured on the six objects with spherical AFM probe. ..	85
Figure 3-48. Comparison between retracted force-curves measured with conical AFM tip on bare Si(111), areas between PCBM phases, areas between tn-ZnPc rods, tn-ZnPc rods, PCBM spherical caps, blanket phase on the substrate, and blanket phase on the rods. All the force-curves, except the one measured for bare silicon, have been measured on mixture samples drop-casted.....	89
Figure 3-49. Adhesion forces measured on the seven different objects with conical AFM probe.	90
Figure 3-50. Summary of the different phases per molecules in single component and the (1:1) mixture at the different evaporation rate investigated.....	93

Chapter 4

Figure 4-1. CAD model of the pattern employed in this work. The x- and y-axis show the two different dimensions: in the large scale pattern the spacing λ ranges from 1.4 to 16 μm , and the diameter \varnothing from 0.7 to 8 μm ; in the small scale pattern the spacing λ ranges from 60 to 720 nm, and the diameter \varnothing from 30 to 360 nm.	96
--	----

Figure 4-2. Schematic of the fabrication process for transfer of the patterns onto the Si substrate. 97

Figure 4-3. Height-AFM images of the large scale pattern etched on Si(111). The areas 1, 2 and 3 refers to the areas containing the corners of the cells of pit of dimensions 0.7 – 1 μm in diameter and 1.4 – 2 μm in spacing, 5.6 – 8 μm in diameter and 11 – 16 μm in spacing, and 0.7 – 1 μm in diameter and 11 – 16 μm in spacing, respectively. 98

Figure 4-4. Height-AFM image of the large dimensions six cells of the small scale pattern. The sizes reported are only for the largest and smallest cell on the diagonal..... 99

Figure 4-5. Height-AFM (left) and phase-AFM (right) images of the structures resulting from spin-coating a solution of a (1:1) tn-ZnPc/PCBM mixture on patterned Si(111). The cell is that in which pits diameter and spacing were 0.7 \times 1.4 μm 100

Figure 4-6. Height-AFM image of the structures resulting from spin-coating a solution of a (1:1) tn-ZnPc/PCBM mixture on patterned Si(111). The cell is that in which pits whose diameter and spacing were 8 \times 16 μm 101

Figure 4-7. Phase-AFM images of the structures resulting from drop-casting a solution of a (1:1) tn-ZnPc/PCBM mixture on patterned Si(111). The left image refers to the area 1, the right image refers to the cell in which pits diameter and spacing were 0.7 \times 1.4 μm , and the graph is the cross section of the edge of the pits showing the blanket phase thickness decreasing as it approaches the center of the pit..... 103

Figure 4-8. Height- and phase-AFM images of the structures resulting from drop-casting a solution of a (1:1) tn-ZnPc/PCBM mixture on patterned Si(111). The images refer to the cell in which pits diameter and spacing were 8 \times 16 μm 103

Figure 4-9. Optical images of the structures resulting from deposition via immersion of the patterned Si(111) (placed vertically into open container) in a solution of a (1:1) tn-ZnPc/PCBM mixture. The left image barely shows the entire pattern and the right image is a magnification of the cell in which pits diameter and spacing were 0.7 \times 1.4 μm 105

Figure 4-10. Height-AFM images of the structures resulting from spin-coating a solution of (1:1) tn-ZnPc/PCBM mixtures onto the small scale pattern. 106

Figure 4-11. Magnified height- and phase-AFM images of the largest and medium dimension cell structures resulting from spin-coating a solution of (1:1) tn-ZnPc/PCBM mixtures onto the small scale pattern..... 107

Figure 4-12. Magnified height- and phase-AFM images acquired within the largest and smallest dimension cell of the drop-casting from a solution of a (2:1) tn-ZnPc/PCBM mixture onto the small scale pattern. 109

Figure 4-13. Magnified height- and phase-AFM images acquired within the largest and smallest dimension cell of the spin-coating from a solution of a (1:1) tn-ZnPc/PCBM mixture onto H-terminated small scale pattern. 113

Figure 4-14. Magnified height- and phase-AFM images acquired within the largest dimension and medium dimension cell of the drop-casting from a solution of a (2:1) tn-ZnPc/PCBM mixture onto H-terminated small scale pattern 115

Chapter 5

Figure 5-1. Representation of Rayleigh, Raman Anti-Stokes and Raman Stokes scattering 119

Figure 5-2. Raman spectrum of tn-ZnPc powder and fluorescence spectrum of PCBM powder..... 120

Figure 5-3. Raman spectra of tn-ZnPc powder and rod-like crystals deposited from tn-ZnPc/chloroform solution. 122

Figure 5-4. Comparison between Raman spectra from the areas between rod-like crystals after depositions from tn-ZnPc-alone solution and from a solution of a mixture between tn-ZnPc and PCBM. The peaks indicated by arrows correspond to Raman scattering from the silicon substrate..... 123

Figure 5-5. Raman spectrum measured from the PCBM blanket phase covered tn-ZnPc rods. Both the fluorescence spectrum of PCBM and the characteristic narrow peaks assigned to tn-ZnPc are observed. 124

Figure 5-6. Schematic of ATR principle..... 125

Figure 5-7. Decay length of the evanescent intensity as a function of the incident light frequency..... 126

Figure 5-8. Transmission-FTIR and ATR-FTIR absorption spectra measured from tn-ZnPc raw powder, and normalized to the highest measured intensity..... 128

Figure 5-9. Transmission-FTIR and ATR-FTIR absorption spectra measured from PCBM raw powder, and normalized to the highest measured intensity.	128
Figure 5-10. Comparison between ATR-FTIR spectra of raw powders and powders deriving after solvation and evaporation of chloroform of tn-ZnPc (left) and PCBM (right).	131
Figure 5-11. ATR-FTIR spectrum measured from liquid chloroform (left) and absorption frequencies with group assignments (right).	132
Figure 5-12. Schematic illustration of s- and p-polarization.	132
Figure 5-13. Polarized ATR-FTIR spectra measured from tn-ZnPc (left panel) and PCBM (right panel) drop-casted onto the Ge ATR crystal.	133
Figure 5-14. Polarized ATR-FTIR spectra of the (1:1) tn-ZnPc/PCBM mixture drop-casted onto the Ge ATR crystal from chloroform solution (left). Comparison of the s-polarized spectra of the tn-ZnPc, PCBM and mixture drop-casted on the ATR crystal (right).	135
Figure 5-15. Magnification of the fingerprint region of the s-polarized spectra of the tn-ZnPc, PCBM and mixture drop-casted on the ATR crystal.	135
Figure 5-16. Schematics of the orientation of tn-ZnPc and PCBM molecules deposited via drop-casting on semiconductor substrates. The configuration of the PCBM is reported only in the PCBM-alone case because PCBM molecules are not well detectable in the mixture.	137

Chapter 6

Figure 6-1. Schematic of a droplet resting on a substrate.	138
Figure 6-2. Schematics of the "constant contact angle" and "constant contact radius" modes.	139
Figure 6-3. Marangoni convection inside a droplet (left). ²⁵ Evaporation fluxes on the surfaces of the droplet (right). ²⁷	141
Figure 6-4. Schematics of the different flows occurring inside the droplet in presence of the stagnation point on the free surface of the droplet. ²⁷	143

Figure 6-5. Contact angle and contact radius as a function of time.....	144
Figure 6-6. Mass change as a function of time, for the pure chloroform, the PCBM, tn-ZnPc, and (1:1) mixture solutions.....	147
Figure 6-7. Derivative of the mass of the solution as function of time (left). Slope of the evaporation rate (right).	149
Figure 6-8. Derivative of the mass and $R(t)$ as a function of time for the four solutions.	150
Figure 6-9. Schematic of the initial contact angle.	151
Figure 6-10. Fitting of the droplet surface to an arc to verify the gravity effect.	152

Appendix A

Figure A-1. Comparison of optical images of the structures resulting from deposition from a solution of a (1:2) tn-ZnPc/PCBM mixture (top images) and from a solution of a (2:1) tn-ZnPc/PCBM mixture (bottom images) via drop-casting	159
Figure A-2. Optical images of the structures resulting from deposition from a solution of a (1:2) tn-ZnPc/PCBM mixture modified in order to remove the distortion of the optical background (left). Ring-ring distance as a function of the position on the substrate (right).	160
Figure A-3. Radial distance between adjacent pinning objects (upper graph). Arc chord length of adjacent pinned arcs (bottom graph).	161

Appendix B

Figure B-1. XRD pattern of PCBM raw powder.	162
Figure B-2. Comparison between observed XRD pattern of PCBM and calculated with LeBail method.....	164
Figure B-3. XRD pattern of tn-ZnPc raw powder.	165

Appendix C

Figure C-1. UV-Vis spectra of PCBM (left) ⁹⁹ and tn-ZnPc (right). ¹⁰⁰	176
---	-----

Figure C-2. Emission spectra of drop-casted film on silicon of PCBM (black), tn-ZnPc (red), and the mixture (blue) with relative decay times. 177

Appendix D

Figure D-1. XPS spectrum of tn-ZnPc deposited via drop-casting on Si(111). 180

Figure D-2. Fitting of Equation (D-2) of the F vs. P curve measured for tn-ZnPc rods. 183

Figure D-3. 3D geometry used for COMSOL simulations to obtain the Young's modulus of tn-ZnPc. 184

Figure D-4. Plot of E_{cyl} vs. Δm . The intercept of the linear fit of this curve is the estimated Young's modulus of tn-ZnPc. 185

Figure D-5. 2D axial-symmetric geometry used for COMSOL simulations to obtain the thickness of tn-ZnPc wetting-layer. 186

Figure D-6. Plot of $t_{wl,COMSOL}$ vs. Δm . The intercept of the linear fit of this curve is the estimated thickness of the wetting layer. 187

Chapter 1 – Introduction

1.1 Motivation

Understanding the underlying science behind the arrangements of small organic molecules in mixtures is important for numerous technological applications. Among these, application to organic solar cells (OSCs) is especially noteworthy, given the drive toward alternative energy sources. Organic solar cell technology has attracted much interest in recent research because of the amenability of solution-processable deposition techniques, inexpensive cost of fabrication, and structural flexibility, all of which combine to make OSCs potentially suitable for application on a large scale. In particular, the advantage of the “bulk heterojunction” (BHJ) structure (in which the electron donor and electron acceptor molecules are mixed together prior the deposition), over a bilayer structure (in which a layer of one type of molecule is deposited on top of a layer of the other one) is a greatly increased interfacial area available, which is spatially distributed over the entire volume of the active layer. As exciton dissociation into free charges is much more probable at donor molecule/acceptor molecule domain interfaces, larger interface area leads to an increased power conversion efficiency (PCE).¹ However, the PCE of BHJ-OSCs is still very low as compared to that of crystalline silicon solar cells: 11.9% compared to 25%, as reported by the National Renewable Energy Laboratory chart on record cells efficiencies.² This relatively low efficiency is mainly due to the fact that, after the light absorption-induced formation of an exciton, its recombination is likely before it can diffuse to a donor/acceptor interface. The lower efficiency makes organics photovoltaics unsuitable at present for large-scale commercialization.

An important process on which many applications of organic molecular mixtures, such as organic solar cells, depend is their phase separation. The spontaneous formation of a particular morphology during phase separation from a solvent-based, bimolecular solution onto a substrate is a complex problem; there are four components: the individual molecules, the solvent and the substrate. The mode of the separation is expected to depend on several parameters, including relative molecular concentrations, solubilities of each type of molecule in the solvent, interaction of individual molecules with the substrate surface, layer thickness, solvent evaporation rate, and annealing temperature and time. Controlling the morphology of domains of different molecules will require an understanding of the interactions between like and unlike molecules in the solvent, in the solvent-free mixture and with the substrate.

Based on analogy with crystal growth from solution we anticipate that under certain conditions the substrate will play an important role in the phase separation process. We expect that for small enough supersaturation of the individual molecule/solvent solution the phase separation between molecules of different species should be via nucleation and growth, rather than spontaneous decomposition. In this case the activation barrier between a homogeneous solution and the phase separated mixture (ΔG^*) is expected to decrease at the substrate, providing adsorption of the individual molecules and thus decreasing the overall interface energy of the system. If the phase separation nucleates at the substrate it should then propagate into the solution, given sufficient supersaturation. This should give rise to “vertical” domain growth (i.e. at right angles to the substrate surface). A further expectation, based on analogy with classical nucleation theory, is that the presence of preferred nucleation sites or “seeds” on the

substrate such as cavities might locally promote the nucleation of the new phases: the critical nucleation volume can be significantly smaller in the presence of suitable sites. This brings up the issue of the *persistence* of the length scale of the phase separation as it propagates into solution. From classical capillarity theory the fastest growing wavelength should depend on the ratio of the interfacial tension between two phases to the driving force for separation per volume.³ Therefore, patterning the substrate with features at a particular pitch may or may not result in persistence of that length scale. We anticipate that it should be possible to drive the phase separation *at resonance* if the pattern length scale matches the *fastest growing wavelength* set by capillarity. We further anticipate that the latter should be tunable via modification of the individual interface tensions. Combining appropriate patterning and interface tension control it may be possible to achieve vertical self-assembly of molecular phase separation at a desirable lateral length scale.

1.2 Objective

The major purpose of this thesis is to understand how the self-assembly of the molecular domains studied here depends upon the deposition parameters that we can control. We assume that the supersaturation rate can be practically controlled to some extent via controlling the evaporation rate of the solvent during deposition.

As detailed below, the goals in this thesis are (1) to investigate whether we can practically drive a solute phase separation via a nucleation and growth process or a spontaneous decomposition of organic mixtures and (2) to determine whether the phase separation can be selectively nucleated at particular sites, of a desired spacing, on

patterned substrates. A third goal is to determine whether the minimum site spacing can be altered by adding surfactant, in order to reduce the interfacial tensions.

1.3 Background

As a large part of the technological motivation for this work is eventual application to organic solar cells, in this section we will describe the phase separation process between electron-donor/electron-acceptor mixtures that is essential for a high efficiency organic solar cell.

The phase separation process can be thought as a type of phase transformation and, therefore, under certain conditions, the kinetics can be described by the classical nucleation theory. Understanding phase formation processes is crucial in order to appropriately choose initial and boundary conditions under which self-assembly of molecules into desirable configurations occur.

For a ternary system (two solutes plus a solvent), the thermodynamics underlying phase separation can be illustrated with a phase diagram (Figure 1-1) describing the different phases occurring on changing the concentration of solutes in the solvent (supersaturations – y-axis) at a given composition of the solutes in the solvent (x-axis). In Figure 1-1, we present the schematic of this phase diagram considering the two solutes (tn-ZnPc and PCBM) and the solvent (chloroform) used in this work. For the formation of solid phases from the liquid solution, the difference of the chemical potential $\Delta\mu$ of each component molecule between that in a solid phase and that in solution is a convenient measure of its supersaturation. We note in passing that our description will hold only in the limit that the system remains close enough to equilibrium that the

chemical potentials can be defined. In the homogeneous region (point A) the solution is stable and there is no driving force for phase separation. In this case the solutes are completely dissolved in the solvent. The binodal curve (intersected at point B) describes the coexistence of phases of different solute concentrations under given conditions and corresponds to a saturated solution. As we increase the supersaturation (via evaporation of the solvent) we cross the binodal, and the system begins to phase separate, via nucleation into individual domains of different solute concentrations which then grow. Further solvent evaporation moves the system from the binodal towards the spinodal. If the nucleation did not take place at the binodal region, then, at the point of crossing of the spinodal (point C) decomposition into different solute concentration regions occurs spontaneously. This occurs when there is essentially no barrier for nucleation. Inside the spinodal region (point D) the mixture decomposes, initially at a fixed wavelength, followed by a regime of coarsening of the individual phase separated domains.

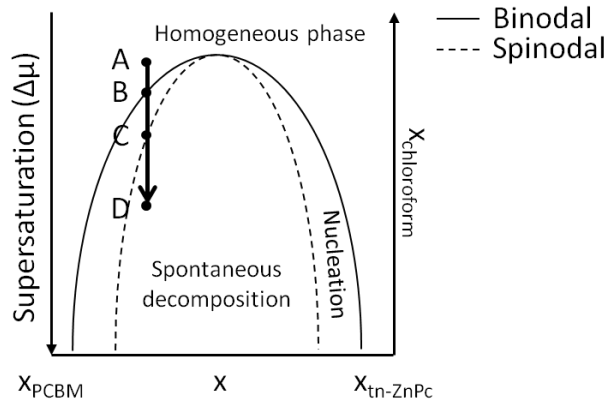


Figure 1-1. Phase diagram showing the binodal and spinodal curves.

For a supersaturation between the binodal and spinodal, when a cluster reaches a size greater than a critical value, a stable nucleus is formed. For the simplest case of a spherical cluster, the value for the critical radius is given by:³

$$r^* = \frac{2\gamma_{SL}}{\Delta G_v} \quad (1-1)$$

where γ_{SL} is the solid/liquid interfacial free energy/area and ΔG_v is the change of free energy per volume on formation of the new phase. The value of the activation (free) energy required to form a spherical nucleus is:³

$$\Delta G_{hom}^* = \frac{16\pi\gamma_{SL}^3}{3(\Delta G_v)^2} \quad (1-2)$$

In order to decrease this energy barrier, the interfacial energy/area must be reduced. This can occur if the new phase wets a planar substrate, leading to preferential heterogeneous nucleation. The value of the energy barrier for heterogeneous nucleation is:³

$$\Delta G_{het}^* = \frac{16\pi\gamma_{SL}^3 S(\theta)}{3(\Delta G_v)^2} \quad (1-3)$$

where $S(\theta)$ is the “shape factor” that can be described (for simple cases) via a “wetting” angle between the surface of the nucleus and the substrate where their contact ends (Figure 1-2).

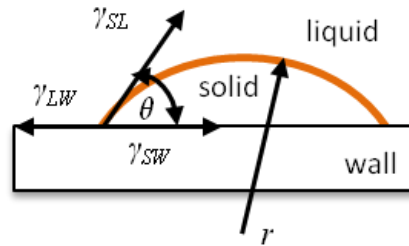


Figure 1-2. Schematic of the nucleus forming on the substrate wall and forming the contact angle.

Small wetting angles correspond to a small shape factor and a small substrate/adsorbate interfacial free energy; thus, the energy barrier for nucleation is decreased. Equation (1-3) says that the barrier for heterogeneous nucleation is smaller than the homogenous

nucleation barrier by the shape factor. The critical radius r^* for heterogeneous nucleation has the same value as the homogeneous case, meaning that it only depends on the supersaturation or equivalently on ΔG_v . In the presence of cavities on the substrates, the nucleation barrier can be reduced even further, because the critical volume of the nucleus V^* formed at the bottom of the cavity can be very small even at large contact angles:³

$$\Delta G_{cavity}^* = \frac{1}{2} V^* \Delta G_v \quad (1-4)$$

There is a limit to how small the cavity can be however, which is imposed by capillarity. The cavity must be large enough that the nucleus radius does not decrease below r^* .³ In Figure 1-3 we present schematically the activation barrier as a function of the nucleus radius for the three different nucleation processes described (in liquid, on a substrate, and in a cavity).

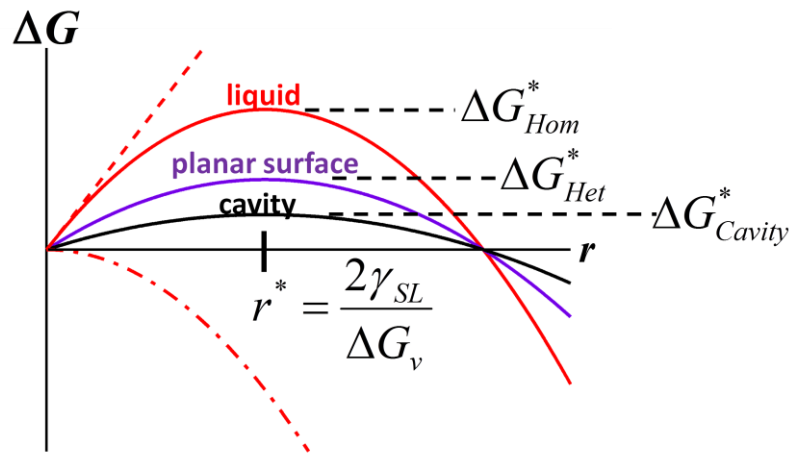


Figure 1-3. Activation barrier (ΔG) as function of the nucleus radius for the three different nucleation processes (in liquid, on a substrate, and in a cavity).

In this thesis project a principal goal is to investigate whether, by choosing appropriate conditions of supersaturation, substrate surface tension and nucleation sites,

we can promote a small length scale vertical self-ordering of two organic components from solution.

Toward the particular application of highly efficient organic solar cells, it is necessary to understand how closely packed donor/acceptor molecular domain boundaries should be for high PCE. We consider the diffusion of excitons in a phase separated mixture. The diffusion length of an exciton (L) can be written as:⁴

$$L = \sqrt{D\tau} \quad (1-5)$$

where D is the exciton diffusion coefficient and τ is the exciton lifetime (time to recombination). In organic materials this length is typically of the order of 10 nm.⁵ Efficient charge separation can occur if the individual domain size (δ) is comparable to or less than L . In Figure 1-4 we show a schematic of the process of photocurrent generation in an OSC and the expression of the External Quantum Efficiency (EQE) used in this field for quantifying the efficiency of a solar cell.

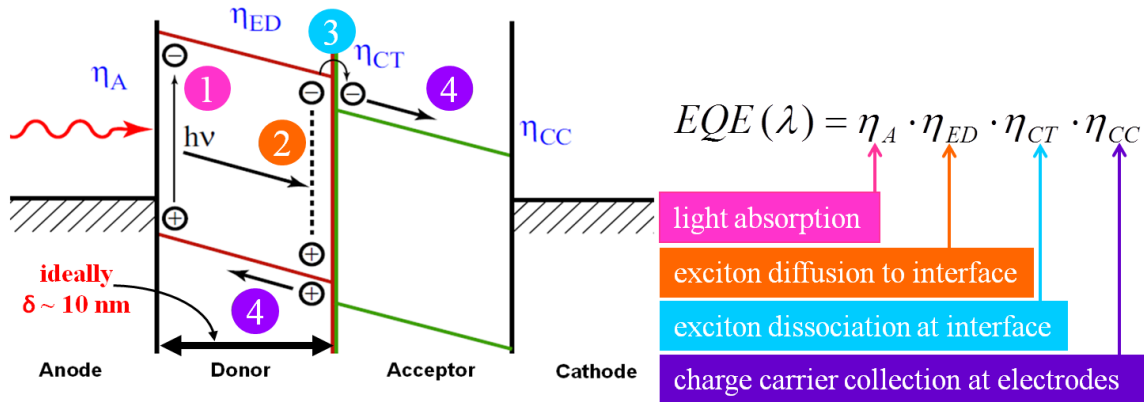


Figure 1-4. Schematic of the photocurrent generation process occurring in an OSC. EQE is the external quantum efficiency.

In organic semiconductors, exciton diffusion occurs through successive energy transfer hops between molecules of the same species, which are called Förster Resonance

Energy Transfer events. According to the Förster theory, the rate of energy transfer (k_F) is given by:⁶

$$k_F = \frac{1}{\tau} \left(\frac{R_0}{d} \right)^6 \quad (1-6)$$

where R_0 is the Förster radius, defined as the molecular distance at which the efficiency for energy transfer is 50% and d is the intermolecular separation. Förster derived an expression that linked the exciton diffusion coefficient with the molecular properties and with R_0 , which is:⁷

$$D = \frac{A}{\tau} R_0^6 \rho^{4/3} \quad (1-7)$$

where A is a parameter accounting for the disorder in the molecular distribution and ρ is the number density. In this model a highly ordered and packed donor molecular organization should lead to an increased diffusion coefficient.⁸ In Figure 1-5 is shown a schematic of the effect that high crystallinity has on the hopping of excitons between molecules.

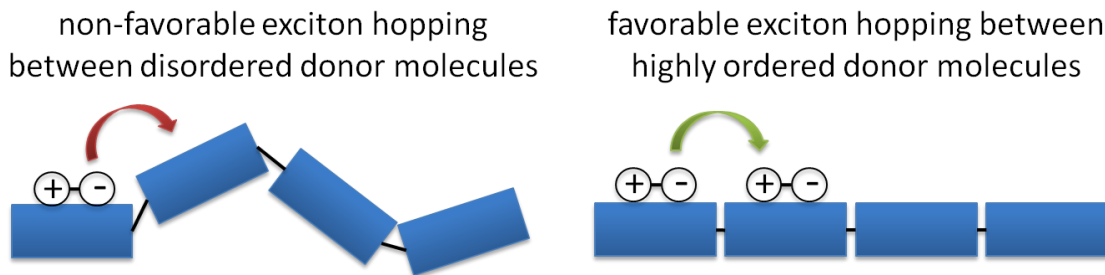


Figure 1-5. Schematic of the effect of the high crystallinity on the diffusion of excitons.

Improvement of the efficiency of a BHJ organic solar cell should be possible by either reducing the length of the donor/acceptor phase separation to the diffusion length of the exciton, or by increasing L , which in turn might be accomplished by modifying the

donor chemical structure for an enhanced self-ordering, and thus an increased diffusion coefficient.

Once separated, free charges must reach the electrodes to produce current. The probability for this to occur will depend on the morphology of the domain structure of the molecular mixture. A simple hypothesis is that creating continuous and aligned interpenetrating networks of donor and acceptor molecules (Figure 1-6) should allow free charges to have clear and shorter paths towards the electrodes, facilitating their transport.⁹

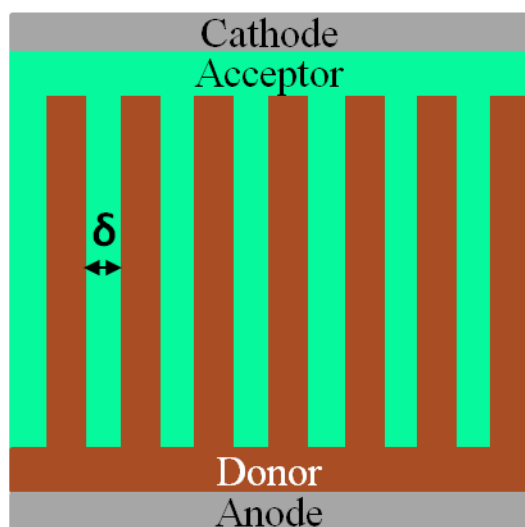


Figure 1-6. Schematic of the optimal geometry of the active layer in an organic solar cell.

Based on what we have said above, the length scale δ of the donor/acceptor phase separation, the crystallinity of the two phases, and the connectivity of the domains to electrodes all play important roles in the performance of an organic solar cell. Toward this end, in this thesis we investigate the possibility of spontaneous assembly of phase separated molecular mixtures with a target lateral domain sizes approaching 10 nm, high crystallinity of individual domains and vertical connectivity of domains of each phase between electrodes.

Chapter 2 – Materials and Experimental Methods

2.1 Approach

In this thesis, we carry out a study of molecular mixtures in a prototypical system consisting of tetranitro zinc-phthalocyanine (tn-ZnPc) and [6,6]-phenyl-C₆₁-butyric acid methyl ester (PCBM) using chloroform as a solvent, and native oxide-covered Si(111) substrates, to see whether capillarity and patterning might be used to control the nucleation and propagation, and thus the length scale of the phase separation.

The crystallinity of clusters of phase separating organic molecules is expected to depend on several factors, including the mutual interaction between molecules of the same species, the evaporation rate of the solvent during solution-processable depositions, interaction with impurity molecules, and annealing conditions. Our approaches in investigating these effects involve (1) varying the evaporation rate of the solvent during molecular deposition onto the substrate, (2) performing solvent vapor-annealing (SVA) and temperature-annealing of the deposited films, and (3) changing the stoichiometry of the mixture solutions.

The rate at which the solvent evaporates can be crucial in determining the morphology of individual molecular domains on a substrate. Very fast rates of evaporation favor spontaneous (“spinodal”) decomposition over nucleation. In addition, qualitatively, we expect that very fast solvent evaporation should limit the degree to which solute molecules can order within a domain. In contrast, slow enough solvent evaporation rates should place the system, at least initially, in the range of supersaturation where nucleation of the phase separation is favored. In addition, qualitatively, we expect

that slow evaporation should allow for more intermolecular interaction, leading to more ordered structures.

When allowing solvent vapor molecules to interact with polymeric organic films, it is known that they can adsorb onto the films and become partially dissolved within the macromolecules, acting as “plasticizers”, increasing the mobility of film molecules,¹⁰ and favoring ordered self-assembly in crystalline structures much larger than the amorphous structures.¹¹⁻¹⁴

We note that thermal annealing has been widely used to induce the formation of, and modify the morphology of phase-separated regions of donor and acceptor materials.¹⁵⁻¹⁷

The simple model illustrated schematically in Figure 1-1 suggests that the concentration of the individual molecules in the mixture solution determines the phase transformation kinetics as function of the supersaturation. For the case illustrated by the schematic, a 1:1 stoichiometry would lead to a spinodal decomposition rather than nucleation and growth for any finite supersaturation, whereas off 1:1 a range of supersaturations producing nucleation and growth kinetics would exist. To explore this effect, in this thesis we investigate the results on the phase formation derived by different stoichiometries.

During molecular deposition onto a substrate, the tendency of molecules to deposit in a particular region depends not only on the molecule-substrate interaction, but also on the interactions occurring between solvent and solute. A goal of this thesis is to gain an understanding of such interactions during the evaporation of the solvent for eventual predictability and control of the molecular domains on the underlying substrate.

As a first step toward this understanding, we investigate the phenomena that occur during the evaporation of a sessile droplet of solvent, in this case chloroform, on an oxide-terminated silicon substrate in presence of, and in the absence of organic molecular solutes.

Finally, we explore the role that a topographically-patterned surface might play in directing the phase separation of individual molecules from a solvent-containing mixture. We adopt a combinatorial approach, fabricating arrays of topographical pits whose diameter and spacing are varied independently. In our initial investigations the pit diameters are varied over a range from 0.7 to 8 μm , the spacing from 1.4 to 16 μm with the average depth of the pits fixed at (48 ± 1) nm. We will see that these large characteristic size-features do not obviously affect the self assembly of the molecules. Later, we lowered the size of the pattern to 30 – 360 nm for the diameter and to 60 – 720 nm for the spacing. The depth varies from ~ 30 to ~ 70 nm depending on the sizes of the pits and exceeds the RMS roughness amplitude by nearly two orders of magnitude, and should allow the imposed pattern to dominate the topography. Our combinatorial approach should allow us to study the relation between particular domain morphologies and specific pattern size.

Additionally, we modified the patterned silicon surface tension, using a hydrosilylation process, in order to have H-terminated patterned silicon surfaces, to determine whether the hydrogen atoms at the surface provide a stronger interaction of the organic molecules with the pattern.

2.2 Materials and Methods

As a prototypical system for exploration of directing phase separation we have chosen tetranitro zinc phthalocyanine (tn-ZnPc) and phenyl-C₆₁-butyric acid methyl ester (PCBM) as component molecules, chloroform (CHCl₃) as a solvent, and Si(111) as a substrate.

Tn-ZnPc's are phthalocyanine molecules (Pc) with nitrite functional groups (–NO₂) attached to the four isoindole groups, as illustrated schematically in the left panel of Figure 2-1. Nitrite functional groups are capable of strongly withdrawing electrons from the metal core of a Pc molecule, making these molecules very good electron-donor organic semiconductors.¹⁸ Phthalocyanines molecules were selected as electron-donor component because of their thermal and chemical stability.¹⁹ Additionally, phthalocyanines functionalized with –NO₂ groups are more soluble in organic solvents.²⁰ Another advantage of using phthalocyanines is based on the necessity to enlarge the harvested fraction of the solar spectrum. Therefore, since almost half of the total energy of the sunlight appears at wavelengths below 700 nm, phthalocyanines are good candidates because exhibit light absorption at ~ 690 nm.¹⁹

PCBM is a fullerene derivative molecule, created by adding a phenyl group (–C₆H₅) and a methoxy group (–O–CH₃) to the Buckminsterfullerene C₆₀, as illustrated in the right panel of Figure 2-1. Both of these functional groups are electron-donating, making the PCBM molecule an excellent electron-acceptor. PCBM is one of the most commonly used electron-acceptor component molecules in organic solar cells research field, because of its high electron affinity and ability to transport charges, as well as high solubility in many organic solvents.²¹

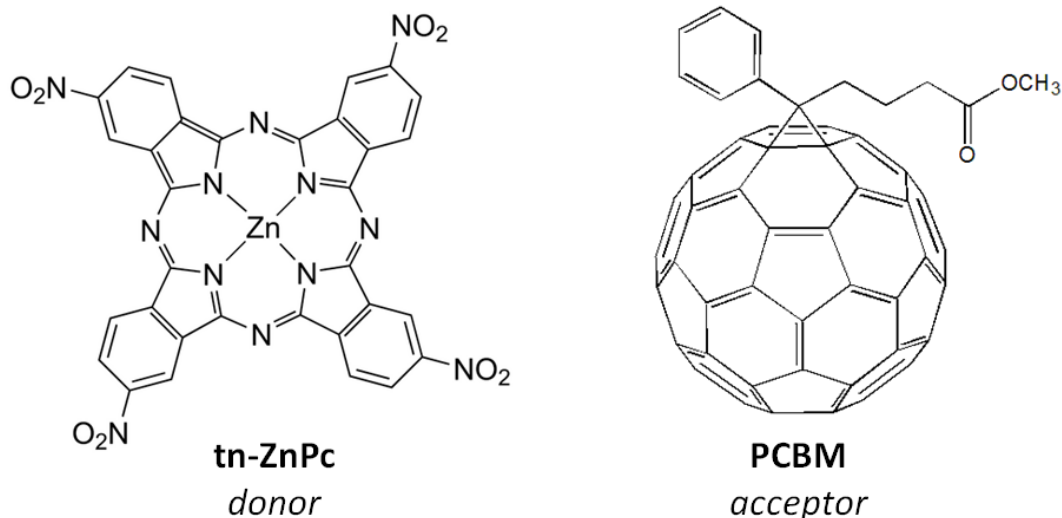


Figure 2-1. Tetranitro zinc phthalocyanine (tn-ZnPc) and phenyl-C₆₁-butyric acid methyl ester (PCBM) molecules.

The molecules are deposited in chloroform-based solutions onto silicon substrates using a variety of techniques in this work. We choose chloroform as solvent based on preliminary solubility tests.

The choice of Si(111) substrates was mainly due to the near-atomic surface flatness available. We prepared the substrates via RCA cleaning²² prior to molecular deposition; however, the presence of naturally occurring native oxide and hydrocarbons at the surface is nearly inevitable.

A number of techniques were used in characterizing the structures and properties of our samples. We characterized the morphology of the substrates before and after deposition using atomic force microscopy (AFM) and scanning electron microscopy (SEM). The sizes of molecular clusters in solution were analyzed through dynamic light scattering (DLS) measurements. The chemical composition of the deposited films was investigated via X-ray photoelectron spectroscopy (XPS) and energy dispersive X-ray spectrometry (EDS). To characterize the local properties of the deposited films, we

performed force-curve experiments in an ambient-controlled AFM system; this allows determination of the adhesive interaction between a spherical AFM probe and sample, and provides a means of testing the local surface termination. The crystallographic properties of both powders of single-component molecular solids and of deposited molecular films were investigated through X-ray diffraction analysis (XRD). The optical properties of tn-ZnPc and PCBM molecules in solution and in deposited films were measured with a UV/visible/near-IR monochromator. Their vibrational characteristics (related to the type of chemical bonds) were probed via Fourier transform infrared spectroscopy (FTIR) and Raman scattering spectroscopy. The interactions of the molecules with the silicon substrate (i.e. the orientation of the molecules on the substrate) were analyzed with FTIR spectroscopy in an attenuated total reflectance (ATR) mode, with incident polarized light.

Individual molecular solutions were prepared in chloroform at a concentration of 0.25 mM and followed by sonication for 10 minutes. For molecular mixtures solutions each type of molecule in chloroform were mixed in a ratio of 1:1. For such a mixture, the individual molecular concentrations are halved to 0.125 mM. Additional investigations on stoichiometries different than 1:1 are also reported in this work. The single molecules and their mixture were deposited onto the substrate in a N₂-glovebox using three different approaches: (1) spin-coating, (2) drop-casting, and (3) immersion in solution, as illustrated in Figure 2-2.

Spin-coating results in relatively rapid evaporation of solvent, suppressing the subsequent action of solvent vapor on the deposited molecular film. Abrupt increases in solute concentration might be expected to favor spontaneous decomposition, rather than

nucleation of the phase separation. In addition, the rapid loss of solvent might be expected to suppress order within clusters of molecules. We investigated the results of this mode of deposition for four different spin rates: 500, 1000, 2000, 3000 rpm, in each case for a duration of 45 seconds. Each spin-coating process can be thought of as consisting of two stages. In the first stage the initial outflow of solution is dominant and the evaporation of the solvent can be neglected; consequently, the concentration of solute in the solution does not change appreciably in this stage. Once the thickness of the solution drops to a certain level (approximately 1/3 of its initial value) then the flow of solution nearly ceases, and significant solvent evaporation dominates this final stage.²³ During this stage, the solute concentration rapidly increases and the evaporation rate can be estimated by the formula proposed by Bornside *et al.*:²⁴

$$e = \kappa(x_l^0 - x_{l\infty}) \quad (2-1)$$

where κ is the mass-transfer coefficient, x_l^0 is the initial mass fraction of the solvent in the coating solution and $x_{l\infty}$ is the solvent mass fraction in the coating solution that would be in equilibrium with the solvent mass fraction in the vapor phase. The expression for the mass-transfer coefficient is given by:

$$\kappa = \left(\frac{cD_v}{\nu_v^{1/2} \rho} \right) \left(\frac{p_l^0 M_l}{RT} \right) \omega^{1/2} \quad (2-2)$$

where c is a constant that depends on the Schmidt number of the overlying vapor, D_v is the binary diffusivity of the solvent in the overlying vapor, ν_v is the kinematic viscosity of the overlying vapor, ρ is the solution density, p_l^0 is the vapor pressure of the pure solvent at temperature T , M_l is the solvent molecular weight, R is the ideal gas constant and ω is the spinning rate. Due to a lack of numerical values for many of the parameters

needed to calculate the evaporation, we do not have estimations for the rate at which the solvent evaporates during spin-coating, but we find visual indications that they are the fastest of the techniques we study here.

In the *drop-casting* method, significant solvent vapor annealing (SVA) takes place only if the deposition is performed in a closed or nearly-closed environment; in such a case the solvent vapor does not escape, but instead evaporates and recondenses continuously, remaining in intimate contact with the molecular film. In this work, drop-casting was performed instead in an open system, so that the vapors of the chloroform solvent escaped without significant interaction with the surface. The drop-casting method allows performing depositions at lower rates of evaporation than spin-coating, typically very close to the “standard” rate of the solvent in ambient condition.

During molecular deposition via *immersion in solution*, the substrate was placed into a cylindrical container with one open end. We found that the rate of evaporation of the solvent was much lower in this case than for the first two methods. Slow enough solvent evaporation should favor nucleation and growth molecular phase separation kinetics. This method allows enhanced molecular self-ordering on the SiO₂ surface. Once the solvent has evaporated we expect some continued interaction of its vapor with the adsorbed PCBM and tn-ZnPc phases, due to the shape of the container. In a variation on this technique we further decreased the evaporation rate by covering the cylindrical well with a cap containing a small aperture. We expect that this more nearly-closed configuration should enhance SVA effects. Figure 2-2 shows a schematic representation of the three methods of deposition described above, along with the small aperture-variation of the third method.

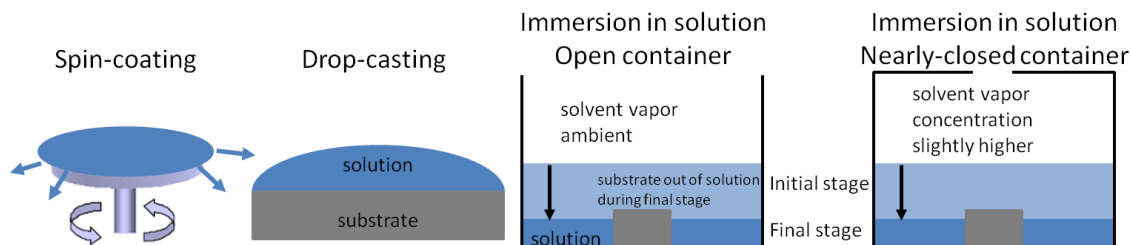


Figure 2-2. Schematic representation of the three methods of deposition used in this work. Last image shows the variation of the method of deposition by immersion, in order to reach even lower evaporation rates.

The evaporation rates for the last two approaches were determined by measuring the change in mass with time using a microbalance. We observed slight differences between the evaporation rate of the solvent in presence of the organic molecules during drop-casting deposition (reported in detailed in Chapter 6), but for simplicity in this chapter we approximate the evaporation rate as essentially the same as that for the pure solvent. As we discuss in Chapter 6, the evaporation of solvent during drop-casting method shows two regimes: an initial faster stage and a final, slower stage. We will discuss this in terms of the presence of small concentrations of insoluble impurities or particles (which increase as the solvent evaporates) that suppresses the thermal Marangoni effect on the free surface, by reducing the radial flow, and this slows the evaporation rate.²⁵ On the other hand, the evaporation rates for the two variations we investigate on immersion (open and nearly-closed container) comprise two regimes as for drop-casting. However in this case, given the large amount of liquid (3 mL), the difference in rate we will attribute to the action of the vapor, which evaporates and recondenses, not to the shape of the liquid or internal flows as for drop-casting, where the surface-to-volume ratio is larger. In the two variations of immersion in solution employed here, the initial regime is linear. This is due mainly to the fact that the liquid layer is

uniformly flat, and that the aperture of the container acted as a throttle. The final regime initiates when the volume of the remaining liquid becomes relatively small and the effect of the shape of the container becomes negligible. During the final stage of deposition via immersion, the substrate surface is physically above the top of the solution; continued changes in the rate of solvent loss beyond this are likely not significant for the organization of the molecules on the substrate. In contrast, in deposition via drop-casting, the final regime is important in determining the self-organization of the organic molecules on the substrate. In Figure 2-3 we report the graph of the mass change of chloroform for the drop-casting, immersion in open cylinder and immersion in nearly-closed cylinder.

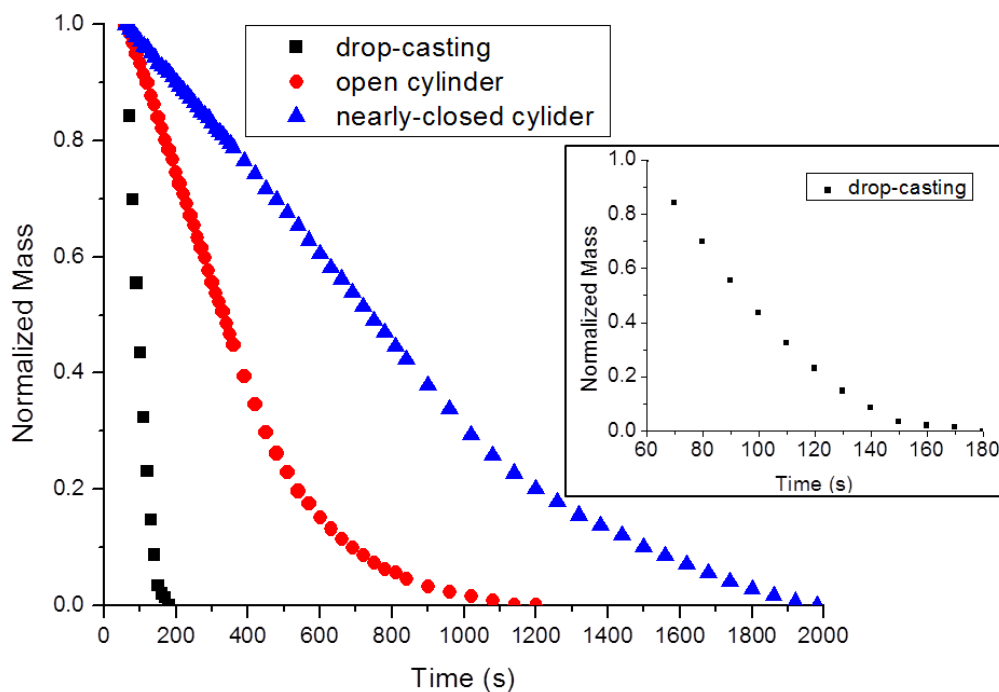


Figure 2-3. Mass change of chloroform as a function of time, for the drop-casting, immersion in open container, and immersion in nearly-closed container.

For a simple comparison, we list estimations of the evaporation rate during spin-coating and the *initial* rates for the three cases for which we have made a determination: $>> 10^{-2}$ ml/min, (0.030 ± 0.002) mL/min, (0.00347 ± 0.00001) mL/min and (0.0017 ± 0.0005) mL/min for deposition via spin-coating, drop-casting, immersion in open cylinder and immersion in nearly-closed cylinder, respectively. In Table 2-1 are reported the values of the evaporation rates in the initial and final regimes.

Evaporation rate (mL/min)	Drop-casting	Open cylinder	Nearly-closed cylinder
Initial regime	0.030 ± 0.002	0.00347 ± 0.00001	0.0017 ± 0.0005
Final regime	0.022 ± 0.006	0.02 ± 0.01	0.010 ± 0.004

Table 2-1. Values of the evaporation rates of chloroform of the initial and final regimes for the drop-casting, immersion in open cylinder, and nearly-closed cylinder.

Chapter 3 – Phase Separation and Crystallization on Unpatterned Substrates

In this chapter, we present the results of experiments based upon: the various deposition methods described in Chapter 2 on unpatterned substrates, variation of the relative concentrations of the individual molecules within the mixtures, the effect of the solvent vapor annealing and thermal annealing on the phase separation of the two components. We also present results of investigations of molecular aggregation while still in liquid solution based upon dynamic light scattering analysis. Finally, we present the results of characterization of the adhesion forces between the two materials deposited on silicon and the AFM probe through force curve measurements.

3.1 Deposition onto Unpatterned Si(111) Substrates

In the first major phase of this work we investigated the behavior of the molecules when deposited from solution onto a nominally flat, native-oxide-terminated Si(111) surface.

The single molecules and their mixture were deposited from a chloroform-based solution according to the four methods of deposition described above. Our first results were for a 1:1 relative molecular composition of the tn-ZnPc/PCBM mixture, i.e. the same molarity of each in solution. Below we describe the results of each method of deposition for each solution.

3.1.1 Deposition Method by Spin-Coating

3.1.1.1 Spin-Coating Deposition of PCBM only

Example results for PCBM molecules deposited via spin-coating are shown in the form of height-contrast AFM images in Figure 3-1(a-d). The molecules in this case aggregate in a uniform and quasi-continuous layer (that we will refer to as a “blanket” phase) for the lowest rate investigated. This is seen in Figure 3-1(a), where the blanket phase is detectable via the presence of small holes, exposing the underlying substrate. The thickness of this blanket is (4.4 ± 0.3) nm. This blanket form of assembly gradually breaks down as the spin rate is increased, with molecules aggregating into spherical caps, and the holes in the blanket increasing in density; this is seen in Figure 3-1(b). The left panel of Figure 3-2 shows that the area coverage of the PCBM domains (calculated from AFM images as the area projected by the PCBM domains on the surface) decreases as we increase the rate of spinning. By a spin rate of 2000 rpm, the blanket phase is no longer obvious (Figure 3-1(c)), instead we observe spherical caps. Our XRD measurements subsequent to spin deposition at 2000 rpm do not show detectable crystalline character of the PCBM spherical caps; i.e. we do not observe Bragg peaks in the scattered X-ray intensity. This might be due to either an amorphous PCBM structure or to very weak peaks whose intensity is below the noise level of the measurement from this phase; by contrast, below we will show evidence for crystallinity of PCBM clusters for much slower solvent evaporation rates. The diameter of the base of the spherical caps decreases as the spin rate increases: ~ 80 nm at 2000 rpm and ~ 60 nm at 3000 rpm. This is qualitatively consistent with the increase of supersaturation as the evaporation rate of the

solvent increases, and the fact that the critical radius is inversely proportional to the supersaturation (Equation (1-1)).

3.1.1.2 Spin-Coating Deposition of tn-ZnPc only

We find that tn-ZnPc molecules assemble into rod-shaped clusters across the range of spin rates we have investigated. Example AFM images are shown in Figure 3-1(i-l). The area coverage is relatively constant ($\sim 10.25\%$) across this range as shown in the left panel of Figure 3-2. As for the case of PCBM alone, the sizes of the rods decrease as the spinning rate increases, as shown in Figure 3-3. Here the measured “width” and “height” only are summarized; we note that in addition the length changes considerably (from $(0.29 \pm 0.05) \mu\text{m}$ to $(2.3 \pm 0.5) \mu\text{m}$). Once again, this qualitatively consistent with what might be expected based on the supersaturation increasing with the solvent evaporation rate.

A simple analysis based of the tn-ZnPc coverage suggests that most of the molecules deposited onto the substrate are spun away with the solvent during the initial outflow. The theoretical coverage that we would expect if all the tn-ZnPc molecules remained is $\Theta = 6.035 \times 10^{15}$ molecules/cm², while the average coverage determined from the AFM images of spin-coated tn-ZnPc is $\Theta = 1.123 \times 10^{15}$ molecules/cm². Thus we find that the actual tn-ZnPc coverage is approximately a factor of 5.36 lower than the theoretical case in which no outflow is present.

Given the low solubility of tn-ZnPc in chloroform (estimated experimentally ~ 0.28 mg/mL, i.e. 0.37 mM) and the high evaporation rate of the solvent, it is reasonable to ask if they might start to agglomerate in rods while still in liquid solution, and then

simply precipitate onto the substrate. Below we will see evidence that most of these molecules exist in stable agglomerates of $R_h \sim 100$ nm, even at low concentrations, and that at higher concentrations they aggregate into much larger clusters (microns sizes).

As a means of identifying the molecules comprising the various phases adsorbed onto the silicon substrate, we measured adhesion forces (F_{ad}) between the AFM tip and different regions of the sample surface. We carried out force-curve measurements in the “flat” regions between the tn-ZnPc rods, which we contrast with similar measurements from a “bare” (i.e. native oxide-covered) Si(111) substrate. The values are different: (352 ± 7) nN for bare silicon vs. (656 ± 7) nN for the flat regions between rods of tn-ZnPc, shown in Figure 3-4. The very large adhesive force in the second case is consistent with a substantial electrostatic dipole moment for the initial uniform “wetting” layer. The formation of this wetting layer indicates that the interaction between substrate and tn-ZnPc molecules dominates the intermolecular interaction in the formation of this phase. We believe that the formation of the wetting layer is an indication that not all the tn-ZnPc molecules cluster into rods in liquid solution, that there is an equilibrium between a low density dissolved phase and the rods. It is likely that the fraction that assembly into rod-like structures in solution increases with the supersaturation.

3.1.1.3 Spin-Coating Deposition of PCBM/tn-ZnPc (1:1) Mixtures

PCBM molecules when deposited onto the substrate from a mixture with tn-ZnPc in ratio 1:1 in a chloroform-based solution do not assemble into a uniform blanket-like phase at the lowest rate investigated (Figure 3-1(e)). We can see that the PCBM molecules (highest areas in the AFM image), instead of wetting the surface as in Figure

3-1(a), tend to agglomerate, leaving larger uncovered spots on the surface and growing in height. The thickness (or height) of this phase is (10 ± 1) nm. We interpret this difference in behavior as due to the presence of an underlying wetting layer, most likely of tn-ZnPc molecules. A plausible explanation is that this wetting layer lowers the interface plus surface tensions more than would the PCBM blanket-like phase. As we increase the spin rate, the formation of small spherical caps is observable (Figure 3-1(f-h)), as was the case for spin-coating of pure PCBM. Moreover, the left panel of Figure 3-2 shows that the area coverage of the PCBM domains decreases significantly at low spin rates when mixed with tn-ZnPc, consistent with PCBM agglomeration in the presence of the wetting layer of tn-ZnPc. All these results suggest that the PCBM molecules tend to separate from tn-ZnPc molecules and self-assemble into a separate phase.

Next we consider the effect of the spin rate on deposition of a mixture from solution. As shown in the right plot of Figure 3-2, as the spin rate is increased, the ratio between the area coverage of PCBM deposited from a single component solution and from the mixed solution decreases asymptotically to 1. A plausible explanation is that the tendency for the formation of the initial wetting layer of tn-ZnPc molecules decreases with increasing spin rate. For example, the larger supersaturation may enhance the tendency for tn-ZnPc molecules to aggregate from solution into rods, leaving fewer molecules in solution to wet the substrate. We also observe a dependence of the size and spacing of the PCBM spherical caps on spin rate: on increasing the rate from 2000 rpm to 3000 rpm, the diameters decrease from ~ 100 nm to ~ 50 nm, while the density of spherical caps per unit area increases from ~ 69 $/\mu\text{m}^2$ to ~ 254 $/\mu\text{m}^2$. This is again consistent with an increase in PCBM supersaturation with spin rate.

In spin-coating deposition of (1:1) mixtures of PCBM/tn-ZnPc from chloroform-based solution (Figure 3-1(m-p)) the sizes of the rod-like clusters decrease as compared with those forming from tn-ZnPc alone, as shown in Figure 3-3. This is likely due to the halving of the concentration of the tn-ZnPc molecules in the mixture in combining the two solutions: there being fewer tn-ZnPc molecules, the rods might be expected to be smaller. We do not find evidence that the decrease in size is due instead to the presence of the PCBM molecules; observations done for other evaporation rates (reported below) prove the stability of tn-ZnPc morphology on the substrate. The halving in the area coverage compared to that for deposition from a tn-ZnPc-alone solution to a spin rate-independent value of $\sim 4.5\%$ is consistent with the halving of concentration of tn-ZnPc molecules in the mixture; this can be seen in the left panel of Figure 3-2. Also, the slight decrease in the size of the rods as the evaporation rate gets faster, as discussed above for the previous cases, is consistent with the idea that they do not have time to coarsen significantly before coming out of solution.

An examination of the summary plots in Figure 3-2 makes clear a marked difference in the effect of adding a second type of molecule to the assembly of clusters of the two types of molecules, i.e. PCBM clusters and tn-ZnPc rods.

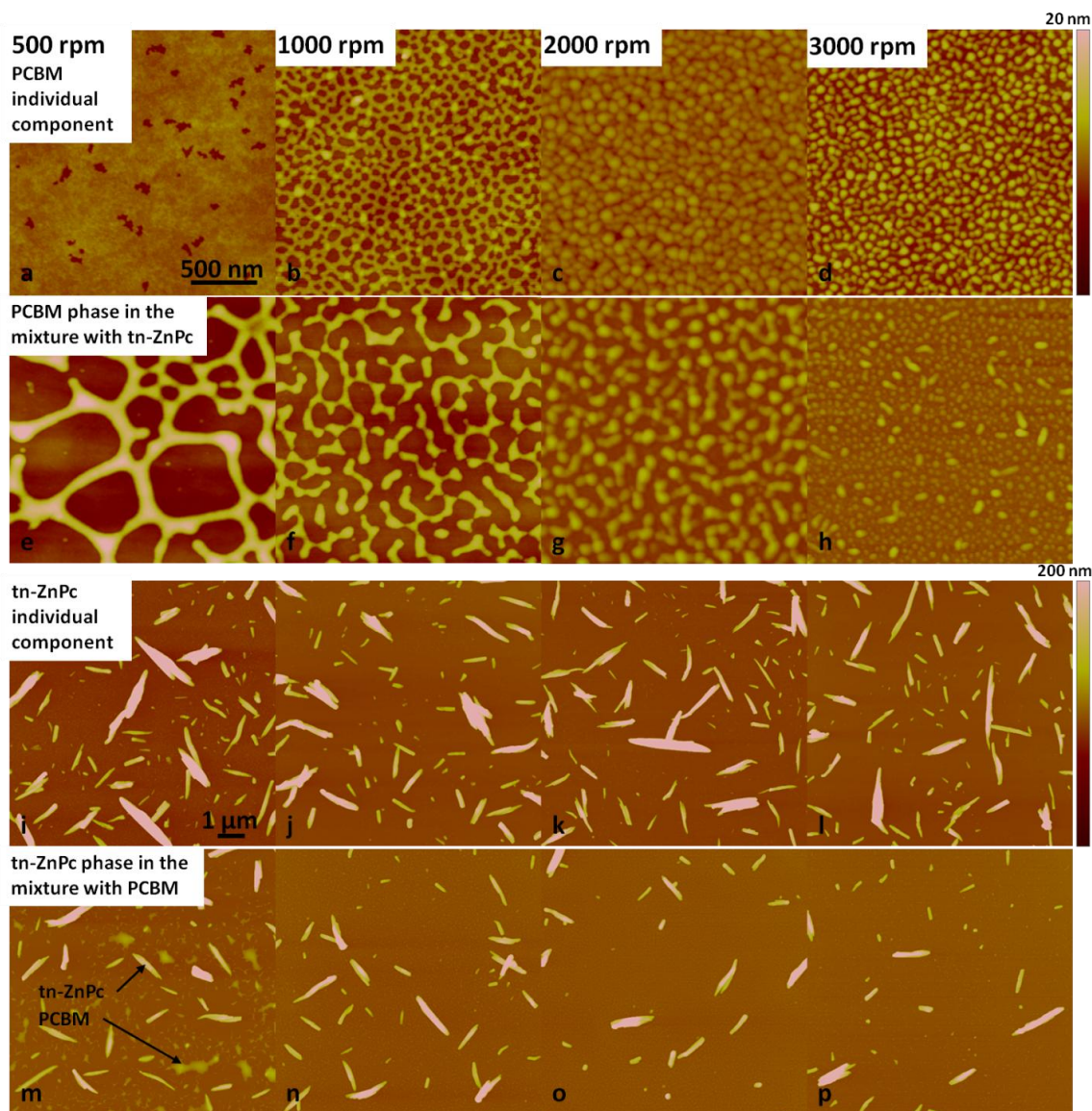


Figure 3-1. Height-contrast AFM images of the PCBM molecules deposited via spin-coating through single component solution and from the mixture with tn-ZnPc at (a, e) 500 rpm, (b, f) 1000 rpm, (c, g) 2000 rpm and (d, h) 3000 rpm, respectively. Height-contrast AFM images of the tn-ZnPc molecules deposited via spin-coating through single component solution and from the mixture with PCBM at (i, m) 500 rpm, (j, n) 1000 rpm, (k, o) 2000 rpm and (l, p) 3000 rpm, respectively.

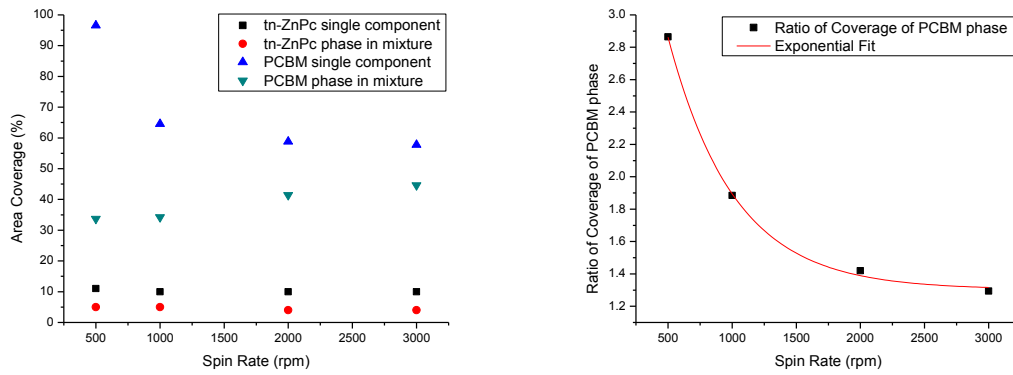


Figure 3-2. Projected area coverage, calculated in percentage for the PCBM and tn-ZnPc clusters domains deposited through single component solution and from the mixture with the other component at different spin rates (left). Ratio of the coverage of the PCBM phase deposited from single component solution and from the mixture, showing the asymptotical trend (right).

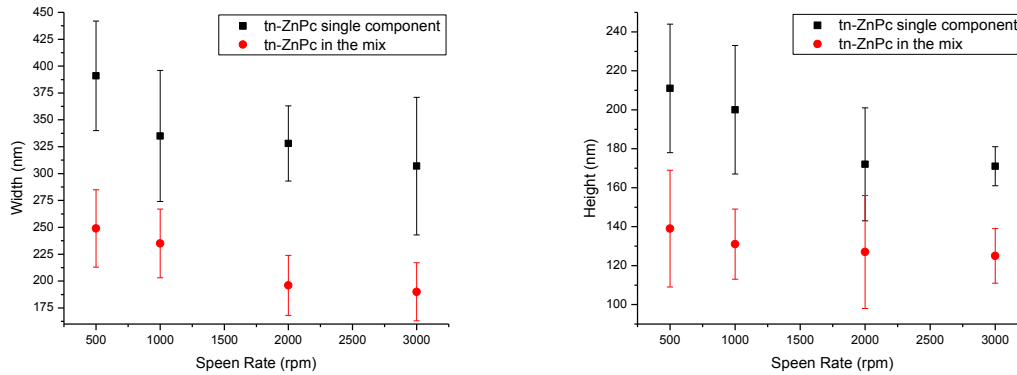


Figure 3-3. Width (left) and height (right) of tn-ZnPc rods deposited by spin-coating at different spin rates from single component solution and from the mixture.

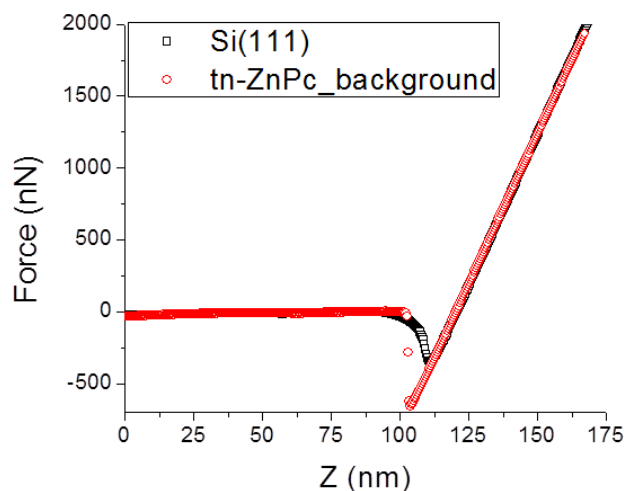


Figure 3-4. Adhesive forces measured on the silicon dioxide of Si(111) surfaces and on the flat regions between rods of tn-ZnPc deposited through spin-coating.

3.1.1.4 Conclusions for Spin-Coating Deposition Results

Here we summarize the results of spin-coating deposition on unpatterned native oxide-terminated Si(111) substrates. A general observation is that all the molecular domains investigated decrease in size as the evaporation rate increases, i.e. as the supersaturation rate increases. This does not give enough time to the clusters to coarsen before coming out of solution. We find that the self-assembly of PCBM clusters is highly affected by the presence of the tn-ZnPc, in particular at high evaporation rates, while tn-ZnPc seems to be very stable in presence of the other component. This suggests that at high evaporation rates PCBM molecules follow a spinodal decomposition, while at slower rates they assemble on the substrate via nucleation, and the form and size of the clusters depend on the surface tension and supersaturation. The formation of the stable tn-ZnPc rod-like clusters is likely to occur in solution; their assembly shows no obvious evidence for interaction with PCBM while in solution. Those tn-ZnPc molecules which do not assemble into rods strongly interact with the substrate, forming a wetting layer.

3.1.2 Deposition Method by Drop-Casting

3.1.2.1 Drop-Casting Deposition of PCBM only

Deposition via drop-casting allows each type of molecule present in the solution to interact with the oxide-covered Si substrate. In our experiments the substrate surfaces were oriented precisely horizontal to avoid the drops running off the surface, and visual observations showed that the solvent started to evaporate from the edges, and the evaporation front progressed inward, towards the center. In Figure 3-5 we show a photograph of a Si(111) substrate after PCBM deposition via drop-casting, showing macroscopic variations in contrast; we show below that this is due to differences in the local density, shape and sizes of molecular assemblies.

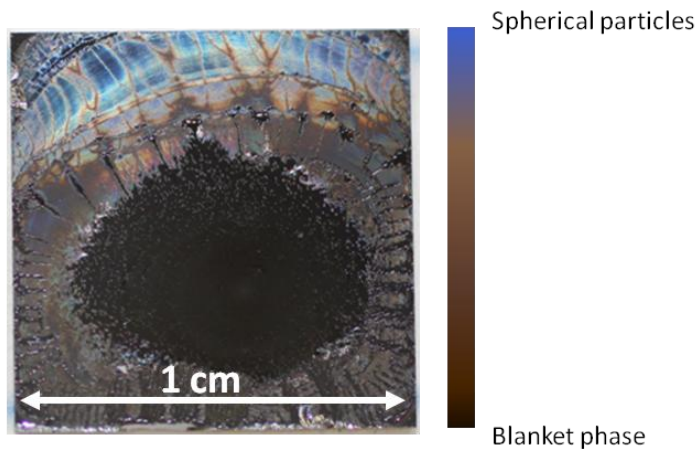


Figure 3-5. Photograph of a Si(111) substrate onto which PCBM molecules have been deposited via drop-casting.

We find that PCBM shows different growth habits, depending on the evaporation rate of the droplet. As seen in the optical microscopy image presented in Figure 3-6(a), PCBM molecules from a chloroform-based solution assemble on drop-casting into spherical caps at the edges of the substrates. As solvent evaporation initiates here, we

assume precipitation occurs first here as well. Figure 3-6(b) shows an image from the same sample, recorded near the center, in which the spherical domains have coalesced into a nearly continuous uniform layer. An analysis of our AFM images indicates that the average PCBM coverage in these regions ($\Theta = 8.146 \times 10^{15}$ molecules/cm²) is approximately a factor of 10 higher than near the edges ($\Theta = 8.143 \times 10^{14}$ molecules/cm²), and suggests that the coalescence is driven by a locally higher supersaturation; we discuss a possible mechanism for this below. XRD measurements on this phase did not show sharp reflections, suggesting that this coalesced phase of PCBM is amorphous. At the center of this phase, we observe occasional circular voids, in the center of which regions of taller, nearly faceted structures have seemingly nucleated; this is illustrated in Figure 3-6(c-e). A logical conclusion is that the growth of these (likely ordered phase) nuclei depletes the surrounding area of PCBM molecules. We find evidence, shown below, that such nuclei are the initial stage of hexagonal crystals that will grow further if we lower the evaporation rate further during the deposition.

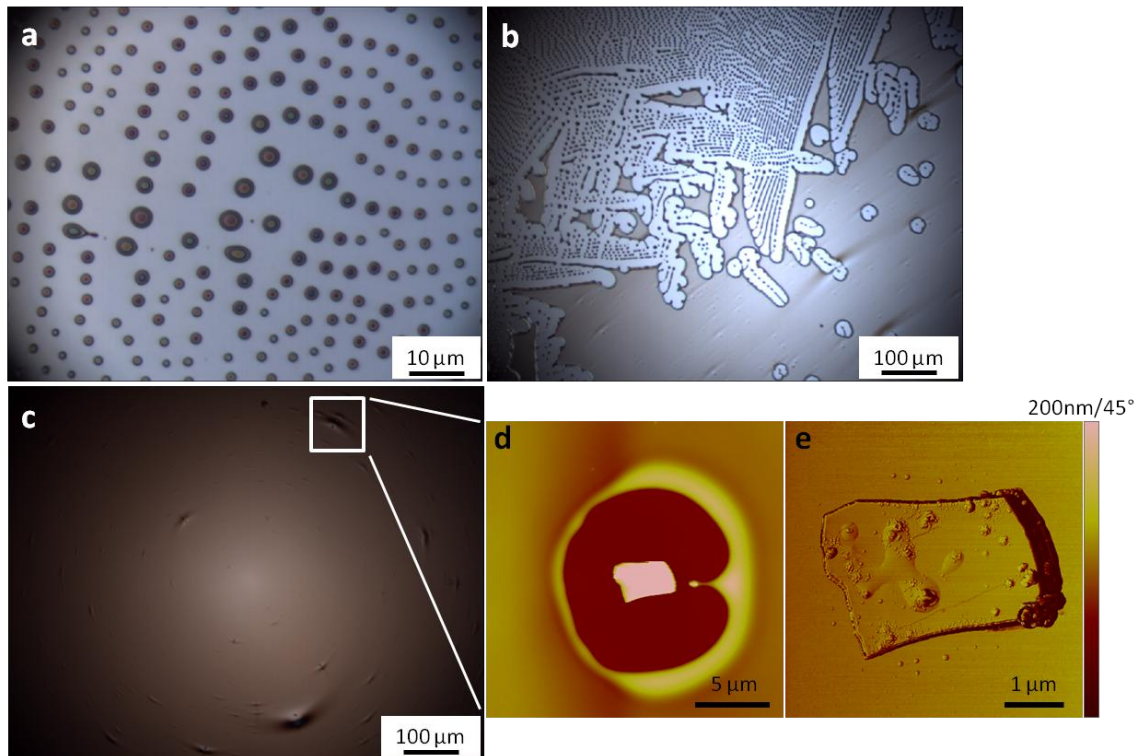


Figure 3-6. Optical images of the PCBM deposited through drop-casting onto Si(111) surface, from the edge of the sample (a), to the intermediate region where the blanket-like phase starts to form (b) to the center of the sample where the blanket-like phase is predominant (c). Images (d) and (e) are the height-contrast AFM image of one circular depletion zone appearing in the blanket-like phase and the phase-contrast AFM image of the magnification of the crystal visible at the center, respectively.

We now consider why a higher concentration of PCBM molecules is observed at the center of the substrate, as compared to at the edges. In the analysis of the evaporation of a droplet, the Marangoni number is defined as the ratio between the driving force and the viscous resistive force. It has been found that for Marangoni numbers above a critical value the flow inside the droplet will not be the same in the entire droplet bulk, but it will be separated into two regions by a so-called stagnation point that will appear on the free surface of the droplet (as it is illustrated in Figure 3-7).²⁶ The region adjacent to the contact line will be characterized by an outward flow directed towards the edge of the droplet, while the region far from the contact line will exhibit a convective flow in which

the motion is outward initially, but then turns towards the center of the droplet. At the stagnation point the surface flow will change its direction. Therefore, the particles transported in the convection flow region will move inward and deposit at the center of the substrate and those transported in the outward flow region will be directly deposited at the edge of the droplet forming the commonly observed “coffee- rings”.²⁷

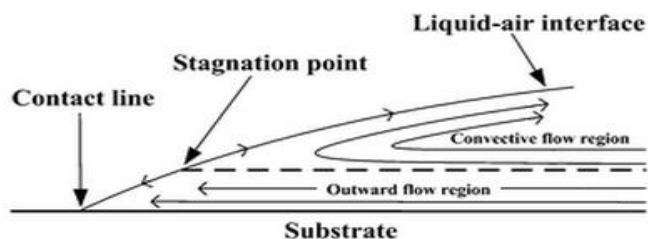


Figure 3-7. Schematics of the different flows occurring inside the droplet in presence of the stagnation point on the free surface of the droplet.²⁷ Highly soluble molecules are transported towards the center of the droplet, while less soluble molecules are transported towards the center of the droplet.

The tendency of molecules to be transported in these two different flows depends on the interaction solute/solvent. In presence of two solutes with different solubilities, in the early stages of solvent evaporation, one solute will be supersaturated while the other will be not. Supersaturated molecules will effectively have a repulsive interaction with the solvent and so tend to be transported toward the edge of the droplet where the loss of solvent is higher, whereas well subsaturated molecules that have attractive interaction with the solvent will be transported toward the center of the droplet, as shown in the schematics of Figure 3-8; where the darker regions denote higher concentration of material.

Given the patterns of molecular clusters observed on the substrate for both PCBM and tn-ZnPc, as we will see in the next sub-paragraph, it is likely that we are in the

regime in which the stagnation point originates on the surface of the droplet, generating different flux directions on the surface. Given the high solubility of PCBM in chloroform (estimated experimentally ~ 25 mg/mL, i.e. 27.5 mM), a larger amount of these molecules will likely be transported at the center of the droplet and then deposited at the central part of the substrate (Figure 3-8(a)).

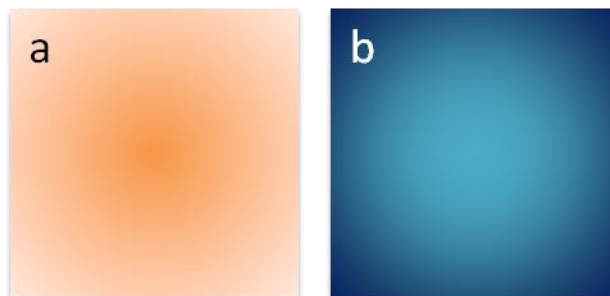


Figure 3-8. Schematic coverage maps of PCBM (a) and tn-ZnPc (b) after drop-casting deposition. The darker regions denote higher concentration of material.

3.1.2.2 Drop-Casting Deposition of tn-ZnPc only

In Figure 3-9 we show a photograph of a silicon substrate coated with tn-ZnPc molecules deposited via drop-casting from tn-ZnPc/chloroform solutions, showing visible contrast due to variations in the local density of rod-shaped clusters. We find that tn-ZnPc molecular clusters arrange in “coffee-ring” patterns that follow the contact line of the droplet as it shrinks. The coffee rings are visible across the entire substrate, but a larger concentration is observable at the edges of the sample rather than the center, suggesting that the deposition occurs through an outward flow from the droplet bulk to the edges of the droplet. This is consistent with the low solubility of tn-ZnPc in chloroform: a low solubility involves less molecules-solvent interactions and a faster reaching of the supersaturation. Therefore, the molecules, instead of flowing to the central region of the droplet, as occurs for PCBM, apparently tend to come out of the solution quickly and so

are transported towards the contact line, where the solvent evaporation rate is higher, depositing there (Figure 3-8 (b)).

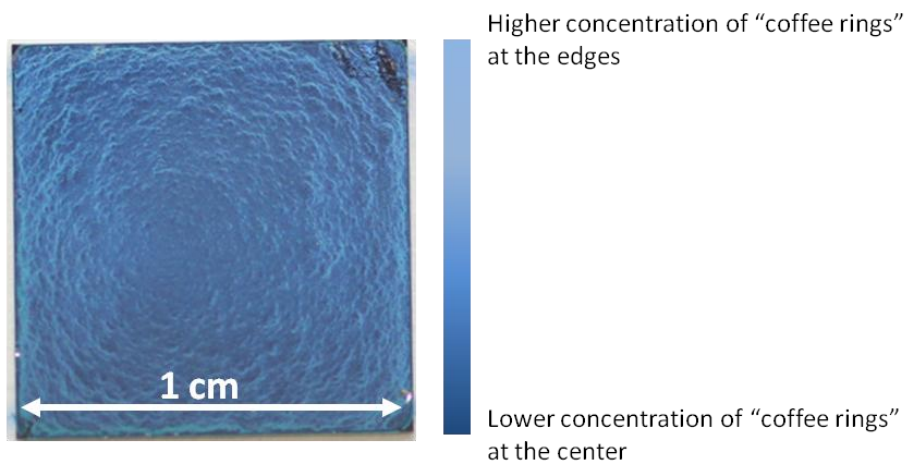


Figure 3-9. Photograph of a Si(111) substrate onto which tn-ZnPc molecules have been deposited via drop-casting.

The characteristic rod-like clusters of tn-ZnPc are visible in the SEM image of Figure 3-10(a). Figure 3-10(b) shows the optical image of a portion of a "coffee-ring" of tn-ZnPc clusters.

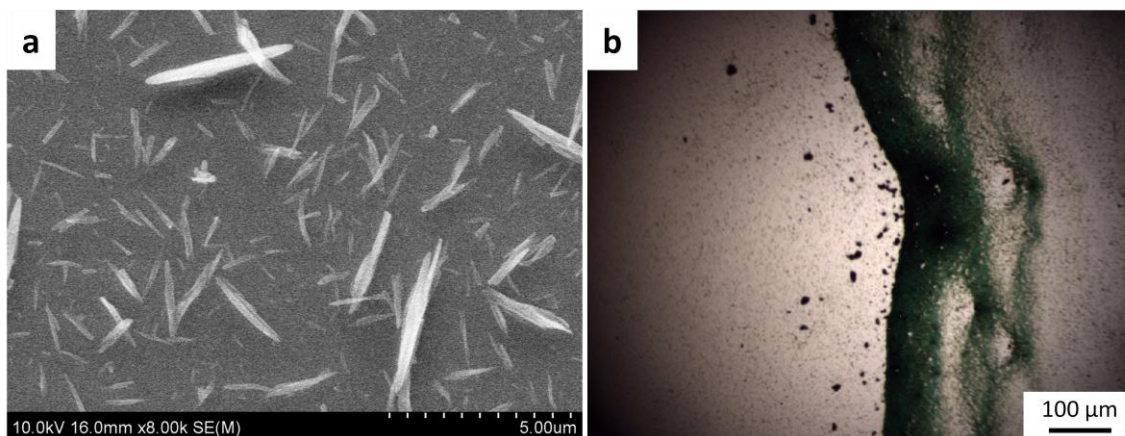


Figure 3-10. SEM image (a) and optical image (b) of the tn-ZnPc deposited through drop-casting onto Si(111) surface. Image (b) shows a portion of a "coffee-ring".

3.1.2.3 Drop-Casting Deposition of PCBM/tn-ZnPc (1:1) Mixtures

The molecular pattern of the drop-casted (1:1) mixtures of PCBM and tn-ZnPc molecules deposited from a chloroform-based solution is shown in the photograph of Figure 3-11. We can see that the “coffee-ring” pattern is dominant and that the overall color is grayish rather than bright blue (as for the pure tn-ZnPc, Figure 3-9). The grayish color suggests the presence of the blanket phase of PCBM (as discussed above for deposition of PCBM alone).

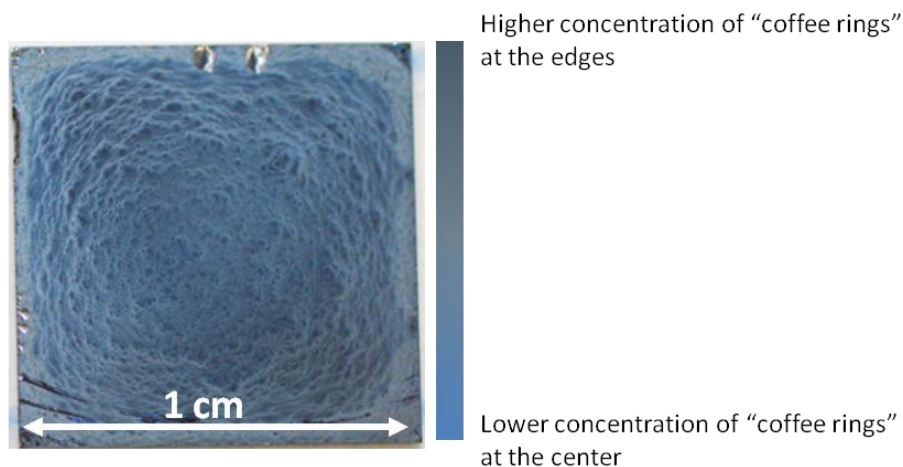


Figure 3-11. Photograph of a Si(111) substrate onto which the mixture in ratio 1:1 has been deposited via drop-casting.

The SEM image and the height-contrast AFM image (Figure 3-12(a-b)) show evidence for an amorphous blanket-like phase uniformly enshrouding a “carpet” of tn-ZnPc rods. In particular, the edges of the rods in both SEM and height-contrast AFM images are not well defined. This is most evident by the comparison between height-AFM and phase-AFM images (Figure 3-12(b-c)), which is sensitive to the elastic modulus of the components.

This molecular domain-coverage variation with position is consistent with the following model of interaction occurring between solvent and solutes: tn-ZnPc reaches supersaturations first and flows from the droplet bulk to the contact line precipitating on the substrate first and the PCBM that supersaturates later, is transported in an opposite convective flow depositing on top of the tn-ZnPc clusters.

An interesting observation based on our examinations of the molecular clusters is that the PCBM blanket phase does not show the beginning of the growth of ordered structures that we showed in Figure 3-6. The crystallization of PCBM might be prevented by the vicinity of the tn-ZnPc molecules.

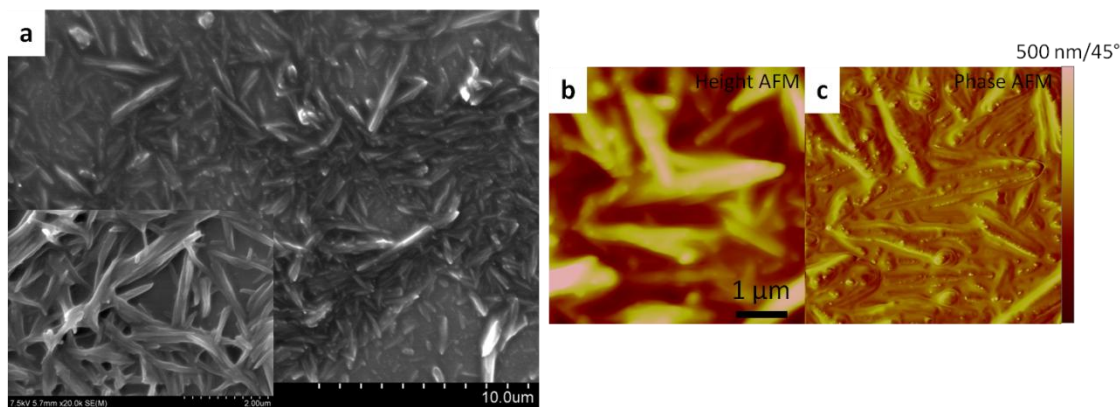


Figure 3-12. SEM images (a) and height- and phase-contrast AFM images (b, c) of drop-casted mixture of tn-ZnPc and PCBM in ratio 1:1.

3.1.2.4 Conclusions for Drop-Casting Deposition Results

From observations of the distribution across the substrate of molecular domains resulting from drop casting deposition of single molecular solute solutions as well as (1:1) tn-ZnPc/PCBM mixtures, we have gained insights into the individual solute-solvent interactions. We find that tn-ZnPc molecules, which precipitate first from solution, flow from the droplet bulk to the edges. We also find that the PCBM molecules, which are

more highly soluble in chloroform and thus stay in solution longer, are transported from the top of the droplet down to the center of the substrate; this is illustrated in Figure 3-7.

We have also shown that the on drop-casting from solution in the absence of *tn*-ZnPc, PCBM domains exhibit different growth habits depending of the initial evaporation rate of the chloroform, with indications of the beginning of a crystalline order. When instead mixed in solution with *tn*-ZnPc, the dominant PCBM domain type is a blanket phase, and the hexagonal plates suggestive of ordered structures are not observed. Finally, *tn*-ZnPc clusters into rods both in the presence of and in the absence of PCBM.

3.1.3 Deposition Method by Immersion

3.1.3.1 Immersion in PCBM/chloroform Solution

We first performed deposition via immersion in solution by placing the Si substrate in an open cylindrical container. We find that this procedure produces a solvent evaporation rate approximately one order of magnitude slower than that for drop-casting. This gives the PCBM and *tn*-ZnPc solute molecules more time to interact with the substrate surface while still dissolved in liquid solution. Even after the bulk liquid evaporates to a level below that of the substrate the solvent vapors remain in the contact with the deposited film for a finite time, allowing additional adsorption. Figure 3-13(a) is an optical micrograph showing several hexagonal clusters of PCBM molecules deposited from PCBM/chloroform solution. Most of these clusters are single hexagons, with width ranging from 40 – 100 μm and thickness from 250 – 700 nm; however some of them appear to be stacked vertically. This is suggestive of the beginning of a pyramidal-type of

growth, leading to an eventual dendritic growth front emanating from the base of each pyramid, as illustrated in Figure 3-13(c-d).

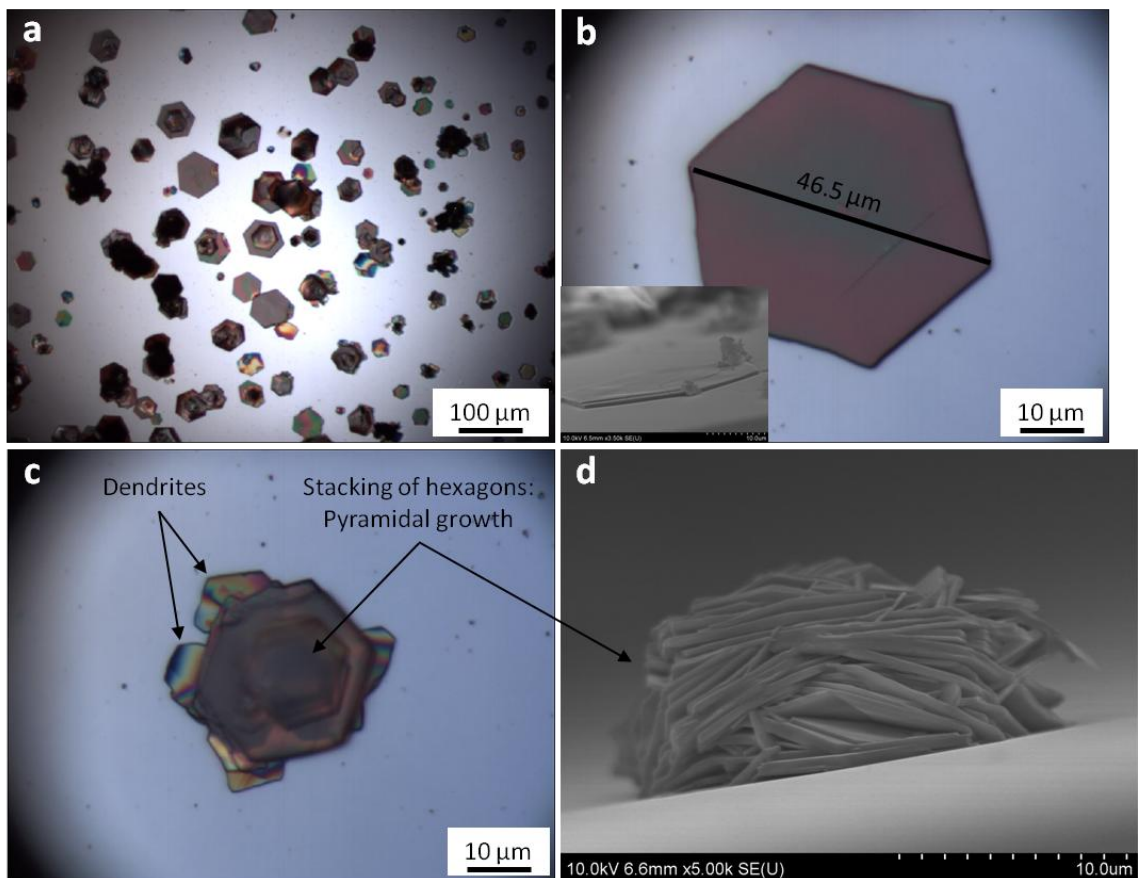


Figure 3-13. Optical images (a-c) and SEM cross-section image (insert) of the PCBM crystal phase observable at evaporation rate of 0.00347 mL/min (immersion in open cylindrical container) followed by SVA, promoting the crystallization of PCBM molecules in hexagons. SEM cross-section image (d) of the stacking of hexagons at the surface.

Despite the indication, based upon the hexagonal plate shapes, of crystallinity, X-ray diffraction (XRD) did not show Bragg peaks, probably due to a low signal associated with crystals which are relatively thin.

Deposition at even lower solvent evaporation rates was achieved by covering the cylindrical container with a cap containing a small aperture (diameter ~ 0.5 cm). The

optical images in Figure 3-14(a-b) show a vertical pyramidal crystal structure grown around a central and possibly seed hexagon that is visible on the apex of the pyramid. This might act as nucleation site for the growth of the pyramid. The growth front at the base of the pyramids evolves in a horizontal dendritic fashion. This behavior could be an indication of the presence of small concentrations of impurities (of unknown composition) on the surface, and/or in the raw materials promoting cellular growth³ (Figure 3-14(c)). Some dendrite arms exhibit perpendicular cells rather than secondary arms, typical of the presence of a homogeneous impurity distribution between primary dendrites arms.²⁸ These interfaces instabilities, might be also due, in analogy with Mullins-Sekerka instabilities, to a small spatial gradient in the supersaturation with the presence of an impurity at these low evaporation rates.^{29,30}

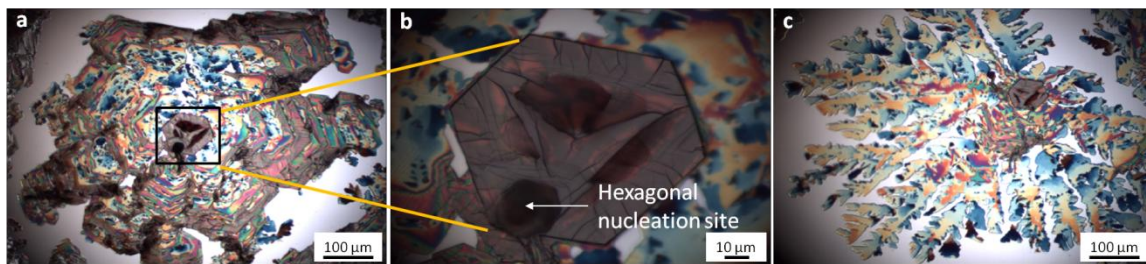


Figure 3-14. Deposition of PCBM via immersion in PCBM/chloroform solution in a quasi-closed cylindrical container (evaporation rate of 0.0017mL/min). Pyramidal growth of PCBM molecules activated by the initial single hexagon that acts as nucleation site (a, b). Dendritic and cellular growth at the base of the pyramid (c).

Unlike results for PCBM domains resulting from both spin-coating and drop-casting, EDS analysis performed on PCBM hexagons show the presence of Cl atoms, confirming the contribution of SVA to the formation of the hexagonal domains (Figure 3-15).

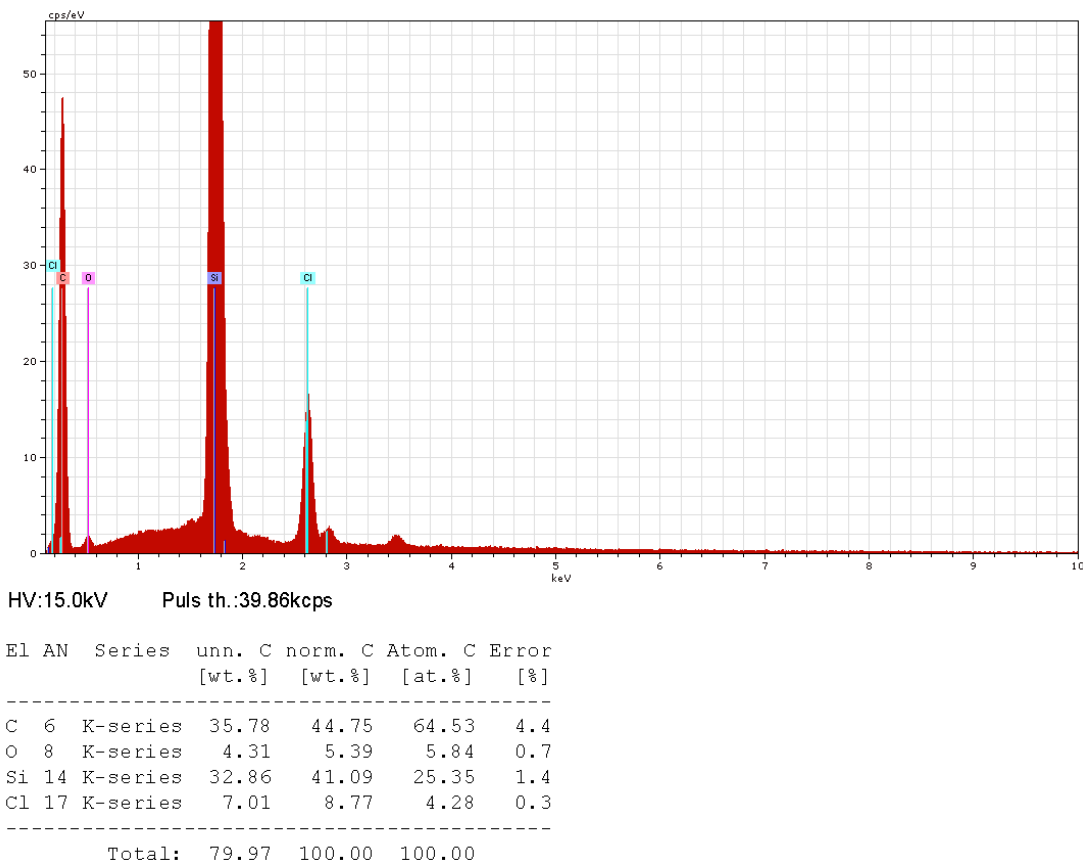


Figure 3-15. EDS spectrum measured at hexagons of PCBM formed on silicon substrate via immersion in PCBM/chloroform solutions.

3.1.3.2 Immersion in tn-ZnPc/chloroform Solution

Deposition of tn-ZnPc molecules via immersion of the substrate into tn-ZnPc/chloroform solutions in either an open container (Figure 3-16(a)) or nearly-closed container (Figure 3-16(b)) produces the same characteristic rod-like clusters for as did the other types of deposition. Small quantities of chlorine atoms were detected on the rods by EDS (Figure 3-17), indicating that the solvent molecules do adsorb onto the molecular cluster surface, but the indication is of little or no role of SVA in controlling the rod-cluster shapes: Cl atoms were not detected on tn-ZnPc rods formed by spin-coating and drop-casting. Overall, our results indicate that over a very wide range of

values the solvent evaporation rate does not affect the morphology of the tn-ZnPc rod-clusters. The area-density covered by rods is higher for this method as we can see from a comparison between the spin-coated (Figure 3-1(i-l)), drop-casted (Figure 3-10(a)) and deposited via immersion (Figure 3-16(a-b)) tn-ZnPc molecules, but this is consistent with the much larger amount of solution used in these two last deposition methods.

While the rod shapes suggest that the clusters might be crystalline, again XRD measurements showed no obvious Bragg reflections.

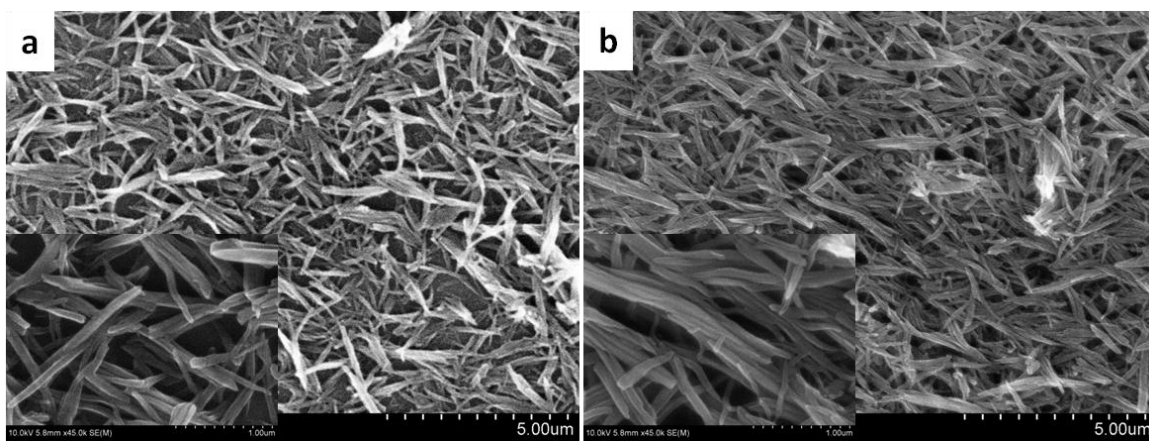


Figure 3-16. SEM images of tn-ZnPc rod-like clusters deposited from single component solution through vertical substrate orientation immersion in solution at 0.00347 mL/min (open container) (a) and 0.0017 mL/min (nearly-closed container) (b).

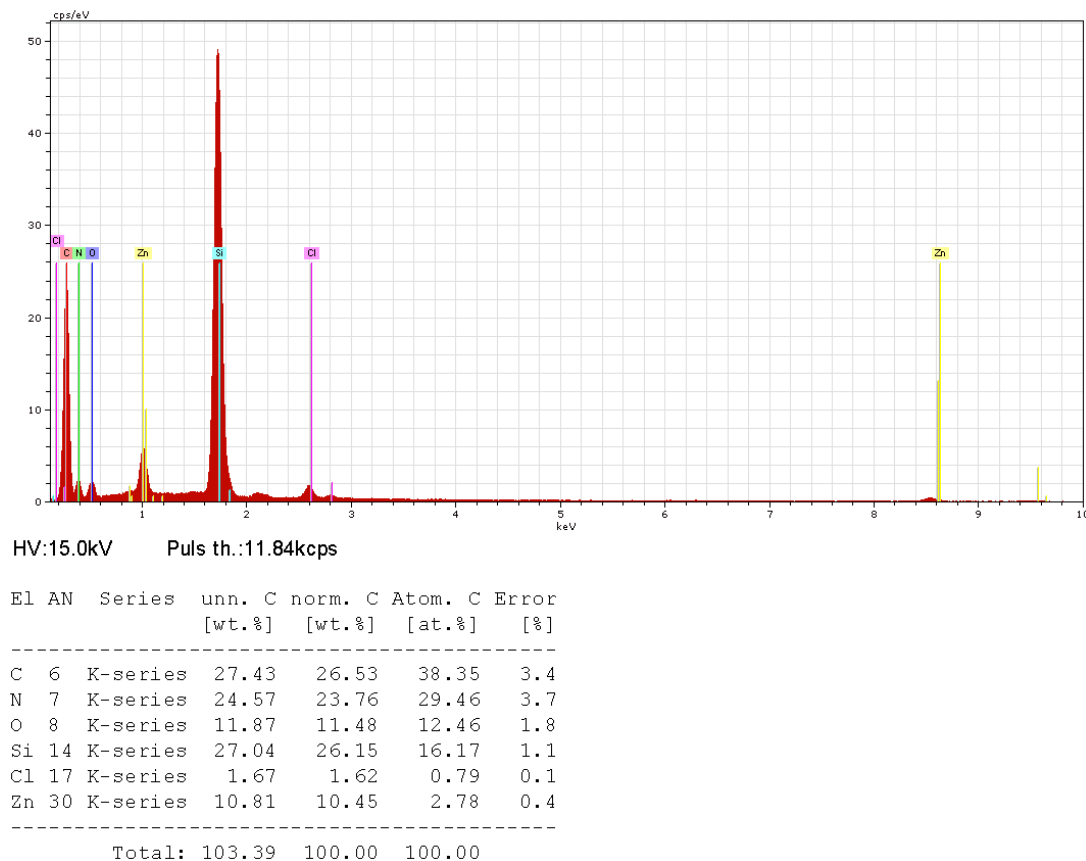


Figure 3-17. EDS spectrum measured at an agglomeration of tn-ZnPc rods on silicon substrate during immersion in tn-ZnPc/chloroform solutions.

3.1.3.2.1 Effect of Substrate Orientation

During deposition of tn-ZnPc via immersion, we noticed that placing the substrate horizontally at the bottom of the container led to very non uniform films, whereas the walls of the container were uniformly covered in a highly packed “ring” fashion. Based upon this, we hypothesize that tn-ZnPc molecules are transported at the edges of the liquid-vapor-solid phase as an effect of their very low solubility in chloroform. Seemingly, the interaction forces between solvent and organic molecules are very weak, and the molecules deposit on the first surface that they encounter. Based upon these observations, subsequent depositions of the tn-ZnPc via immersion were performed by

placing the substrate vertically into the container. Similar considerations do not seem to apply to the PCBM molecules. On the contrary, these apparently have a stronger tendency to stay in solution. Therefore, the deposition of PCBM molecules via immersion in solution was performed by placing the substrates horizontally into the cylindrical wells.

3.1.3.3 Immersion in (1:1) PCBM/tn-ZnPc Mixed Solution

Given the dependence on orientation of the substrate during deposition of the tn-ZnPc, the deposition of (1:1) tn-ZnPc/PCBM mixtures through immersion in solution was performed using both vertical and horizontal orientations of the substrate in the cylindrical cell. The motivation was to determine whether the substrate orientation played a role in the mutual interactions between different molecules.

Deposition through immersion with the vertical sample orientation, and at an evaporation rate of 0.00347 mL/min produces plate-shaped clusters (presumably PCBM domains) that do not exhibit a clear hexagonal shape along with rod-shaped clusters (presumably tn-ZnPc) as illustrated in Figure 3-18(a). During vertical-substrate orientation immersion deposition, a “carpet” of rods resulted; their density was not uniform, but rather they clustered in horizontal bands of width $\sim 286 \mu\text{m}$, separated by areas with low density of rods. This can be seen in Figure 3-18(b) and Figure 3-19. We observed different growth habits for PCBM clusters depending on the density of nearby rods. In areas with a high density of tn-ZnPc rods, the formation of hexagons of PCBM molecules is seemingly prevented. Where PCBM assembles the domains follow a dendritic growth front, as seen in Figure 3-18(d). In areas where the concentration of rods

is lower the plates are still not hexagonal, we instead observe a stacking of quasi-hexagonal plates that seem to show an initial dendritic frontal growth characterized by larger arms (Figure 3-18(c)). The presence of the chlorine atoms is detectable from EDS measurements on agglomerations of tn-ZnPc rods (as shown in Figure 3-20) and on PCBM dendrites (Figure 3-21) and plates (Figure 3-22). The presence of the tn-ZnPc seemingly impedes the transformation of the PCBM blanket-phase into hexagonal plates; a plausible explanation is that not all tn-ZnPc molecules aggregate into rods or wetting layer, and that some diluted tn-ZnPc molecules might float in chloroform, decorating either the PCBM domain surface or PCBM/substrate interface. We do detect a small amount of Zn signal in EDS measurements at PCBM dendrites and plates (Figure 3-21 and Figure 3-22); however this could also be due to the underlying tn-ZnPc rod-“carpet”.

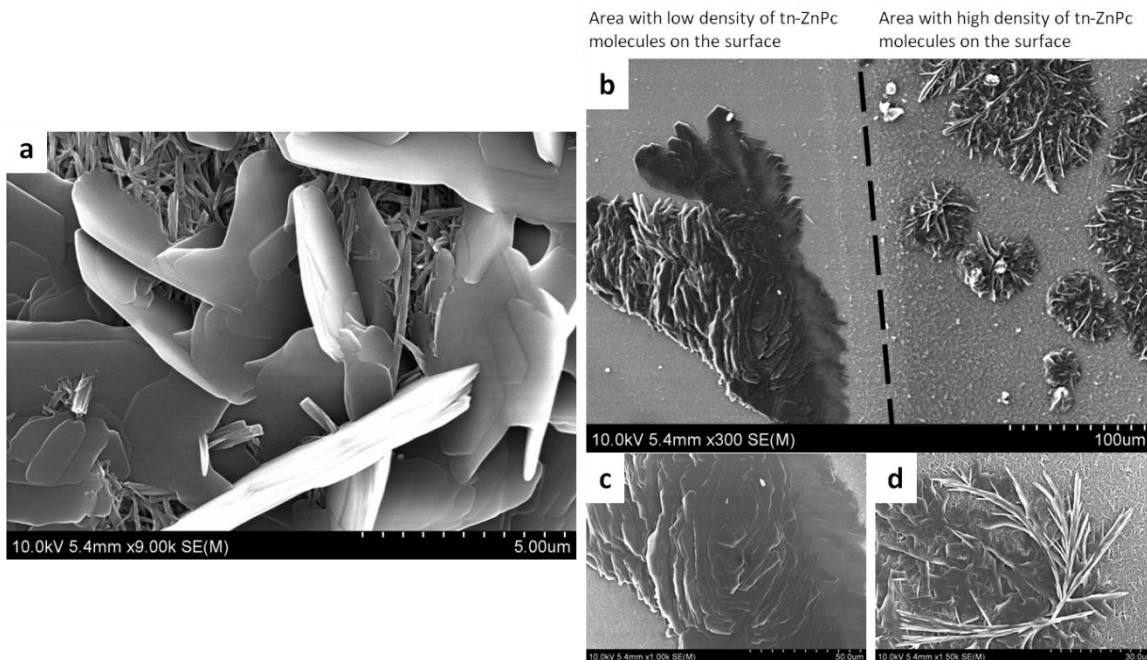


Figure 3-18. SEM images of the structures resulting from deposition of a (1:1) tn-ZnPc/PCBM mixture via immersion with vertical substrate orientation in open container (0.00347 mL/min). Plates do not show a clear hexagonal shape (a). Areas with low and high density of rods (b). Stacking of plates in low rods density areas (c), and dendritic growth in high rods density areas (d).

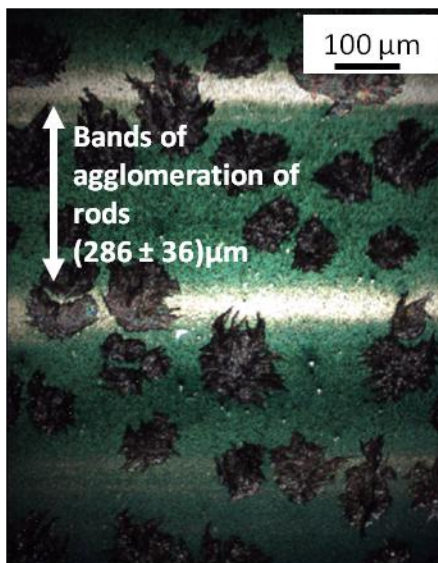


Figure 3-19. Optical image of the structures resulting from deposition of a (1:1) tn-ZnPc/PCBM mixture deposited via immersion with vertical substrate orientation in open container (0.00347 mL/min). The horizontal strips of agglomeration of rods are observed.

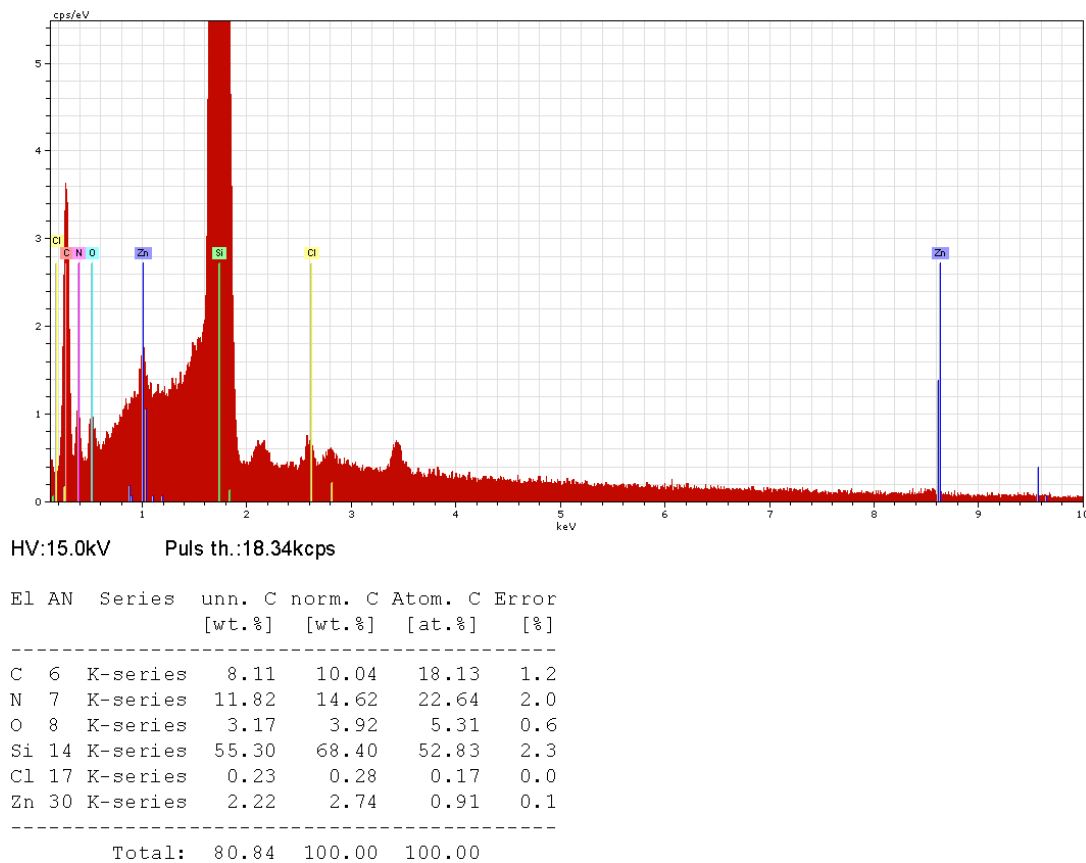
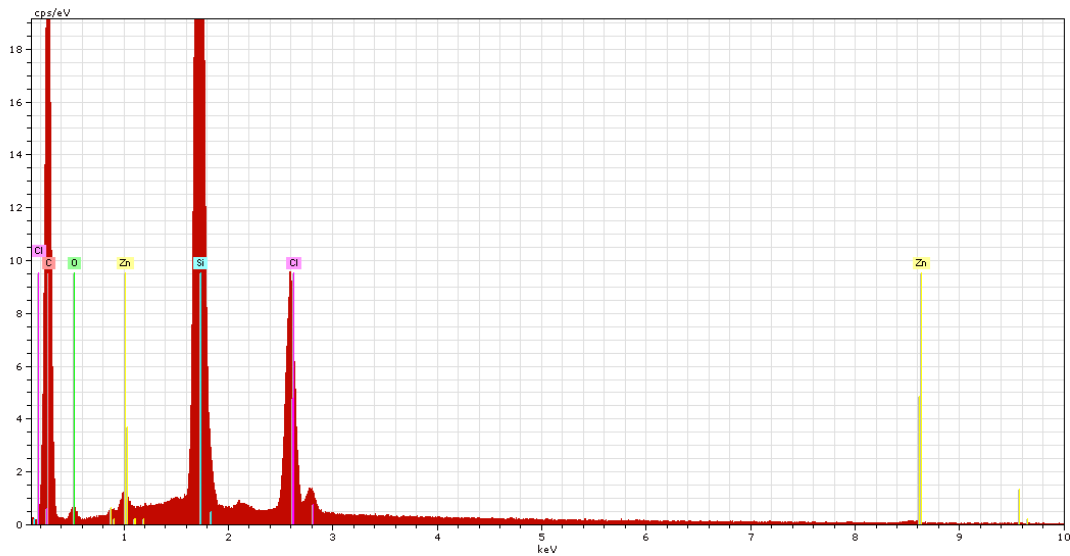


Figure 3-20. EDS spectrum measured at an agglomeration of tn-ZnPc rods on the silicon substrate during immersion in a (1:1) tn-ZnPc/PCBM mixture solution.



HV:15.0kV Puls th.:12.26kcps

El	AN	Series	unn. [wt.%]	norm. [wt.%]	Atom. [at.%]	Error [%]
C	6	K-series	47.34	53.10	72.27	5.6
O	8	K-series	5.15	5.77	5.90	0.8
Si	14	K-series	25.39	28.48	16.58	1.1
Cl	17	K-series	8.81	9.89	4.56	0.3
Zn	30	K-series	2.47	2.76	0.69	0.1
Total:			89.16	100.00	100.00	

Figure 3-21. EDS spectrum measured at PCBM dendrites formed on a silicon substrate during immersion in a (1:1) tn-ZnPc/PCBM mixture solution.

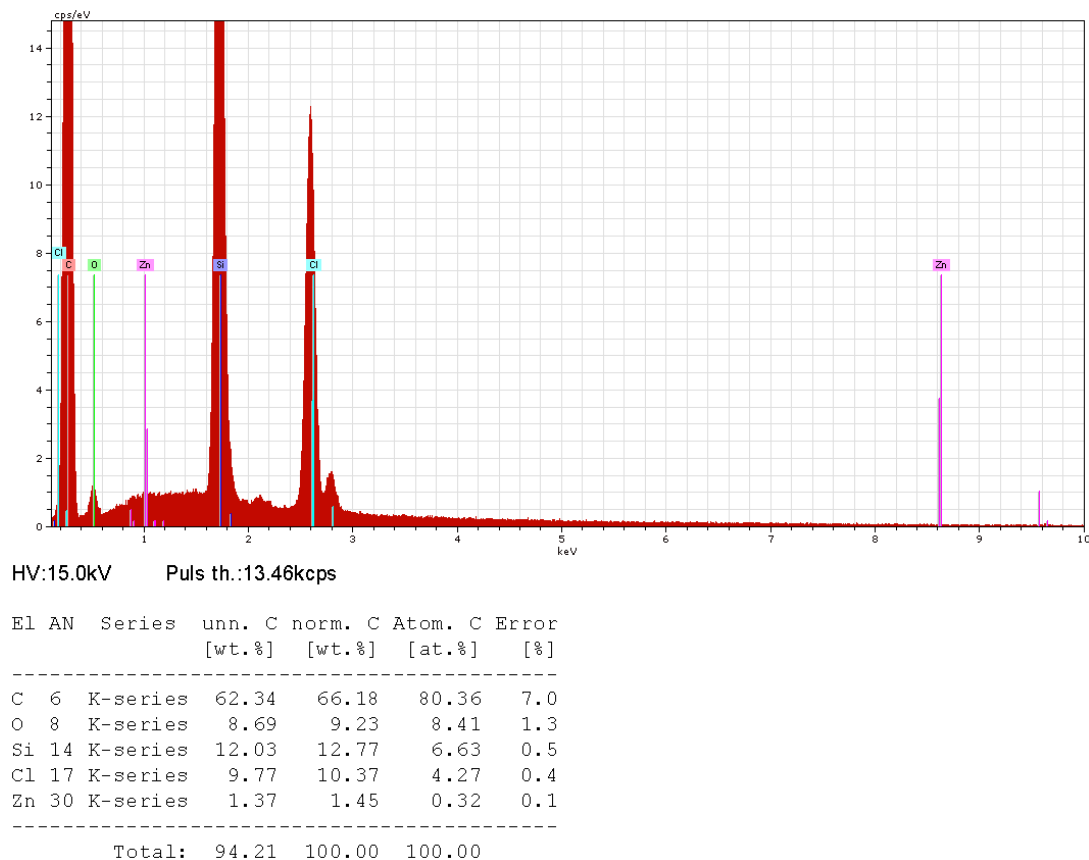


Figure 3-22. EDS spectrum measured at quasi-hexagonal plates of PCBM formed on a silicon substrate during immersion in a (1:1) tn-ZnPc/PCBM mixture solution.

After lowering the evaporation rate even further, to 0.0017 mL/min, evidence for dendritic and plate-like growth is still observable, again without formation of hexagonal plates of PCBM (Figure 3-23(a-b)). Again we see strips with low and high density of tn-ZnPc rods (similar to Figure 3-19). We observed the same correlation between the growth habits of PCBM and the density of rods on the substrate. Areas with high concentration of rods show a dendritic growth of the PCBM domains: Figure 3-23(a) shows some indication of an evolution of the structure. Areas with low concentration of rods show a stacking of plates with a dendritic growth front but with very few secondary arms (Figure 3-23(b)). A comparison between Figure 3-18 and Figure 3-23 (mixed solution deposited

with a vertical substrate orientation via immersion at 0.00347 mL/min and 0.0017 mL/min, respectively), shows that the evolution of the dendritic phase and stacking-plates phase is suppressed by the higher solvent evaporation rate (0.00347 mL/min), but promoted at lower solvent evaporation rate. This is evidently a supersaturation effect; we speculate that in analogy with the Mullins-Sekerka instability that unstable growth might be favored by a small spatial gradient in the supersaturation for low evaporation rates, and the presence of some impurity at the PCBM domain growth front.

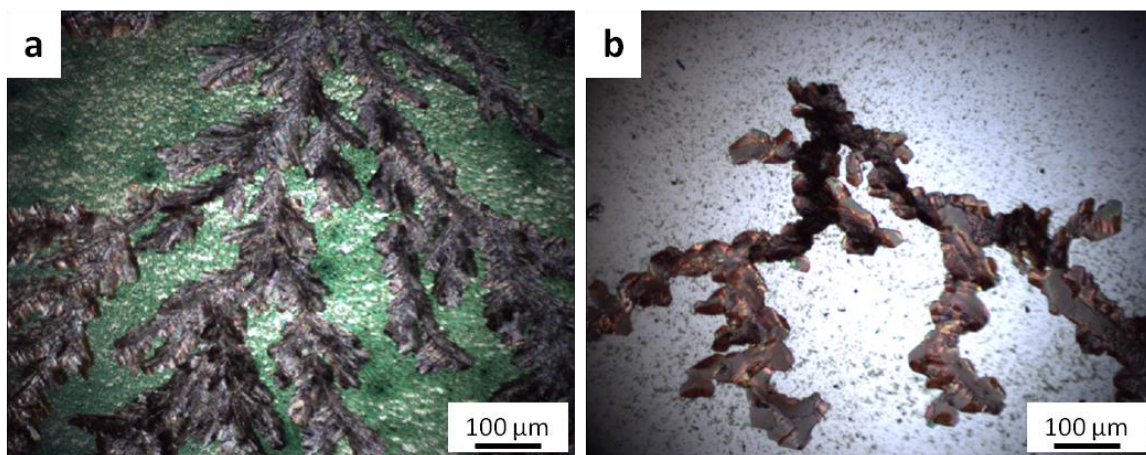


Figure 3-23. Optical images of the structures resulting from deposition of a (1:1) tn-ZnPc/PCBM mixture deposited via immersion with a vertical substrate orientation at the rate of 0.0017 mL/min of (a) an area with high density of tn-ZnPc rods and (b) an area with low density of rods.

In order to further probe what is the cause of the evolution of this dendritic growth we performed the deposition of PCBM in chloroform without tn-ZnPc, immersing the substrate into the solution in a vertical orientation. In this case, we observe that hexagonal plate form (Figure 3-24(a)). The formation of hexagons occurs independent of the orientation of the substrate, suggesting that the absence of hexagons of PCBM in the mixed film is seemingly due to the interaction with the tn-ZnPc molecules. We again observe the same growth habit of dendrites (Figure 3-24(b)), as we had seen in the case

of the mixture. If the dendrites are an indication of cellular growth as speculated above, these results suggest that the impurity is not tn-ZnPc, however when the PCBM is mixed with the tn-ZnPc, the concentration of this unknown impurity might be different depending on the concentration of rods. Therefore, the tn-ZnPc clusters might exert an indirect influence on the growth habit of the PCBM domains.

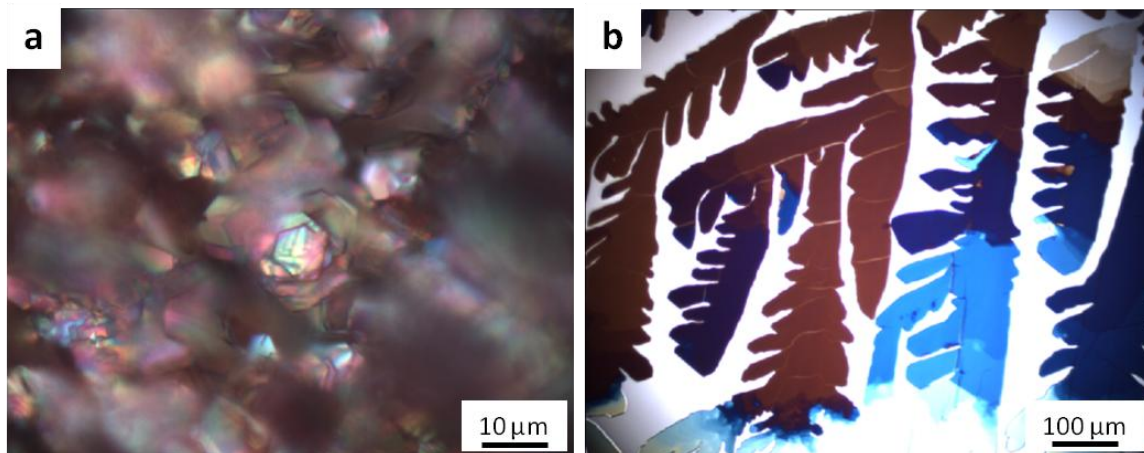


Figure 3-24. Optical microscopy images of the structures resulting from deposition of PCBM via immersion, with a vertical substrate orientation at the rate of 0.0017 mL/min showing (a) stacking of hexagons and (b) dendrites.

Finally, we compare the morphologies of clusters of PCBM deposited from the mixture with that from single species solution for a horizontal substrate orientation. We performed the deposition at a very low rate of solvent evaporation (0.0017 mL/min) by placing the substrate horizontally at the bottom of the container covered with a plate with a small aperture. Most of the tn-ZnPc molecules deposit on the walls of the container. As a result there are areas on the substrate with very low density of rods and areas with kind of irregular “coffee-rings” of high concentration of rods (Figure 3-25). Optical images of the resulting structures are shown in Figure 3-26(a-b).

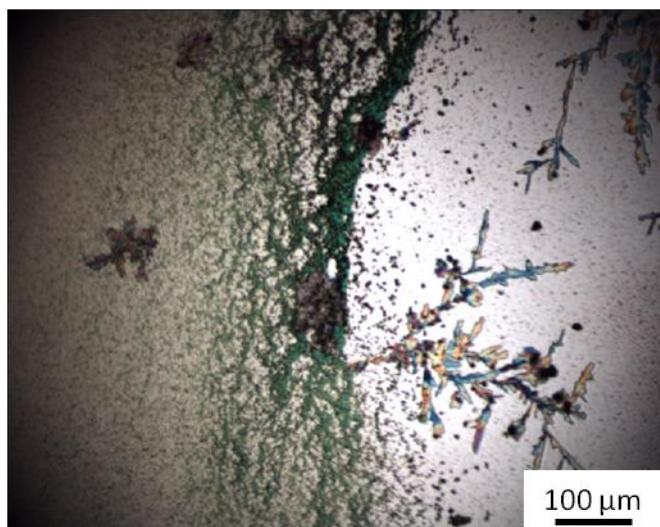


Figure 3-25. Optical image of the structures resulting from deposition of a (1:1) tn-ZnPc/PCBM mixture deposited via immersion with horizontal substrate orientation in nearly-closed container (0.0017 mL/min). Portion of an irregular “coffee-ring”.

In contrast to what we observed for immersion deposition with a vertical substrate orientation, for a horizontal substrate orientation in regions with low density of rods the dendritic growth of PCBM is observable (Figure 3-26(a)), without obvious seed hexagonal plates, while stacking of plates is observable in regions with high density of rods (Figure 3-26(b)). Although we do not have a detailed understanding of this phenomenon, this opposite correlation between tn-ZnPc rod density and growth habits of PCBM molecules is likely due to the convection currents that generate inside the solution during deposition. These currents might move the diluted tn-ZnPc molecules inside chloroform in specific directions; therefore the interaction between PCBM domains and diluted tn-ZnPc molecules might be different depending on the substrate orientation.

Finally we note that the dendrite arms are much smaller in size than for the case of deposition from PCBM alone in chloroform (Figure 3-14(c)). This indicates that the presence of either the tn-ZnPc molecules in solution, or the influence of the tn-ZnPc on

the concentration of some trace impurity decreases the length scale of the PCBM domain formation.

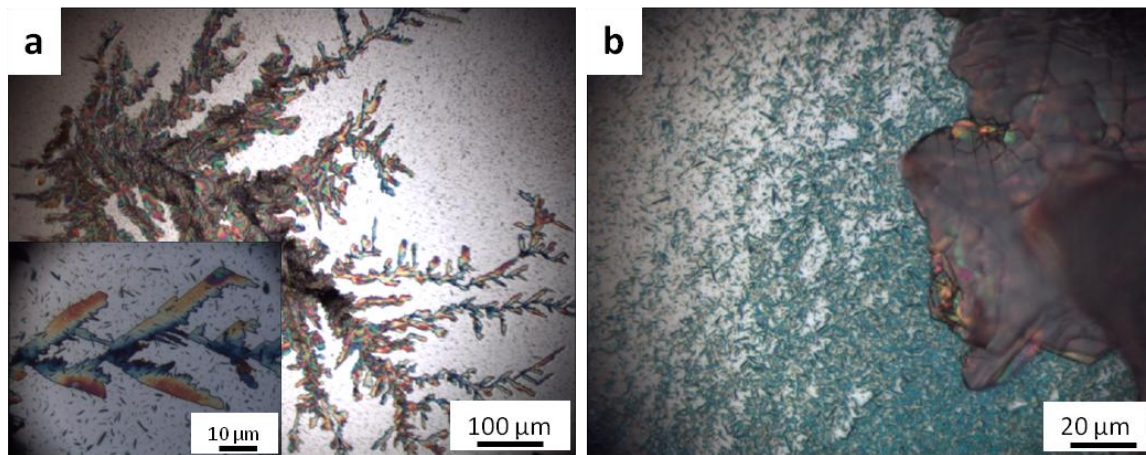


Figure 3-26. Optical images of the structures resulting from deposition of a (1:1) tn-ZnPc/PCBM mixture deposited via immersion with horizontal substrate orientation at the rate of 0.0017 mL/min. Areas with low density of rods show dendritic growth (a), and areas with high density of rods show stacking of plates (b).

3.1.3.4 Conclusions for Deposition via Immersion Results

We now summarize the results obtained by deposition via immersion in an open and nearly-closed container.

PCBM deposition alone produces seemingly crystalline domains, as evidenced by the formation of hexagons on the substrate. We find evidence for growth in pyramidal shapes if we lower the rate of evaporation, suggesting that the phase formation of PCBM occurs through nucleation and growth. But, we also find that very low solvent evaporation rates can result in apparent instabilities, i.e. formation of dendritic frontal growth at the base of the pyramids.

The tn-ZnPc molecules again form rod-like clusters, suggesting that at high supersaturations it already decomposed and aggregate in solution. Our observation that

the SVA does not have any visible effect on the rod clusters morphology is indication of high intermolecular forces between tn-ZnPc molecules.

When mixed together in ratio 1:1, the tn-ZnPc cluster shape does not change but the PCBM phase transformation is highly affected by the interaction with the tn-ZnPc. In effect, the formation of hexagonal PCBM clusters is suppressed despite of the action of the SVA. This might indicate that not all tn-ZnPc molecules form the condensed phases of rods and wetting layer, but some of diluted tn-ZnPc molecules might deposit on PCBM domains, changing its kinetics of phase transformation. Again in this case, at the lowest evaporation rate investigated, we find evidence for interface instabilities suggesting cellular growth, and thus impurity effects on PCBM cluster evolution.

We also observed a correlation between growth habits of PCBM and density of tn-ZnPc rods, and surprisingly find that this correlation depends itself on the orientation of the substrate during deposition.

Finally, we find evidence that under conditions of unstable growth the PCBM domains sizes decrease when interact with the tn-ZnPc.

3.2 Effect of Temperature-Annealing on Spin-Coated Samples

It has previously been demonstrated that thermal annealing induces the formation of phase-separated domains of pure donor and acceptor materials.¹⁵ In this section, we investigated whether it is possible to initiate temperature-driven diffusion of tn-ZnPc and PCBM molecules deposited from single component solutions and from the mixture solution on Si(111) substrates via thermal annealing.

After chemical cleaning (RCA cleaning)²² silicon substrates were covered with single-solute molecular solutions or with the (1:1) tn-ZnPc/PCBM mixture solution via spin-coating at 2000 rpm for 45 seconds. Subsequently the substrates were heated on a hot-plate at a series of temperatures: 100 °C, 150 °C, 170 °C, and 200 °C for 30 minutes each. For the chemically similar ZnPc molecule (without functional nitro groups) thin films thermally evaporated on glass substrates at room temperature, it has been reported that ZnPc crystals undergo a phase transformation from tetragonal (α) to monoclinic (β) when the substrate was heated in the range 150 – 200 °C.³¹ Additionally, differential scanning calorimetry studies reported on ZnPc flash-evaporated films on glass substrates undergo an α to β phase transition at the substrate temperature of 265 °C.³² Therefore we further heated substrates on which tn-ZnPc had been deposited to 250 °C, 265 °C, and 285 °C for 30 minutes each. On the substrates was etched a “landmark” so that to facilitate the analysis of the same area. AFM images of the three samples were taken at room temperature and after each heating cycle.

To monitor possible changes in molecular clusters morphology with temperature, we measured the length, width, radius of gyration and volume of the tn-ZnPc rods, for the tn-ZnPc-alone films and for the films deposited from a (1:1) tn-ZnPc/PCBM mixture solution. We measured the diameter and height of the PCBM clusters for the PCBM-alone films and for films deposited from a (1:1) tn-ZnPc/PCBM mixture solution.

The dimensions of tn-ZnPc rods in the pure tn-ZnPc sample and in the mixture with the PCBM remained relatively constant over the entire thermal annealing process. In Figure 3-27 we show evidence for the stability of the radius of gyration with temperature of single component films (left panel) and films deposited from a (1:1) tn-ZnPc/PCBM

mixture solution (right panel). We find no evidence for changes in the shape of the tn-ZnPc rods, both alone and in the mixture during annealing. The lack of coarsening indicates little or no temperature driven diffusion at these temperatures, perhaps because the internal molecular forces are very strong and stable.

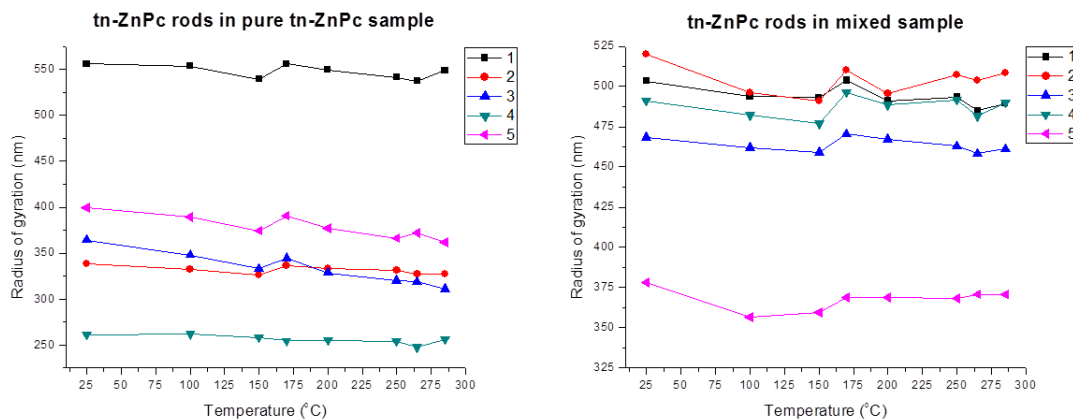


Figure 3-27. Radius of gyration of tn-ZnPc rods, in the single component sample (left) and in the mixture in ratio 1:1 with the PCBM (right).

The overall constant size of the tn-ZnPc aggregates around 265 °C suggests that, unlike ZnPc, the material does not undergo a phase transition. However, it is possible that an isochoric transition is occurring in this temperature range. Therefore, other tests, like force-curve analysis of the modulus or differential scanning calorimetry, should be performed to further investigate this issue.

When PCBM-alone solution is deposited through spin-coating onto the Si substrate, the molecules self-assemble in spherical cap clusters in close vicinity with one another, as we have seen above. In Figure 3-28 are shown the base diameter and the height of spherical cap clusters deposited from single component-PCBM solution. We note that there is an inverse relationship between the evolution with annealing temperature of the base diameter and the height: an overall increasing trend in the

diameters (slope = $(0.06 \pm 0.02) \text{ nm}/^\circ\text{C}$) and decreasing trend in the height (slope = $(-5 \times 10^{-4} \pm 3 \times 10^{-4}) \text{ nm}/^\circ\text{C}$). This indicates that PCBM molecules diffuse across clusters at these temperatures, spreading out into a more uniform layer: the wetting angle *decreases*.

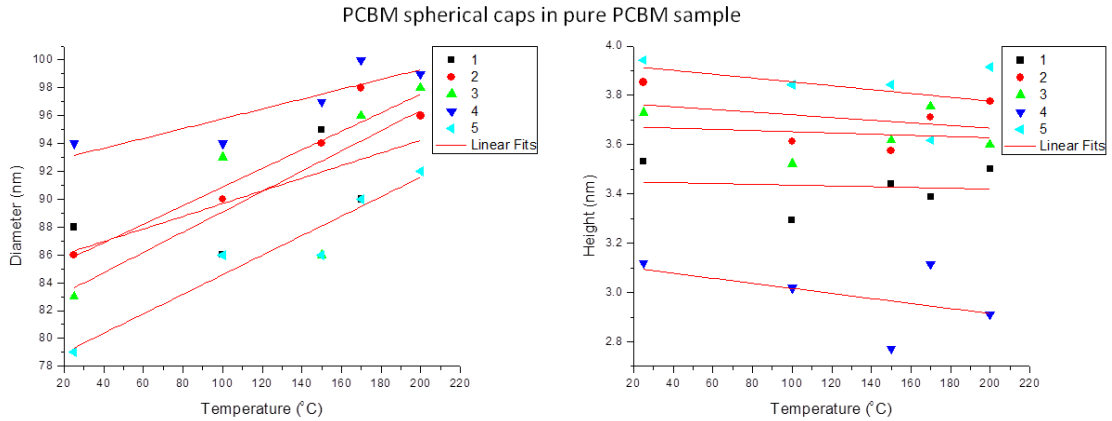


Figure 3-28. Diameter (left) and height (right) of the PCBM spherical caps in the pure PCBM samples at different temperatures.

In contrast, for films on which PCBM molecules are deposited from a mixed solution with tn-ZnPc, we find the opposite behavior: a decreasing trend in the diameter (slope = $(-0.07 \pm 0.02) \text{ nm}/^\circ\text{C}$) and an increasing trend in the height (slope = $(0.006 \pm 0.002) \text{ nm}/^\circ\text{C}$) (Figure 3-29). This behavior is due to the presence of the wetting layer of tn-ZnPc underneath the PCBM spherical caps that might decrease the surface energy, making energetically less favorable for the PCBM molecules to wet. The annealing process provides the energy necessary for the PCBM molecules to diffuse vertically and reduce their interface contact area with the tn-ZnPc layer.

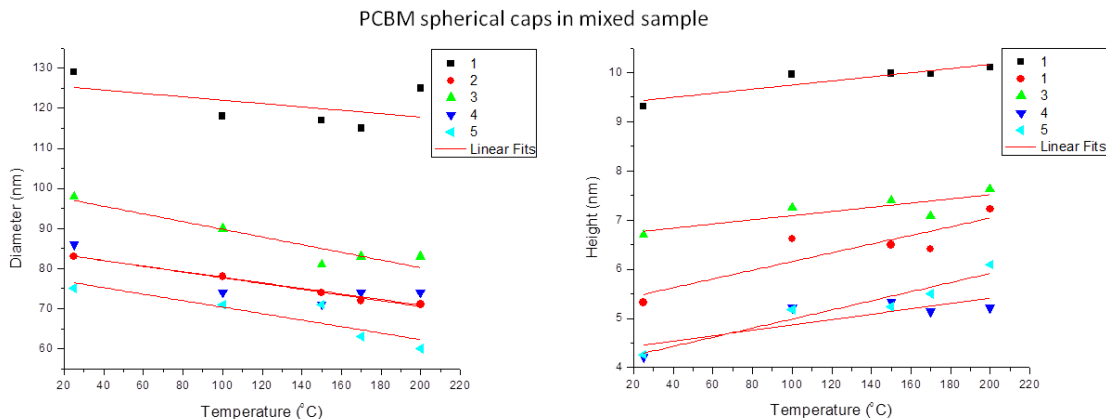


Figure 3-29. Diameter (left) and height (right) of the PCBM spherical caps in the mixture samples at different temperatures.

In conclusion, we investigated whether it was possible to initiate temperature-driven molecular diffusion of spin-coated PCBM, tn-ZnPc, and PCBM/tn-ZnPc mixed films, in order to direct the morphology of the phase separation in the two single molecular domains when mixed, by annealing the samples up to 200 °C for the PCBM sample and up to 285 °C for the tn-ZnPc and the mixture samples. The morphology of tn-ZnPc domains remained very stable in both the pure tn-ZnPc and mixture films across the entire annealing temperature range explored. Evidently tn-ZnPc clusters remain unaffected by interactions with PCBM molecules or with the SiO₂-terminated substrate. Unlike ZnPc, it does not seem to exhibit a phase transition near 265 °C. In contrast, PCBM molecules diffuse resulting in small but measurable changes in the spherical cap clusters morphology when heated. In particular, for the pure PCBM films the clusters tend to spread more uniformly on the Si substrate; in contrast, for mixed (1:1) tn-ZnPc/PCBM films, the spherical cap clusters tend to decrease the interface area with the substrate as molecules diffuse vertically, increasing the height. This latter observation further supports our determination of the presence of an underlying wetting layer of tn-

ZnPc molecules on the mixed-film samples, which causes the PCBM spherical particles to dewet the surface. Such an effect would be useful in promoting a vertical phase separation if the condensed phases of the donor molecules were mobile as well.

3.3 Stoichiometries (1:2) and (2:1) of tn-ZnPc/PCBM Mixtures

In addition to the 1:1 ratio mixture, we investigated the effect of mixture stoichiometry. One motivation for this, as discussed in Chapter 1, was to explore the possible effect of the range of supersaturation for which phase separation is via nucleation. We analyzed the results of deposition of other mixtures, with tn-ZnPc/PCBM ratios of 1:2 and 2:1, performing depositions via drop-casting and immersion because they favor the crystallization of the PCBM.

3.3.1 (1:2) tn-ZnPc/PCBM Mixtures

In this part of the project we analyzed the structures which form from solutions based upon a (1:2) tn-ZnPc/PCBM ratio mixture deposited via drop-casting, and immersion in solution with both vertical and horizontal orientation of the substrate in the container.

3.3.1.1 Drop-casting of (1:2) tn-ZnPc/PCBM Mixture Solutions

Given more PCBM, we expect that the blanket phase be dominant. In Figure 3-30, we see the optical images of the central part of the samples, where the coffee rings are visible, and the AFM images measured at the sample center (a), between two adjacent rings (b) and on a ring (c). The blanket phase at the center, where the initial evaporation of the solvent is slower, is visible via the presence of small holes of width (111 ± 2) nm

and depth (11 ± 1) nm. The coalescence of the blanket phase which leaves behind isolated holes is slow at the sample center compared to at the edges of the sample where the evaporation is faster.

Between two adjacent rings (Figure 3-30(b)), the overall molecular coverage is smaller compared to that at the rings. Here there are no holes, but we observe evidence for the blanket phase from the diffuse edges of the tn-ZnPc rods.

At the rings there is a larger overall molecular coverage (Figure 3-30(c)), and we note that the holes in the blanket appear deeper ((74 ± 6) nm) than at the center. This seems to be a local, “coffee-ring” effect. For the (1:2) tn-ZnPc/PCBM mixture solutions we find a higher concentration of rings closer to the center of the sample, and thus the coarse-grained concentration of PCBM, like that for the (1:1) mixture is higher near the sample center. We also note the presence of small particles inside the holes, visible in the phase-contrast AFM image in the inset of Figure 3-30(c). These may again be an indication of an impurity whose concentration is correlated with the presence of the tn-ZnPc rods, and which keeps the blanket phase from wetting the substrate.

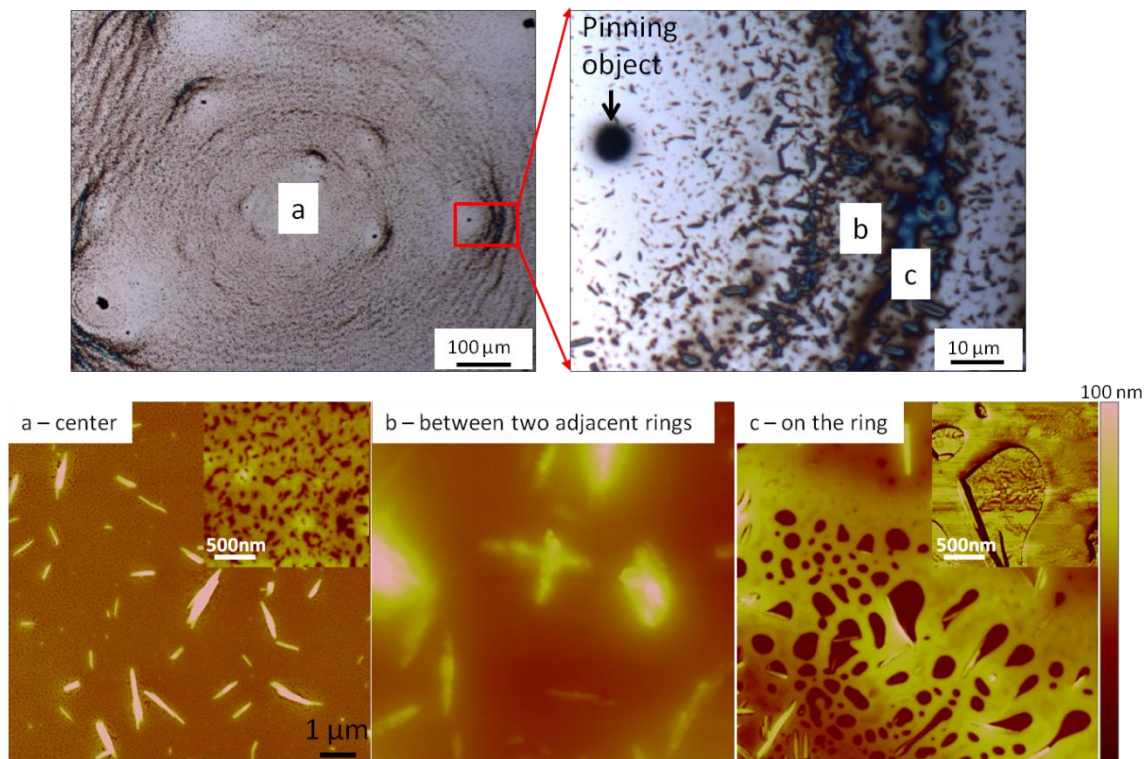


Figure 3-30. Results of drop-casting of a solution of a (1:2) tn-ZnPc/PCBM mixture. Optical image of the sample (above). The inset in (a) is an AFM topography map (height scale 20 nm). The inset in (c) is an AFM phase map (data scale 20°).

The process of separation of the blanket phase of PCBM into small spherical cap clusters is observable via the presence of small, nearly circular protrusions on top of the rods and on the substrate; this is observable in the phase-contrast AFM images in Figure 3-31. Here as well, we see small particles on the substrate, which may again be clusters of PCBM that did not coalesce in the blanket phase.

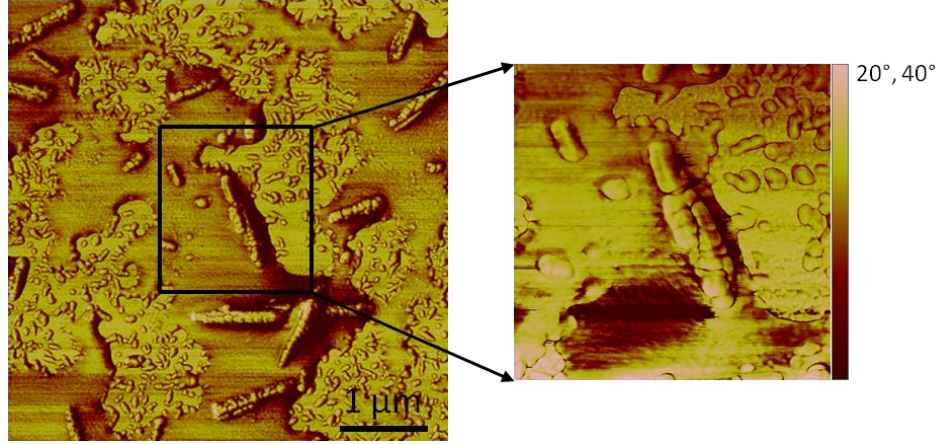


Figure 3-31. Phase-contrast AFM images of a section where the blanket phase of PCBM starts to break down into spherical cap clusters.

In order to estimate the thickness of this blanket phase on top of the rods, based upon the difference in appearance, we hypothesize that the phase-contrast AFM images show the shape of the underlying, relatively stiff *tn*-ZnPc rod clusters, and that the height-contrast AFM images show the shape of the rods including the thickness of the blanket phase. Based on this hypothesis we calculated the aspect ratio between length and width measured in the phase-contrast and in the height-contrast AFM images. We call a and b the length and width of the rod in the phase-AFM image and $(a + \delta)$ and $(b + \delta)$, the length and width of the rod in the height-AFM image, where δ is the thickness of the blanket phase. We obtained δ from the following ratio:

$$x = \frac{\frac{a}{b}}{\frac{(a + \delta)}{(b + \delta)}} \Rightarrow \delta = \frac{ab(1 - x)}{bx - a} \quad (3-1)$$

The result is (88 ± 9) nm, which is in rough agreement with the thickness of the blanket phase measured through the depth of the holes on the rings ((74 ± 6) nm).

We note that the rings have an apparent impurity or “pinning object” (right optical image in Figure 3-30) that seemingly creates higher agglomeration in its vicinity. As

discussed earlier, the drying of the droplet initiates from the edges of the sample, and propagates toward its center. Based on the shape of the rings we propose that this pinning object is likely to have deposited early during solvent evaporation, subsequently pinning the contact line for a long period of time, and creating a large agglomeration of molecules along the contact line. Similar behavior was described in a report by Deegan in 2000.³³ In Figure 3-32 we show SEM images of this object from the top view and by tilting the SEM stage at 40°. As we can see, this pinning object is a highly packed aggregate of t_n-ZnPc rods that evidently formed in solution and settled on the substrate surface, locally pinning the solution/substrate contact line as the solvent evaporates.

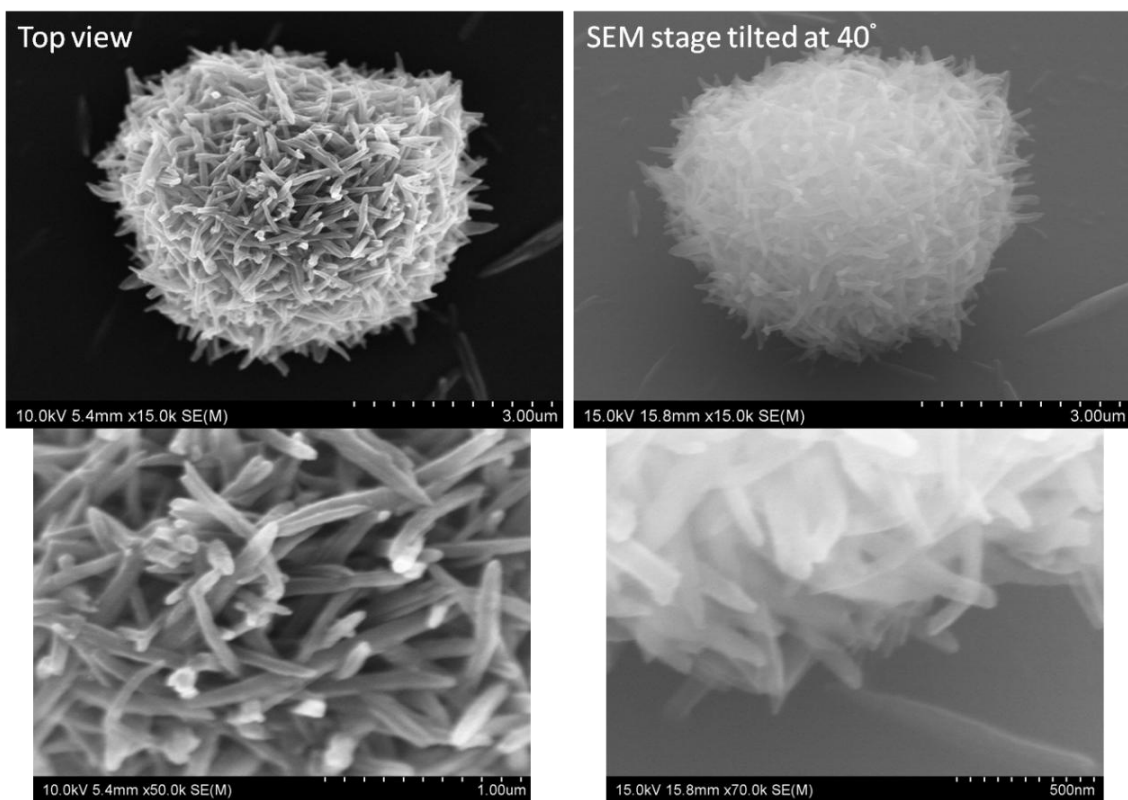


Figure 3-32. SEM images of a "pinning object" formed via drop-casting of a (1:2) t_n-ZnPc/PCBM mixture solution, shown in top view (left) and with the SEM stage tilted at 40° (right). The images at the bottom are magnifications of the images above.

In conclusion, we find that the overall trend of molecular domains formation on the substrate for drop-casting a solution of a (1:2) tn-ZnPc/PCBM mixture is similar to that for a solution of a (1:1) mixture, but in this case we observe evidence for more extensive interaction between the two materials: the PCBM forms a blanket phase that breaks down into small spherical cap clusters where the initial evaporation is faster (at the edges of the droplet where the loss of solvent is faster). At the very center of the sample the blanket shows holes that are less deep than those formed where there is high density of molecules, i.e. at the rings. We again see no evidence of crystallinity of the PCBM domains, as discussed earlier (Section 3.1.2). We surmise that, even for this more PCBM-concentrated mixture, the tn-ZnPc suppresses PCBM crystallization at this solvent evaporation rate.

3.3.1.2 Immersion in (1:2) tn-ZnPc/PCBM Mixture Solutions

In this part of the study we performed the deposition via immersion in a solution of a (1:2) tn-ZnPc/PCBM mixture, placing the substrate in both vertical and horizontal orientations in the container. In this case, we performed only the deposition method that created the slowest solvent evaporation rate (i.e. nearly-closed container).

Results for the vertical orientation of the substrate are reported in Figure 3-33. Here the tn-ZnPc rods deposit in horizontal bands, i.e. there are areas with low rod density, and areas with high density of rods. Unlike the case for immersion in a 1:1 ratio mixture solution, hexagonal clusters of PCBM form, suggesting crystallinity. We find that the clusters are slightly more regular in areas with low density of rods (Figure

3-33(a)), whereas, they show an onset of dendrites formation, suggesting cellular growth in areas with higher density of tn-ZnPc rods (Figure 3-33(b)).

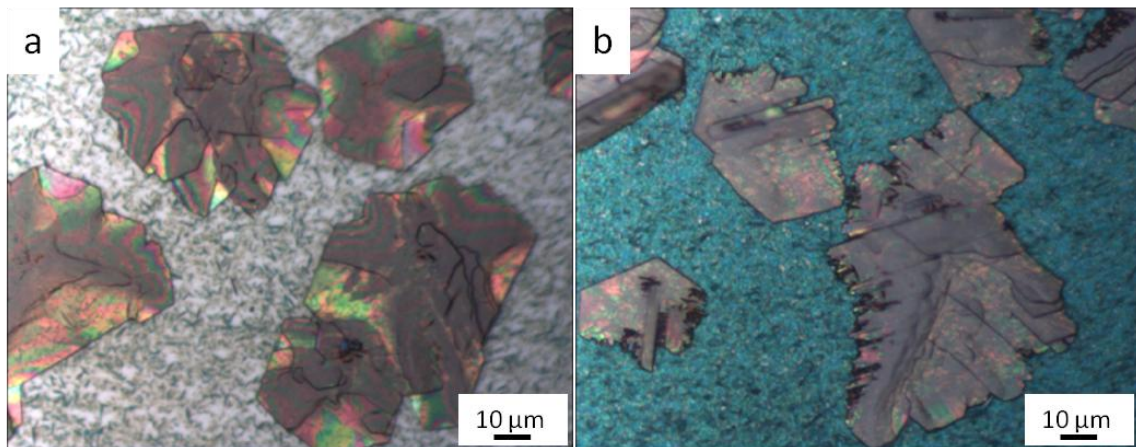


Figure 3-33. Optical images of structures which form during deposition via immersion in a solution of a (1:2) tn-ZnPc/PCBM mixture; deposition was in a nearly-closed container, with a vertical orientation of the substrate. (a) Image recorded in an area with low density of tn-ZnPc rods; (b) image recorded in an area with high density of rods.

Immersion into a solution of (1:2) tn-ZnPc/PCBM mixture with the substrate orientated horizontally again produces bands of high density of rods; however the bands are not linear, but dendritic. The formation of hexagonal clusters is again observed, but the density of rods does not seem to affect the regularity of the PCBM domains in this case. Highly regular hexagonal clusters are visible in both areas of low and high density of rods (Figure 3-34) and no obvious indication of cellular growth is observed, although there was some plate stacking where the rod density was higher; this seemingly is related to the higher local density of PCBM molecules deposited here. Evidently, the horizontal orientation of the substrate during deposition via immersion of the (1:2) tn-ZnPc/PCBM mixture favors the stability of the crystalline growth of PCBM domains, even in presence of the tn-ZnPc.

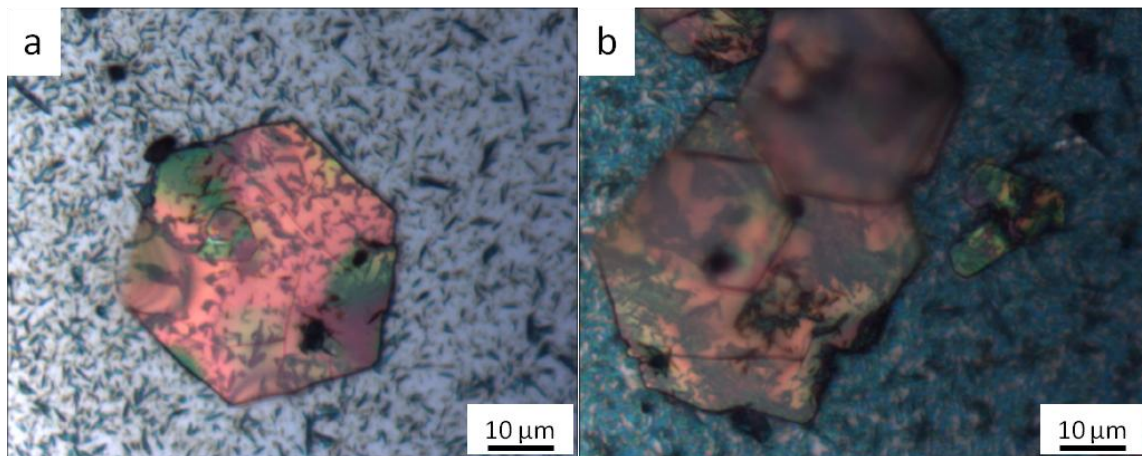


Figure 3-34. Optical images of structures which form during deposition via immersion in a solution of a (1:2) tn-ZnPc/PCBM mixture; deposition was in a nearly-closed container, with a horizontal orientation of the substrate. (a) Image recorded in an area with low density of tn-ZnPc rods; (b) image recorded in an area with high density of rods.

3.3.2 (2:1) tn-ZnPc/PCBM Mixtures

In this section we report results for deposition from solutions of (2:1) tn-ZnPc/PCBM mixtures. As in the previous section, deposition was via drop-casting, as well as immersion into solution with vertical and horizontal orientations of the substrate.

3.3.2.1 Drop-casting of (2:1) tn-ZnPc/PCBM Mixture Solutions

Optical images of the structures resulting from the drop-casting of the solutions of (2:1) tn-ZnPc/PCBM mixtures do not show coffee-rings at the center of the samples (first image in Figure 3-35). Rings do form toward the sample edges however. We find that they are not circular as they were in the case of drop-casting from solutions of (1:2) tn-ZnPc/PCBM mixtures (second image in Figure 3-35). However, they do exhibit similar pinning objects, along with an agglomeration of molecules. The last two panels in Figure 3-35 show the vicinity of a pinning object in which there are two adjacent arcs with a

selective order: based upon the color, the arc closer to the pinning object is apparently tn-ZnPc-rich (bluish) and the outer one is apparently PCBM-rich (brownish).

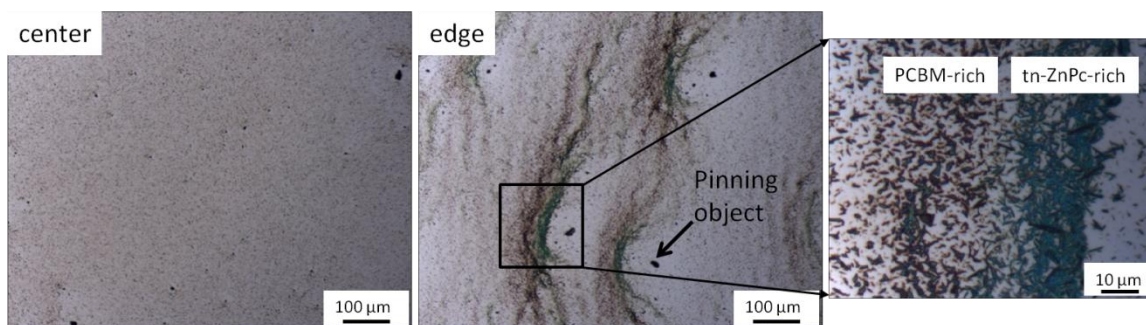


Figure 3-35. Optical images of structures which form during deposition via drop casting of a solution of a (2:1) tn-ZnPc/PCBM mixture.

The pinning objects, as the previous case, are highly packed agglomerations of rods, presumably forming in solution and settling on the substrate. They pin the contact line that the droplet makes with the substrate during solvent evaporation for a time long enough to let other molecules concentrate in its vicinity. Our observation that other tn-ZnPc rod clusters concentrate close to the pinning object, and that PCBM clusters concentrate next to them could be explained in the following way: because of the larger density of tn-ZnPc rods with respect to the PCBM in the mixture, the rods deposit before the PCBM but subsequent to the heavier pinning objects; thus, the single rods form the arc because the front is pinned during their deposition while the PCBM deposits later, and is seemingly repelled by the rods. This in turn suggests that the phase separation takes place just above the substrate.

In Figure 3-36, we show a SEM image of a pinning object resulting from drop-casting deposition from a solution of a (2:1) tn-ZnPc/PCBM mixture, taken with the stage tilted at 40°. We can see that it is similar to that for the (1:2) mixture: it is an agglomeration of rods. The right panel of Figure 3-36 shows the contact line of this

object with the silicon substrates and suggests that it was formed in solution and settled on the substrate.

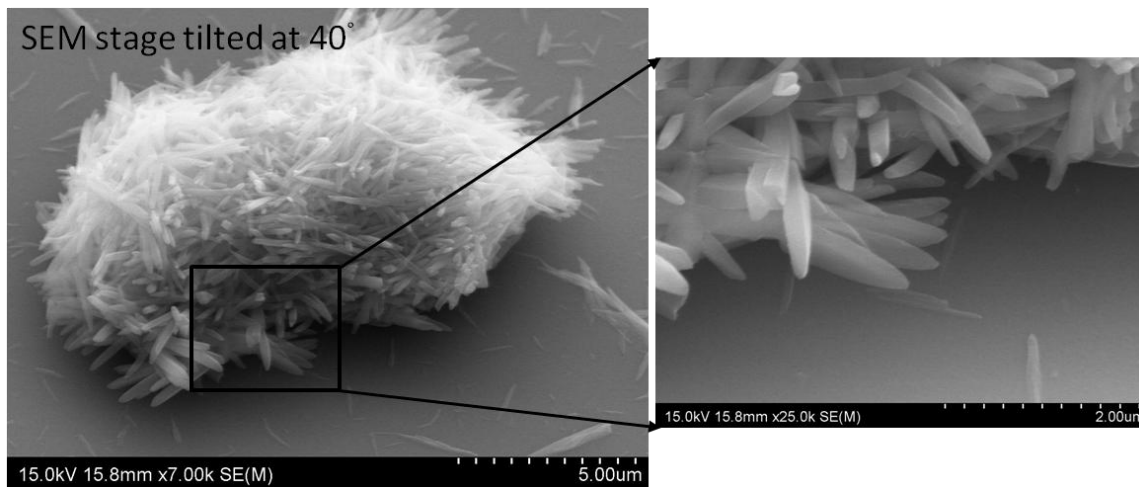


Figure 3-36. SEM images of the "pinning object" resulting from drop-casting deposition from a solution of a (2:1) tn-ZnPc/PCBM mixture taken with the SEM stage tilted at 40°. The image at the right is magnifications of the contact area.

In Figure 3-37(a) we show the AFM topography maps recorded at the center of the sample. The PCBM blanket is no longer apparent; instead there are small clusters around the tn-ZnPc rods. However, some indication of a small region of blanket phase is observed in the phase-AFM image in Figure 3-37(b). We speculate that, initially the blanket formed, but because of the small amount of PCBM, it dewets quickly. Figure 3-37(c-d) shows the AFM topography images acquired within a PCBM-rich arc and a tn-ZnPc-rich arc, respectively. We find that the edges of the rods in Figure 3-37(c) are not as well defined as those in Figure 3-37(d). This suggests that within the PCBM-rich arcs the rods are partially covered with PCBM-blanket phase, while within the tn-ZnPc-rich arcs the tn-ZnPc rods are completely phase separated from the PCBM. The small regions of blanket phase observable in Figure 3-37(b) are (10 ± 2) nm thick, much smaller than the blanket thickness observed for deposition via drop-casting of a solution of (1:2) tn-

ZnPc/PCBM mixtures (~ 74 nm). This is seemingly due to a strong tendency for the PCBM to agglomerate into spherical cap clusters.

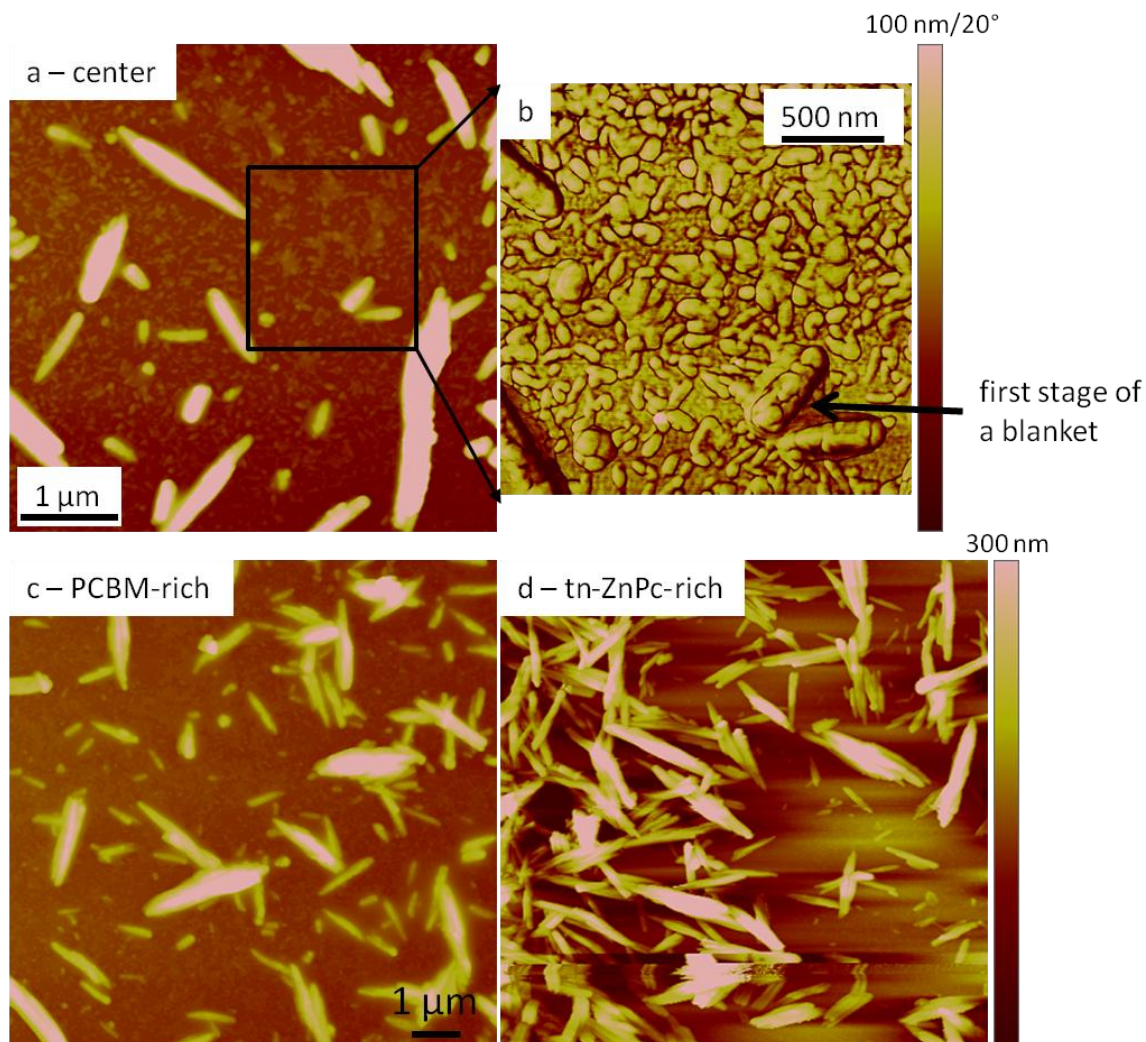


Figure 3-37. AFM topography images of structures resulting from drop casting deposition from a solution of a (2:1) tn-ZnPc/PCBM mixture measured (a) near the center of the sample, (c) within in a PCBM-rich arc, and (d) within a tn-ZnPc-rich arc. Panel (b) shows a phase-AFM image of a magnificated region of panel (a), as indicated by the square.

3.3.2.2 Immersion in (2:1) tn-ZnPc/PCBM Mixture Solutions

In this part of our study we deposited via immersion in a (2:1) tn-ZnPc/PCBM mixture solution in the nearly-closed container, for both vertical and horizontal orientations of the substrate. We find that, not only are hexagonal clusters of PCBM

formed, as was the case for the (1:2) tn-ZnPc/PCBM mixture, but also the regularity of the hexagonal domains, and thus most likely the degree of crystallinity is higher; this despite of the larger admixture of tn-ZnPc.

Figure 3-38 shows the optical images of the hexagonal domains of PCBM recorded in an area with a low density of tn-ZnPc rods (panel a) and in an area with a high density of rods (panel b). Surprisingly, we note that formation of highly regular hexagonal domains of PCBM is favored on areas with high density of the phthalocyanine component, while the hexagons are far less regular on areas with a smaller coverage of tn-ZnPc rods. Also, we note that certain PCBM domains show an elongation along two parallel sides (Figure 3-38(b)).

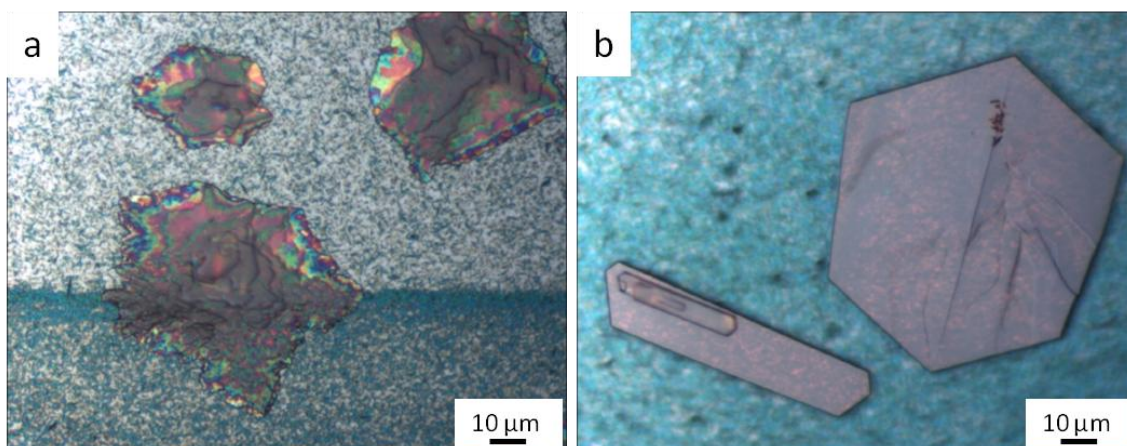


Figure 3-38. Optical images of structures which form during deposition via immersion in a solution of a (2:1) tn-ZnPc/PCBM mixture; deposition was in a nearly-closed container, with a vertical orientation of the substrate. (a) Image recorded in an area with low density of rods; (b) image recorded in an area with high density of rods.

Results from the deposition on the substrate immersed horizontally in the (2:1) tn-ZnPc/PCBM mixture solution are shown in Figure 3-39. Once again, we observe a correlation between growth habits of PCBM and density of rods on the substrate, which also depends on the orientation of the substrate during deposition. In particular, we find

the opposite correlation between PCBM domains shape and tn-ZnPc rods coverage compared to that for vertical substrate orientation: on areas with low density of tn-ZnPc rods, the hexagonal domains are highly regular, while on areas with high density of phthalocyanines, the degree of hexagonal domains regularity is slightly lower. In this case, we do not observe examples of “elongated hexagonal” domains of PCBM.

For neither substrate orientations is obvious dendritic growth. Therefore, we conclude that by increasing the amount of phthalocyanine molecules, we can increase the degree of crystallization of the fullerene derivative.

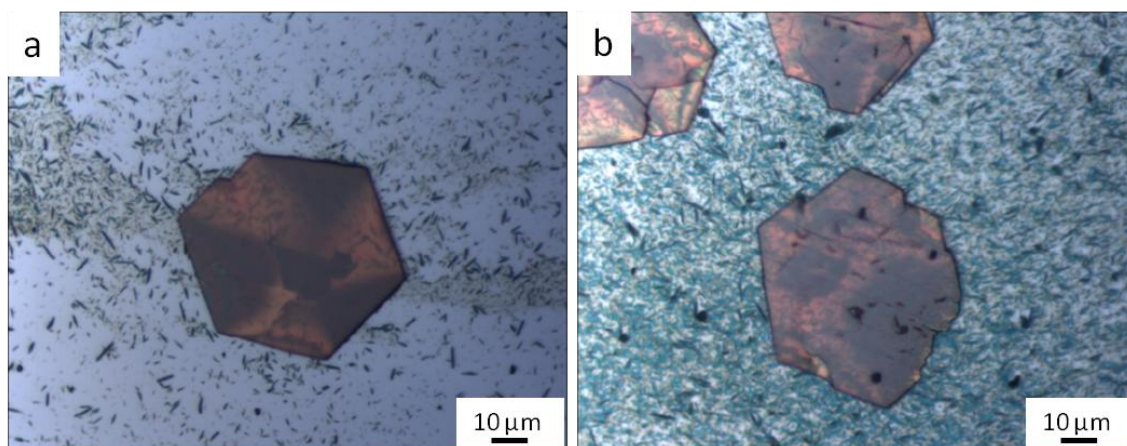


Figure 3-39. Optical images of structures which form during deposition via immersion in a solution of a (2:1) tn-ZnPc/PCBM mixture; deposition was in a nearly-closed container, with a horizontal orientation of the substrate. (a) Image recorded in an area with low density of rods; (b) image recorded in an area with high density of rods

3.3.3 Conclusions for the Results of Stoichiometries (1:2) and (2:1) tn-ZnPc/PCBM Mixtures

In conclusion, we demonstrated that deposition from solutions with tn-ZnPc/PCBM mixtures different that (1:1) favor the formation of hexagonal domains, presumably crystalline, of the PCBM, while deposition from solutions with (1:1) tn-ZnPc/PCBM mixtures suppresses it. This suggests that the ratio 1:1 produces spinodal

decomposition of PCBM, while changing the relative amount of individual molecules favors the nucleation of PCBM.

In particular, we have seen that by increasing the amount of tn-ZnPc, we seemingly obtain an even higher degree of crystallization of the PCBM. This can be explained with the fact that phthalocyanine molecules have a strong tendency to bond to each other. Therefore, a large amount of tn-ZnPc molecules will provide stronger interactions, leaving less single molecules in solution. As consequence, PCBM molecules will encounter an environment more “tn-ZnPc-free”, so that their crystallization is not suppressed.

We also confirmed that the orientation of the substrate during the deposition of the mixture via immersion is crucial, and allows for different growth habits of the PCBM in correlation with the local density of tn-ZnPc rods.

Finally, the arrangements of molecular domains formed on the substrate by drop-casting different admixtures of the two components confirms the Marangoni model discussed above for the (1:1) admixture: (1) tn-ZnPc molecules/clusters seemingly flow toward the edges of the droplet where they deposit and pin the contact line, resulting in a stick-slip motion as additional solvent evaporation generates a large enough pressure to overcome this – the result is formation of irregular lines, and (2) PCBM molecules flow toward the center making concentric coffee-rings with the tn-ZnPc near the center of the sample.

3.4 Dynamic Light Scattering Analysis

In order to investigate clustering of the tn-ZnPc and PCBM molecules in solution as the solvent evaporates, we performed Dynamic Light Scattering (DLS) measurements at different concentrations. We analyzed the single component solutions and the mixture of both at 1:1 ratio. The concentrations analyzed for each case were 0.125, 0.25, 0.5, 1 mM (only for PCBM, we analyzed also 2.5 mM). The measurements have been performed at the Light Scattering Center at the Institute for Physical Science and Technology (University of Maryland) using the multi-angle dynamic light scattering spectrometer (Photocor Instruments). The light source employed was He-Ne laser (wavelength 633 nm) and the light scattering was observed at a scattering angle of 90°.

The main property obtained with DLS is the time-dependent autocorrelation function $G(\tau)$ of the light-scattering-intensity fluctuations, which can be expressed by:³⁴

$$G(\tau) = b \left[1 + \varepsilon \exp\left(-\frac{\tau}{\tau_D}\right) \right] \quad (3-2)$$

where b is the baseline of the correlation function which is proportional to the total light-scattering intensity, τ is the “delay” time that defines the time-scale of the measured correlation function, τ_D is the decay time, i.e. the characteristic time of diffusion at a given length scale, and ε is a coefficient that depends on the amount of stray light and on the light-collecting aperture.

The diffusion coefficient D of the particles is directly related to the decay time τ_D by the following relationship:

$$\frac{1}{\tau_D} = 2Dq^2 \quad (3-3)$$

where q is the wavenumber of the scattered light, defined as:

$$q = \frac{4\pi n}{\lambda} \sin\left(\frac{\theta}{2}\right) \quad (3-4)$$

where n is the refractive index of the solvent, λ is the wavelength of the incident light, and θ is the scattering angle.

Given the diffusion coefficient, it is possible to obtain information about the size of the particles diffusing in Brownian motion in a solution via the Stokes–Einstein equation.³⁵

$$D = \frac{k_B T}{6\pi\eta R_h} \quad (3-5)$$

where k_B is Boltzmann’s constant, T is the temperature, and η is the shear viscosity of the solvent, and R_h is the “hydrodynamic radius” of the particles, which is defined as the radius of a hard sphere diffusing at the same rate as the particle under observation.

The Stokes–Einstein equation is valid for non-interacting particles (Brownian motion). When particles start to interact by developing clusters larger than 10 μm , they no longer diffuse as free particles, but gravity becomes important, and this decreases diffusion and velocity of the clusters. Therefore, when such a large particle crosses the laser beam, the crossing-time detected by the correlator is very large. The illicit application of the Stokes-Einstein equation causes the reported size to be erroneously large. While the reported sizes do not reflect the “real” cluster sizes, this equation is still applicable in order to verify the aggregation of particles.

The PCBM/chloroform solutions at all concentrations tested do not show evidence of agglomeration. For simplicity, in Figure 3-40, we reported only the result obtained for the largest concentration 2.5 mM. This plot shows that there is no detectable

correlation in the fluctuations of the intensity of scattered light as function of time. This indicates that there are not large agglomerations of molecules in this solution.

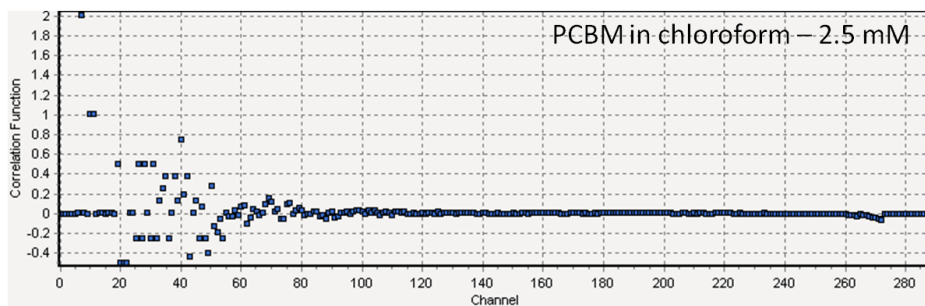


Figure 3-40. Absence of the detectable autocorrelation function of PCBM/chloroform solution at 2.5 mM

The tn-ZnPc/chloroform solutions show an interesting behavior. Figure 3-41 reports the autocorrelation functions and the submicron particle size referred to the tn-ZnPc solutions at different concentrations. In Table 3-1 we reported the hydrodynamic radius of the aggregates detected in the tn-ZnPc solution. At the lower concentration of 0.125 and 0.25 mM we see only one type of monodisperse equilibrium agglomerates of size ~ 100 nm. However, we note that at 0.25 mM the sizes decrease. The concentration of 0.5 and 1 mM are higher than the solubility of tn-ZnPc in chloroform (0.37 mM); thus, we assume that the solution has reached the supersaturation. Unlike the dilute solutions, these two, with larger concentrations, show that the mean and the peak position values of the distribution curves are very different, with a very high standard deviation. This behavior suggests that at 0.5 mM, this solution starts to form large polydisperse aggregates. Given the very low solubility of this substance, it is evident that the equilibrium molecular clusters under supersaturation start to aggregate in even larger particles at the expenses of the small ones.

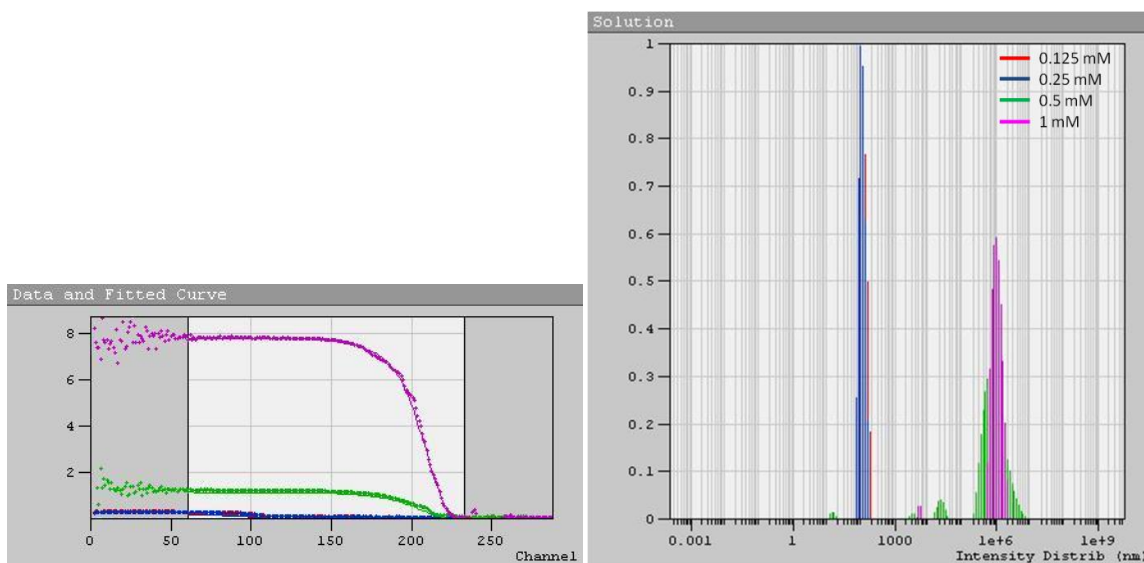


Figure 3-41. Autocorrelation functions (left) and hydrodynamic radius of particles (right) of tn-ZnPc/chloroform solutions.

Concentration (mM)	R_h (nm)		
	Mean	Peak Position	Standard Deviation
0.125	114 ± 27		
0.25	101 ± 21		
0.5	1.1×10^6	6.2×10^5	9.1×10^5 ($\chi^2 = 0.014$)
1	1.1×10^6	9.8×10^5	3.7×10^5 ($\chi^2 = 0.071$)

Table 3-1. Hydrodynamic radius of particles present in the tn-ZnPc solutions at different concentrations.

The analysis of the mixture of the both substances with 1:1 ratio is reported in Figure 3-42, where the autocorrelation functions along with the sizes of the particles are shown. This case, unlike the previous one, shows monodisperse distribution of the equilibrium aggregates at all concentrations tested. These aggregates slightly decrease in size as the concentration increases (Table 3-2). This behavior, as the previous case, can be interpreted as the diffusion of small aggregates toward each other resulting in larger clusters at the expenses of the small ones. However, at high concentrations, the larger

agglomerates are weakly detectable, due to the very small quantity. This is indicated in the right graph of Figure 3-42, where the presence of very large scatters with much larger decay time is observable via the “relative” size of the order on 10^6 nm.

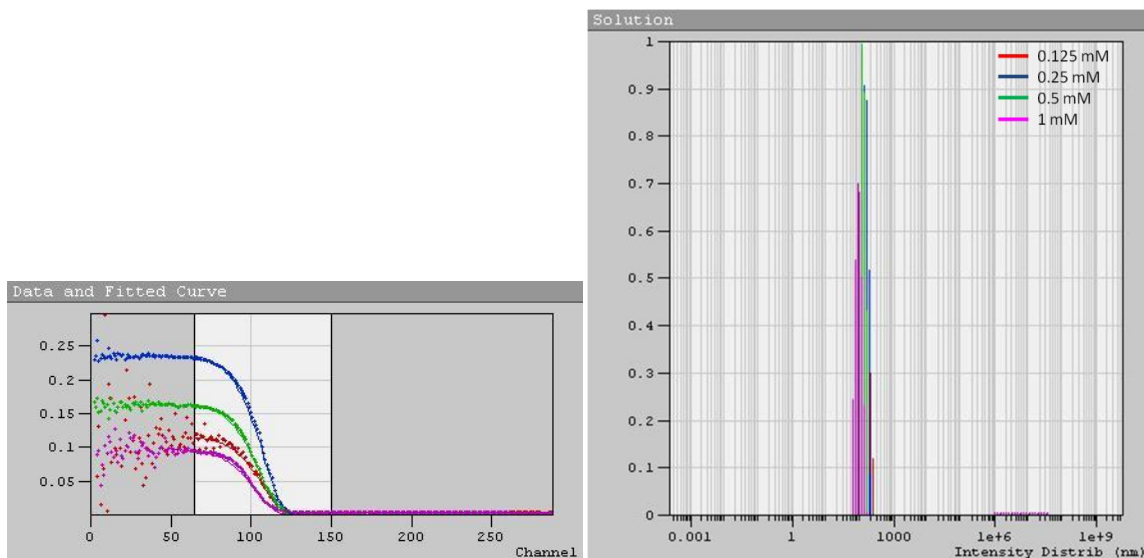


Figure 3-42. Autocorrelation functions (left) and hydrodynamic radius of particles (right) of Mix/chloroform solutions.

Concentration (mM)	R_h (nm)
0.125	138 ± 40
0.25	137 ± 26
0.5	116 ± 19
1	85 ± 28

Table 3-2. Hydrodynamic radius of particles present in the mixture solutions at different concentrations.

Interesting information that we can obtain from these measurements is to what extent the anisotropy of the aggregates is relevant. In other words, whether the aggregates are spherical (isotropic) or rod-like (anisotropic) particles. The vertically-polarized component of the incident light contains both anisotropic and isotropic contributions, and the “depolarization ratio” can be defined as follows:³⁶

$$\Delta_V = \frac{V^H}{V^V} \quad (3-6)$$

where V^H and V^V are the intensities of the horizontal and vertical polarization component of the scattered light, respectively. This ratio, calculated for tn-ZnPc-alone and the mixture solution, varies between 25% and 30%, depending on the concentration, indicating that the scatters are significantly anisotropic. Therefore, it is likely that the equilibrium aggregates of tn-ZnPc molecules have a rod shape in solution with equilibrium sizes of ~ 100 nm that sharply increases when the solution is supersaturated. We can also say that, given the similar behavior of the tn-ZnPc-alone and the mixture solutions, the equilibrium agglomerates observed in the mixture are formed by tn-ZnPc only, while PCBM molecules are likely to be still well dissolved.

In conclusion, we can say that the PCBM molecules are well dissolved in chloroform even at higher concentration, whereas the majority of tn-ZnPc molecules agglomerate in equilibrium clusters of $R_h \sim 100$ nm even at very low concentrations. At higher concentrations we observe the formation of much larger (micron-size) polydisperse aggregates at the expenses of those at the equilibrium. This event occurs beyond the solubility threshold, thus suggesting that the formation of the rod-like crystals (also order of microns) that we observe on the substrates start already in solution.

3.5 Force-Curves Results

In this work, force-curves measurements have been carried out to investigate the adhesion force between tip and molecular film.

The purpose was to verify the presence of a wetting layer of tn-ZnPc between tn-ZnPc agglomerations during spin-coating deposition, whose presence was hypothesized

by the different morphology/size of the PCBM phase when deposited from the mixture, and compare the adhesion between same molecular aggregates in the single component molecular film and in the mixture in ratio 1:1 with the other component, to investigate how they affect one another.

The adhesion forces are attractive forces that hold two bodies in contact; therefore, the information about them is contained in the jump-off contact during the withdrawing of the AFM tip from the sample surface, as the pulling force needs to separate tip from sample.

In our case, we can neglect the capillary forces, since we performed the analysis in nitrogen environment; therefore, the contribution of the water meniscus is negligible.

The force between two molecules $F(r)$ separated by a distance r is given by the gradient of their potential energy $W(r)$:³⁷

$$F(r) = -\frac{\partial W(r)}{\partial r} \quad (3-7)$$

The weakest intermolecular forces, the van der Waals interactions, are responsible for the adhesion forces. These interactions occur in the range of a few Å up to 10 nm.

Van der Waals attractive forces comprise three subgroups:

- Dipole-dipole forces (Keesom forces) – which occur between molecules having permanent dipoles (polar molecules):³⁸

$$W_K(r) = -\frac{C_K}{r^6} = -\frac{\mu_1^2 \mu_2^2}{3(4\pi\epsilon_0\epsilon)^2 k_B T r^6} \quad (3-8)$$

where r is the distance between the two molecules, $\mu_{1,2}$ are the dipole moments of the molecules, ϵ_0 and ϵ are the dielectric constant of the vacuum and the medium, respectively, k_B is the Boltzmann's constant and T is the temperature;

- Dipole-induced dipole forces (Debye forces) – which occur when the field of a permanent dipole induces a dipole in a non-polar molecule or alters its dipole in a polar molecule.³⁸

$$W_D(r) = -\frac{C_D}{r^6} = -\frac{\mu_1^2\alpha_{02} + \mu_2^2\alpha_{01}}{(4\pi\epsilon_0\epsilon)^2r^6} \quad (3-9)$$

where α_0 are the electronic polarizabilities of the two molecules;

- Dispersion forces (London forces) – which occur between instantaneous dipoles created inside a non polar or polar molecule due to fluctuation of charge distribution in neighboring molecules.³⁸

$$W_L(r) = -\frac{C_L}{r^6} = -\frac{3}{2} \frac{\alpha_{02}\alpha_{01}}{(4\pi\epsilon_0)^2r^6} \frac{h\nu_1\nu_2}{\nu_1 + \nu_2} \quad (3-10)$$

where $h\nu_{1,2}$ are the first ionization potentials of the molecules and h is the Planck's constant.

The total van der Waals potential is given by the sum of all these interactions:³⁸

$$W_{vdW}(r) = -\frac{3k_B T}{(4\pi\epsilon_0\epsilon)^2r^6} \left(\frac{\mu_1^2}{3k_B T} + \alpha_{01} \right) \left(\frac{\mu_2^2}{3k_B T} + \alpha_{02} \right) - \frac{3}{2} \frac{\alpha_{02}\alpha_{01}}{(4\pi\epsilon_0)^2r^6} \frac{h\nu_1\nu_2}{\nu_1 + \nu_2} \quad (3-11)$$

The first term acts only between polar molecules, and the second term acts between every atom or molecule; therefore, this latter is the most important and dominates the van der Waals interaction, because, despite the weakness of individual contacts, the cumulative effect of a series of such interaction can be energetically significant.³⁸

The nitro functional groups ($-\text{NO}_2$) in the tn-ZnPc and the phenyl group ($-\text{C}_6\text{H}_5$) and the methoxy group ($-\text{O}-\text{CH}_3$) in the PCBM are highly electronegative: electrons are pulled from the metal core to the oxygen atoms in a tn-ZnPc molecule, and from the

hydrogen to the carbon atoms and into the fullerene cage in a PCBM molecule. Therefore, the external atoms of the *tn*-ZnPc show a negative charge, while those at the functional groups of PCBM show a positive charge. The four individual Zn-NO₂ “arms” have a dipole moment in the molecular plane that might be larger than that for ZnPc (4.05 D)³⁹ because of the presence of the nitro groups. However, since *tn*-ZnPc is a planar and symmetrical molecule, it has zero net dipole. Therefore, *tn*-ZnPc is considered a non-polar molecule. The PCBM molecule exhibits a strong dipole moment of ~ 5 D pointing from the center of the fullerene cage to the oxygen atoms in the methoxy group,⁴⁰ and it has a net intrinsic dipole of ~ 1.88 D pointing from the center of the cage to the carbon atom that links the bucky-ball to the functional group along the molecular axis. Therefore, PCBM is a polar molecule. The value of the PCBM intrinsic dipole has been calculated given the electron distribution inside the molecule, which is 0.11 electrons that are transferred from the functional groups into the fullerene cage.⁴¹ The schematics of the dipoles in *tn*-ZnPc and PCBM are shown in Figure 3-43 in the negative-to-positive charge convention.

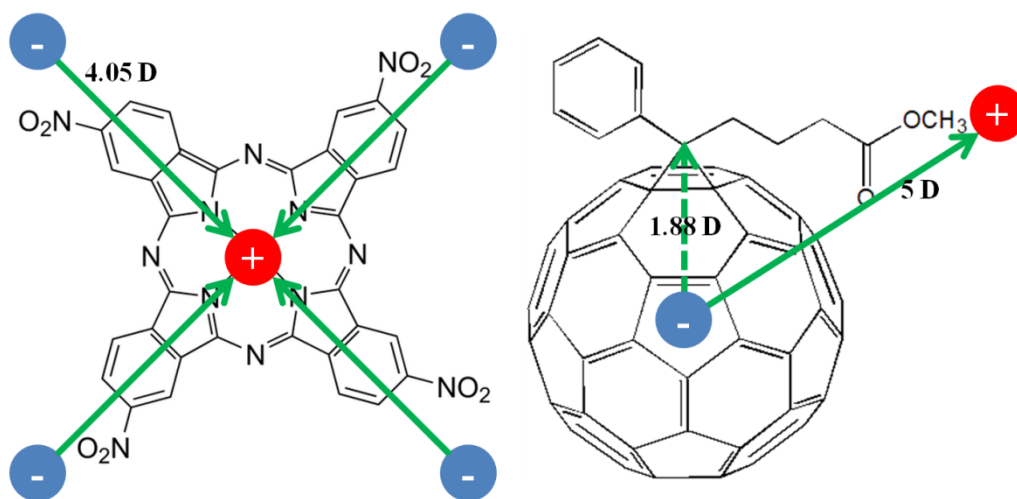


Figure 3-43. Schematics of the dipoles of *tn*-ZnPc (left) and PCBM (right) molecules (in the negative-to-positive charge convention).

These dipoles interact with the atoms at the end of the AFM tip through van der Waals attractions, and the result of these interactions is given by the adhesion force, which is represented by the depth of the well in the retracted curve of the force-displacement curve. The entity of this force is given by several factors, like the strength of the dipoles, the size and shape of the molecules and the polarizability of the molecules.

The force curves have been performed in nitrogen environment, for eliminating the effect of the water meniscus formed between tip and sample. We used a spherical silica (which is non-polar) AFM probe of diameter $\sim 1.9 \mu\text{m}$, and a conical silica AFM probe of tip radius $\sim 8 \text{ nm}$ and conical angle $\sim 30^\circ$ for areas on the substrate that are in between particles very close to each other, for which the spherical tip is too large.

The silicon substrates used for obtaining the force-curves relative to bare silicon and for the depositions have been cleaned with RCA-cleaning, but the presence of naturally occurring native oxide and hydrocarbons is inevitable (Figure 3-44). Therefore, it is expected that the atoms with which the AFM probe interacts on bare silicon, and the atoms with which the organic molecules interact when deposited, are oxygen atoms derived from the native oxide and hydrogen atoms derived from the hydrocarbons. These contaminants are non-polar.

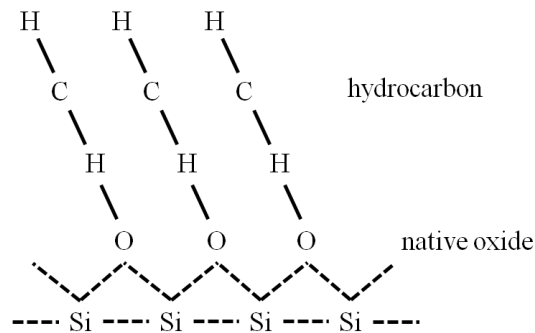


Figure 3-44. Schematics of native oxide and hydrocarbons present on Si(111) surfaces.

3.5.1 Force-Curves Measured with Spherical AFM Probe

For the analysis of the organic molecules, they have been deposited onto Si(111) substrates through spin-coating (2000 rpm, 45 seconds).

We measured the force curves between our spherical probe and the following areas:

1. bare Si(111) substrate coated with native oxide and hydrocarbons;
2. areas between tn-ZnPc rods deposited from single-component solution;
3. tn-ZnPc rods deposited from single-component solution;
4. tn-ZnPc rods deposited from (1:1) mixture solution;
5. PCBM spherical caps deposited from single-component solution;
6. PCBM spherical caps deposited from (1:1) mixture solution.

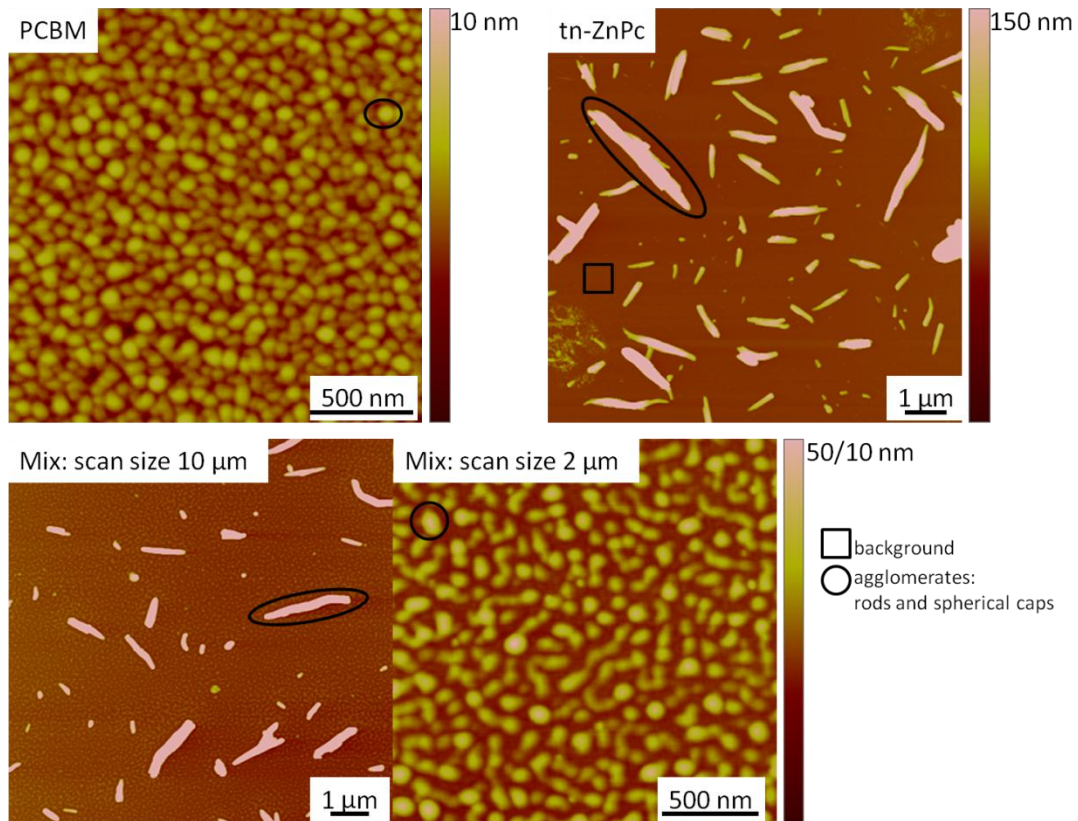


Figure 3-45. Objects under examination on spin-coated samples in force curves analysis.

In the case 1, the silica probe interacts with only the contaminants present on the silicon surface; therefore the interactions taking place are dispersive and described by Equation (3-10).

When tn-ZnPc is deposited on the silicon surface (case 2 and 3) and interacts with the silica probe the interactions are dispersive as well, because tn-ZnPc does not have a permanent dipole. However, in near-contact the presence of the individual dipoles in the tn-ZnPc molecules makes these interactions stronger than the interactions occurring in the case 1, especially if the tn-ZnPc lay flat on the substrate, because the charge distribution in the molecular plane is not uniform.

When PCBM is deposited on the silicon surface (case 5) the permanent dipoles in these molecules induce a dipole in the silica atoms of the tip, leading to dipole-induced dipole interactions described by Equation (3-9). The strong dipoles of PCBM make this term higher than the dispersive terms in the case 1, 2 and 3.

The background between rods of tn-ZnPc looks like bare silicon at the AFM microscope (Figure 3-45), but the force curves measured on these areas show a very strong adhesion compared to that for pure silicon substrate coated with native oxide and hydrocarbons (left plot in Figure 3-46). This proves the interaction of the AFM probe with the tn-ZnPc molecules, presumably laying flat on the substrate; we will demonstrate in Chapter 5 that tn-ZnPc molecules in the wetting layer lay flat on the silicon substrate. This demonstrates that, in a first stage, the tn-ZnPc molecules interact with the contaminants present on silicon, forming a wetting layer.

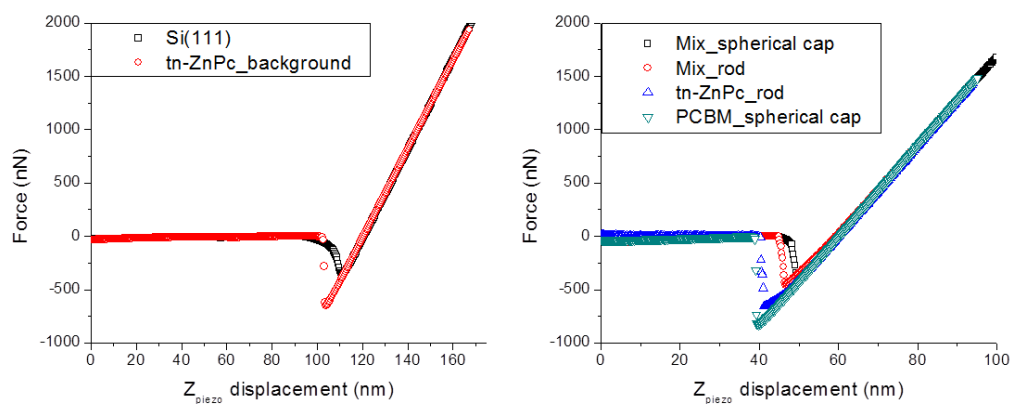


Figure 3-46. Comparison between retracted force-curves measured with spherical AFM tip on bare Si(111) and areas between tn-ZnPc rods on sample spin-coated with pure tn-ZnPc solution (left), and on PCBM spherical caps and tn-ZnPc rods present in the mixture-coated sample, on PCBM spherical caps present on PCBM-coated sample and on the tn-ZnPc rods present on the tn-ZnPc-coated sample (right).

The results for the aggregates in the mixture films (right plot of Figure 3-46) show that the overall dipole moment of the system tn-ZnPc/PCBM decreases (Mix_rod and Mix_spherical cap), compared to that for the single components aggregates (tn-ZnPc_rod and PCBM_spherical cap). The values of the adhesion forces are reported in Figure 3-47.

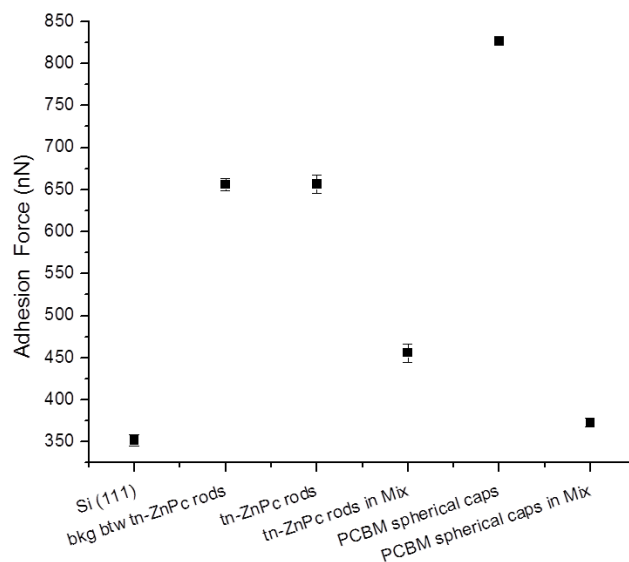


Figure 3-47. Adhesion forces measured on the six objects with spherical AFM probe.

In the mixture samples, what is interacting with the tip is a weak or non polar molecular system with low polarizability. The polarizabilities values α_0 for the two molecules are estimated using the Clausius-Mossotti formula:⁴²

$$\frac{\varepsilon_r - 1}{\varepsilon_r + 2} \frac{M}{\delta} = \frac{N_A \alpha_0}{3\varepsilon_0} \quad (3-12)$$

where ε_r and ε_0 are the relative dielectric constant of the molecules and the dielectric constant of the vacuum, respectively, M is the molar mass, δ is the density, and N_A is the Avogadro's number. The relative dielectric constant of tn-ZnPc is approximated to that for ZnPc, which is ~ 3.23 , and it is calculated dividing the ZnPc permittivity (2.86×10^{-11} C/V·m)⁴³ by the dielectric constant of the vacuum. While the relative dielectric constant of PCBM is equal to (4.0 ± 0.1) .⁴⁴ The molar masses are 757.9 g/mol and 910.88 g/mol for tn-ZnPc and PCBM, respectively. The densities are 1.63 g/cm³ for tn-ZnPc (approximated to that for ZnPc),⁴⁵ and 2.567 g/cm³ for PCBM (given by the manufacturer SES Research). The calculated values of α_0 are 8.75×10^{-39} C·m²/V for tn-ZnPc and 7.83×10^{-39} C·m²/V for PCBM. The tn-ZnPc molecules are slightly easier to be polarized than the PCBM molecules. The polarizability of the Silica atoms (taken from a work done by Kwaadgras *et al.*)⁴⁶ is equal to 5.25 Å³ which can be converted into C·m²/V by the following formula:⁴⁷

$$\alpha \left(\frac{\text{C} \cdot \text{m}^2}{\text{V}} \right) = 4\pi\varepsilon_0 \alpha (\text{m}^3) \quad (3-13)$$

The converted value is 5.8×10^{-40} C·m²/V, which is one order of magnitude lower than that for the organic molecules; therefore, the major contribution to the tip-sample dipole is given by the polarizability of the organic molecules in the sample.

In the mixtures, even though the volume of a tn-ZnPc molecule is larger than the volume of a PCBM molecule ($V_{tn-ZnPc} \sim 8 \times 10^{-22} \text{ cm}^3$, $V_{PCBM} \sim 5.9 \times 10^{-22} \text{ cm}^3$), the strong dipole moment of PCBM will induce a larger asymmetry in the charge distribution in the tn-ZnPc. This asymmetry might be such that the overall dipole is weak.

Based on the values of the adhesive forces reported in Figure 3-47, we can qualitatively describe the mutual interaction of the two components in terms of dipoles. The overall dipoles can be written in the following order: $\mu_{mix} \ll \mu_{tn-ZnPc} < \mu_{PCBM}$. The last inequality is given by the net intrinsic dipoles of the single molecules (i.e. $\mu_{tn-ZnPc} = 0$, $\mu_{PCBM} \sim 1.88 \text{ D}$). While the first inequality suggests that the interaction between tn-ZnPc and PCBM molecules lowers the overall dipole with which the AFM tip comes into interaction.

If we consider now the spherical agglomeration of PCBM in the single component film and in the mixture with the tn-ZnPc, we see that the adhesion force of the latter case is even lower. This might be explained in the following way: the aggregates of PCBM in both films are very small – $\sim 80 \text{ nm}$ in base diameter and $\sim 3 \text{ nm}$ in height – therefore the charge distribution might be affected by the underlying substrate; if the wetting layer of tn-ZnPc is present in the mixture as well the individual dipoles of tn-ZnPc could compensate or even cancel the dipoles on the overlying PCBM, and since PCBM has a lower polarizability, it will produce a very weak dipole with the tip through dispersion forces. In the next section, the presence of the wetting layer will be proved by performing force-curves with a conical tip between aggregates in the mixture.

These results prove that tn-ZnPc has a significant interaction with the naturally occurring contaminants of the silicon substrate, producing a wetting layer; and when the

PCBM and tn-ZnPc molecules are in close vicinity, their mutual orientation is such that the overall dipole moment of the system tn-ZnPc/PCBM is very weak.

3.5.2 Force-Curves Measured with Conical AFM Probe

The presence of the tn-ZnPc “wetting-layer” has been proved by force-curves performed with spherical tips on regions between rods in pure tn-ZnPc samples. In order to verify whether the wetting layer is present even when the tn-ZnPc interacts with the PCBM, we employed a conical AFM probe with a tip radius of 8 nm and conical angle $\sim 30^\circ$. The small tip radius allows us to probe the areas in between small spherical caps observed in the mixtures samples, and also provide a small contact area. This allows for more limited interactions with surface atoms. Therefore, in order to further characterize the nature of the particles that we “see” on the substrate, we also investigated the adhesion forces of the blanket phase of PCBM, along with the same objects that we tested in the previous set of samples.

In order to have the blanket phase, the molecules have been deposited through drop-casting. The objects investigated with the conical AFM probe are the following:

1. bare Si(111) coated with native oxide and hydrocarbon;
2. areas between PCBM phases in the mixture;
3. areas between tn-ZnPc rods in the mixture;
4. tn-ZnPc rods in the mixture;
5. PCBM spherical caps in the mixture;
6. blanket phase on the substrate in the mixture;
7. blanket phase on the rods in the mixture.

We note that the adhesion forces are much smaller than the cases measured with spherical tip. This is due, as we said above, to the smaller contact surface of the conical tip, allowing for small interaction forces, compared to the large contact area between the macroscopic spherical tip (1.9 μm) and the objects underneath. In Figure 3-48 we reported the force-curves obtained for all the seven cases. We plotted in such a way that we can do comparison in terms of adhesion forces (depth of the well in the retracted curve). The values of the adhesion forces are reported in the plot of Figure 3-49.

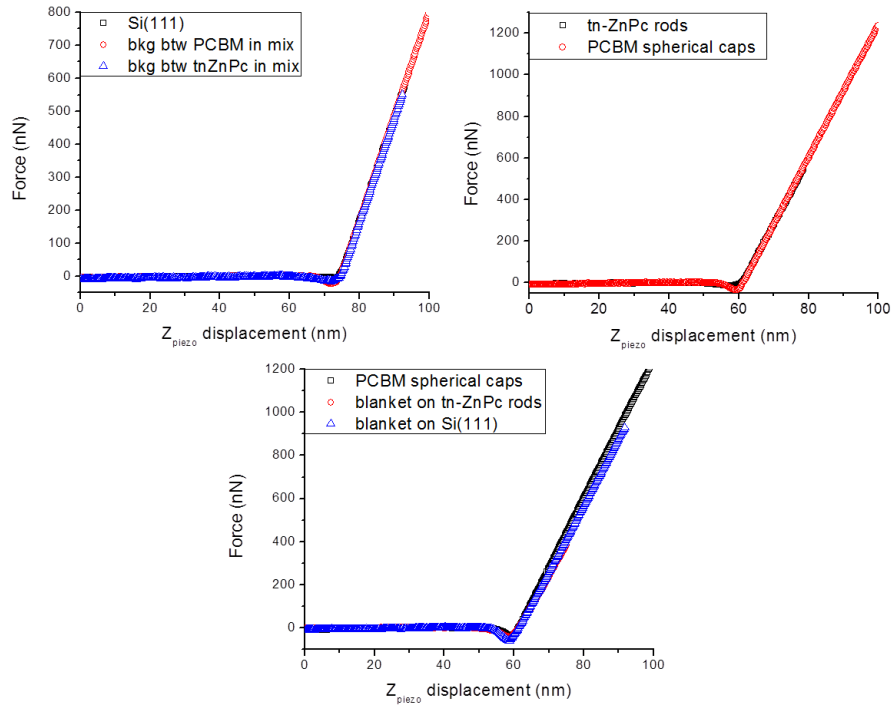


Figure 3-48. Comparison between retracted force-curves measured with conical AFM tip on bare Si(111), areas between PCBM phases, areas between tn-ZnPc rods, tn-ZnPc rods, PCBM spherical caps, blanket phase on the substrate, and blanket phase on the rods. All the force-curves, except the one measured for bare silicon, have been measured on mixture samples drop-casted.

We note that the areas between PCBM phases and rods of tn-ZnPc (areas that at AFM microscope looks like bare silicon) are coated with a layer that causes a larger

adhesion force. This layer has the same nature in terms of dipoles because the forces are similar in within the error. These forces are also very similar to the force obtained for the tn-ZnPc rod. This tells us that the layer on the background has the same nature of the tn-ZnPc rod. Again, this confirms that the tn-ZnPc wets the silicon substrate in the early stages of the depositions even in presence of the PCBM. That is why the morphology of PCBM changes when mixed with the tn-ZnPc: the PCBM does not interact with silicon when it is in the mixture, but it interacts with the wetting layer of tn-ZnPc.

On the other hand, the adhesion forces obtained for the PCBM spherical caps, the blanket phase on top of the rods, and the blanket phase on top of the substrate are very similar in nature of dipoles in within the error. This confirms that the molecular nature of the blanket is PCBM. The increasing of the adhesion forces of the PCBM phases compared with the tn-ZnPc phase is confirmed, as we saw in the previous section.

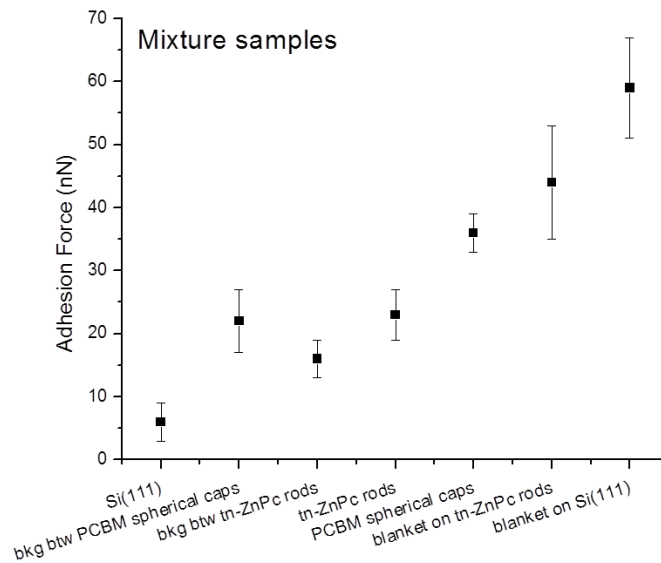


Figure 3-49. Adhesion forces measured on the seven different objects with conical AFM probe.

3.5.3 Conclusions for Force-Curves Results

In conclusion, we have proved that the tn-ZnPc in the very early stage of its depositions from both single component solution and the mixture with the PCBM, forms a wetting layer on the native oxide of the silicon substrate.

We have also proven that the nature of the blanket phase that we observe in the mixture is the same of the PCBM.

Finally, we have seen that the aggregates in the mixtures exhibit lower adhesion forces compared to the single component aggregates, suggesting a mutual interaction at the molecular level that lower the overall dipole moment of the system tn-ZnPc/PCBM.

3.6 Summary and Conclusions

From these results on unpatterned native oxide-terminated Si(111) substrates, we found that the two types of molecules selected for this study self-assemble into domains in qualitatively different ways during deposition from chloroform-based solution. Indications of crystalline growth of PCBM are observable for the lowest solvent evaporation rates studied during the deposition and under conditions allowing solvent vapor annealing (SVA) to act on the deposited molecular film. The tn-ZnPc molecules aggregate into rod-shaped clusters for all the solvent evaporation rates investigated; neither their formation nor their shape is significantly affected by the SVA. When deposited from a mixed solution, the morphology of the PCBM clusters formed is significantly affected by the presence of the tn-ZnPc, whereas the tn-ZnPc clusters are insensitive to the presence of the PCBM. Separate phases of the two types of molecules are formed over the entire range of solvent evaporation rates studied. Our observations

can be explained based upon the following model: (1) the tn-ZnPc molecules have very strong intermolecular forces and thereby aggregate – strongly dominating any interaction with the PCBM; the observation of a wetting layer suggests that some fraction of the tn-ZnPc deposits onto the substrate and (2) PCBM because of its higher solubility deposits subsequently; because the presence of the tn-ZnPc wetting layer on the substrate does not produce a favorable balance of surface/interface tensions for the PCBM to wet the surface uniformly, deposited PCBM molecules dewet the substrate forming clusters with a finite wetting angle relative to the surface. In addition, we observe that the size of the domains has an inverse relationship with the solvent evaporation rate: PCBM molecules form small spherical cap clusters at very high evaporation rates that increase in size, developing into large pyramidal-type structures as the rate of solvent evaporation decreases. In contrast, tn-ZnPc molecules agglomerate into single rods at very high evaporation rates, which become packed in larger rod-agglomerations as the rate of evaporation decreases. The characteristic size of PCBM clusters decreases in the presence of tn-ZnPc in the mixture at any solvent evaporation rate investigated. The apparent interaction also seemingly suppresses crystallization of PCBM, when mixed in ratio 1:1, and gives further support to the idea that not all tn-ZnPc molecules aggregate into rods or in the wetting layer. We observe a correlation between growth habits of PCBM and local densities of tn-ZnPc rod-domains, and find that this correlation changes depending on the orientation of the substrate during immersion deposition.

A pictorial summary of the different domains phases for each of the different deposition techniques/evaporation rates investigated in this work on unpatterned substrates employing a (1:1) tn-ZnPc/PCBM mixture are collected in Figure 3-50.

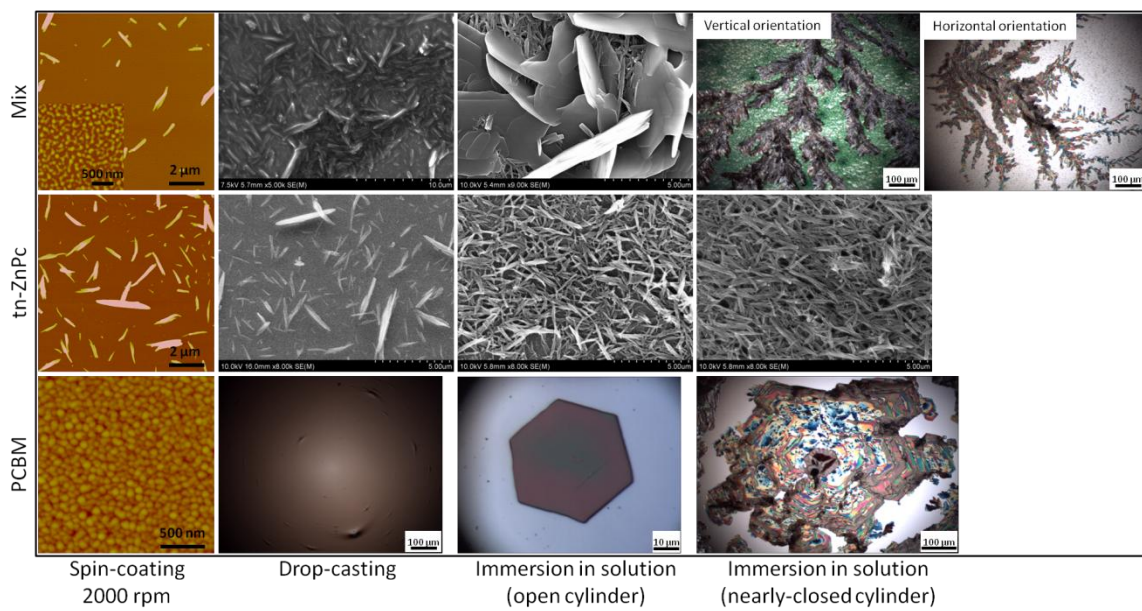


Figure 3-50. Summary of the different phases per molecules in single component and the (1:1) mixture at the different evaporation rate investigated.

We have demonstrated via force-curves analysis that the tn-ZnPc, with or without the presence of the PCBM, forms a wetting layer on the native oxide of the silicon substrate. We have also demonstrated that a “blanket” phase that we observed in the mixtures is made up of PCBM.

Our dynamic light scattering results demonstrate that PCBM molecules are well dissolved in solution at the concentrations we have studied, while most of the tn-ZnPc molecules exist in equilibrium agglomerates of $R_h \sim 100$ nm even at these concentrations. At higher supersaturations of tn-ZnPc, we observed the formation of clusters with R_h of the order of microns, suggesting that the formation of the stable rod-like clusters of tn-ZnPc that we observed at any evaporation rate investigated, occurs in solution.

We investigated the effect that different ratios of individual molecules in solution have on the self-assembly behavior of the molecules. We demonstrated that by changing, in particular increasing, the admixture of phthalocyanines, we observe the formation of

larger, more regular shaped of hexagonal domains, suggesting a higher degree of crystallization of the PCBM. This confirms that the mixture ratio 1:1 produces a spinodal decomposition of PCBM, and different individual molecules concentrations favors nucleation of PCBM.

Temperature-annealing experiments on spin-coated molecular domains demonstrate the thermal stability of tn-ZnPc rods over the range of temperatures used in this work, while the PCBM domains slightly change in their morphology upon heating. We have noted that the pure PCBM tends to wet, i.e. spread horizontally on the Si surface; while, when mixed with the tn-ZnPc, it diffuses vertically increasing the height of the domains and reducing the contact area. This is consistent with the presence of the underlying wetting layer of tn-ZnPc and also suggests that a vertical phase separation of the PCBM from more mobile agglomerations than those of tn-ZnPc could be initiated and promoted by temperature-annealing.

Chapter 4 – Results of Depositions on Patterned Substrates and on Surface Tension Modified Patterned Substrates

4.1 Native Oxide-Covered Patterned Si(111) Substrates

In this chapter, we present preliminary results of experiments based upon the various deposition methods employed in this work, on native oxide-covered patterned substrates and on H-terminated patterned substrates.

In the previous paragraphs we have presented studies of the mutual interactions of the phthalocyanine and fullerene-derivative molecules on a flat substrate and we investigated how they affect each other kinetics of aggregation. In this section we introduce a new variable: the morphology of the substrate. We tested the feasibility of driving a vertical phase separation of the two individual molecular domains via patterning the silicon surfaces by etching a periodical pattern. The pattern is a combinatorial array of pits that change in diameter and spacing. We employed two scales: the large scale dimensions range from 1.4 to 16 μm (spacing, λ) and from 0.7 to 8 μm (diameter, \emptyset), and the small scale dimensions range from 60 to 720 nm (spacing) and from 30 to 360 nm (diameter). The side length of each square cell, containing pits of the same diameter and spacing, is $\sim 65 \mu\text{m}$ for the large scale pattern and $\sim 10 \mu\text{m}$ for the small scale pattern. The CAD model of the patterns (large and small) employed in this work are reported in Figure 4-1. We employed the large scale pattern first because of the immediate

availability of the CAD model. Finding that the large scale pattern produced little effect on the molecular domain organization we reduced the scale, as discussed below.

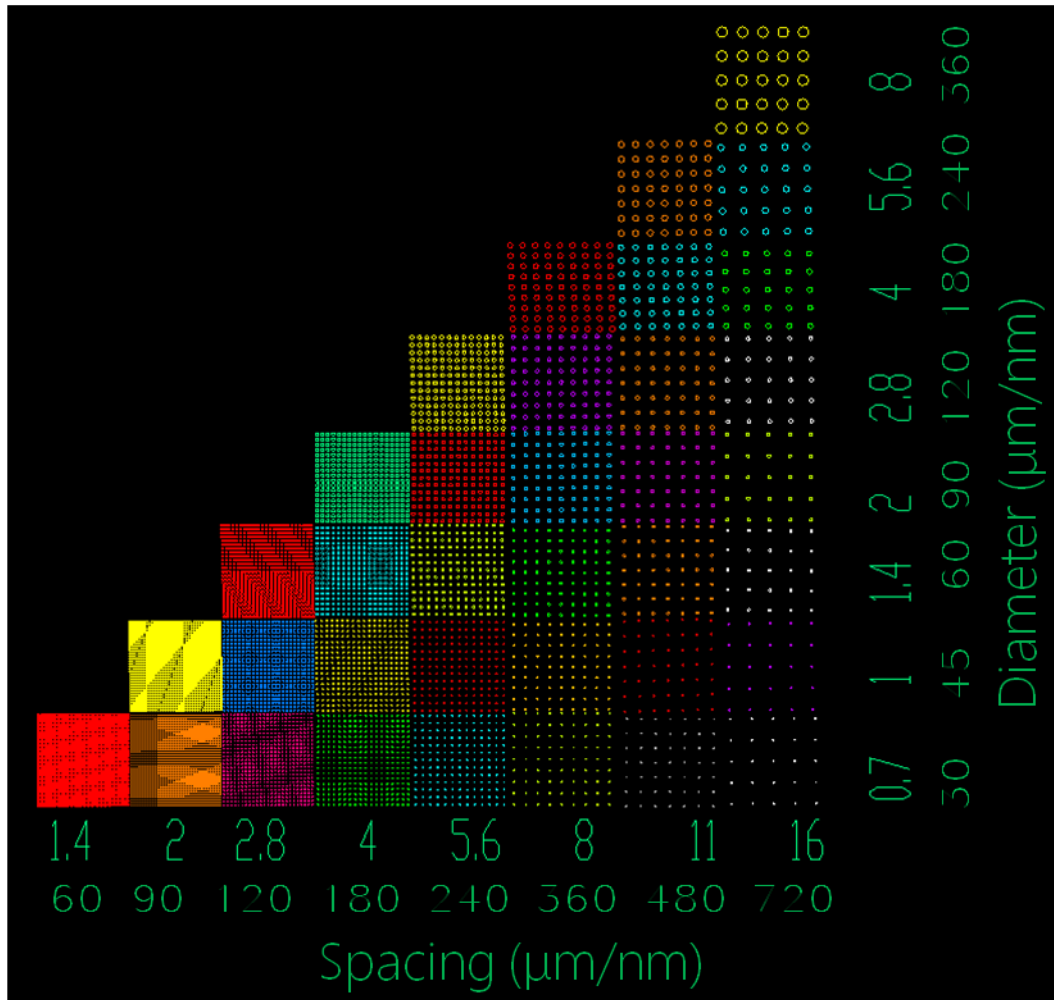


Figure 4-1. CAD model of the pattern employed in this work. The x- and y-axis show the two different dimensions: in the large scale pattern the spacing λ ranges from 1.4 to 16 μm , and the diameter ϕ from 0.7 to 8 μm ; in the small scale pattern the spacing λ ranges from 60 to 720 nm, and the diameter ϕ from 30 to 360 nm.

The patterns were fabricated at the FabLab NanoCenter (University of Maryland) via e-beam lithography using the Reith e-Line system (Reith). Figure 4-2 shows a schematic of the fabrication process. The silicon etching was performed with an inductively coupled plasma (ICP) reactive ion etcher (RIE) (Oxford Plasmalab System

100 – Oxford Instruments) using fluoroform gas (CHF_3) and sulfur hexafluoride gas (SF_6) for 10 seconds. This process allowed us to achieve a pits depth of (48 ± 1) nm for the large size pattern, but did not produce the same depth for all pits in the small size pattern (see below).

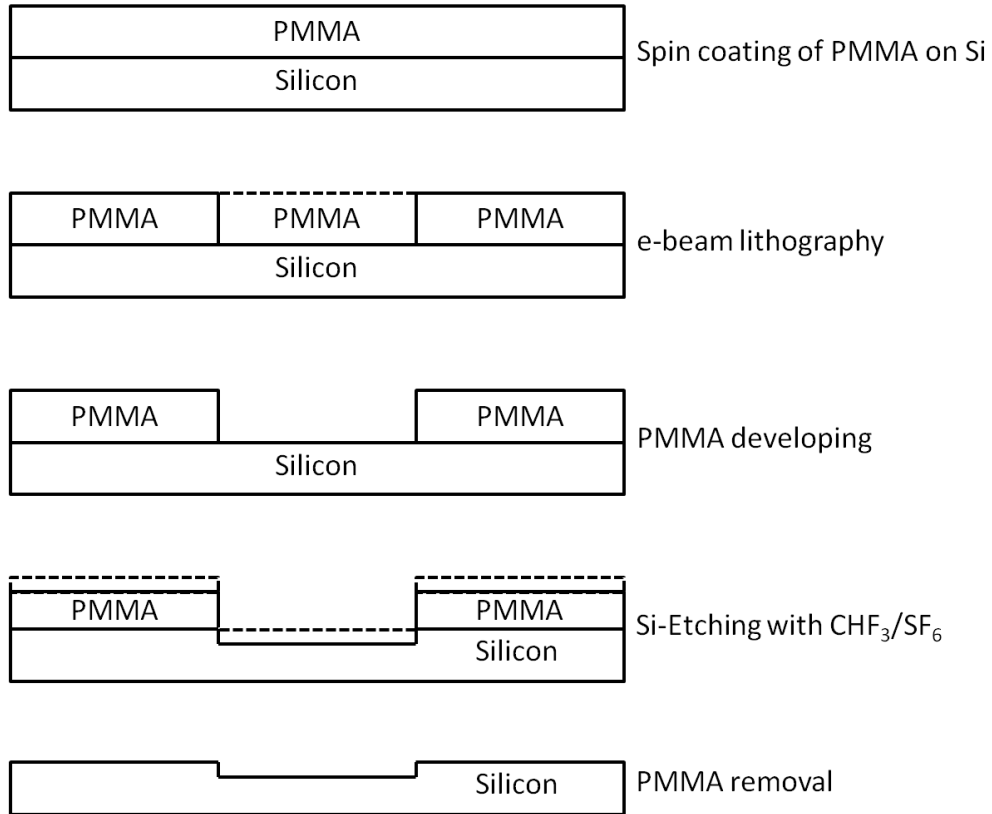


Figure 4-2. Schematic of the fabrication process for transfer of the patterns onto the Si substrate.

Prior to any depositions, the surfaces were cleaned via a standard (RCA) chemical etch, and the quality of the pattern was checked with AFM.

In Figure 4-3 are shown the AFM topography images of the large scale pattern before deposition. The first, second and third image comprises the areas containing the corners of the cells of pit dimensions $\varnothing = 0.7 - 1 \mu\text{m}$ and $\lambda = 1.4 - 2 \mu\text{m}$, $\varnothing = 5.6 - 8 \mu\text{m}$ and $\lambda = 11 - 16 \mu\text{m}$, and $\varnothing = 0.7 - 1 \mu\text{m}$ and $\lambda = 11 - 16 \mu\text{m}$, respectively.

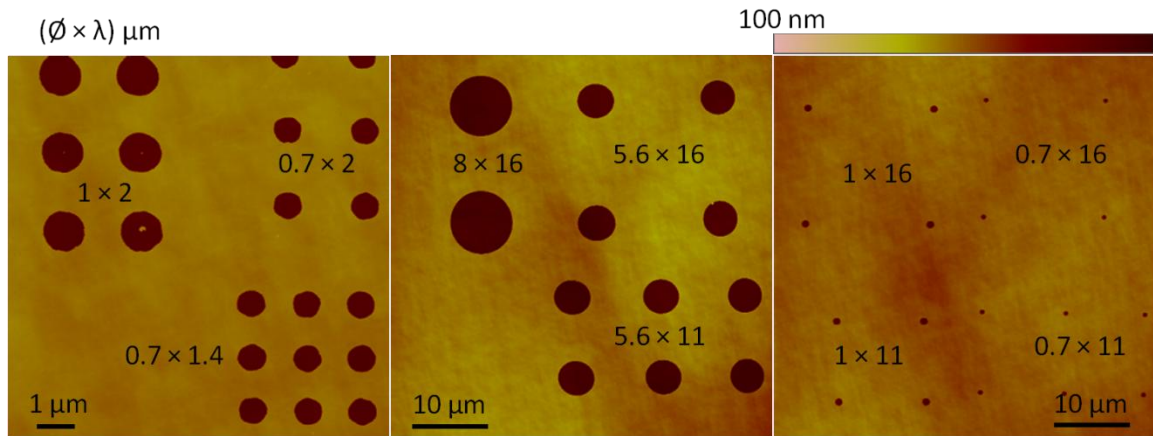


Figure 4-3. Height-AFM images of the large scale pattern etched on Si(111). The areas 1, 2 and 3 refers to the areas containing the corners of the cells of pit of dimensions $0.7 - 1 \mu\text{m}$ in diameter and $1.4 - 2 \mu\text{m}$ in spacing, $5.6 - 8 \mu\text{m}$ in diameter and $11 - 16 \mu\text{m}$ in spacing, and $0.7 - 1 \mu\text{m}$ in diameter and $11 - 16 \mu\text{m}$ in spacing, respectively.

For the small size pattern, the etching parameters have not been optimized, and only the largest dimensions six cells have been etched (Figure 4-4). Moreover, the diameters of the pits resulting were smaller than the design. We reported results on the analysis of the three cells on the diagonal: the dimensions resulting from the pattern fabrication are $(\varnothing \times \lambda) = 303 \times 723 \text{ nm}$ for the largest sizes pits, $(\varnothing \times \lambda) = 113 \times 484 \text{ nm}$ for the medium sizes pits and $(\varnothing \times \lambda) = 98 \times 364 \text{ nm}$ for the smallest sizes pits. We found that the depths of the pits varies depending on the diameters of the pits: $(70 \pm 2) \text{ nm}$ for the largest, $(39 \pm 9) \text{ nm}$ for the medium, and $(30 \pm 4) \text{ nm}$ for the smallest diameters pits.

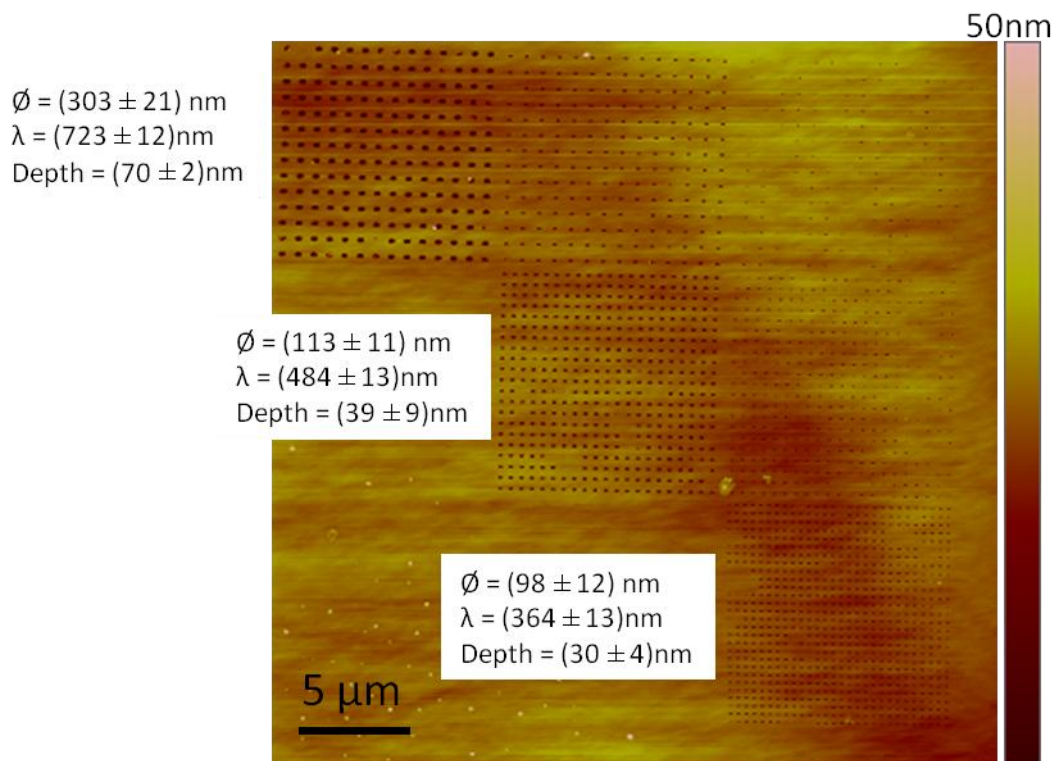


Figure 4-4. Height-AFM image of the large dimensions six cells of the small scale pattern. The sizes reported are only for the largest and smallest cell on the diagonal.

4.1.1 Depositions on Large Scale Patterns on Si(111)

We started with depositions of the tn-ZnPc/PCBM mixture in ratio 1:1 on the large scale patterns. The methods we used are spin-coating, drop-casting and immersion in nearly-closed container.

The results of spin-coating depositions (at 2000 rpm for 45 seconds) on the smallest dimension cell ($(\varnothing \times \lambda) = 0.7 \times 1.4 \mu\text{m}$) of the large scale pattern are reported in Figure 4-5. We find that the tn-ZnPc rods are not affected by the presence of the periodic pattern; this is as might be expected, because they form stable agglomerations in solution. The diameters of base of the PCBM spherical cap clusters are slightly smaller between the pits, and they get larger outside the square (left image in Figure 4-5). The values are

(48 ± 3) nm and (92 ± 6) nm inside and outside the $0.7 \times 1.4 \mu\text{m}$ cell, respectively. Although some of the PCBM clusters deposit inside the pits, as seen in the phase-AFM image (right image in Figure 4-5), the PCBM molecules seemingly avoid the edges of the pits, leaving a depletion zone around the pits, as it is seen more clearly in the AFM topography map. The aggregation of PCBM into spherical cap clusters is seemingly confined on the flat regions between the edges. No evidence of modification of the wetting layer of tn-ZnPc is observed.

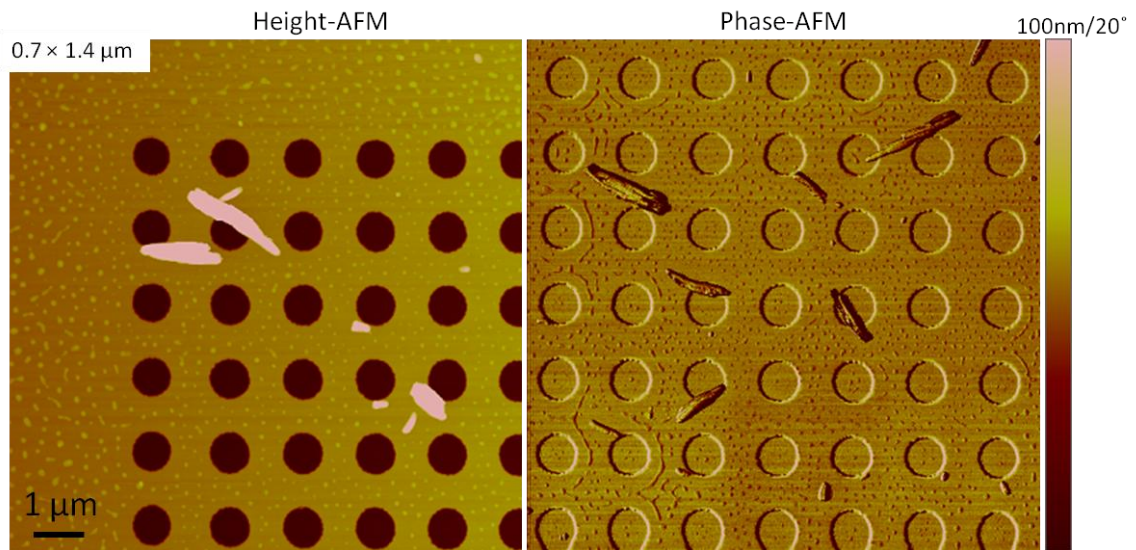


Figure 4-5. Height-AFM (left) and phase-AFM (right) images of the structures resulting from spin-coating a solution of a (1:1) tn-ZnPc/PCBM mixture on patterned Si(111). The cell is that in which pits diameter and spacing were $0.7 \times 1.4 \mu\text{m}$.

On the largest dimension cell ($\emptyset \times \lambda = 8 \times 16 \mu\text{m}$), we see again that the tn-ZnPc rods are not affected by the pattern, and the diameters of the PCBM spherical cap domains between pits, outside the cell and inside the pit are essentially the same: (89 ± 5) nm, (89 ± 4) nm, and (90 ± 5) nm, respectively (Figure 4-6). By comparison, the base diameter of the PCBM spherical cap clusters in the mixture spin-coated on unpatterned substrate is ~ 100 nm. Therefore, we can see that the sizes of the PCBM clusters do not

change significantly. The tn-ZnPc wetting layer does not seem to be affected by the different topography introduced by the pattern.

The depth of the pits measured after the deposition is the same to within the error in the determination: (50 ± 3) nm.

We conclude that the scale of this pattern is so coarse that does not influence nucleation of the molecular clusters. The sole interesting results that we see are for the smallest diameter \times spacing size ($0.7 \times 1.4 \mu\text{m}$), in which the PCBM clusters tend to decrease in size between the pits, getting larger far from the edges of the pits.

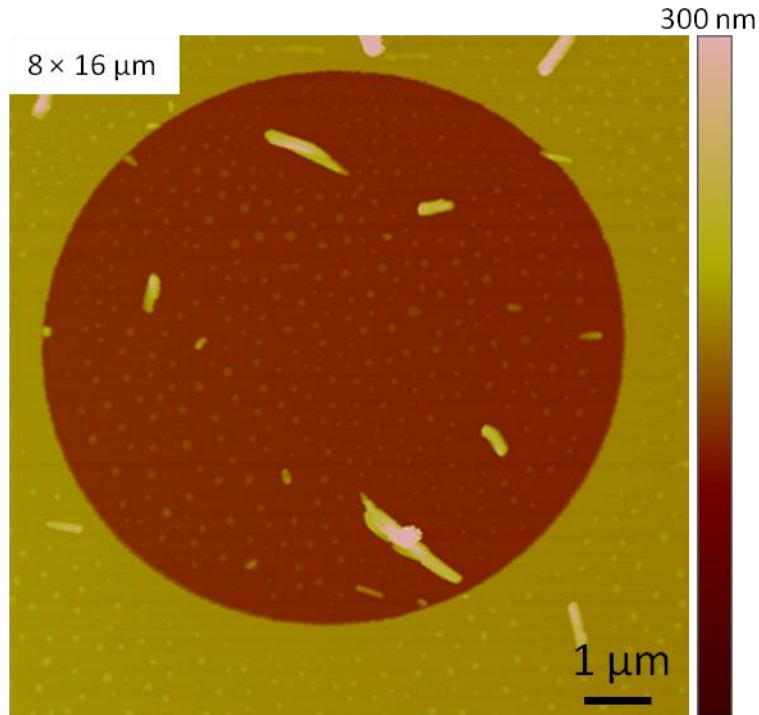


Figure 4-6. Height-AFM image of the structures resulting from spin-coating a solution of a (1:1) tn-ZnPc/PCBM mixture on patterned Si(111). The cell is that in which pits whose diameter and spacing were $8 \times 16 \mu\text{m}$.

Depositions at the lower solvent evaporation rate (drop-casting) are reported in Figure 4-7 for the small size pits, which shows phase-AFM images of the (1:1) mixture of the area 1 and the magnification of the cell in which pits diameter and spacing were $0.7 \times$

1.4 μm . While Figure 4-8 shows height- and phase-AFM images for the largest size pits. We note that the blanket phase of PCBM is confined only on top of the tn-ZnPc rods and inside the pits toward the internal edges. The blanket is not visible on flat regions between pits and inside the pits; instead the PCBM forms small irregular agglomerates of radius of gyration $R_g = (51 \pm 6)$ nm. This result is most likely due to the presence of the tn-ZnPc wetting layer underneath, rather than the different topography introduced by the pattern. In fact, this result is consistent with the results obtained from drop-casting depositions of the mixtures on flat surfaces: the blanket is confined on top of the rods. The thickness of the blanket on top of the rods is estimated being (75 ± 13) nm (close to the value for the case of unpatterned surfaces, (88 ± 9) nm), while inside the pits at the edges the blanket is not flat but it decreases as it approaches the center of the pit (cross-section graph in Figure 4-7). The depth of the pits measured after the drop-casting deposition is not very different from the depth before deposition: (47 ± 2) nm.

As we observed before, the periodic topography introduced by the pattern does not affect significantly the kinetics of agglomeration of the molecules.

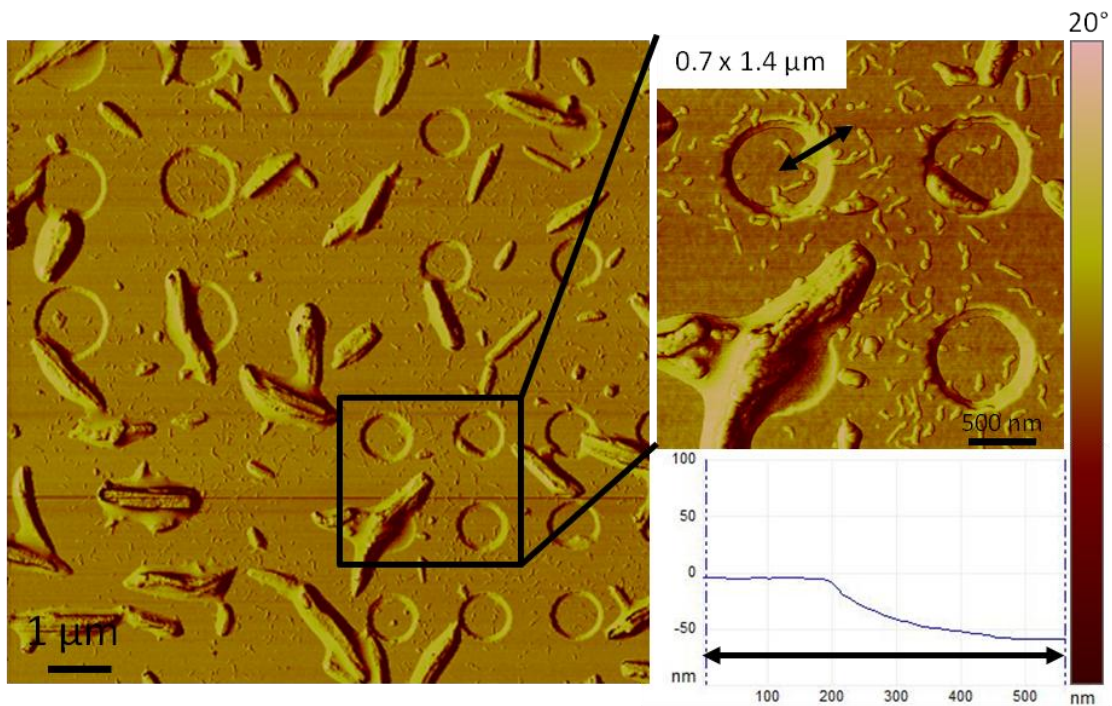


Figure 4-7. Phase-AFM images of the structures resulting from drop-casting a solution of a (1:1) tn-ZnPc/PCBM mixture on patterned Si(111). The left image refers to the area 1, the right image refers to the cell in which pits diameter and spacing were $0.7 \times 1.4 \mu\text{m}$, and the graph is the cross section of the edge of the pits showing the blanket phase thickness decreasing as it approaches the center of the pit.

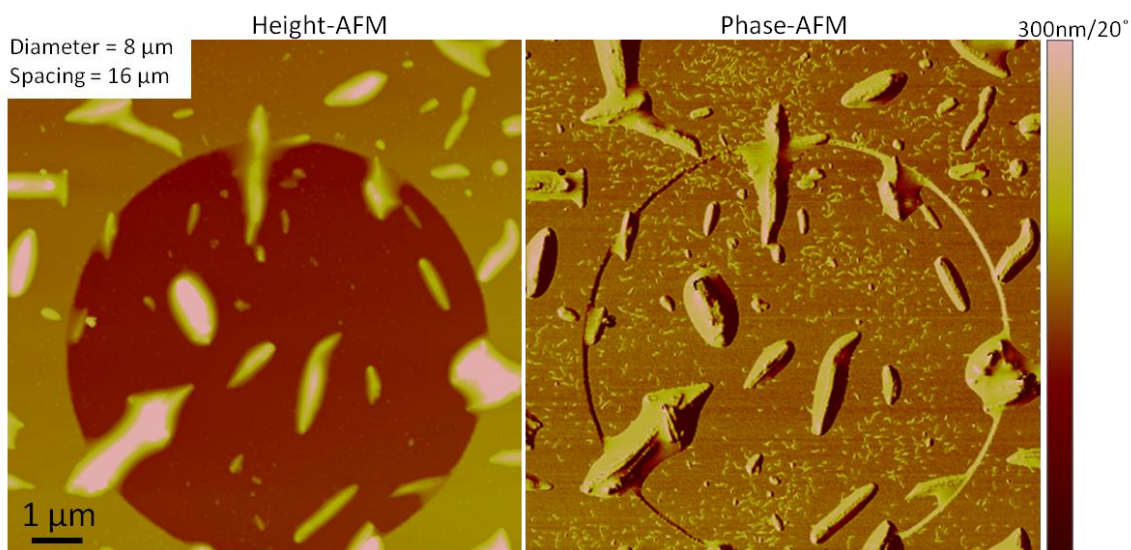


Figure 4-8. Height- and phase-AFM images of the structures resulting from drop-casting a solution of a (1:1) tn-ZnPc/PCBM mixture on patterned Si(111). The images refer to the cell in which pits diameter and spacing were $8 \times 16 \mu\text{m}$.

For the lowest evaporation rate, we performed the deposition via immersion by placing the substrate vertically in the nearly-closed container. Figure 4-9 shows an optical image of the entire pattern (left) and a magnification of the cell in which pits diameter and spacing were $0.7 \times 1.4 \mu\text{m}$. We can see that the pattern was barely visible because of the large amount of material deposited on it. We estimated the thickness of this tn-ZnPc “carpet” with AFM, because all the depositions via immersion using a vertical configuration of the substrate were performed leaving a small portion ($\sim 1.5 \text{ mm}$) of the substrate outside the solution. Therefore, the thickness of this film could be estimated performing an AFM scan at the interface between uncovered and covered surface substrate. The step at the interface has a height of $(983 \pm 257) \text{ nm}$. Given the limit of the AFM scan length ($\sim 80 \mu\text{m}$), this is the height of the molecular film at $\sim 80 \mu\text{m}$ from the interface. It gives perhaps a lower limit on the film thickness, which might be expected to increase toward the center of the sample. SEM analysis shows that the superficial layer has not particular directional growth. Therefore, even though there might be a directional growth of the molecular domains, this would have occurred at the interface pattern/molecules, and this growth certainly did not persist over the thickness of the molecular film.

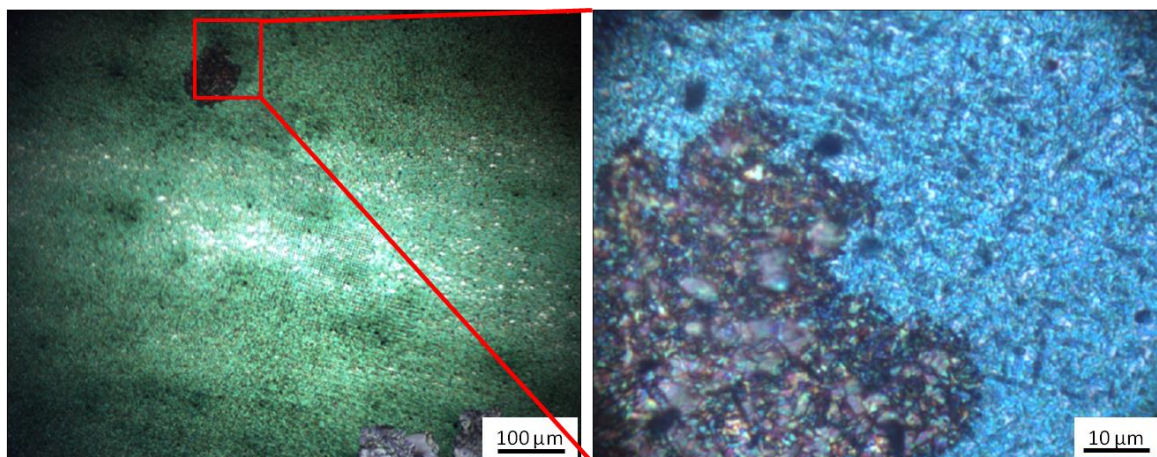


Figure 4-9. Optical images of the structures resulting from deposition via immersion of the patterned Si(111) (placed vertically into open container) in a solution of a (1:1) tn-ZnPc/PCBM mixture. The left image barely shows the entire pattern and the right image is a magnification of the cell in which pits diameter and spacing were $0.7 \times 1.4 \mu\text{m}$.

In conclusion, the large scale topographic patterns do not affect the arrangement of tn-ZnPc rod clusters; they do slightly, but not significantly, affect the assembly of PCBM clusters, but only at the fastest evaporation rate investigated here. However, overall we conclude that for the combination of deposition methods we employed in this work with the large scale topographic pattern does not direct a vertical phase separation.

4.1.2 Depositions on Small Scale Patterns on Si(111)

To determine whether smaller dimension topographical features at the substrate can direct the molecular phase separation, we fabricated a pattern whose characteristic dimensions were approximately one order of magnitude smaller than that discussed above. The smallest dimension cell corresponds to pits dimensions $\varnothing \times \lambda = 30 \times 60 \text{ nm}$ and the largest to $360 \times 720 \text{ nm}$. However, due to non-optimized etching parameters, only the large diameters pits, with the larger spacing were etched (from 180 to 360 nm in diameters and from 360 to 720 nm in spacing). The depth of the pits along the diagonal of

the pattern is (70 ± 2) nm , (39 ± 9) nm and (30 ± 4) nm for the largest, medium and smallest dimension pits, respectively.

We deposited from a solution of 1:1 ratio tn-ZnPc/PCBM mixture via spin-coating, for immediate comparison with the deposition on large scale pattern, and the 2:1 ratio tn-ZnPc/PCBM mixture via drop-casting and immersion, because we have confirmed a larger degree of crystallization on unpatterned substrates at this stoichiometry, as discussed in Chapter 3. In particular, the deposition via immersion showed a higher degree of crystallization and the one via drop-casting showed a smaller length scale of the PCBM blanket phase, which instead of being continuous, is separated into small spherical cap clusters.

The results of the deposition via spin-coating are reported in Figure 4-10 for two cells of pits (303×723 nm and 113×484 nm). We note, as the case of large scale pattern, that the PCBM phase tends to agglomerate far from the edges of the pits. Given the small spacing (compared with the large scale pattern), the PCBM molecules that get far from the edges of the pits, merge into a continuous phase (blanket).

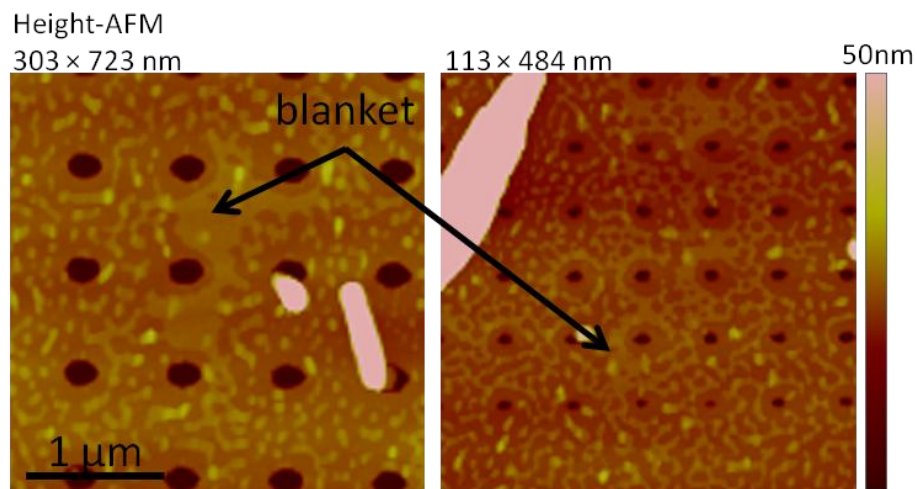


Figure 4-10. Height-AFM images of the structures resulting from spin-coating a solution of (1:1) tn-ZnPc/PCBM mixtures onto the small scale pattern.

However, some small individual aggregates are still observable (Figure 4-11). The radii of gyration of these aggregates in between the pits and outside the pattern are essentially similar: (71 ± 14) nm and (73 ± 10) nm, respectively. From the phase-AFM images in Figure 4-11, we also note that the edges of the pits show different phases, suggesting that molecules aggregate around the edges of the pits creating different stiffness's. However, this aggregation does not significantly increase in height, as we can see from the height-AFM images of Figure 4-11.

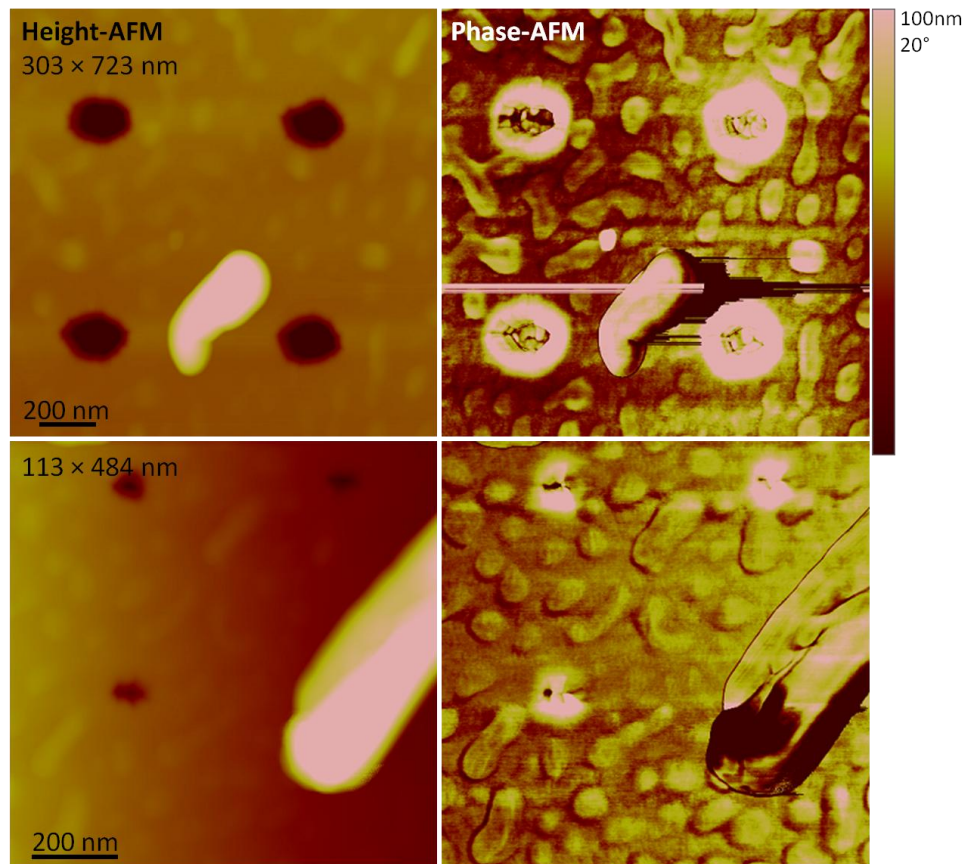


Figure 4-11. Magnified height- and phase-AFM images of the largest and medium dimension cell structures resulting from spin-coating a solution of (1:1) tn-ZnPc/PCBM mixtures onto the small scale pattern.

We measured the diameters, spacing and depth of the pits, and find that these values change considerably after the spin-coating deposition. The diameters and spacing

of the cell of dimension 303×723 nm now become $(178 \pm 13) \times (737 \pm 13)$ nm, and the depth increases from (70 ± 2) nm to (80 ± 2) nm. The diameters and spacing of the cell of dimension 113×484 nm become $(99 \pm 13) \times (490 \pm 9)$ nm, and the depth is relatively constant: from (39 ± 9) nm to (42 ± 4) nm. In Table 4-1 are reported the values of the diameters, spacing and depth of the pits before and after spin-coating deposition on small scale pattern on native silicon oxide.

Native Oxide Spin-Coating	Diameter \times Spacing (nm)		Depth (nm)	
	Before	303×723	113×484	70 ± 2
After	178×737	99×490	80 ± 2	42 ± 4

Table 4-1. Values of diameters, spacing and depth of the largest and medium dimension cells on the diagonal of the small scale pattern before and after deposition via spin-coating of the (1:1) tn-ZnPc/PCBM mixture.

The analysis of the first cell (larger spacing (723 nm)) suggests that the molecular film is growing in a vertical direction outside the pits (because the pits depth increases), and in the horizontal direction (vertically to the walls) inside the pits (because the diameter of the pits decreases). The analysis of the second cell (smaller spacing (484 nm)) suggests that the molecular film is growing in the horizontal direction inside the pit (because the diameter of the pits decreases) and, probably, the vertical growth inside and outside the pits is the same (because the depth remains constant). A reasonable explanation for these results is that molecular domains at the periodical spacing of ~ 720 nm grow on top of the “crests” of this periodic topography. However, the lateral length scale of these vertical domains increases because the growth occurs also horizontally. In contrast, the smaller spacing of ~ 480 nm does not favor a preferential vertical growth.

For the lower solvent evaporation rate approaches, we deposited from solutions of a (2:1) tn-ZnPc/PCBM mixture, because we observe that during drop-casting from this solution the length scale of the PCBM domains decreases and during immersion in the mixture the crystallinity of PCBM is enhanced.

The results of the molecular film morphology via drop-casting are reported in Figure 4-12.

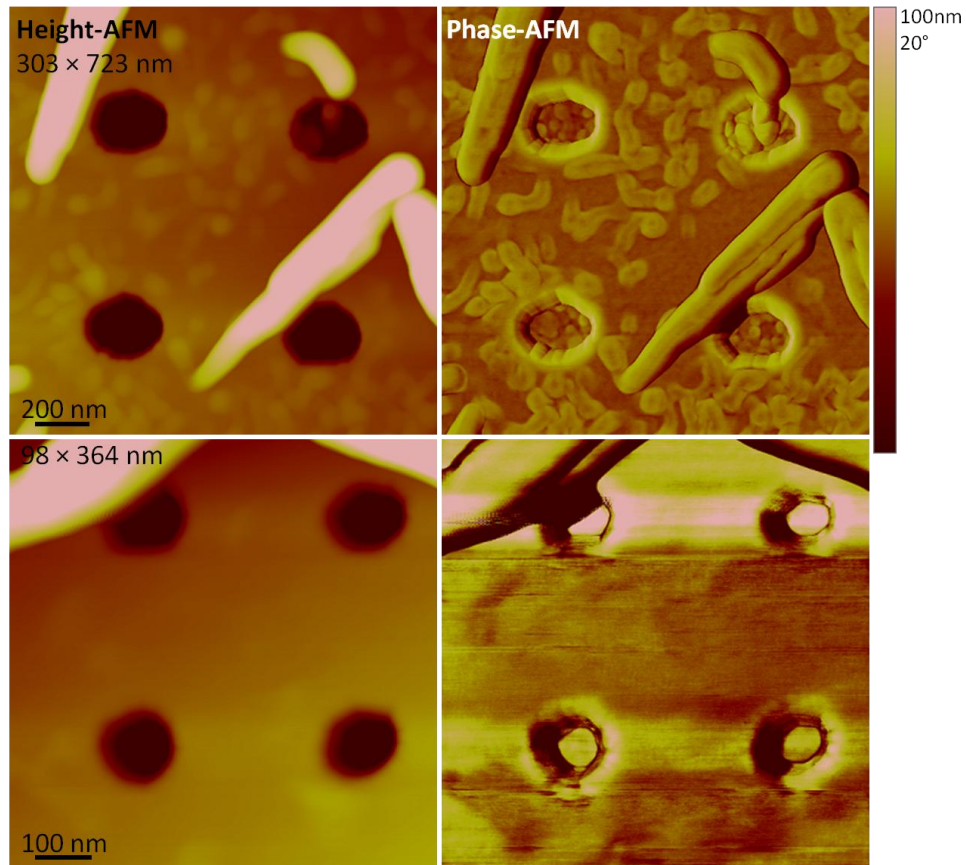


Figure 4-12. Magnified height- and phase-AFM images acquired within the largest and smallest dimension cell of the drop-casting from a solution of a (2:1) tn-ZnPc/PCBM mixture onto the small scale pattern.

We note that the dimensions of the pits change, as we observed in the spin-coating case. For the largest spacing (723 nm), the diameters of the pits decrease from 303 to (267 ± 13) nm and the depth increases from 70 to (82 ± 1) nm. In comparison, for

the small spacing (364 nm), the diameters stay constant to within the uncertainty in the determination ((99 ± 12) nm), but the depth increases from 30 to (65 ± 3) nm. Not surprisingly, the spacing remains relatively constant: (735 ± 10) nm and (367 ± 10) nm. Table 4-2 shows the values of the pit-dimension of two cells of pits before and after drop-casting deposition.

Native Oxide Drop-Casting	Diameter \times Spacing (nm)		Depth (nm)	
	Before	303×723	98×364	70 ± 2
After	267×735	99×367	82 ± 1	65 ± 3

Table 4-2. Values of diameters, spacing and depth of the largest and smallest dimension cells on the diagonal of the small scale pattern before and after deposition via drop-casting of the (2:1) tn-ZnPc/PCBM mixture.

These changes suggest again, that the molecules interact with this small scale pattern; in particular, the spacing of ~ 720 nm favors the vertical growth of the molecular film on the “crests” of the periodic topography, but also increases laterally the length scale of the grown domains (because the domain grows also horizontally along the walls of the pits (as the spin-coating results), while now the spacing of ~ 360 nm favors the vertical growth only on the “crests”; as consequence, the lateral length scale of the domains is expected to be smaller than for the spin-coated case. Therefore, at this low evaporation rate, the spacing of ~ 360 nm seems to favor a preferential vertical growth on top of the “crests”, with a smaller lateral length scale.

The deposition via immersion produced such a thick molecular film that the pattern was completely covered and not visible; the results were similar to the results of depositions via immersion on unpatterned substrates with mixtures in 2:1 ratio. For this reasons we did not include the images of the resulting structures in this section. As for the

case of deposition onto the large scale pattern, no directional growth of the molecular domains was observable on the surface layer. Therefore, even though a directional growth might have occurred at the interface pattern/molecules, it did not persist.

In conclusion, we find that topographic patterns of pits whose characteristic lateral dimensions are sufficiently small seem to direct the assembly of the molecular domains, presumably PCBM. In particular, we observed a promotion of the vertical growth of the molecular domains on the “crests” of an array of cavities of period ~ 360 nm, when the evaporation of solvent is slower (drop-casting).

Further work is needed, however, to identify the composition of the domain that grows because of the pattern: i.e. tn-ZnPc, or PCBM; and also to study the mutual interactions of the two types of molecules on the small scale patterned substrate. However, it is important to choose different types of molecules that both exhibit selective nucleation at the pits.

4.2 H-terminated Patterned Si(111) Substrates

Based on the results on small scale patterns etched into silicon substrates covered with native oxide, we find some evidence for vertical domain growth. However, we do not find evidence for a vertical phase separation, because seemingly only one domain (presumably PCBM) is affected by the presence of the pattern. The final step we performed in order to investigate whether the vertical phase separation can form and persist was to reduce the interfacial tensions.

We immerse the patterned substrates in a buffered HF solution for 30 seconds followed by a rinse in DI water. This procedure allows producing H-terminated Si surfaces.⁴⁸

Deposition via spin-coating on H-terminated patterns was performed for comparison with the case of native oxide-covered pattern. To allow for a direct comparison we investigated deposition from a solution of a (1:1) molecular mixture. We see in Figure 4-13 that this deposition produces a more homogeneous molecular layer than for the native oxide: PCBM domains are almost flat. While the pit spacings remain constant ((727 ± 16) nm and (362 ± 13) nm), we find that the diameters of the pits decrease (from (303 ± 21) to (258 ± 6) nm and from (98 ± 12) to (76 ± 10) nm), and the depth increases (from (70 ± 2) to (76 ± 2) nm and from (30 ± 4) to (62 ± 2) nm). Table 4-3 shows a summary of these values. These results suggest that the molecular domains are growing on the internal walls of the pits and on the flat regions between adjacent pits, i.e. perpendicular to the surface. Therefore, a pattern-correlated molecular domain growth is observed, in this case for both of the pit spacings investigated (~ 720 and ~ 360 nm).

In order to estimate the length scale of the vertical domain growth we calculated the percentage of increasing of the pits depth, which correspond qualitatively to the “thickness” of the molecular domain that grows on the “crests”. We do this calculation for the results obtained for the spacing at which we see the vertical growth in both cases, which is the spacing of ~ 720 nm. The percentages of increasing of the molecular domains on the “crests” are 14.2% and 8.6% for the native oxide-covered and H-terminated surfaces, respectively. Therefore, the vertical growth of the domains decreases on H-terminated surface compared to that on native oxide covered-surface.

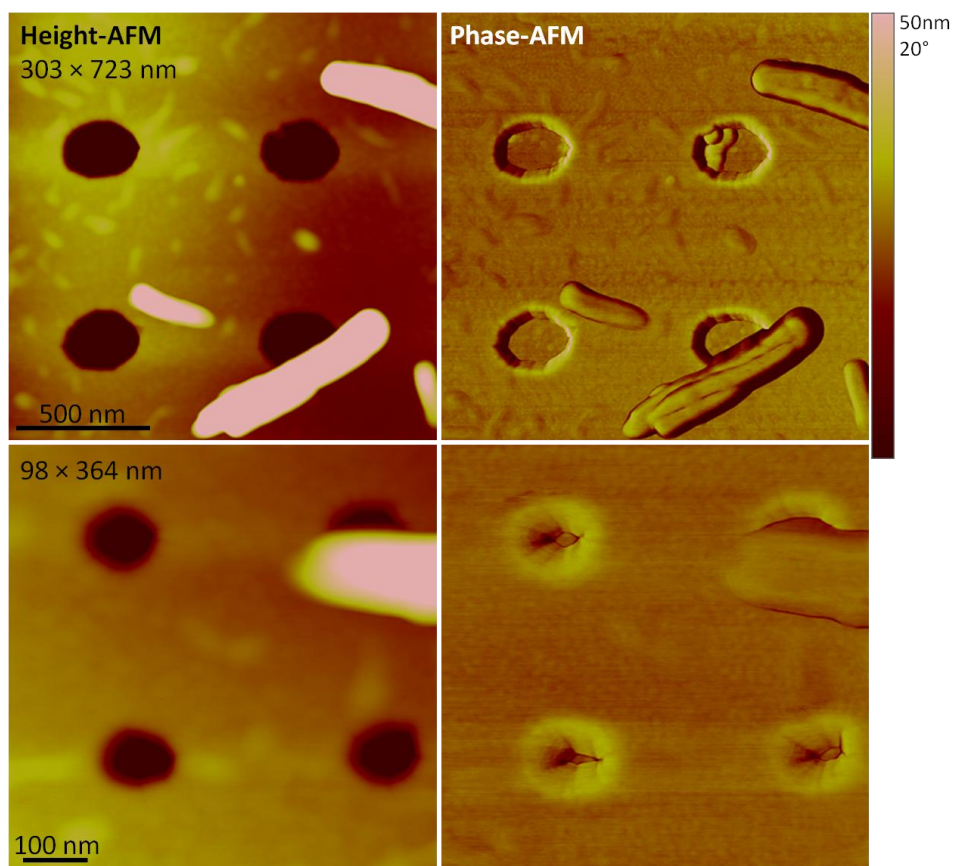


Figure 4-13. Magnified height- and phase-AFM images acquired within the largest and smallest dimension cell of the spin-coating from a solution of a (1:1) tn-ZnPc/PCBM mixture onto H-terminated small scale pattern.

H-termination Spin-Coating	Diameter × Spacing (nm)		Depth (nm)	
	Before	303 × 723	98 × 364	70 ± 2
After	258 × 727	76 × 362	76 ± 2	62 ± 2

Table 4-3. Values of diameters, spacing and depth of the largest and smallest dimension cells on the diagonal of the small scale pattern before and after deposition via spin-coating of the (1:1) tn-ZnPc/PCBM mixture on H-terminated surfaces.

For deposition via drop-casting, we again employed a solution of (2:1) tn-ZnPc/PCBM mixtures for comparison with results for the native oxide-covered pattern.

The morphology is shown in Figure 4-14 . By analyzing the sizes we find that, while the measured pit spacings remain constant (724 ± 18) and (482 ± 10) nm), the diameters of the pits decrease from (303 ± 21) to (213 ± 9) nm and from (113 ± 11) to (78 ± 15) nm. Unlike the previous cases, we find that the pit depth decreases (from (70 ± 2) to (58 ± 8) nm and from (39 ± 9) to (22 ± 3) nm). Table 4-4 shows a summary of these values. These results, unlike the drop-casted case on native oxide-covered patterns, suggest that the molecular film is filling the pits growing at the bottom of the wells faster than the “crests”. Therefore, instead of enhancing the vertical growth on large distances and forming long vertical domains, the molecular film tends to become flatter. This combination of surface tension and rate of evaporation of the solvent during the deposition, does not favor a vertical phase separation, instead it decreases the periodic topography and increases the spatial homogeneity of the molecular film.

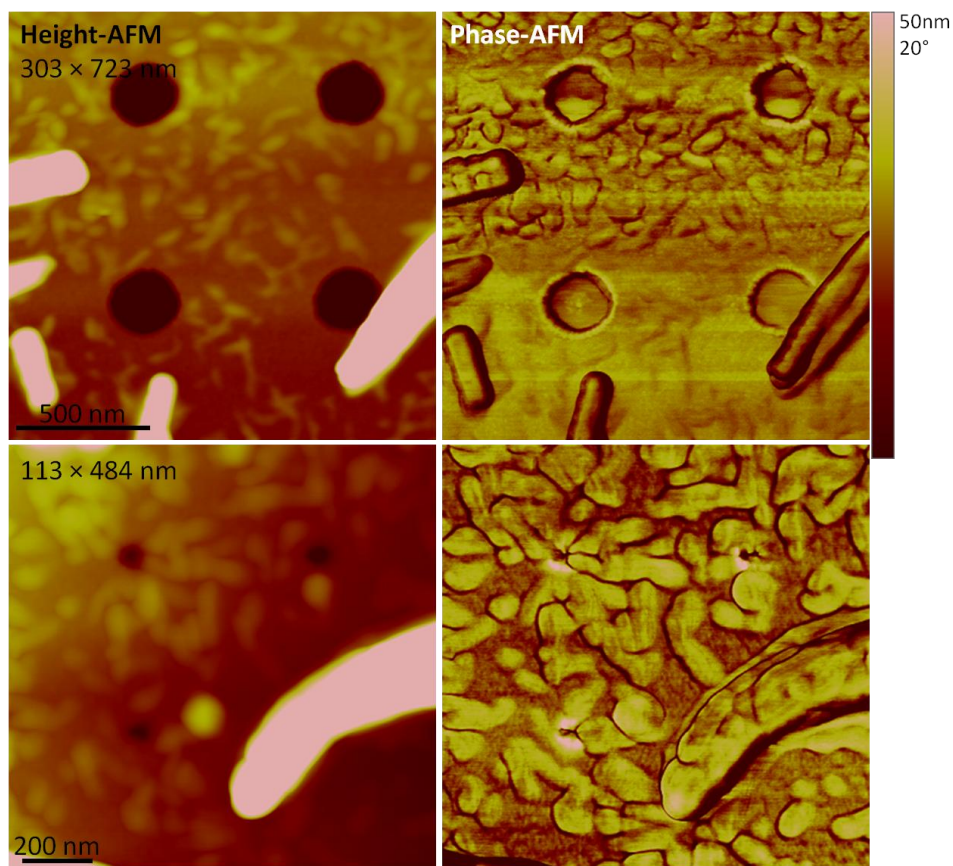


Figure 4-14. Magnified height- and phase-AFM images acquired within the largest dimension and medium dimension cell of the drop-casting from a solution of a (2:1) *tn*-ZnPc/PCBM mixture onto H-terminated small scale pattern

H-termination Drop-Casting	Diameter × Spacing (nm)		Depth (nm)	
	Before	303 × 723	113 × 484	70 ± 2
After	213 × 724	78 × 482	58 ± 8	22 ± 3

Table 4-4. Values of diameters, spacing and depth of the largest and medium dimension cells on the diagonal of the small scale pattern before and after deposition via drop-casting of the (2:1) *tn*-ZnPc/PCBM mixture on H-terminated surfaces.

Deposition via immersion gave essentially identical results to those we obtained for the native oxide-covered patterns (large and small scale); i.e. the pattern was

completely covered by a thick molecular film in which remnant features from the pattern were not identifiable. No particular evidence for ordered self-assembly was observable at the surface layer.

In conclusion, changing the surface tension of the silicon oxide surfaces via hydrosilylation did not produce evidence for a vertical phase separation nor for an increase vertical growth of the molecular domains. To the contrary, by decreasing the evaporation rate of the solvent, we find evidence for even more homogenous film morphology.

Further investigations should be carried out choosing different surface tension modifications.

4.3 Conclusions for Native Oxide-Covered and H-terminated Patterned Substrates

We have observed some promising results, based upon our patterning of the silicon substrate for cavities of relatively small diameter and spacing (from 120 to 360 nm in diameter and from 360 to 720 nm in spacing).

We observed a correlation between vertical growth of molecular domains and the pattern, in particular for spin-coating on native oxide-covered pits at $\lambda \sim 720$ nm, spin-coating on H-terminated pits at both $\lambda \sim 720$ nm and $\lambda \sim 360$ nm, and drop-casting on native oxide-covered pits at $\lambda \sim 360$ nm.

The H-terminated periodic arrays of pits in combination with drop-casting deposition seem to not promote the ordered self-assembly of the molecules, nor did casting via immersion.

Future works would be to further investigate the interaction between periodic patterns and molecular domains in order to promote a vertical phase separation and its persistence over a thick molecular film. We suggest changing the rate at which the solvent evaporates, as it was done in this work, while choosing different types of molecules that both shows selective nucleation on the pattern. Moreover, we suggest decreasing even further the diameters and spacing of the pits, adding different types of surfactants, and increase the depth of the pits to the optimal value for the formation of a critical volume.

Chapter 5 – Vibrational Spectroscopy

Both Raman spectroscopy and Fourier Transform Infrared (FTIR) spectroscopy provide spectral “fingerprints” of organic molecules. In this work we employed these two techniques for identification of the molecules and investigation of their interactions with the solvent and with the substrate.

5.1 Raman Scattering Spectroscopy

Certain matter-light interactions can be interpreted as a coupling between a vibrating molecule and an incident photon. This phenomenon can result in either absorption or scattering of light. In the case of scattering, the incident light interacts with the molecular electron cloud exciting the molecule to “virtual” energy states. This is unlike what happens in “fluorescence”, where the molecule is excited to discrete energy levels after absorption of photons.⁴⁹

Light can be scattered in two ways: (1) elastically, in which the incident photon energy and the molecular energy do not change after the collision (also called Rayleigh scattering), and (2) inelastically, in which the incident photon energy is no longer conserved – the difference in energy corresponds to the difference between an excited vibrational states and the ground state (also referred as Raman scattering). In an inelastic scattering process, the molecular vibrational energy can increase or decrease, meaning that the incident photon can lose or gain energy during the scattering. If the molecular vibrational energy is increased, the incident photon is shifted to a lower energy; this is called Raman Stokes scattering. If the vibrational energy is instead decreased (e.g. if the

molecule returns to its ground state), the scattered photon is shifted to a higher energy; this is called Raman anti-stokes scattering. The latter can occur only in molecules that are vibrationally excited before the scattering.⁵⁰ These two types of scattering are represented schematically in Figure 5-1. Since most of the molecules are in the ground vibrational state at room temperature, with a very low population in the first excited vibrational state, Raman Stokes scattering usually occurs with higher probability.

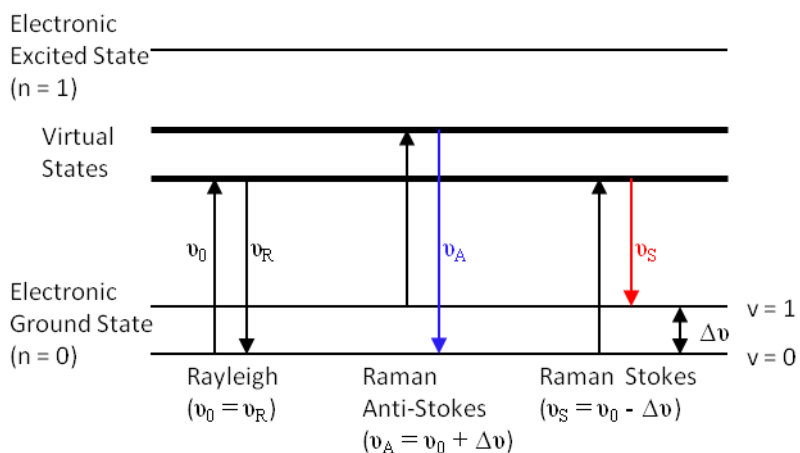


Figure 5-1. Representation of Rayleigh, Raman Anti-Stokes and Raman Stokes scattering.

In this work we employed Raman spectroscopy in order to characterize the organization of molecules deposited on silicon substrates. The Raman spectra were recorded at the Surface Analysis Center (University of Maryland) using a Raman Microscope (Horiba Jobin Yvon LabRam ARAMIS) employing an optical excitation wavelength of 633 nm.

PCBM in both powder form and as deposited onto silicon does not show Raman activity. Instead it shows fluorescence; at 633 nm excitation this molecule is excited into discrete energy levels. Its broad emission spectrum is centered near 2411 cm^{-1} .⁵¹ On the

other hand, tn-ZnPc shows characteristic sharp scattering peaks in the region 50 – 1750 cm^{-1} (635-712 nm). At higher frequencies (toward the near-IR) tn-ZnPc also exhibits fluorescence with a broad spectrum centered near 4689 cm^{-1} . The highest frequency Raman scattering peak is observed at 1514 cm^{-1} and corresponds to out-of-phase stretching of the C-N-C bridges.⁵² The Raman/fluorescence spectrum of tn-ZnPc powder and the fluorescence spectrum of PCBM powder are shown in Figure 5-2.

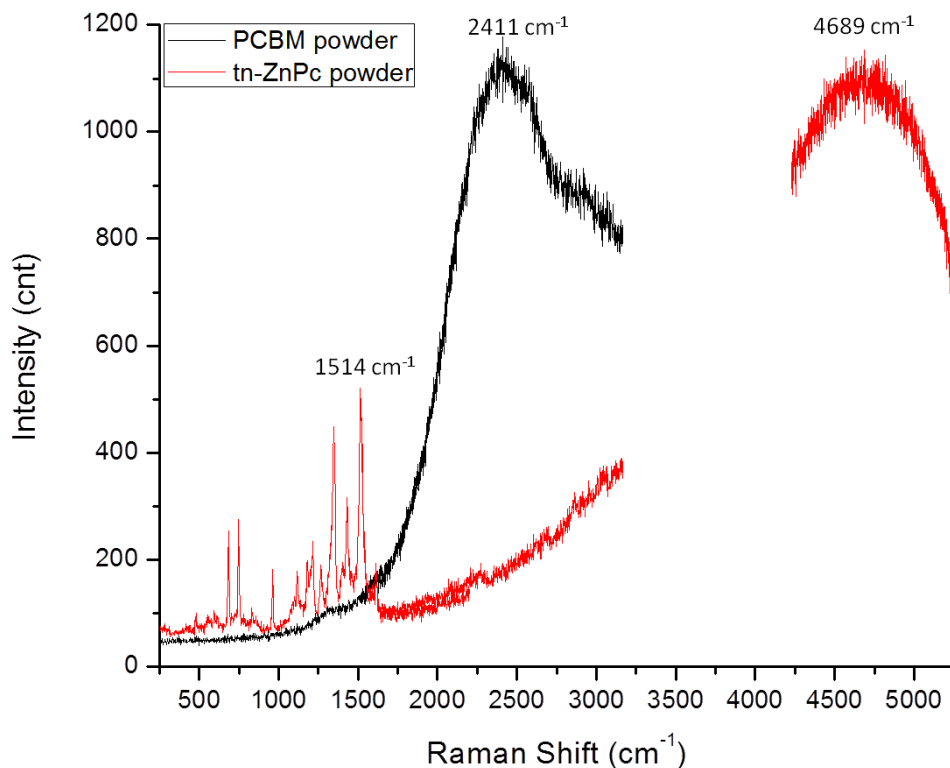


Figure 5-2. Raman spectrum of tn-ZnPc powder and fluorescence spectrum of PCBM powder.

The complete list of Raman frequencies and group assignments for the vibrational modes of tn-ZnPc powder are reported in Table 5-1.⁵²⁻⁵⁷

ν (cm ⁻¹)	Intensity	Group Assignment
80	w	N-O torsion
130	w	Benzene rotation
234	w	N-O twisting
478	v	Pc breathing
556	w	N-O rocking
594	w	Pc breathing
619	w	Pc breathing
683	m	C-N-C bridge symmetric stretching coupled with deformation in indole and benzene
749	m	N-O wagging
960	w	Benzene in-phase expansion
1119	w	Zn-N in-phase stretching coupled with indole deformation and benzene expansion
1179	m	Indole and benzene out-of-phase expansion
1214	m	C-N stretching in NO ₂ group
1265	w	C-N out-of-phase stretching in indole
1344	s	Zn-N in-phase symmetric stretching (Pc breathing)
1428	m	C-C out-phase stretching in benzene
1514	vs	C-N-C bridge out-of-phase stretching
1613	w	N-O asymmetric stretching

Table 5-1. Raman frequencies and group assignments of tn-ZnPc molecules.

A comparison between the Raman spectra of rod-like crystals formed on silicon substrates from tn-ZnPc/chloroform solution and tn-ZnPc powder is shown in Figure 5-3.

As we can see, the characteristic peaks of tn-ZnPc are observed without any shift in position. This indicates that after the evaporation of the solvent, the tn-ZnPc molecules do not show any measurable effect of an interaction with the solvent; it suggests that they maintain their structure, and that no residues of solvent are present within the rods.

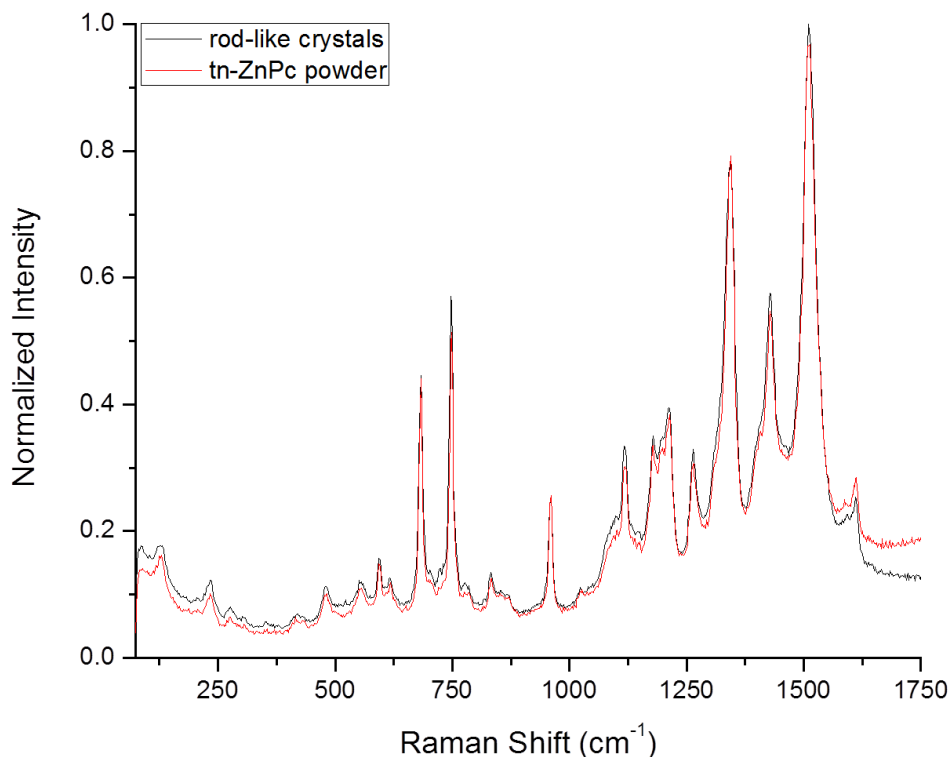


Figure 5-3. Raman spectra of tn-ZnPc powder and rod-like crystals deposited from tn-ZnPc/chloroform solution.

In order to further test the assignment of identity of the wetting layer molecules on the silicon surface as being tn-ZnPc, we compared the Raman spectra recorded on the areas between rod-like crystals deposited on silicon from tn-ZnPc/chloroform solution and from the mixture with the PCBM (Figure 5-4). The peaks at 304, 522 and 964 cm⁻¹ reported on the plots can be assigned to Raman scattering from the silicon substrate.^{58,59}

Comparison of the two spectra indicates that indeed the silicon surface is covered by a thin wetting layer of tn-ZnPc molecules.

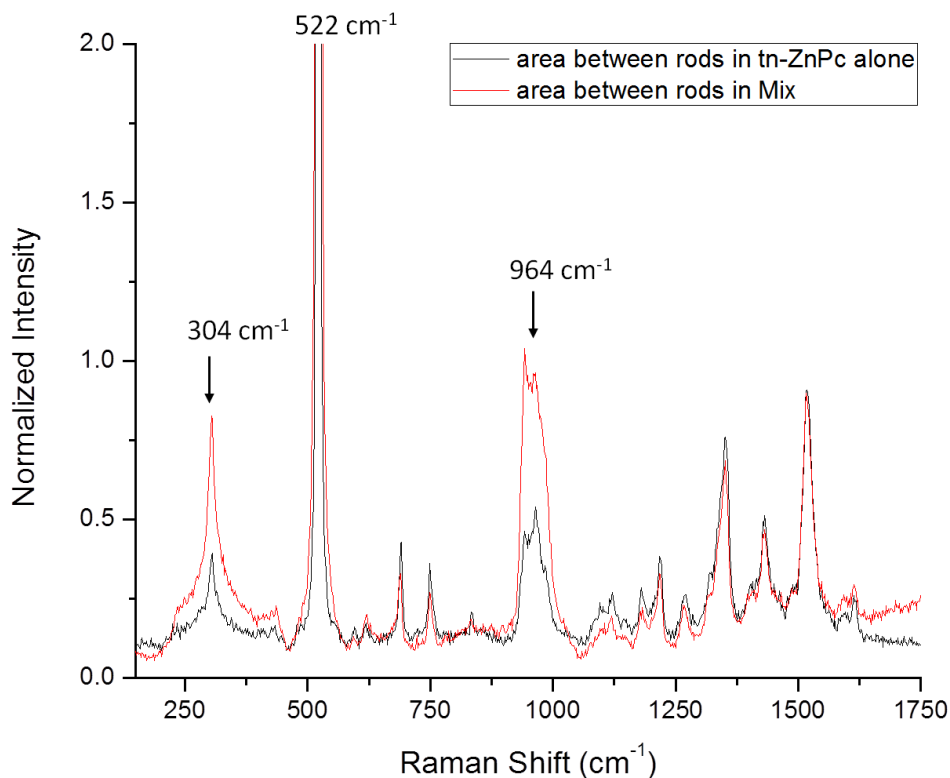


Figure 5-4. Comparison between Raman spectra from the areas between rod-like crystals after depositions from tn-ZnPc-alone solution and from a solution of a mixture between tn-ZnPc and PCBM. The peaks indicated by arrows correspond to Raman scattering from the silicon substrate.

The Raman spectrum measured from the blanket phase on top of tn-ZnPc rods shows the fluorescence spectrum expected for the PCBM, along with the characteristic peaks from tn-ZnPc (Figure 5-5).

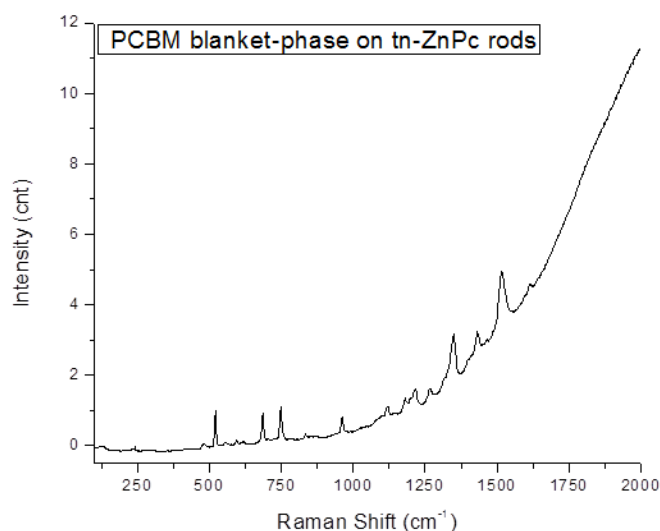


Figure 5-5. Raman spectrum measured from the PCBM blanket phase covered tn-ZnPc rods. Both the fluorescence spectrum of PCBM and the characteristic narrow peaks assigned to tn-ZnPc are observed.

5.2 FTIR and ATR-FTIR Spectroscopy

Using Fourier transform infrared spectroscopy (FTIR) we investigated optical absorption and transmission of our molecular films in the infrared region. Unlike Raman spectroscopy, in which the spectra are the result of the scattering of light, features in the FTIR spectra are due to the absorption of infrared light, exciting molecular vibrations. This absorption causes the stretching and bending of the chemical bonds in the molecules at specific wavelengths.⁶⁰

In addition to transmission-FTIR analysis, we measured FTIR spectra in attenuated total reflectance (ATR) mode using polarized incident light, which gives information about the orientation of the adsorbed molecules on the substrate.^{61–65} The ATR-FTIR technique uses an internal reflectance element (ATR crystal) with a relatively high refractive index (n_1). The sample, with refractive index $n_2 < n_1$, is placed in

intimate contact with the ATR crystal. An infrared beam of light is directed into the crystal at a certain incident angle (ϑ). For incident angles above a critical value ϑ_c the incident light is totally reflected from the internal surface of the crystal, and only incident and reflected waves will be present in this regime (Figure 5-6). The transmitted “evanescent” light is confined to the region near the interface between the crystal and sample. Its intensity damps exponentially into the sample as a function of distance:^{66,67}

$$I(z) = I(0)e^{-\frac{z}{d_p}} \quad (5-1)$$

where $I(z)$ is the intensity at the perpendicular distance z from the interface, $I(0)$ is the intensity at the interface, and d_p is the decay length within the sample, which usually ranges from 50 nm to 2 μm .⁶⁸ The decay length can be calculated by the following formula:

$$d_p = \frac{\lambda}{2\pi\sqrt{n_1^2 \sin^2 \vartheta - n_2^2}} \quad (5-2)$$

We estimated the decay length as function of the incident wavenumbers (4000-650 cm^{-1}), given $n_1 = 4$ (refractive index of the Germanium ATR crystal), $n_2 = 1.6$ (approximated refractive index of tn-ZnPc)^{32,69} and $\vartheta = 45^\circ$. The plot is reported in Figure 5-7.

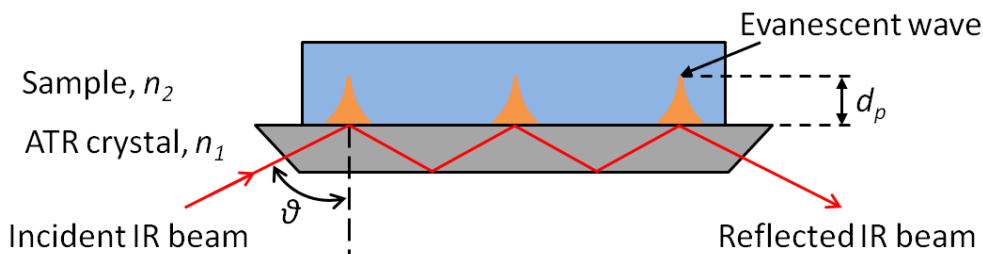


Figure 5-6. Schematic of ATR principle.

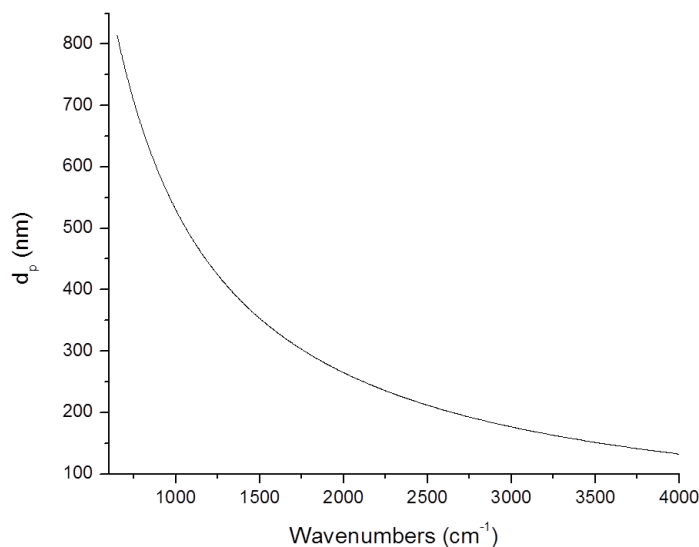


Figure 5-7. Decay length of the evanescent intensity as a function of the incident light frequency.

In this work we collected transmission-FTIR spectra from both tn-ZnPc and PCBM raw powders, after making KBr pellets in ratio 1:30 (sample/KBr). We also measured ATR-FTIR spectra of the raw powders. This was necessary to allow us to identify the molecular vibrations of the raw materials.

In order to further investigate the effect of the molecules/solvent interactions, we compared the ATR-FTIR spectra from the raw powders with those of powders after solvation and evaporation of the solvent.

Finally we analyzed the polarized ATR-FTIR spectra of the molecules deposited onto the Germanium ATR crystal through drop-casting. We did not employ a Silicon ATR crystal because of the silicon lattice absorption in the region below 1500 cm⁻¹ (where the IR activity of the molecules under examination is very high, see below).⁷⁰ We assume that the surface properties of native oxide-covered Ge are similar to those of

native oxide-covered Si, and that the interaction between molecules we study and the two types of substrates are similar.

The analysis was performed at the Optical Instrumentation Facility (Department of Chemistry and Biochemistry, University of Maryland), using the Thermo-Nicolet Nexus 670 FTIR spectrometer (Thermo Scientific) and the ATR accessory Smart SpeculATR with Ge ATR crystal.

5.2.1 FTIR and ATR-FTIR Spectra from Powders

The FTIR spectra from the powders in both transmission and ATR modes are reported in Figure 5-8 for the tn-ZnPc, and in Figure 5-9 for the PCBM. The two types of spectra, transmission-FTIR and ATR-FTIR, are in good agreement for both powders. As we can see, these molecules show high infrared activity in the so-called “fingerprint” frequency region between $1800 - 400 \text{ cm}^{-1}$ (corresponding to optical wavelengths between $5.6 - 25 \text{ }\mu\text{m}$).

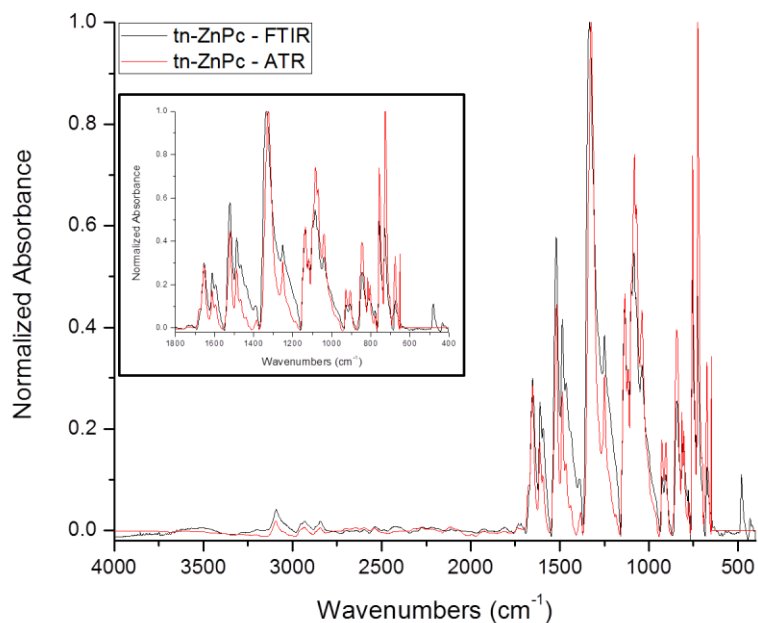


Figure 5-8. Transmission-FTIR and ATR-FTIR absorption spectra measured from tn-ZnPc raw powder, and normalized to the highest measured intensity.

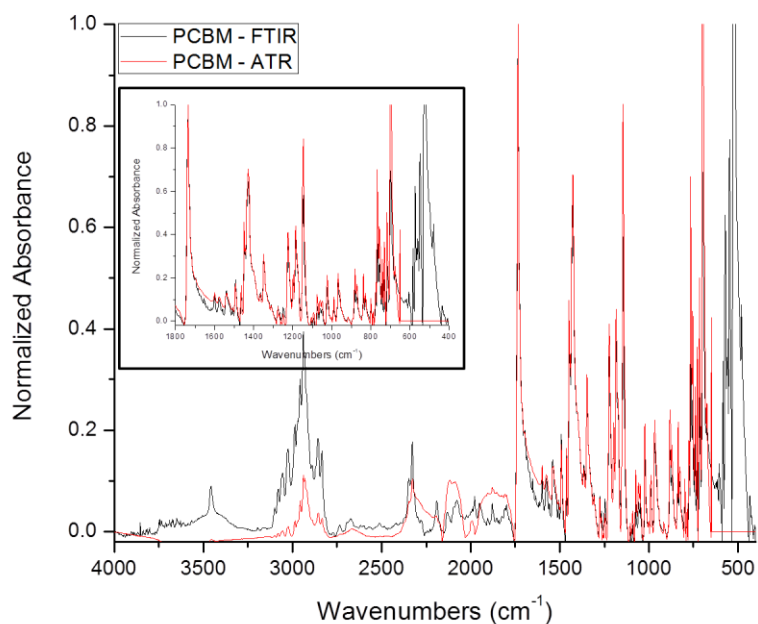


Figure 5-9. Transmission-FTIR and ATR-FTIR absorption spectra measured from PCBM raw powder, and normalized to the highest measured intensity.

The complete list of FTIR absorption frequencies and vibration assignments for tn-ZnPc⁷¹⁻⁷⁷ and PCBM^{41,75,77-80} molecules are reported in Table 5-2 and Table 5-3, respectively.

v (cm⁻¹)	Intensity	Group Assignment
480	w	N-O rocking
652	sh/vw	C-C macrocycle ring deformation (Pc breathing)
677	w	Pc breathing
729	s	C-H out-of-plane bending Pc ring
756	s	C-H wagging of Pc ring
779	sh	C-N stretching
804	w	Pc ring vibrations
816	w	C-H out-of-plane deformation
843	m	C-H out-of-plane deformation
906	w	C-H out-of-plane bending
928	w	C-H out-of-plane bending
1039	sh/m	C-H in-plane bending
1072	sh	Isoindole deformation
1084	s	C-H in-plane bending
1099	sh	C-H in-plane bending
1116	sh	Isoindole breathing + C-H in-plane bending
1136	s	C-H bending
1250	sh/m	N-O symmetric stretching
1334	vs	N-O symmetric stretching
1390	sh	N-O symmetric stretching
1439	sh	C-C isoindole stretching
1466	sh	C-C isoindole stretching
1487	m	N-O asymmetric stretching
1521	s	N-O asymmetric stretching
1593	sh	C-C symmetric stretching in benzene ring
1610	m	N-O in-plane bending
1653	m	N-O in-plane bending
2842	vw	C-H asymmetric stretching as alkyl
2931	vw	C-H symmetric stretching as alkyl
3091	vw	C-H asymmetric stretching in benzene ring

Table 5-2. Characteristic FTIR absorption frequencies and group assignments of tn-ZnPc molecules. vw: very weak, w: weak, m: medium, s: strong, vs: very strong, sh: shoulder.

v (cm⁻¹)	Intensity	Group Assignment
523	vs	C-C stretching in C ₆₀ cage (vibration in fullerene cage)
573	s	C-C stretching in C ₆₀ cage
700	s	C-H stretching in phenyl ring
1146	m	C-C stretching in phenyl ring
1184	m	C-O stretching in alkyl chain
1223	m	C-C stretching in C ₆₀ cage
1277	w	C-H bending into alkyl chain
1348	w	C-H wagging into alkyl chain
1365	w	C-H wagging into alkyl chain
1427	m	C-H bending of ending methyl group
1448	m	C-C stretching in C ₆₀ cage
1493	w	C-H in-plane bending in phenyl ring
1736	vs	C=O stretching in carbonyl group
2835	sh/w	C-H stretching in alkyl chain
2858	sh/w	C-H stretching in alkyl chain
2939	w	C-H stretching in alkyl chain
2987	sh/w	C-H stretching in alkyl chain near phenyl group
3055	sh/w	C-H symmetric stretching of ending methyl group
3101	sh/w	C-H stretching in phenyl ring

Table 5-3. Characteristic FTIR absorption frequencies and group assignments of PCBM molecules. w: weak, m: medium, s: strong, vs: very strong, sh: shoulder.

Before analyzing the IR spectra of the deposited molecules, we tested as to whether the solvent residues were present after solvation and evaporation. We shown above that Raman spectroscopy from tn-ZnPc rods does not show indication of solvent residues. Here, we wanted to look for signs of solvent/PCBM interactions, and indications of possible solvent/tn-ZnPc interactions in the infrared region. To do so, we compared the ATR-FTIR spectra of the raw powders with the powders after solvation and evaporation of chloroform. The comparison is reported in Figure 5-10. We can see that again the tn-ZnPc spectra do not show evidence of solvent residues or interaction of solvent with tn-ZnPc; after the solvent evaporates, no signature of solvent molecules are

left. On the other hand, as we can see in the right panel of Figure 5-10, the PCBM powder shows indications of chloroform residues, suggesting an attractive interaction with the solvent. This is visible via the appearance of new peaks assigned to vibrations in chloroform molecules, as well as the shift of some vibrational modes of PCBM: the peaks at 667 cm^{-1} , 750 cm^{-1} and 3022 cm^{-1} visible in the PCBM powder obtained after interaction with chloroform refers to C-Cl bending, C-Cl stretching and C-H stretching in CHCl_3 molecules, respectively. The peaks at 1173 cm^{-1} and 1265 cm^{-1} are likely shifted peaks from 1146 cm^{-1} (C-C stretching in phenyl ring) and 1223 cm^{-1} (C_{60} vibration) due to the presence of chloroform molecules near the phenyl ring and the fullerene cage. To support these assignments, in Figure 5-11 we show the ATR-FTIR spectrum of liquid chloroform along with the absorption frequencies and respective group assignments.^{81,82} Our results confirm earlier reports that PCBM molecules retain chloroform molecules, even after prolonged heat treatment.⁸³

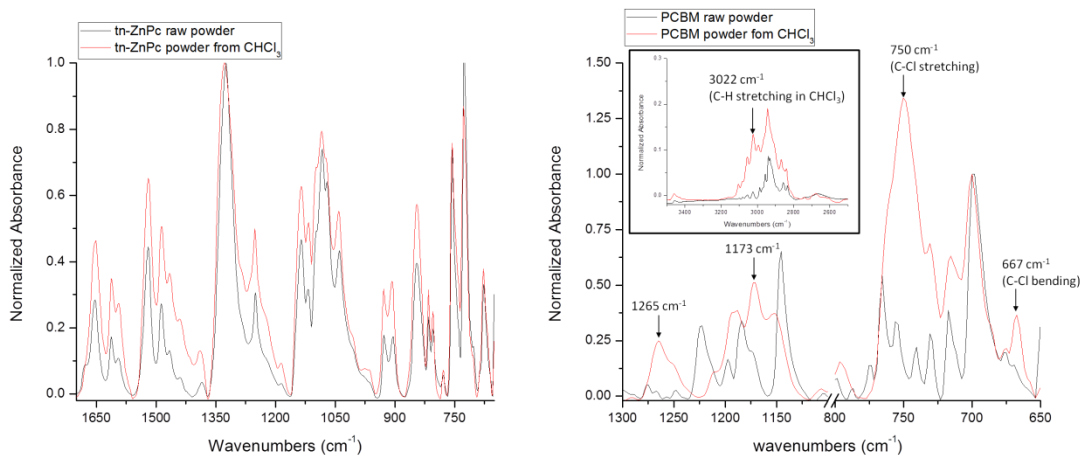


Figure 5-10. Comparison between ATR-FTIR spectra of raw powders and powders deriving after solvation and evaporation of chloroform of tn-ZnPc (left) and PCBM (right).

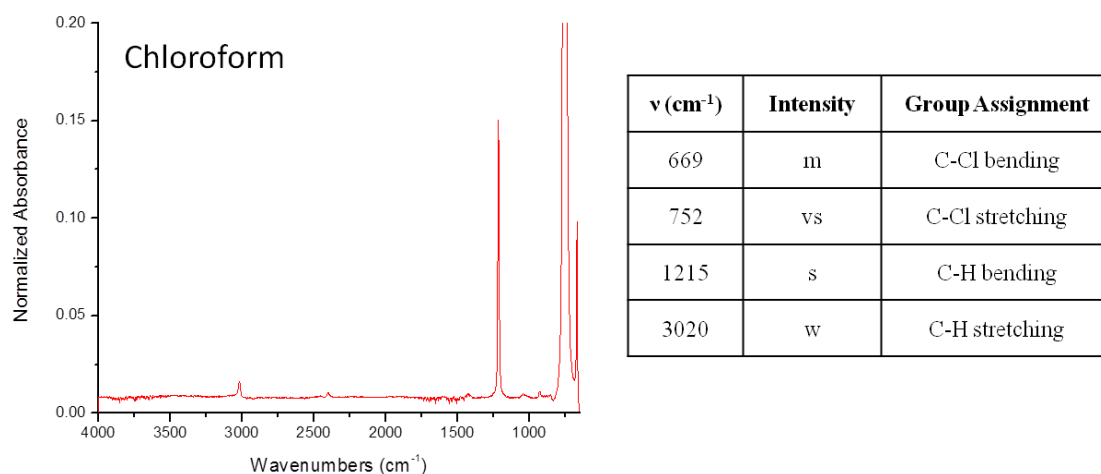


Figure 5-11. ATR-FTIR spectrum measured from liquid chloroform (left) and absorption frequencies with group assignments (right).

5.2.2 Polarized ATR-FTIR of Deposited Molecules

To determine the orientation of the two types of molecules studied here when deposited on the Si surface, we compared the ATR-FTIR spectra of the molecules deposited onto the ATR crystal via drop-casting obtained using incident s- and p-polarized light. As shown schematically in Figure 5-12, for s-polarized light the electric field vector oscillates perpendicular to the plane of incidence (90°), while for p-polarized light the electric field vector oscillates within the plane of incidence (0°). The plane of incidence is defined by the incident and specularly-reflected light beams.

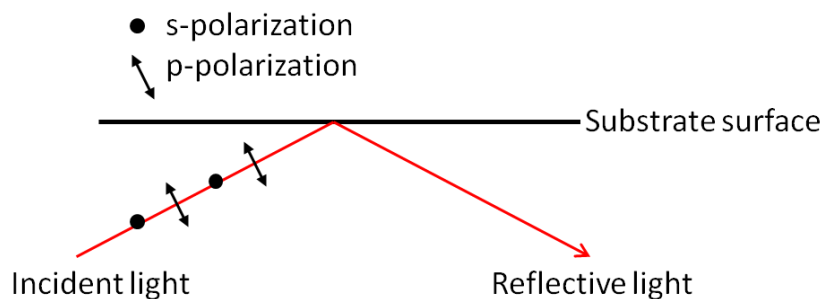


Figure 5-12. Schematic illustration of s- and p-polarization.

The spectra collected for the tn-ZnPc and the PCBM deposited via drop-casting on the Ge ATR crystal are reported in Figure 5-13, in the left and right panels, respectively.

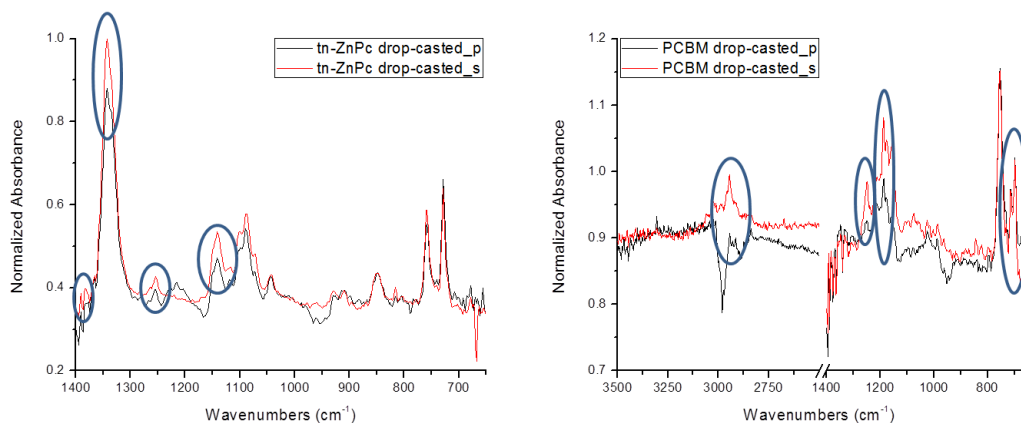


Figure 5-13. Polarized ATR-FTIR spectra measured from tn-ZnPc (left panel) and PCBM (right panel) drop-casted onto the Ge ATR crystal.

We note that the peaks at 1383 cm^{-1} , 1254 cm^{-1} and 1142 cm^{-1} (N-O symmetric stretching) and 1142 cm^{-1} (C-H bending) of the tn-ZnPc molecules are slightly more intense in the s-polarized spectrum (left panel of Figure 5-13). This means that the N-O stretching of the nitro groups and the C-H bending of the isoindole vibrate along the perpendicular direction of the plane of incident; therefore, parallel to the substrate surface. This suggests that the phthalocyanine molecules deposit with the molecular plane parallel to the substrate surface. Similar behavior has already been reported for the chemically similar CuPc molecules deposited on native oxide-covered Si(111).⁸⁴

The polarized spectra measured from PCBM (right panel of Figure 5-13) show that the peaks at 698 cm^{-1} (C-H stretching in phenyl ring), 1188 cm^{-1} (C-O stretching in alkyl chain), 1247 cm^{-1} (weakly – C-C stretching in cage), and 2944 cm^{-1} (C-H stretching in alkyl chain) are more intense in the s-polarized spectrum. In particular, the peak 1188

cm^{-1} increases in intensity by 100%, and the 1247 cm^{-1} peak increases by 67% (Table 5-4). These observations suggest that the alkyl chain lays parallel to the substrate. Therefore, the PCBM lays on its side on the substrate.

	Percentage of increasing of the intensity of the s-polarized peaks (%)	
$\nu \text{ (cm}^{-1}\text{)}$	PCBM spectrum	Assignment
2944	38	C-H stretching in alkyl chain
1247	67	C-C stretching in cage
1188	100	C-O stretching in alkyl chain
698	33	C-H stretching in phenyl ring

Table 5-4. Percentage of increasing of the intensity of the peaks in the s-polarized spectra of PCBM.

The polarized spectra of the (1:1) tn-ZnPc/PCBM mixture are reported in the left panel of Figure 5-14. We note that the spectrum is almost identical to that for tn-ZnPc (right panel of Figure 5-14). In order to determine whether the presence of the PCBM is observable, we show in Figure 5-15 a magnification of the intensity within the fingerprint region from the right panel of Figure 5-14, using the same baseline. We note that the peaks of the spectrum measured from the mixture are at the same frequencies as those for the tn-ZnPc spectrum, but with a decreased intensity. This trend is visible for the entire spectrum, except for three peaks (1184 , 1173 , and 700 cm^{-1}) which appear with higher intensity. These exceptional peaks can be assigned to PCBM vibrational modes; this provides evidence of the presence of the PCBM in the mixture. The fact that the tn-ZnPc peaks are much more intense in the mixture than the PCBM peaks we interpret as due to the fact that the layer that wets the Ge crystal is tn-ZnPc. Therefore, the PCBM signal is

attenuated, as the evanescent light from the crystal must first pass through the tn-ZnPc layer before reaching the PCBM.

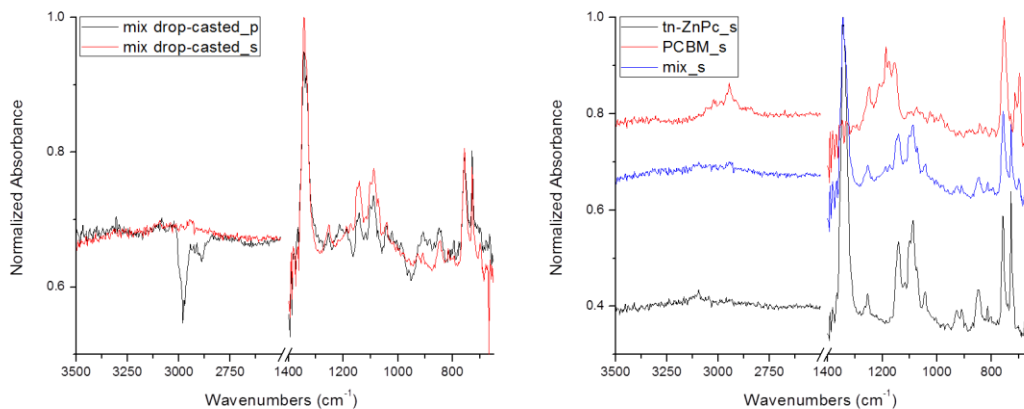


Figure 5-14. Polarized ATR-FTIR spectra of the (1:1) tn-ZnPc/PCBM mixture drop-casted onto the Ge ATR crystal from chloroform solution (left). Comparison of the s-polarized spectra of the tn-ZnPc, PCBM and mixture drop-casted on the ATR crystal (right).

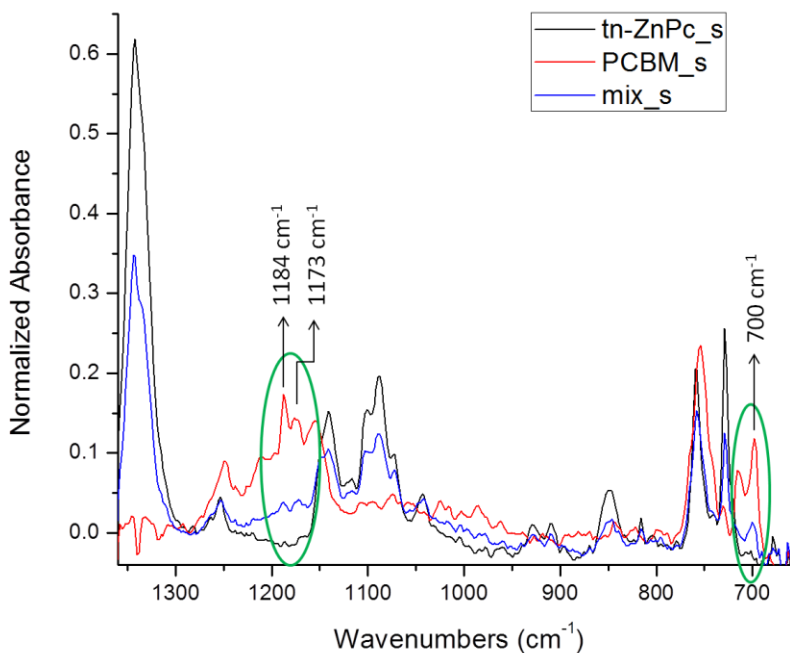


Figure 5-15. Magnification of the fingerprint region of the s-polarized spectra of the tn-ZnPc, PCBM and mixture drop-casted on the ATR crystal.

Another characteristic to notice in Figure 5-14 is that the spectrum from the mixture shows enhancement in the s-polarization intensities for the same peaks as for tn-ZnPc alone. In Table 5-5 we show the calculated percentage increase for s-polarization of the peaks for tn-ZnPc-only and for the mixture. We note that the percentage increase of the peaks at 1383 cm^{-1} , 1342 cm^{-1} and 1254 cm^{-1} obtained from the mixture are not as high as that for the pure tn-ZnPc, and the C-H bending peak at 1142 cm^{-1} increases more in the mixture. This might indicate that the phthalocyanine molecules in the wetting layer are not completely parallel to the substrate, but they are tilted with a certain angle very close to 0° (given the increasing in the s-polarized spectra in any case), and the C-H bending in the isoindole are now parallel to the surface. The presence of the PCBM above this layer might modify the orientation of the phthalocyanine molecules on the substrate.

ν (cm^{-1})	Percentage of increasing of the intensity of the s-polarized peaks (%)		Assignment
	tn-ZnPc spectrum	Mix spectrum	
1383	100	20	N-O symmetric stretching
1342	14	5	N-O symmetric stretching
1254	25	0	N-O symmetric stretching
1142	29	50	C-H bending

Table 5-5. Percentage of increasing of the intensity of the peaks in the s-polarized spectra of tn-ZnPc and the mixture.

In Figure 5-16 we present a schematic of our interpretation of the orientation of tn-ZnPc (in the tn-ZnPc-alone case and in the mixture) and PCBM molecules (only in the PCBM-alone case) deposited via drop-casting on native oxide-covered Si and Ge substrates.

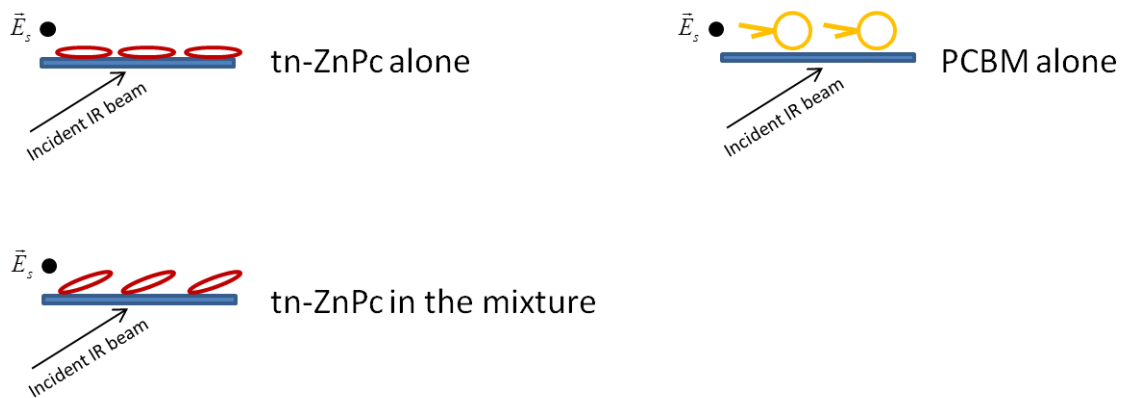


Figure 5-16. Schematics of the orientation of tn-ZnPc and PCBM molecules deposited via drop-casting on semiconductor substrates. The configuration of the PCBM is reported only in the PCBM-alone case because PCBM molecules are not well detectable in the mixture.

Chapter 6 – Evaporation of a Sessile Droplet of Chloroform Resting on an Isothermal Si(111) Substrate

6.1 Theoretical Basis

Understanding the phenomena that occur during the evaporation of a sessile droplet on a substrate is important for predicting and controlling the molecular pattern deposition onto the underlying substrate during drop-casting deposition.

A sessile droplet on a substrate can be considered as a spherical cap (Figure 6-1). The static contact angle, θ_s , between the liquid drop and the solid surface is the contact angle at the thermodynamic equilibrium between the three phases (solid, liquid and vapor) and is given by the Young's equation:⁸⁵

$$\gamma_{LV} \cos \theta_s = \gamma_{SV} - \gamma_{LS} \quad (6-1)$$

which describes the force balance between the interfacial tensions at the solid-liquid-vapor interface. This angle provides information about the surface tensions, and from it the presence of contaminants or surfactant can be determined, as well as the wettability of the liquid on a particular substrate.

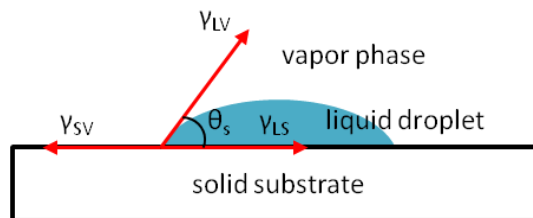


Figure 6-1. Schematic of a droplet resting on a substrate.

On the other hand, when the system is not in equilibrium, for instance during evaporation, the liquid droplet surface changes with time, therefore, a dynamic contact angle, θ_d , must be considered.

From experimental observations of a water droplet on a glass cover slip, Hu and Larson⁸⁶ have found that, when the contact angle is less than 90° , droplet evaporation occurs in two main stages. In the first initial stage, the contact angle decreases, while the contact radius is pinned (CCR mode), while in the second phase, the contact radius recedes while the contact angle remains constant and very small (CCA mode). These two modes are represented in the schematics of Figure 6-2. At the final stage of the evaporation, referred to as a “mixed mode”, both contact radius and contact angle decrease.

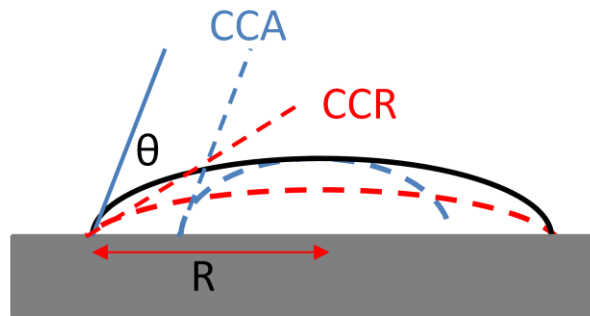


Figure 6-2. Schematics of the "constant contact angle" and "constant contact radius" modes.

In our experiments on the evaporation of chloroform we have observed that the evaporation of the droplet varies from a CCA mode to a CCR mode alternatively. We believe that this different, interesting behavior is due to the fast volatility of the chloroform and the presence of impurity on the substrate: i.e. the contact line pins and depins alternatively. We find however, evidence that the CCA is the dominant mode,

because the contact angle oscillates around a well defined constant value. This alternating transition of evaporation mode from CCR to CCA has been explained as a stick-slip motion of the contact line when the drop crosses regions of different wettability.⁸⁷ Therefore, the motion of the contact line is determined by the molecular interactions within the three-phase zone, where liquid, solid and vapor meet. The driving force for the contact line motion is given by the out-of-balance surface tension that arises from perturbing the equilibrium as the wetting line moves across the solid surface changing the local surface tensions:⁸⁸

$$F = \gamma_{LV}(\cos \theta_s - \cos \theta_d) \quad (6-2)$$

In their study considering several liquids resting on different substrates, Stauber et al.⁸⁹ have shown that, for the case of a small initial contact angle, the lifetime of the CCA mode is longer than that of the CCR mode by a factor of 3/2.

An important phenomenon that takes place during the evaporation of a droplet that cannot be neglected is the Marangoni effect, which describes the movement of a liquid surface induced by a surface tension gradient, which can be generated either by a composition- or a temperature-variation along the free surface.²⁵

In the case of a pure solvent, the main cause of gradient of surface tension is self-induced variation of temperature on the liquid surface due to the latent heat of evaporation. On the other hand, in presence of dissolved organic molecules, the surface tension gradient is primarily caused by a solute concentration gradient. In both cases for the results discussed here, an appropriate combination of both gradients shall be considered.

During the CCR stage, the flow inside the droplet, known as Marangoni convection (which is a result of this interfacial hydrodynamic instability induced by surface tension gradient at the interface)⁹⁰ carries the molecules toward the droplet's edges (as shown in the left schematic of Figure 6-3). As a result the evaporation flux at the edges is much higher than that at the center (as shown in the right left schematic of Figure 6-3).

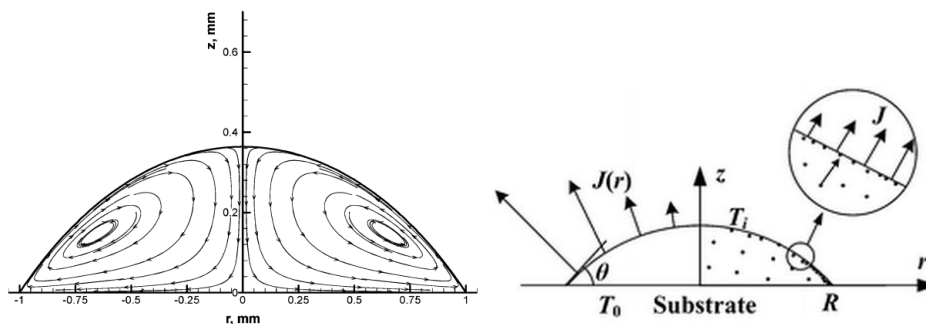


Figure 6-3. Marangoni convection inside a droplet (left).²⁵ Evaporation fluxes on the surfaces of the droplet (right).²⁷

This effect leads to a more solvent loss at the edges, which needs to be compensated in order to maintain the contact line pinned. The result is a solvent molecular flux from the droplet top-center towards the edges. During this flow a non-uniform distribution of solute (or contaminants in the pure solvent) occurs at the edges of the droplets, leading to the common “coffee ring” effect. This was explained by Deegan in terms of capillary flow.⁹¹ This flow generated inside the droplet causes vortices and turbulence at the droplet free surface, and results in a non uniform surface. These turbulences are visually observed in this work on the free surface of the droplet of chloroform during its evaporation.

The intensity of the Marangoni effect is described by the Marangoni number, Ma , which represents the ratio between the driving surface tension force and the viscous resistive force:²⁵

$$Ma = -\frac{\beta\Delta T t}{\mu R} \quad (6-3)$$

where β is the surface tension-temperature coefficient of the liquid, ΔT is the difference in temperature between the edge and the top of the droplet (as the surface temperature increases monotonously from the center to the edge of the droplet)²⁷ t is the drying time, μ is the viscosity of the liquid and R is the contact radius of the droplet. The phenomenon described above, i.e. the solvent flow from the top-center of the droplet towards to edge of the contact line occurs for small Ma . For Ma above a critical value, on the other hand, the flow inside the droplet is not be the same in the entire droplet bulk, but it is separated in two regions by a so-called stagnation point.²⁶ The region adjacent to the contact line are characterized by an outward flow directed towards the edge of the droplet, while the region far from the contact line exhibits a convective flow in which the motion is outward at first, but then turns towards the center of the droplet. At the stagnation point the surface flow changes its direction (Figure 6-4). Therefore, the particles transported in the convection flow region will move inward and deposit at the center of the substrate – we have observed evidence of this for evaporation of chloroform into which PCBM has been dissolved. While those particles transported in the outward flow region will be directly deposited at the edge of the droplet forming the rings – we see evidence for this for chloroform into which tn-ZnPc has been dissolved. Therefore, in presence of dissolved solute, solvent flow inside the droplet will define the distribution of the solute onto the substrate. The probability of a molecule being transported to the surface or inside the

droplet bulk must depend on the molecular interaction between solvent and organic molecules.

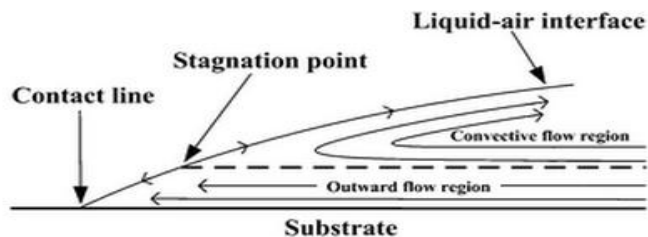


Figure 6-4. Schematics of the different flows occurring inside the droplet in presence of the stagnation point on the free surface of the droplet.²⁷

In their analytical work on a water droplet on a isothermal substrate, Xu et al.²⁷ demonstrated that the critical Marangoni number depends entirely on the contact angle and decreases following almost a power law with increasing contact angle when this latter is not larger than 40° .

6.2 Experiments and Discussions

In this work we studied the behavior of an evaporating droplet of chloroform at room temperature on an isothermal silicon substrate, both pure and in presence of dissolved tn-ZnPc and/or PCBM molecules. Images of the droplet were taken with a Canon digital camera fitted with a macro lens and extension tubes. These were analyzed with two commercial image-processing softwares (ImageJ and Gwyddion). The graphs in Figure 6-5 show the values of contact angles and contact radii measured every 2 seconds.

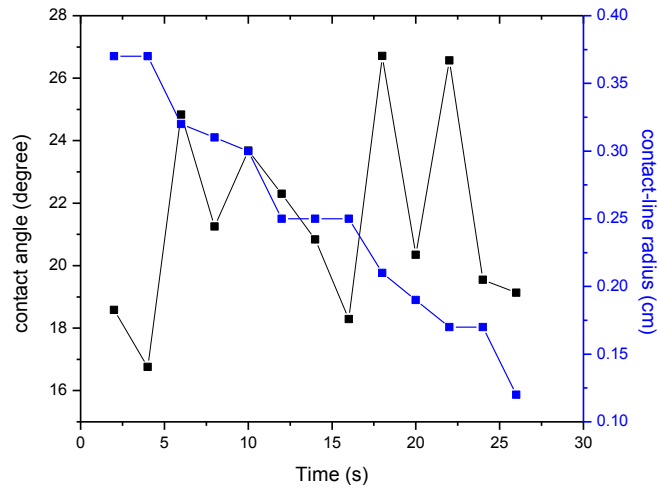


Figure 6-5. Contact angle and contact radius as a function of time.

We have found that the contact angle is very small; it ranges from 17.76° to 26.71° . We note however, that the contact angle measurements are not to be considered very accurate, because of the thinness of the droplet. Thus, it is likely that we are in the regime in which the stagnation point originates on the surface of the droplet, generating different flux directions on the surface. From the graphs we observed that the contact angle oscillates around a constant value of 21° , while the contact radius generally decreases with time. We can see that there are regions where the contact radius is relatively constant, suggesting the pinning/depinning behavior. We also find that there are regions of mixed mode, in which both contact radius and angle decrease. Overall our results indicate the CCA being the dominant mode in our case. As mentioned above, the occurrence of turbulence on its surface is not negligible and combined with the fact that the droplet is almost flat, leads to very fine changes in the contact angle. A more accurate measurement of the contact angle would require a measurement system resolution at the microscale.

For the analysis of the evaporation rate of the solvent we use a microbalance, which allows us to determine the variation of the droplet mass with time. The solutions under examination were: (1) pure chloroform, (2) PCBM and (3) tn-ZnPc solutions in chloroform at the concentration of 0.25 mM, and (4) a mixture solution of both molecules in ratio 1:1 at the same total concentration.

For discussing the behavior of the evaporation of the solutions, it is important to note that the solubilities of these molecules in chloroform are two orders of magnitude different. PCBM is highly soluble in chloroform (27.4 mM), while tn-ZnPc is considerably less soluble (0.37 mM).

We poured four drops of solution on a 1cm^2 silicon substrate, in order to cover the entire surface, and measured the rate of mass change. In Figure 6-6 are shown the plots of the mass change as a function of time of the pure chloroform and the solutions investigated. From these plots we can see that the chloroform and the PCBM solution are nearly indistinguishable. A different dependence is seen for the tn-ZnPc solution, which is nearly indistinguishable from that for the mixture solution. The first two plots exhibit two main regimes, a quasi-linear decreasing regime until 70 seconds followed by a monotonically decreasing regime towards to end of the evaporation. These two different regimes demonstrate the presence of two different evaporation rates: an initial fast rate and a final slower rate. The initial rate, in which the surface-to-volume ratio is relatively small, follows the dynamics explained above, i.e. the Marangoni stress is not negligible. While the final regime is dominated by much more complicated dynamics. This is apparently because the surface-to-volume ratio becomes very large, enhancing the effect of non uniformity of the free surface. The heat of evaporation leads to a non uniform path

length for heat conduction, which produces a non uniform distribution of temperature on the liquid-vapor interface, which drives the thermal Marangoni flow. This non uniformity changes the liquid-vapor surface tension, in turn changing the evaporation rate. It has been found that for large, but less than 40° , contact angles the Marangoni number is positive and the flow inside the droplet is counterclockwise, whereas for very small contact angles ($\sim 10^\circ$) the Marangoni number becomes negative and the circulation inside the droplet changes to clockwise motion from the center toward the edges, decreasing the radial flow.²⁵ As consequence, the evaporation rate will decrease.

An alternative explanation as to the difference seen between evaporation curves in Figure 6-6 could be that the change in the shape of the evaporation curve might also be related to a change in the shape of the sessile droplet, from flat-topped at the beginning (our visual observations indicate that initially the drops are indeed flat-topped) to spherical cap-shaped as the size decreases, due to a domination of gravitational forces by surface tension in the small drop limit. A flat-topped, short, cylindrical drop would evaporate in a nearly linear fashion, while the volume of the cap would follow a $t^{3/2}$ dependence. If the transition required a change in the contact area, it might be suppressed by the rod clusters which pin the contact line.

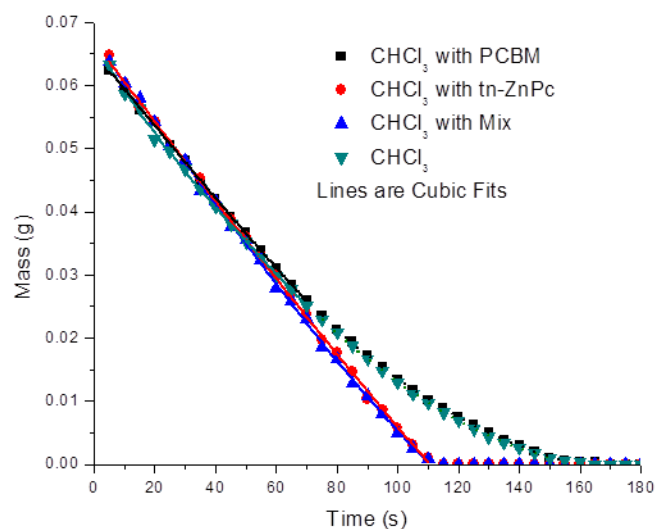


Figure 6-6. Mass change as a function of time, for the pure chloroform, the PCBM, tn-ZnPc, and (1:1) mixture solutions.

In conclusion, the unchanging behavior of chloroform when mixed with PCBM suggests, that the molecules are well dissolved and inert; they do not affect the evaporation rate – the dynamics of evaporation is controlled by the Marangoni convections inside the droplet that change depending on the contact angle and the surface-to-volume ratio. This suggests attractive interactions between chloroform and PCBM. While, the increasing of the overall evaporation rate when chloroform contains tn-ZnPc molecules suggests repulsive interactions with chloroform, leading to a faster solvent loss, and neglecting the change in the currents inside the droplet or the surface-to-volume ratio. When both molecules are dissolved in chloroform, the behavior of the evaporation rate of solvent is dominated by the presence of tn-ZnPc molecules and it is almost identical to the case of only tn-ZnPc molecules dissolved. This last curve suggests that tn-ZnPc interacts repulsively with the chloroform molecules, and ignores the presence of the PCBM molecules, initiating a phase separation already in solution.

The numerical values of the rate of evaporation have been extracted by fitting the different regions with a cubic function:

$$y = a + bx + cx^2 + dx^3 \quad (6-4)$$

where y is the mass and x is time, and ignoring the second and third order, since they are negligible. The slope of the approximated lines, $y \approx a + bx$, was used to calculate the evaporation rates, reported in Table 6-1. The overall values of the evaporation rate for the four solutions investigated are reported in Table 6-2.

Evaporation rate (mL/min) – drop-casting	CHCl ₃ with PCBM	CHCl ₃ with tn-ZnPc	CHCl ₃ with Mix	CHCl ₃
Initial regime (5'' → 70'')	0.027 ± 0.004	0.025 ± 0.002	0.026 ± 0.002	0.030 ± 0.002
Final regime (75'' → 150'')	0.020 ± 0.006			0.022 ± 0.006

Table 6-1. Values of the evaporation rates of the initial and final regimes for the solution under investigations.

Solution	Overall Evaporation Rate (mL/min)
Chloroform	0.017 ± 0.001
PCBM solution	0.0165 ± 0.0004
tn-ZnPc solution	0.0234 ± 0.0004
Mixture solution	0.024 ± 0.001

Table 6-2. Overall values of the evaporation rate for the solutions under investigations.

The variation of the mass of the solutions has been plotted as a function of time (left graph of Figure 6-7), and it shows the almost constant trend of the solvent evaporation in the tn-ZnPc and the mixture solutions, while the chloroform and the PCBM solution lose solvent monotonously. The values of the slope of the linear fits have been plotted and shown on the right graph of Figure 6-7.

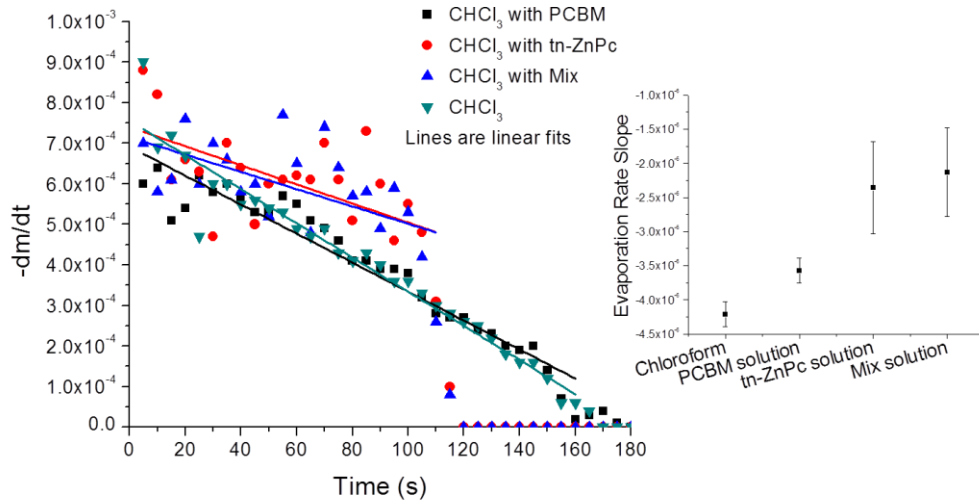


Figure 6-7. Derivative of the mass of the solution as function of time (left). Slope of the evaporation rate (right).

The experimental data of $-dm/dt$ have been fitted with the following formula:⁸⁶

$$-\frac{dm}{dt} = \pi R(t)D(1 - H)c_V(0.27\theta^2 + 1.30) \quad (6-5)$$

where $R(t)$ is the radius of the contact line and it is function of time, D is the vapor diffusion coefficient of chloroform at 25°C in air ($= 0.115 \text{ cm}^2/\text{s}$),⁹² H is the relative humidity (40%), θ is the contact angle and c_V is the saturated vapor concentration ($= 1.265 \times 10^{-3} \text{ g/cm}^3$), calculated by the ideal gas law:

$$c_V = \frac{M}{V} = \frac{Pm}{RT} \quad (6-6)$$

From the fitting we extracted $R(t)$ assuming the contact angle constant and equal to $(21 \pm 3)^\circ$.

The plots in Figure 6-8 demonstrate that at a given contact angle the evaporation rate is proportional to the contact line radius R , as predicted by Hu *et al.*⁸⁶

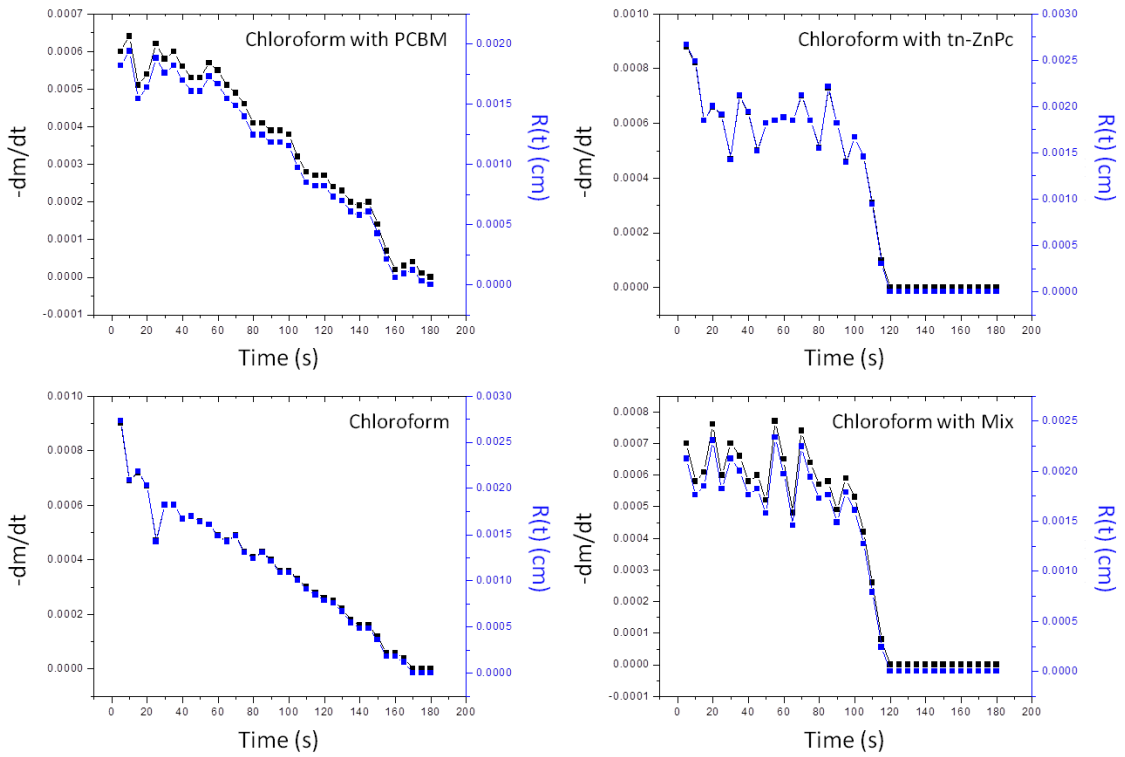


Figure 6-8. Derivative of the mass and $R(t)$ as a function of time for the four solutions.

According to the Nguyen et al.,⁹³ the evaporation rate of a sessile droplet follows a $2/3$ power law in the CCA mode; while for the CCR mode the exponent ranges from 1 (small contact angles) to $2/3$ (large contact angles). By fitting the curves of the mass change versus time (Figure 6-6) with a power law:

$$y = a + bx^c \quad (6-7)$$

we have found that the exponent c is slightly smaller than $2/3$; it is closer to $3/5$ for the pure chloroform and the PCBM solution, while the cases of tn-ZnPc and mix solutions show an almost linear behavior ($c \sim 1$) (Table 6-3). The reasons why we found a $3/5$ power law might be associated with the hydrophobicity/hydrophilicity properties of the

substrate, described by the initial contact angle θ_0 , because the averaged exponent \bar{c} has been found being function of θ_0 by the semianalytical approximation:⁹³

$$\bar{c} = 2 - \exp(0.0722\theta_0^{1.242}) \quad (6-8)$$

where θ_0 is given in radians. We calculated an estimation of the initial contact angle for the four case and we see that at the initial stage the contact angle is very large compared with that measured experimentally. The values are reported in Table 6-3.

	CHCl ₃ with PCBM	CHCl ₃ with tn-ZnPc	CHCl ₃ with mix	CHCl ₃
Parameter \bar{c}	0.63 ± 0.02	0.90 ± 0.03	0.89 ± 0.05	0.60 ± 0.05
Initial contact angle θ_0 (°)	95.80	36.61	39.38	101.08

Table 6-3. Estimation of the initial contact angle.

This might be due to that fact that these studies have been performed by pouring four drops on a small substrate. The SiO₂ surface is relatively hydrophilic for the chloroform, but given the amount of liquid, the edges of the liquid will reach the edges of the substrate where they will meet a different surface tension, responsible for constraining the liquid on the entire substrate, making the initial contact angle very large (Figure 6-9).

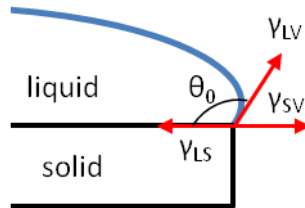


Figure 6-9. Schematic of the initial contact angle.

Another important effect to consider is the gravity. The initial liquid surface is, obviously very large, because cover the entire 1 cm^2 silicon substrate. For large droplets, the gravity will affect the shape of the droplet, deforming its spherical surface, making the droplet relatively flat.⁹⁴

To verify whether we are in the large sessile drop regime, we fitted the shape of the droplet surface to an arc with contact angle equal to 21° (as shown in Figure 6-10). The value of the height that result from the fit is $\sim 0.08 \text{ cm}$ and the measured value of the initial height of the liquid poured on the substrate is $\sim 0.05 \text{ cm}$. Therefore, the gravity action on the droplet cannot be neglected. This can also be a reason of the $3/5$ power law that we have found.



Figure 6-10. Fitting of the droplet surface to an arc to verify the gravity effect.

Chapter 7 – Summary and Conclusions

This work was meant to provide a better understanding of the mutual interactions between small, immiscible molecules, a liquid solvent and a substrate in order to control the length scale of their phase separation. The specific choice of electron donor and acceptor molecules for this study was motivated by potential applications, notably efficient organic solar cells.

In this work we carried out investigations of domain formation of functionalized phthalocyanines (tn-ZnPc) and fullerene-derivative (PCBM) molecules during deposition from chloroform-based solution at different supersaturation rates on flat silicon substrates.

We found that the simplest model, in which the interactions solutes/solvent and solutes/substrate are neglected is not sufficient; instead, these interactions play an important role in formation of molecular domains.

We observed that the majority of the tn-ZnPc molecules form large rod-shaped clusters while still in liquid solution, even at low concentrations. However, we find that some small fraction evidently remain dissolved, and interact strongly with the substrate, forming a wetting layer. We find that the morphology of the tn-ZnPc rod-clusters is not significantly affected by the solvent vapor and thermal annealing, by the evaporation rate of the solvent, or the presence of PCBM.

We find evidence that the PCBM clusters form at the substrate, and that the molecules are well dissolved in chloroform even at relatively high concentrations. The kinetics of crystallization of PCBM is highly affected by the solvent evaporation rate, and

thus supersaturation, as well as by the presence of the tn-ZnPc. We find that a certain level of control over the morphology of these domains is possible using solvent vapor annealing and thermal annealing.

Our studies of the phase separation between these two components were carried out in the presence of a flat substrate. The identification of domains made up of each molecule via atomic force microscopy force-curve measurements was demonstrated. The characteristic length scale of the phase separation was found to increase as the solvent evaporation rate, and thus supersaturation decreases. For OSC applications however, an advantage of using slow rates would be the increasing of the degree of order in the PCBM domains indicated in our studies. Highly ordered molecular domains facilitate the diffusion of excitons; therefore this latter result is desired in application of organic solar cells.

We carried out some first tests of directed phase separation on patterned semiconductor surfaces. These showed some promise for promoting a directional phase separation. In particular, we find that by patterning the substrate with arrays of small cavities with a small periodicity (hundreds of nm) we slightly promote the vertical growth of the domains. Additional studies, to further investigate these phenomena, are needed.

We investigated modification of the surface tension of the patterned surfaces via a hydrosilylation treatment. We did not achieve any increase in the vertical growth of the molecular domains, nor a vertical phase separation. However, other terminations might be effective in this regard, and should be further studied.

Vibrational spectroscopy studies confirm that the first molecules to deposit on the semiconductor surface through drop-casting are tn-ZnPc. We also find that the presence of the PCBM molecules above these seems to affect the orientation of the tn-ZnPc molecules in the wetting layer; tn-ZnPc molecules lay flat when alone, and slightly tilted when covered with PCBM.

In this work we have also studied the phenomena that occur in a sessile droplet during its evaporation. We have found evidence for directional fluxes inside the droplet which influence the arrangement of domains of the two types of molecules across the substrate. These studies give insights into the interactions occurring between individual molecules and solvent. In particular, we find evidence for repulsive interactions between tn-ZnPc and chloroform, and attractive interactions between PCBM and chloroform during deposition.

The results obtained in this work also shed light on the mutual interactions between this particular combination of organic molecules, solvent and substrates. They will hopefully lay the foundations for further investigations on different combinations of donor/acceptor organic molecules, solvent and substrates.

Chapter 8 – Future Work

The extensive studies done on unpatterned semiconductor surfaces presented in this work using functionalized phthalocyanines and fullerene-derivative molecules show that the idea on using these molecules to create interpenetrating networks of donor and acceptor will not work for the system we have chosen. The major issue we found was that these two molecules have very different solubilities in organic solvents; therefore, the majority of the tn-ZnPc clusters aggregated in solution at the very early stage.

Further studies should be done on employing a solvent in which the two molecules has similar solubility, or synthesize new phthalocyanines for achieving a higher solubility. This would eliminate the different interactions molecules/solvent and would potentially favor a smaller length scale phase separation. However, similar interactions with the solvent might lead to a difficulty in creating phase separated domains. Therefore, it is important that each of the two molecules have strong interactions with molecules of the same species.

In the literature there have been reported other mixtures that achieve molecular domains length scales of ~ 10 – 15 nm; these use different type of donor molecules in combinations with fullerene-derivative molecules that have comparable solubility in organic solvents. For example, phenyl-cored thiophene dendrimers (4G1-3S) with PCBM,⁹⁵ and 5,50-bis{(4-(7-hexylthiophen-2-yl)thiophen-2-yl)-[1,2,5]thiadiazolo[3,4-c]pyridine}-3,3'-di-2-ethylhexylsilylene-2,2'-bithiophene (DTS(PTTh₂)₂) with PC₇₀BM.⁹⁶

The insights gained in this thesis on unpatterned surfaces should direct and facilitate further investigations on patterned surfaces. In particular, we believe that small enough periodical arrays of cavities should be promising for a directional growth of the phase separation. Further investigations should be, then, addressed in this direction. In particular, finding the appropriate depth and shape of the cavities for which a nucleus can form, the appropriate combination of diameter/spacing for which the persistent length scale of the vertical domains is increased, and an appropriate choice of donor molecules that exhibit similar solubility in organic solvent than fullerene-derivative molecules, like those reported above.

Finally, we suggest continuing to seek appropriate surfactants, in order to make the interaction between the substrate and molecular domains even more selective.

Appendix A – Arrangement of Molecular Domains across the Substrate for (1:2) and (2:1) tn-ZnPc/PCBM Mixtures

In this section, we analyzed the arrangement of the molecular domains upon deposition via drop-casting of (1:2) and (2:1) tn-ZnPc/PCBM mixtures on native-oxide-covered silicon substrates. The motivation was to further investigate the Marangoni currents inside the droplet, and the interaction solutes/solvent.

Subsequent to deposition from solutions of (1:2) tn-ZnPc/PCBM mixtures optical images we show that the rings of high molecular domains coverage are nearly circular near the center of the substrate, but they are not very regular at the edges (top images in Figure A-1). In contrast, for the deposition from a solution of a (2:1) tn-ZnPc/PCBM mixture, there are no concentric rings of molecular domains evident near the substrate center; instead, as seen in the bottom images in Figure A-1, pinned contact lines, rather than regular rings, are visible – but only toward the edges of the sample.

We showed in Chapter 3 that within the rings that form after deposition from immersion in a solution of (1:2) tn-ZnPc/PCBM mixture, a relatively thick blanket phase of PCBM is observed on top of the tn-ZnPc rods. The average PCBM coverage in these rings ($\Theta = 3.9 \times 10^{14}$ molecules/cm²) is approximately a factor of 0.76 smaller than the average tn-ZnPc coverage ($\Theta = 5.1 \times 10^{14}$ molecules/cm²). On the other hand, the characteristic irregular rings at the edges of the samples in the (2:1) tn-ZnPc/PCBM

mixture are characterized by two types of arc: one almost completely made up of tn-ZnPc rod clusters, and the other one made up of a thin blanket of PCBM on tn-ZnPc rods. The average PCBM coverage in these rings ($\Theta = 2 \times 10^{15}$ molecules/cm²) is approximately a factor of 0.45 smaller than the average tn-ZnPc coverage ($\Theta = 4.5 \times 10^{15}$ molecules/cm²). Overall, both rings in (1:2) and (2:1) mixtures are characterized by a larger amount of tn-ZnPc; however, the first case contains a larger amount of PCBM than the latter one. This behavior is consistent with the Marangoni model for the respective diffusion of molecules/clusters in solution, as discussed in Chapter 6: tn-ZnPc tends to diffuse towards the edge of the droplet and the PCBM toward the center.

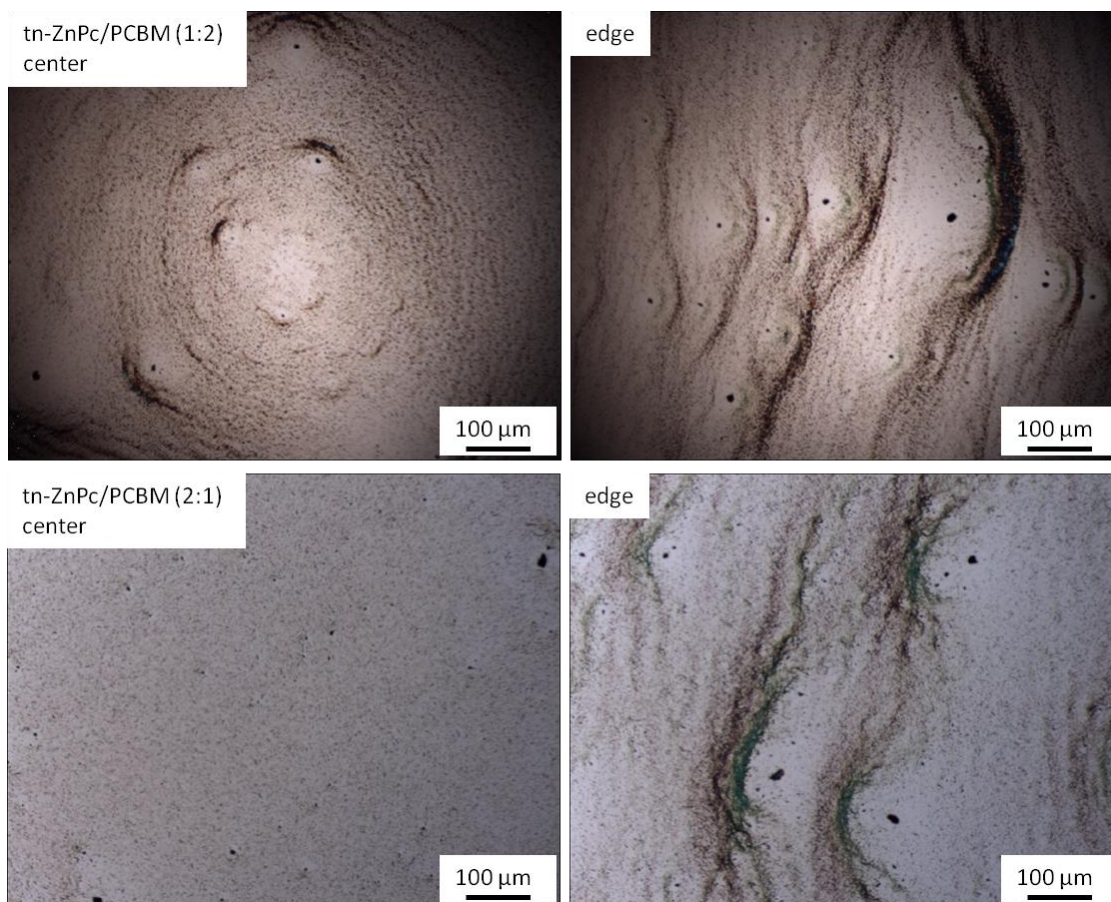


Figure A-1. Comparison of optical images of the structures resulting from deposition from a solution of a (1:2) tn-ZnPc/PCBM mixture (top images) and from a solution of a (2:1) tn-ZnPc/PCBM mixture (bottom images) via drop-casting.

We measured the radial distance between adjacent rings in the molecular pattern formed from a solution of a (1:2) tn-ZnPc/PCBM at a distance of 1800 μm from the first circle at the center (Figure A-2). Because of the sense of the motion of the contact line during solvent evaporation, the first circle at the center is actually the last circle formed. The near neighbor ring-ring radial separation increases approximately with a $3/2$ power law ($y = a + bx^c$) to a limiting value of $\sim 22.5 \mu\text{m}$ (plot in Figure A-2). Our interpretation of this is that during the initial stages of solvent evaporation, approximately every 22.5 μm , the contact line of the droplet is pinned. When the diameter of the droplet drops beneath approximately 500 μm , then the rings start to get closer to each other – this is seemingly a curvature related effect. We find that the last ring has a diameter equal to $(45 \pm 5) \mu\text{m}$. Apparently beneath this limit the driving force for evaporation is sufficiently large to overcome the interfacial forces that generate the “stick-slip” motion of the contact line up until this point

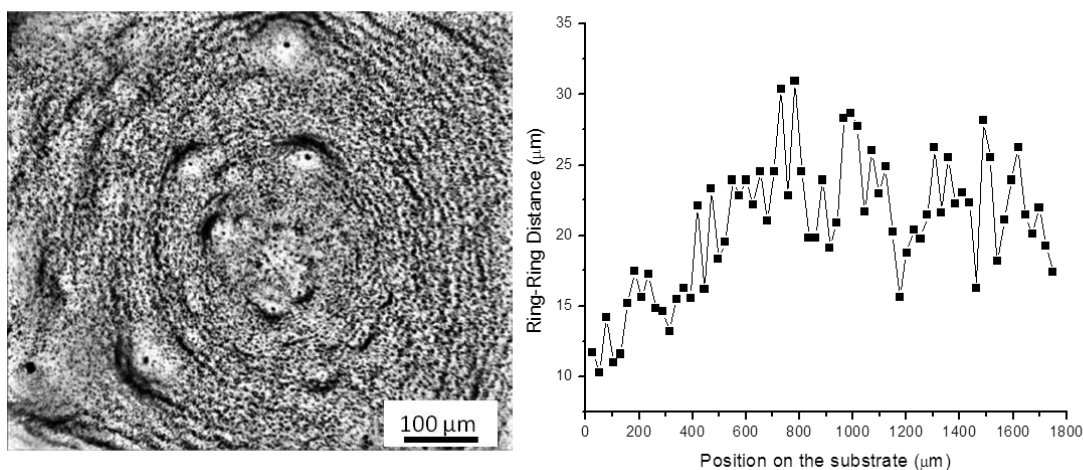


Figure A-2. Optical images of the structures resulting from deposition from a solution of a (1:2) tn-ZnPc/PCBM mixture modified in order to remove the distortion of the optical background (left). Ring-ring distance as a function of the position on the substrate (right).

Finally, we considered the radial distances at which the pinning objects deposited with respect to each other and the length of the arc chord of adjacent pinned arcs. In the optical image shown in Figure A-3 we have identified eight pinning objects. The radial separation decreases as the diameter of the droplet decreases, as does the arc chord length. Basically, separation between successive pinning sites gets smaller as the droplet gets smaller. This is due to the small amount of material left in the droplet at the final stages. Because the morphology of these molecular arrangements on the substrate does not change, we hypothesize that the Marangoni currents inside the droplet do not change with the size of the droplet.

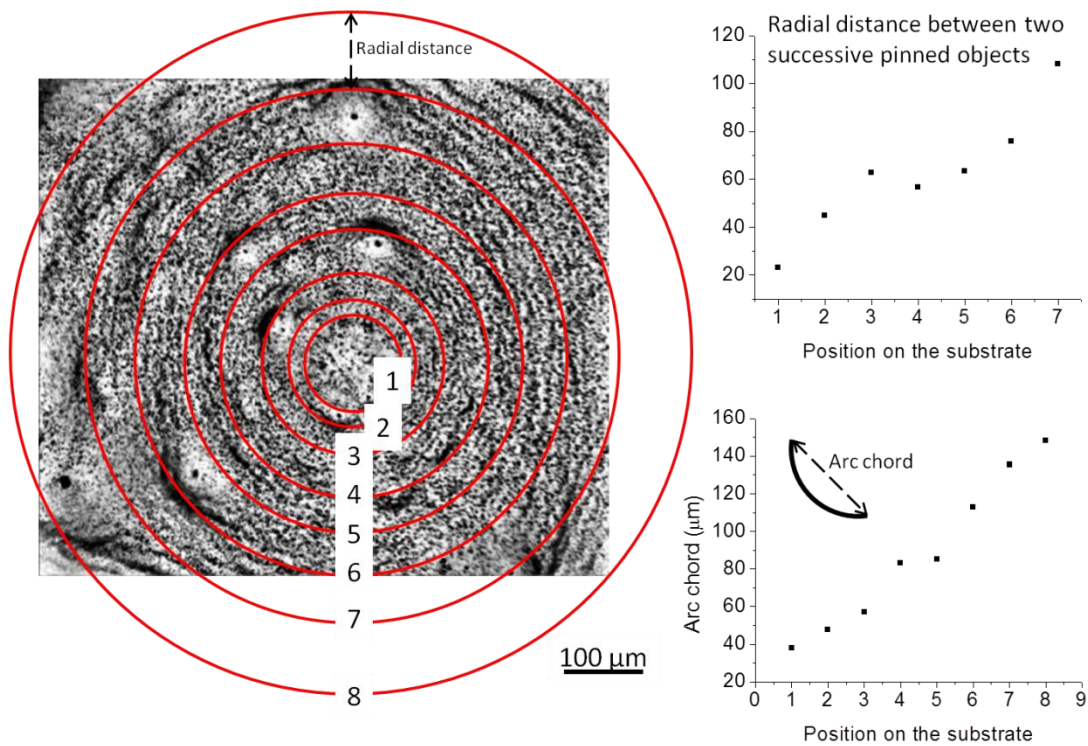


Figure A-3. Radial distance between adjacent pinning objects (upper graph). Arc chord length of adjacent pinned arcs (bottom graph).

Appendix B – XRD Patterns of Powders Materials

Although the deposited molecules, in any shape presented in this work, do not show any crystalline pattern, the powders of the raw materials do exhibit a crystalline pattern.

The measurements have been performed at the X-ray Crystallographic Center (Department of Chemistry and Biochemistry, University of Maryland) using the D8 Advance powder diffractometer (Bruker) equipped with Cu sealed tube ($\lambda = 1.54178 \text{ \AA}$).

The PCBM shows the characteristic crystallographic pattern in Figure B-1.

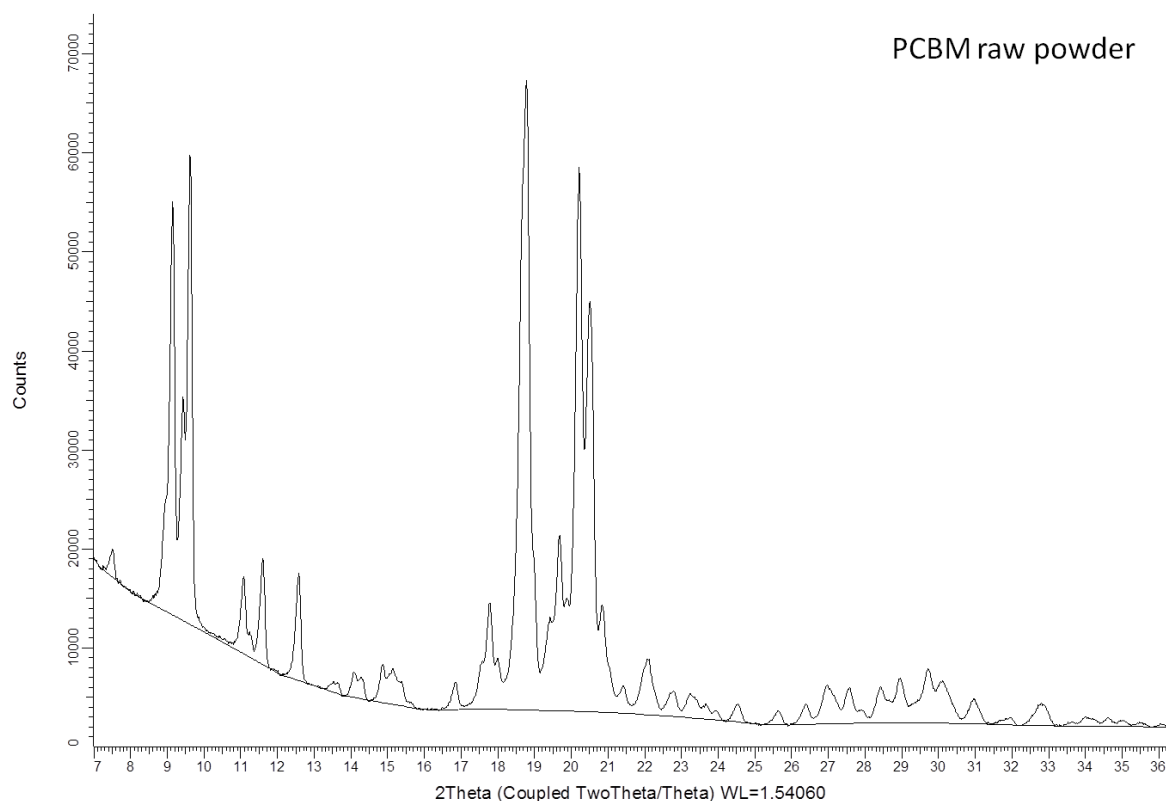


Figure B-1. XRD pattern of PCBM raw powder.

In order to extract the intensities (I_{hkl}) from the powder diffraction data, the LeBail method of fitting was employed, using monoclinic crystal system and space group $P2_1/n$. The lattice parameters of the PCBM used for the initial fitting were taken from the work done by Paternò *et al.*⁹⁷, in which the PCBM crystals were obtained upon solvation in chlorobenzene solution at room temperature, followed by slow drying. The lattice parameters are the following:

$$a = 13.29 \text{ \AA}$$

$$b = 14.93 \text{ \AA}$$

$$c = 19.48 \text{ \AA}$$

$$\beta = 106.33^\circ$$

$$V = 3709.28 \text{ \AA}^3$$

The obtained refined lattice parameters for our case are the following:

$$a = (13.4755 \pm 0.0008) \text{ \AA}$$

$$b = (15.1884 \pm 0.0010) \text{ \AA}$$

$$c = (19.0728 \pm 0.0012) \text{ \AA}$$

$$\beta = (107.166 \pm 0.004)^\circ$$

$$V = (3729.7 \pm 0.4) \text{ \AA}^3$$

with crystallite Lorentzian size equal to (255 ± 8) nm.

The fact that we found a slightly larger unit cell volume is due to the fact that we do not have any residue of solvent.

Our results are in good agreement with those obtained by Casalegno *et al.*⁹⁸, in whose work the crystal data of PCBM were obtained from the as-purchased powder (solvent-free). The value obtained by Casalegno *et al.* are the following:

$$a = (13.4951 \pm 0.0005) \text{ \AA}$$

$$b = (15.1572 \pm 0.0004) \text{ \AA}$$

$$c = (19.0964 \pm 0.0007) \text{ \AA}$$

$$\beta = (107.142 \pm 0.002)^\circ$$

$$V = (3732.6 \pm 0.2) \text{ \AA}^3$$

In Figure B-2, we show the comparison between observed XRD pattern of PCBM and that calculated with LeBail method. The overlapping is almost identical, with a very small difference (gray line in Figure B-2). The obtained profile *R*-factor is 6.3%. In the displayed range used for the fitting, there are 350 reflections found. The (*h*, *k*, *l*) indices, *d* spacing, 2θ angles and the fitted intensities of all 350 reflections are in Table B-1.

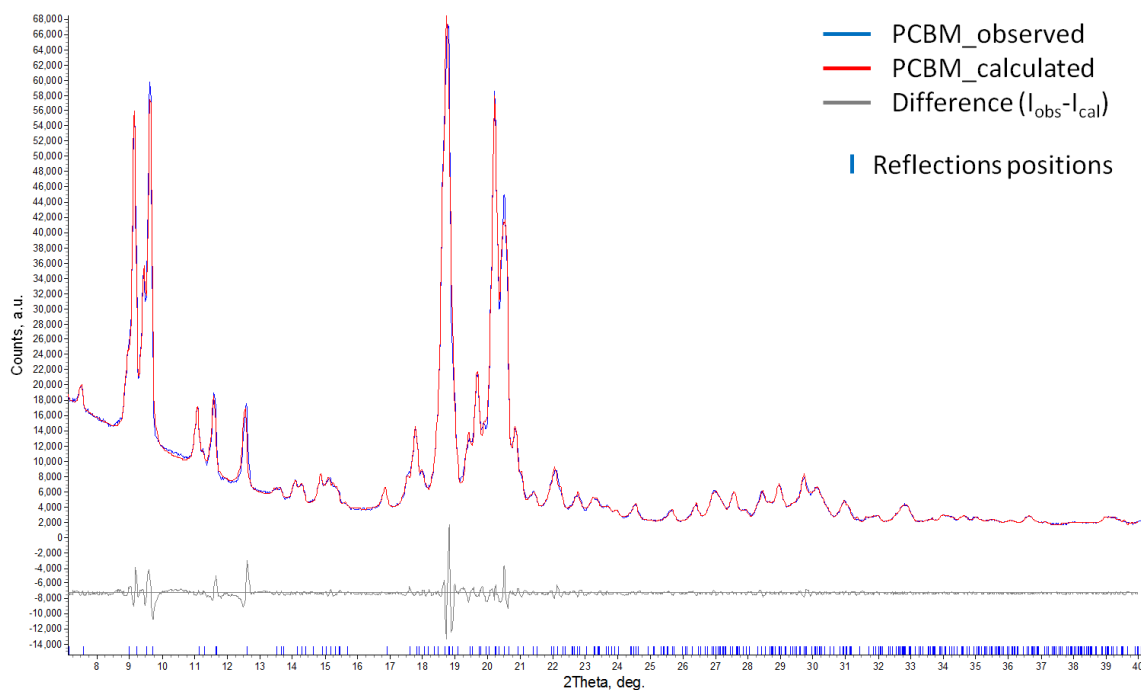


Figure B-2. Comparison between observed XRD pattern of PCBM and calculated with LeBail method.

The tn-ZnPc raw powder show a mild crystallographic pattern (Figure B-3), although it has been reported in literature the high crystalline character of the

phthalocyanine powder without functional groups (ZnPc).^{31,32} Around $2\theta = 40^\circ$ we observe an amorphous character, and the two mild peaks observed at $2\theta \sim 15^\circ$ and $2\theta \sim 26.3^\circ$ might refer to a crystalline structure. Because of lack of lattice parameters information and the weakness of these only two peaks, the plane indices were not calculated.

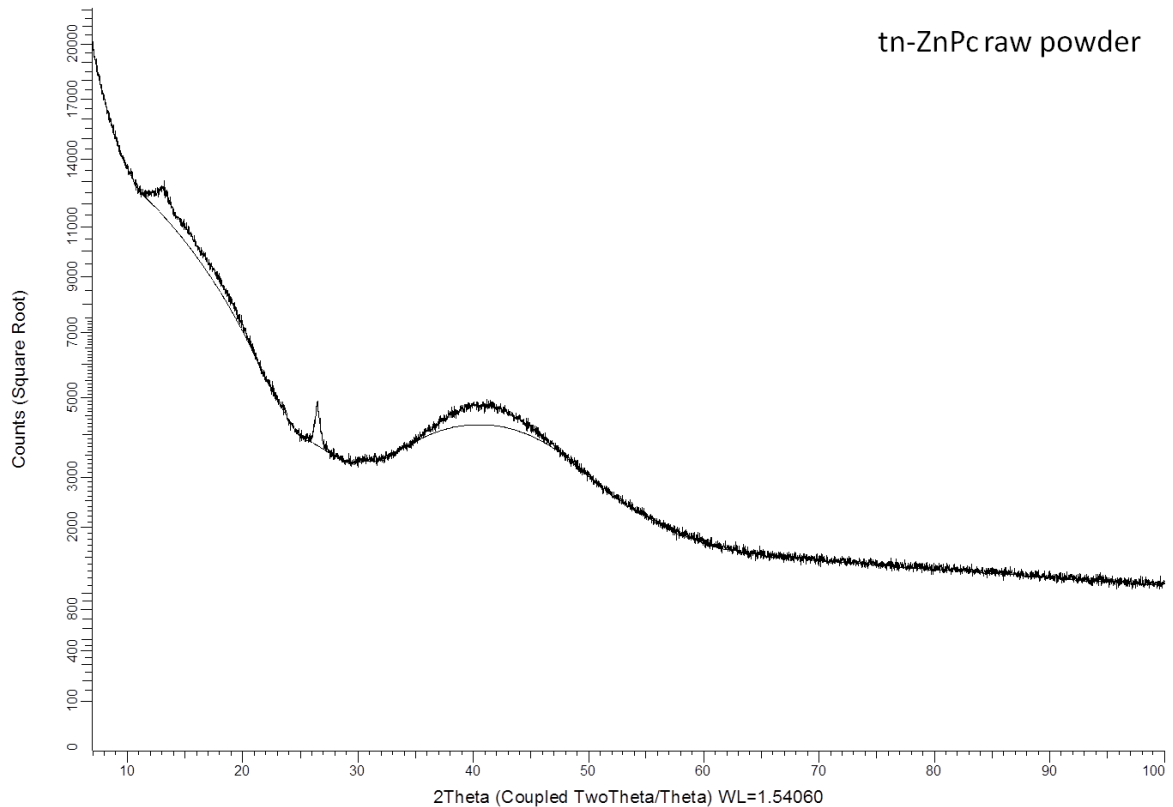


Figure B-3. XRD pattern of tn-ZnPc raw powder.

The reason why the deposited molecules of PCBM do not show any crystalline pattern might be due to the very low signal detectable. On the other hand, for the tn-ZnPc it is possible that the agglomerations in rod-like structures are amorphous.

h	k	l	d	2theta	I(observed)
1	0	-1	12.377	7.14	0.3
0	1	1	11.667	7.57	1.7
1	1	0	9.8212	9.00	4.7
1	-1	-1	9.5947	9.21	28.7
1	0	1	9.3010	9.50	12.2
0	0	2	9.1115	9.70	32.9
1	1	1	7.9319	11.15	7.1
0	1	2	7.8134	11.32	1.5
0	2	0	7.5942	11.64	0.0
1	-1	-2	7.5852	11.66	10.7
0	2	1	7.0098	12.62	12.7
1	2	0	6.5411	13.53	1.2
1	-2	-1	6.4729	13.67	1.4
2	0	0	6.4376	13.74	0.8
1	0	-3	6.2516	14.16	3.9
2	0	-2	6.1885	14.30	1.8
2	-1	-1	6.1494	14.39	3.4
1	1	2	6.0363	14.66	0.0
2	1	0	5.9272	14.93	6.2
1	2	1	5.8824	15.05	2.0
0	2	2	5.8336	15.18	5.2
1	-1	-3	5.7811	15.31	4.0
1	-2	-2	5.7368	15.43	0.0
2	-1	-2	5.7310	15.45	4.7
0	1	3	5.6400	15.70	1.4
2	1	1	5.2337	16.93	6.3
2	-2	-1	5.0348	17.60	7.2
1	2	2	4.9722	17.82	0.2
2	-1	-3	4.9708	17.83	12.1
1	0	3	4.9579	17.88	16.4
2	2	0	4.9106	18.05	9.4
0	3	1	4.8780	18.17	4.8
1	-2	-3	4.8266	18.37	1.9
2	-2	-2	4.7973	18.48	2.5
0	2	3	4.7436	18.69	47.9
1	1	3	4.7132	18.81	145.0
1	3	0	4.7116	18.82	3.8
1	-3	-1	4.6859	18.92	94.6
2	0	2	4.6505	19.07	26.2
0	0	4	4.5558	19.47	18.4
1	-1	-4	4.5415	19.53	8.3
2	2	1	4.4941	19.74	35.9

3	0	-1	4.4831	19.79	23.4
2	1	2	4.4467	19.95	3.9
1	3	1	4.4467	19.95	15.5
0	3	2	4.4255	20.05	0.0
1	-3	-2	4.3828	20.25	0.0
2	0	-4	4.3776	20.27	128.0
0	1	4	4.3637	20.33	76.5
2	-2	-3	4.3244	20.52	73.2
3	-1	-1	4.2997	20.64	127.0
3	-1	-2	4.2418	20.93	35.4
2	-1	-4	4.2063	21.10	15.3
1	2	3	4.1515	21.39	3.2
3	1	0	4.1300	21.50	0.5
3	0	-3	4.1257	21.52	8.5
2	-3	-1	4.0448	21.96	1.5
1	-2	-4	4.0327	22.02	2.2
1	3	2	4.0121	22.14	23.0
3	-1	-3	3.9814	22.31	13.2
2	3	0	3.9796	22.32	0.0
2	2	2	3.9659	22.40	0.5
1	-3	-3	3.9344	22.58	0.0
3	0	1	3.9268	22.63	0.3
2	-3	-2	3.9185	22.67	0.0
0	2	4	3.9067	22.74	0.0
0	3	3	3.8891	22.85	13.9
3	-2	-1	3.8606	23.02	1.5
3	-2	-2	3.8185	23.28	0.2
1	1	4	3.8177	23.28	2.2
1	0	-5	3.8142	23.30	4.8
3	1	1	3.8018	23.38	0.3
0	4	0	3.7971	23.41	0.7
2	-2	-4	3.7926	23.44	8.9
2	1	3	3.7619	23.63	3.5
2	3	1	3.7480	23.72	1.6
3	2	0	3.7364	23.80	5.1
0	4	1	3.7173	23.92	0.0
1	-1	-5	3.6994	24.04	5.6
2	-3	-3	3.6478	24.38	0.0
1	4	0	3.6420	24.42	0.0
1	-4	-1	3.6301	24.50	0.0
3	-2	-3	3.6252	24.54	0.0
3	-1	-4	3.6127	24.62	12.8
2	-1	-5	3.5671	24.94	0.5

0	1	5	3.5440	25.11	0.0
1	3	3	3.5423	25.12	0.0
1	4	1	3.5154	25.31	0.0
0	4	2	3.5049	25.39	0.0
1	2	4	3.5003	25.43	0.0
3	2	1	3.4881	25.52	0.0
1	-4	-2	3.4836	25.55	0.0
1	-3	-4	3.4676	25.67	0.0
2	2	3	3.4572	25.75	12.3
2	3	2	3.4249	26.00	0.0
3	1	2	3.4146	26.08	1.0
1	-2	-5	3.4085	26.12	0.0
0	3	4	3.3865	26.30	0.0
4	0	-2	3.3627	26.49	18.7
3	-3	-1	3.3564	26.54	0.4
3	-2	-4	3.3404	26.67	2.6
3	-3	-2	3.3286	26.76	0.0
2	-3	-4	3.3114	26.90	0.2
2	-4	-1	3.3065	26.94	0.0
2	-2	-5	3.3042	26.96	14.5
3	0	-5	3.2998	27.00	0.1
2	0	4	3.2891	27.09	13.5
1	4	2	3.2886	27.09	0.0
0	2	5	3.2858	27.12	8.1
4	-1	-2	3.2832	27.14	2.7
3	3	0	3.2738	27.22	8.0
2	4	0	3.2706	27.25	1.0
4	-1	-1	3.2651	27.29	1.9
1	0	5	3.2635	27.31	10.9
1	-4	-3	3.2454	27.46	1.1
2	-4	-2	3.2364	27.54	5.2
3	-1	-5	3.2246	27.64	19.4
0	4	3	3.2198	27.68	0.4
4	0	0	3.2188	27.69	7.8
2	1	4	3.2146	27.73	7.3
3	-3	-3	3.1982	27.87	6.0
4	-1	-3	3.1982	27.87	1.0
1	1	5	3.1907	27.94	0.0
3	2	2	3.1819	28.02	15.4
4	1	0	3.1489	28.32	6.1
2	4	1	3.1383	28.42	5.4
2	0	-6	3.1258	28.53	33.3
1	3	4	3.1115	28.67	3.5

1	-1	-6	3.1057	28.72	11.7
3	3	1	3.1029	28.75	0.3
3	0	3	3.1003	28.77	0.3
4	0	-4	3.0942	28.83	5.7
2	3	3	3.0811	28.96	0.6
2	-4	-3	3.0788	28.98	2.3
4	-2	-2	3.0747	29.02	35.7
2	-1	-6	3.0617	29.14	20.3
4	-2	-1	3.0599	29.16	3.3
1	-3	-5	3.0464	29.29	7.3
3	1	3	3.0377	29.38	1.6
0	0	6	3.0372	29.38	7.6
4	-1	-4	3.0320	29.44	3.8
3	-2	-5	3.0265	29.49	5.1
2	2	4	3.0182	29.57	11.1
1	4	3	3.0146	29.61	0.8
4	-2	-3	3.0046	29.71	0.0
1	2	5	2.9983	29.77	0.5
3	-3	-4	2.9975	29.78	1.7
0	5	1	2.9963	29.79	56.8
0	1	6	2.9782	29.98	24.0
2	-3	-5	2.9713	30.05	0.2
1	-4	-4	2.9682	30.08	2.4
4	2	0	2.9636	30.13	7.6
4	1	1	2.9627	30.14	7.4
0	3	5	2.9579	30.19	3.9
1	5	0	2.9565	30.20	21.7
1	-5	-1	2.9501	30.27	8.4
2	4	2	2.9412	30.37	26.6
1	-2	-6	2.9275	30.51	16.8
0	4	4	2.9168	30.63	9.7
3	-4	-1	2.8975	30.84	7.0
2	-2	-6	2.8905	30.91	0.7
1	5	1	2.8876	30.94	1.0
0	5	2	2.8817	31.01	1.4
3	3	2	2.8814	31.01	6.4
3	-4	-2	2.8796	31.03	21.8
3	2	3	2.8703	31.13	1.1
1	-5	-2	2.8698	31.14	0.1
2	-4	-4	2.8684	31.16	0.2
3	-1	-6	2.8659	31.18	1.9
4	-2	-4	2.8655	31.19	23.3
3	4	0	2.8438	31.43	14.0

0	2	6	2.8200	31.70	8.1
4	-1	-5	2.8192	31.71	5.1
4	2	1	2.8068	31.86	3.7
4	-3	-2	2.8011	31.92	10.7
3	-4	-3	2.7939	32.01	0.3
4	-3	-1	2.7899	32.06	1.3
4	0	2	2.7876	32.08	10.4
2	1	5	2.7852	32.11	7.8
2	-5	-1	2.7684	32.31	7.3
3	-3	-5	2.7645	32.36	0.2
2	3	4	2.7581	32.43	4.9
1	5	2	2.7578	32.44	0.2
4	-3	-3	2.7478	32.56	6.5
2	5	0	2.7472	32.57	0.2
1	3	5	2.7430	32.62	4.1
4	1	2	2.7418	32.63	0.0
1	4	4	2.7355	32.71	5.1
1	1	6	2.7331	32.74	2.2
1	-5	-3	2.7322	32.75	0.4
3	4	1	2.7297	32.78	2.3
2	-5	-2	2.7269	32.82	9.8
3	-2	-6	2.7241	32.85	9.4
0	5	3	2.7169	32.94	1.0
4	3	0	2.7163	32.95	14.3
2	4	3	2.7148	32.97	3.4
1	0	-7	2.7119	33.00	15.3
3	1	4	2.7017	33.13	15.5
1	-4	-5	2.6910	33.27	0.2
1	-3	-6	2.6884	33.30	2.6
4	-2	-5	2.6839	33.36	7.8
5	0	-3	2.6710	33.52	5.1
1	-1	-7	2.6697	33.54	1.1
2	5	1	2.6674	33.57	1.4
2	-1	-7	2.6650	33.60	3.1
5	0	-1	2.6608	33.66	2.6
2	-3	-6	2.6597	33.67	0.4
3	-4	-4	2.6571	33.70	1.3
2	2	5	2.6546	33.74	0.6
5	-1	-2	2.6534	33.75	10.9
3	3	3	2.6440	33.88	2.9
4	-3	-4	2.6402	33.93	0.2
2	-4	-5	2.6388	33.95	2.8
2	-5	-3	2.6306	34.05	1.0

5	-1	-3	2.6306	34.05	7.0
4	0	-6	2.6303	34.06	8.7
0	4	5	2.6294	34.07	0.4
5	-1	-1	2.6209	34.18	4.8
4	2	2	2.6168	34.24	13.9
1	2	6	2.6093	34.34	2.0
0	3	6	2.6045	34.41	12.0
4	3	1	2.5941	34.55	0.5
4	-1	-6	2.5917	34.58	5.7
3	0	-7	2.5905	34.60	0.2
1	5	3	2.5902	34.60	1.2
3	2	4	2.5820	34.72	17.7
3	4	2	2.5752	34.81	6.2
0	1	7	2.5659	34.94	4.4
1	-5	-4	2.5606	35.02	2.1
5	-1	-4	2.5565	35.07	10.8
1	-2	-7	2.5539	35.11	2.3
3	-1	-7	2.5536	35.11	0.5
2	-2	-7	2.5499	35.17	4.9
2	5	2	2.5432	35.26	7.3
5	-2	-2	2.5397	35.31	0.5
5	1	0	2.5388	35.32	1.1
0	6	0	2.5314	35.43	0.3
3	-3	-6	2.5284	35.48	2.6
0	5	4	2.5274	35.49	5.7
5	-2	-3	2.5197	35.60	5.1
4	-4	-2	2.5174	35.64	4.2
3	-5	-1	2.5148	35.67	3.8
4	1	3	2.5146	35.68	0.0
5	-2	-1	2.5112	35.73	0.0
4	-4	-1	2.5092	35.76	0.2
0	6	1	2.5073	35.78	4.6
3	-5	-2	2.5030	35.85	2.4
4	-3	-5	2.4961	35.95	0.3
2	-5	-4	2.4957	35.96	0.9
3	-4	-5	2.4907	36.03	1.6
2	4	4	2.4861	36.10	1.4
4	-2	-6	2.4854	36.11	2.4
1	6	0	2.4838	36.13	2.8
1	-6	-1	2.4801	36.19	0.4
3	5	0	2.4794	36.20	0.5
2	0	6	2.4790	36.21	4.0
4	-4	-3	2.4785	36.21	0.5

5	0	-5	2.4754	36.26	1.4
1	4	5	2.4750	36.27	0.6
2	3	5	2.4725	36.31	2.2
0	2	7	2.4626	36.46	0.0
4	4	0	2.4553	36.57	0.0
5	-2	-4	2.4543	36.58	0.0
3	-2	-7	2.4518	36.62	0.0
5	0	1	2.4514	36.63	3.5
2	1	6	2.4466	36.70	4.5
3	-5	-3	2.4461	36.71	2.0
3	0	5	2.4448	36.73	7.6
5	-1	-5	2.4432	36.76	4.0
1	6	1	2.4425	36.77	0.0
4	3	2	2.4419	36.78	0.0
0	6	2	2.4390	36.82	1.2
5	2	0	2.4387	36.83	0.0
1	3	6	2.4358	36.87	1.8
1	-4	-6	2.4347	36.89	3.8
1	-6	-2	2.4318	36.93	1.0
5	1	1	2.4201	37.12	0.0
4	2	3	2.4172	37.17	2.0
1	0	7	2.4169	37.17	0.1
3	1	5	2.4137	37.22	1.8
3	3	4	2.4135	37.22	1.1
2	-4	-6	2.4133	37.23	1.3
1	5	4	2.4067	37.33	0.1
3	5	1	2.4027	37.40	0.0
3	4	3	2.4015	37.42	0.0
4	-4	-4	2.3987	37.46	0.1
2	5	3	2.3925	37.56	0.0
1	-3	-7	2.3905	37.60	0.0
2	-3	-7	2.3872	37.65	0.0
1	1	7	2.3868	37.66	0.0
2	0	-8	2.3796	37.77	0.0
5	-3	-2	2.3789	37.79	0.0
1	-5	-5	2.3762	37.83	0.0
0	4	6	2.3718	37.90	0.0
4	-1	-7	2.3705	37.93	0.0
2	-6	-1	2.3691	37.95	0.0
4	4	1	2.3639	38.04	0.0
1	6	2	2.3625	38.06	2.9
5	-3	-3	2.3624	38.06	0.5
2	2	6	2.3566	38.16	0.0

2	6	0	2.3558	38.17	0.0
5	-3	-1	2.3553	38.18	0.2
5	-2	-5	2.3535	38.21	1.1
3	-5	-4	2.3528	38.22	1.4
2	-1	-8	2.3509	38.25	0.3
1	-6	-3	2.3463	38.33	1.3
2	-6	-2	2.3430	38.39	0.2
2	-5	-5	2.3400	38.44	1.4
1	-1	-8	2.3379	38.48	0.8
0	6	3	2.3366	38.50	0.5
4	-3	-6	2.3341	38.54	0.5
0	5	5	2.3335	38.55	0.6
5	2	1	2.3329	38.56	0.7
3	2	5	2.3271	38.66	3.4
4	0	4	2.3252	38.69	2.4
0	3	7	2.3152	38.87	2.6
3	-4	-6	2.3139	38.89	0.1
5	-3	-4	2.3082	38.99	0.1
3	-3	-7	2.3062	39.03	0.2
5	-1	-6	2.3059	39.03	3.5
2	6	1	2.3049	39.05	9.0
1	2	7	2.3030	39.08	8.8
4	1	4	2.2985	39.16	1.1
3	5	2	2.2953	39.22	11.7
5	3	0	2.2952	39.22	3.9
4	-4	-5	2.2891	39.33	4.2
4	-2	-7	2.2883	39.34	9.0
3	-1	-8	2.2883	39.34	6.6
2	-6	-3	2.2810	39.47	19.8
5	1	2	2.2801	39.49	3.9
0	0	8	2.2779	39.53	1.5
4	3	3	2.2773	39.54	0.1
2	4	5	2.2708	39.66	5.1
2	-2	-8	2.2707	39.66	32.3
1	-2	-8	2.2589	39.88	34.5
1	6	3	2.2545	39.96	5.0
4	-5	-2	2.2541	39.96	3.8
0	1	8	2.2527	39.99	7.1
4	-5	-1	2.2483	40.07	40.6
4	4	2	2.2471	40.10	15.2
1	4	6	2.2423	40.18	23.8
6	0	-2	2.2416	40.20	2.7
2	5	4	2.2316	40.39	74.7

2	3	6	2.2264	40.48	83.1
3	4	4	2.2249	40.51	12.7
1	5	5	2.2235	40.54	2.5
4	2	4	2.2234	40.54	3.8
5	2	2	2.2067	40.86	47.0
3	3	5	2.2015	40.96	14.0
2	1	7	2.1758	41.47	56.3

Table B-1. Miller indices (h , k , l), d spacing, 2θ angles and fitted intensities of PCBM.

Appendix C – Optical Characterization – Charge Transfer Complexes

Given the potential application to organic solar cells, in this section we investigated the photoinduced charge transfer process between tn-ZnPc and PCBM molecules deposited via drop-casting on silicon in a 1:1 ratio mixture.

The measurements have been performed at NNL-CNR-NANO in Lecce (Italy). Emission spectra were obtained with an Edinburgh FLS980 spectrometer equipped with a peltier-cooled Hamamatsu R928 photomultiplier tube (190-900 nm) and a Xe900 450 W Xenon arc lamp as exciting light source. Emission lifetimes in the ns- μ s range were determined with the single photon counting technique by means of the same Edinburgh FLS980 spectrometer using a laser diode as excitation source (1 MHz, λ_{exc} = 405, 515 or 635 nm, 200 ps time resolution after deconvolution) and the above-mentioned PMTs as detectors. Analysis of the luminescence decays was accomplished with the DAS6 Decay Analysis Software provided by the manufacturer. Experimental uncertainties are estimated to be \pm 8% for lifetime determinations and \pm 5 nm for emission peaks.

The absorption spectra of the single components in solution are reported in literature.^{99,100} In Figure C-1 are shown the UV-Vis absorption spectra of PCBM in chloroform at the concentration of 10^{-5} M and tn-ZnPc (in *o*-dichlorobenzene at the concentration of 1.11×10^{-5} M).

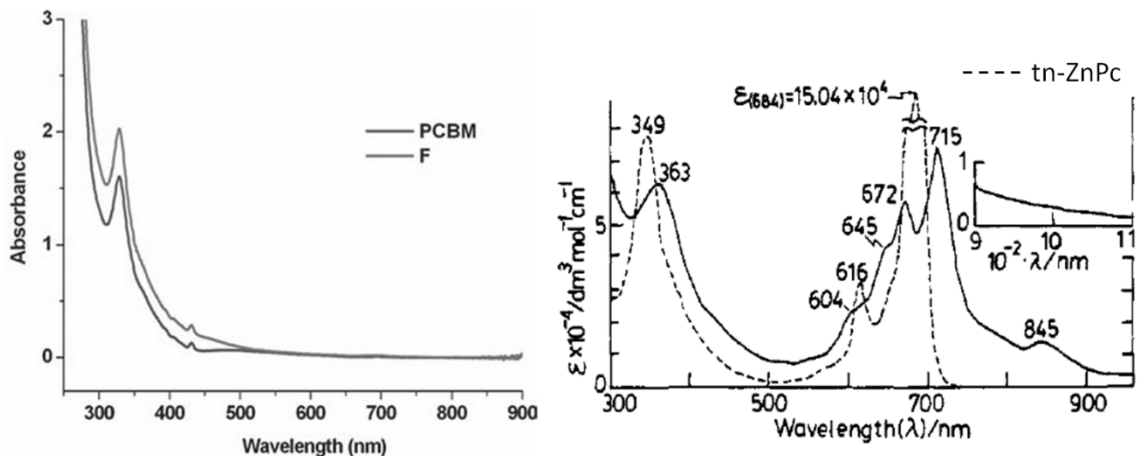


Figure C-1. UV-Vis spectra of PCBM (left)⁹⁹ and tn-ZnPc (right).¹⁰⁰

PCBM absorbs around 330 nm while tn-ZnPc shows three absorption peaks centered at 349, 616, and 684 nm, respectively. Thus, a single excitation wavelength of 330 nm has been selected for both units.

Figure C-2 shows the photoluminescence profiles and the corresponding lifetime values. As reported in literature,¹⁰⁰ the phthalocyanine exhibits two emission peaks at around 450 nm and 690 nm. However, the tendency of this class of molecules to closely pack to each other, when not properly diluted in an optically inert medium, leads to a strong luminescence self-quenching. In fact, in our case only the most intense high-lying energy band (~ 450 nm) is still detectable while the band at ~ 690 nm (see inset, red line) results in a negligible signal.

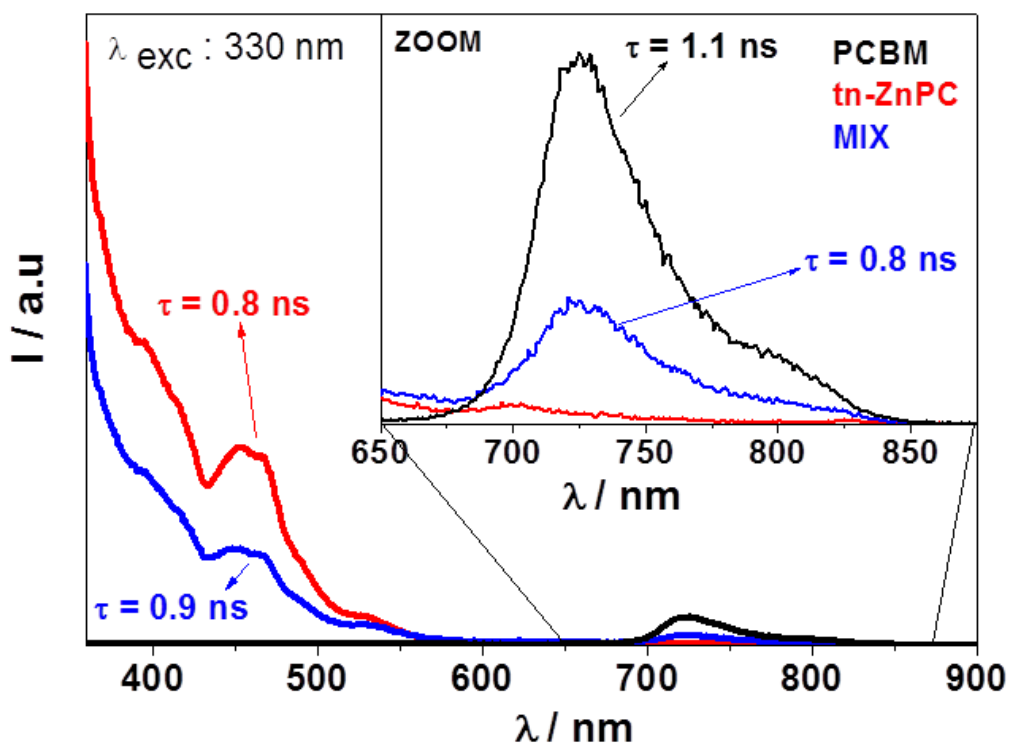


Figure C-2. Emission spectra of drop-casted film on silicon of PCBM (black), tn-ZnPc (red), and the mixture (blue) with relative decay times.

The PCBM shows a peak at 725 nm and, as confirmed by literature,¹⁰¹ does not exhibit any luminescence self-quenching by the close contact between units. In fact, the chemical structure and the electronic features of the fullerene (and its derivatives) guarantee a proper protection of their excited states.

When mixed together in 1:1 ratio and deposited on silicon, we note that the PL intensities of both units decrease, relatively to those of the single components, by almost half because of the repartition of the incident light between them.

However, while the decay lifetimes measured for the tn-ZnPc at 450 nm in the single component film and in the mixture (0.8 and 0.9 ns, respectively) are about the same within experimental error, those of PCBM decrease from 1.1 to 0.8 ns for PCBM

alone and PCBM in MIX, respectively. This, together with the fact that the PCBM emission intensity appears to be even lower than expected would suggest a photoinduced charge transfer process between electronic levels of tn-ZnPc and PCBM at the interface (only). Although, at this stage the experimental evidences are not significant, further tests should be performed to confirm this hypothesis.

Based on these results, we can state that a relatively well defined phase separation at the solid state is present, with a non significant charge transfer at the interface. However, for the purpose of photovoltaics application, this result is not desired since a substantial formation charge separated states (with low recombination rates) is required for optimal performances of the devices.

Appendix D – Determination of the Young’s Modulus of tn-ZnPc and the Thickness of the tn-ZnPc Wetting Layer

As a first approach, we determined the thickness of the tn-ZnPc wetting layer experimentally using measured XPS results. All XPS spectra performed on tn-ZnPc samples (either drop-casted or spin-coated) on areas of $700\ \mu\text{m} \times 300\ \mu\text{m}$, show peaks coming from the electrons escaping from the Si substrate. In Figure D-1 we report the XPS spectrum of tn-ZnPc deposited via drop-casting on silicon.

We calculated the electron effective attenuation length (λ_{EAL}) of tn-ZnPc for quantitative analysis using the NIST Electron Effective-Attenuation-Length Database,¹⁰² and we obtained $\lambda_{EAL}(\text{tn-ZnPc}) = 3.007\ \text{nm}$. We approximate the electron escape depth for tn-ZnPc as 3 times this, or $\sim 9\ \text{nm}$. However, since we are able to detect the silicon substrate underneath, the wetting layer must be thinner than 9 nm. The reason is that XPS gives a contribution from the rods.

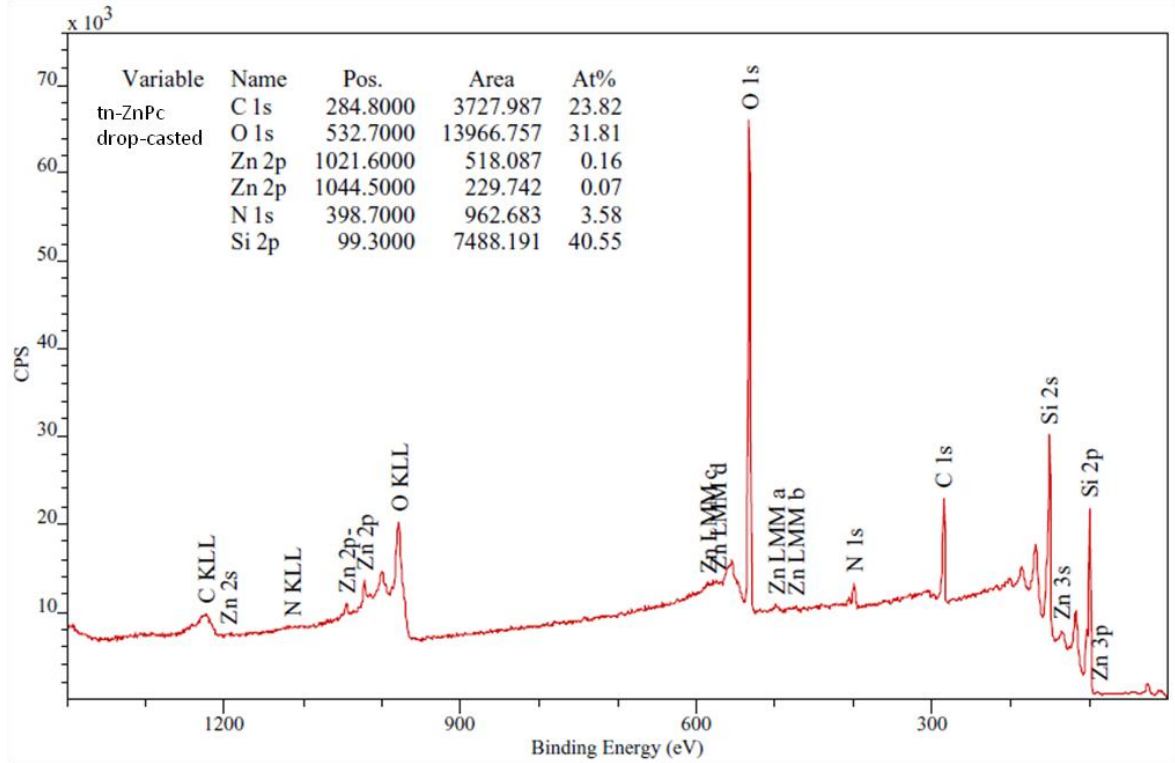


Figure D-1. XPS spectrum of tn-ZnPc deposited via drop-casting on Si(111).

We extracted the approximated thickness (t_{XPS}) of the drop-casted film, considering the film uniform over the entire silicon surface, using the method of the “Thickogram” introduced by Cumpson in 2000.¹⁰³ The approximated thickness for a uniform layer of tn-ZnPc is $t_{XPS} = (3.0 \pm 0.2)$ nm.

Next we consider that the value determined from XPS is approximately the average value from the rods and wetting layer, each weighted by their area fraction in the film. We estimate the area-coverage fraction of the tn-ZnPc rods (A_{rod}) and of the wetting layer (A_{wl}) from AFM images of on drop-casted samples. The values are: $A_{rod} = (0.31 \pm 0.01)$ and $A_{wl} = (0.69 \pm 0.01)$. We extract the thickness of the wetting layer ($t_{wl,XPS}$), through the following formula:

$$t_{wl,XPS} = \frac{t_{XPS} - A_{rod} \cdot 9 \text{ nm}}{A_{wl}} \quad (\text{D-1})$$

We estimate $t_{wl,XPS} = (0.3 \pm 0.1) \text{ nm}$.

In order to test this value of the thickness obtained with XPS analysis, we performed simulations of contact mechanics using a commercial finite element method-based software package (COMSOL Multiphysics), and we compared them with the measured force curves performed with AFM using a silica spherical tip.

We considered, as a first attempt, the results based on Hertzian theory, in which the adhesion is neglected. According to this theory, the relationship between the applied force (F) and the penetration (P) into a slab of infinite thickness and infinite lateral dimensions follows a 3/2-power law:¹⁰⁴

$$F = mP^{3/2} \quad (\text{D-2})$$

where the coefficient m is the slope of the curve and its form depends on the shape of the two bodies that are in contact. For a sphere in contact with a flat slab, m is given by:¹⁰⁴

$$m = E\sqrt{R_{sph}} \quad (\text{D-3})$$

where R_{sph} is the radius of the sphere and E is the modulus of the system related to the Poisson's ratios and Young's moduli of the slab and the sphere:

$$\frac{1}{E} = \frac{3}{4} \left(\frac{1 - \nu_{slb}^2}{E_{slb}} + \frac{1 - \nu_{sph}^2}{E_{sph}} \right) \quad (\text{D-4})$$

For a sphere in contact with an infinitely long cylinder, m is given by:¹⁰⁵

$$m = \frac{D_{sph}^{1/2}}{2QK^{3/2}} \left(-\frac{1}{e} \frac{dE}{de} \right)^{1/2} \quad (\text{D-5})$$

where D_{sph} is the diameter of the sphere, e is the eccentricity of the ellipse of contact, K and E (not to be confused with E , the Young's modulus) are the complete elliptic integrals of the first and second class respectively with modulus e , and Q is given by (for bodies of different materials):

$$Q = \frac{3}{4}(V_{sph} + V_{cyl}) \quad (D-6)$$

where V_{sph} and V_{cyl} are given by:

$$V_{sph,cyl} = \frac{(1 - \nu_{sph,cyl}^2)}{\pi E_{sph,cyl}} \quad (D-7)$$

where $\nu_{sph,cyl}$ and $E_{sph,cyl}$ are the Poisson's ratios and the Young's moduli of the sphere and the cylinder respectively.

A more realistic model would consider adhesion; however this approach should be approximately correct as long as we only consider the contact region of the extended curve (approaching curve) of the F vs. P plot of the measured curves. The fitting to Equation (D-2) of the measured curve for the tn-ZnPc rod is shown in Figure D-2.

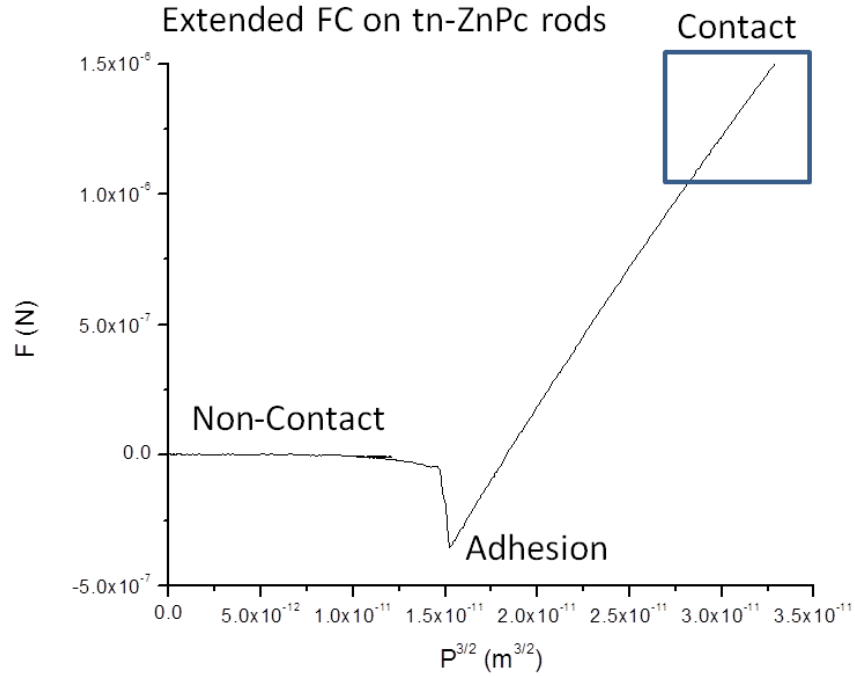


Figure D-2. Fitting of Equation (D-2) of the F vs. P curve measured for tn-ZnPc rods.

We obtained the first estimation of the Young's modulus of the tn-ZnPc rod ($E_{rod_measured}$) from the slope of the curve in Figure D-2, using Equation (D-5). The value is $E_{rod_measured} = (5.06 \times 10^7 \pm 2 \times 10^5)$ Pa. This value is within the order of magnitude of several organic molecules and polymers (50 – 1000 MPa),^{106,107} however it is low compared to the value found in literature for CuPc thin films (9.29 GPa).¹⁰⁸ Because Equation (D-5) is valid for an infinitely long cylinder, it gives only a rough approximation for our case of a finite length cylinder. Therefore, we used this as an initial value to estimate the correct value in numerical simulations of the F vs. P curve. We designed a 4-fold symmetry 3D geometry in which the silica probe is a hemisphere, the tn-ZnPc rod is a cylinder and the silica substrate is an infinitely rigid block (Figure D-3).

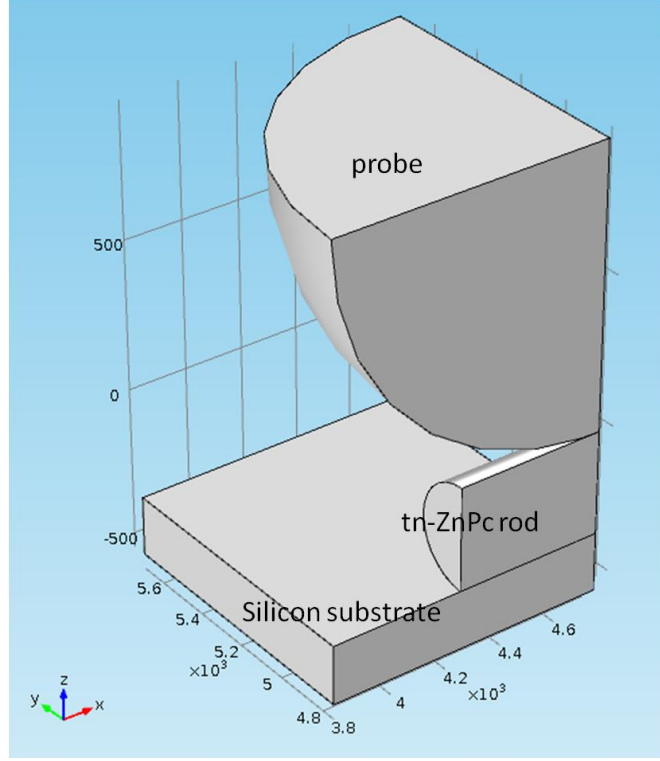


Figure D-3. 3D geometry used for COMSOL simulations to obtain the Young's modulus of tn-ZnPc.

We inserted the following parameters for the sphere and the block, which are both of silica: $\nu_{sph,block} = 0.17$, $\delta_{sph,block} = 2650 \text{ kg/m}^3$ and $E_{sph,block} = 7.2 \times 10^{10} \text{ Pa}$.³⁸ The parameters for the cylinder are: $\nu_{cyl} = 0.45$ (approximated to the one for CuPc thin films),¹⁰⁸ $\delta_{cyl} = 1630 \text{ kg/m}^3$ (approximated to the one for ZnPc thin films)⁴⁵ and the starting $E_{cyl} = 5.06 \times 10^7 \text{ Pa}$. We inserted the real sizes of the probe and the rod: $D_{sph} = 1900 \text{ nm}$ and $D_{cyl} = 350 \text{ nm}$, $L_{cyl} = 1000 \text{ nm}$ (length of the cylinder). We varied E_{cyl} until the slope of the simulated F vs. $P^{3/2}$ curve equals to the slope of the measured one.

In order to estimate the correct value of E_{cyl} we calculated the difference Δm between the simulated slope (m_{sim}) and the measured slope (m_{meas}):

$$\Delta m = m_{sim} - m_{meas} \quad (\text{D-8})$$

We plotted the values of E_{cyl} as a function of Δm . The value of E_{cyl} close to the real value of the Young's modulus of tn-ZnPc rods ($E_{tn-ZnPc}$) is the value for which $\Delta m = 0$, which is the value of the intercept of the linear fit of the plot in Figure D-4. The estimated Young's modulus of tn-ZnPc is $E_{tn-ZnPc} = (1.88 \times 10^8 \pm 2 \times 10^6)$ Pa.

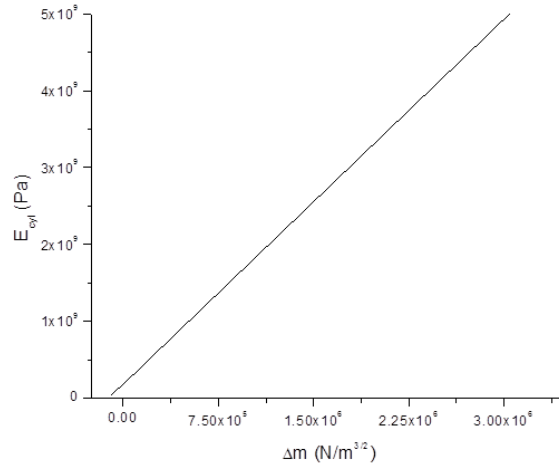


Figure D-4. Plot of E_{cyl} vs. Δm . The intercept of the linear fit of this curve is the estimated Young's modulus of tn-ZnPc.

We next used this estimated value of Young's modulus of tn-ZnPc in order to estimate the thickness of the wetting layer. This case, as the previous, was approximated to the Hertzian theory. We designed a 2D axial-symmetric geometry comprised of a large rigid block (silica substrate), a thin soft block (tn-ZnPc wetting layer) and a hemisphere (spherical probe), as reported in Figure D-5.

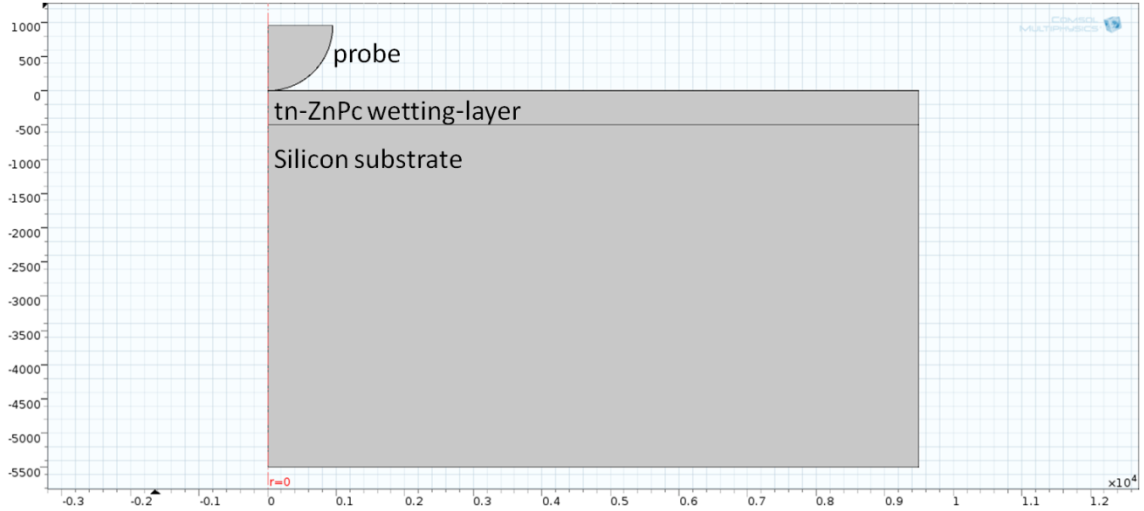


Figure D-5. 2D axial-symmetric geometry used for COMSOL simulations to obtain the thickness of tn-ZnPc wetting-layer.

We varied the thickness of the thin soft block in the range 0.3 – 3 nm until the slope of the simulated F vs. $P^{3/2}$ curve equaled that obtained from force-curve measurements performed with a spherical tip on “flat” regions between rods on films spin-coated from tn-ZnPc/chloroform solution. However, we found that in this range of thicknesses, the slope, which is given by Equation (D-3), is about four orders of magnitude larger than the measured slope: measured slope = $6.6 \times 10^4 \text{ N/m}^{3/2}$, simulated slope $\sim 1.4 \times 10^8 \text{ N/m}^{3/2}$. To extract the value of the wetting layer ($t_{wl,COMSOL}$), we plotted the values of $t_{wl,COMSOL}$ as a function of Δm .

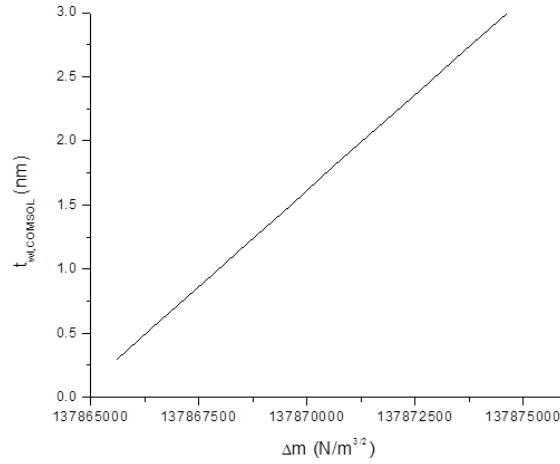


Figure D-6. Plot of $t_{wl,COMSOL}$ vs. Δm . The intercept of the linear fit of this curve is the estimated thickness of the wetting layer.

The intercept of the linear fit of Figure D-6, which should be the value of the thickness of the wetting layer, gives instead a negative number (~ -41359 nm) that has no physical meaning. Therefore, the approximation to Hertzian theory cannot be used, because the thickness of this layer is so thin that adhesion cannot be neglected. We found that the thickness of the layer for which the adhesion can be ignored is ~ 180 nm.

To extract the thickness of a very thin layer we need to employ the JKR theory, which takes into account adhesion. In this case, the relationship between penetration P and force F considering a sphere of radius R and a slab is given by the following formula:³⁷

$$P^{3/2} = \frac{1}{E\sqrt{R}} \left[F + 3\pi RW_{12} + \sqrt{6\pi RW_{12}F + (3\pi RW_{12})^2} \right] \cdot \left[1 - \frac{2}{3} \left(\frac{a_0}{a} \right)^{3/2} \right]^{3/2} \quad (\text{D-9})$$

where E is the elastic modulus of the system, W_{12} is the surface energy per unit area, a is the radius of the contact area under a given F , and a_0 is the radius of the contact area for $F = 0$.

Bibliography

1. Brabec, C. J., Sariciftci, N. S. & Hummelen, J. C. Plastic Solar Cells. *Adv. Funct. Mater.* **11**, 15–26 (2001).
2. Record Cell Efficiencies Chart. at http://www.nrel.gov/ncpv/images/efficiency_chart.jpg
3. Porter, D. A., Easterling, K. E. & Sherif, M. Y. *Phase Transformations in Metals and Alloys*. (CRC Press, 2008).
4. Hofmann, S., Rosenow, T. C., Gather, M. C., Lüssem, B. & Leo, K. Singlet exciton diffusion length in organic light-emitting diodes. *Phys. Rev. B* **85**, 245209 (2012).
5. Walter, M. G., Rudine, A. B. & Wamser, C. C. Porphyrins and phthalocyanines in solar photovoltaic cells. *J. Porphyr. Phthalocyanines* **14**, 759–792 (2010).
6. Feron, K., Belcher, W. J., Fell, C. J. & Dastoor, P. C. Organic solar cells: understanding the role of Förster resonance energy transfer. *Int. J. Mol. Sci.* **13**, 17019–17047 (2012).
7. Ahn, T.-S., Wright, N. & Bardeen, C. J. The effects of orientational and energetic disorder on Förster energy migration along a one-dimensional lattice. *Chem. Phys. Lett.* **446**, 43–48 (2007).
8. Huijser, A., Savenije, T. J. & Siebbeles, L. D. a. Effect of the structure of substituents on charge separation in meso-tetraphenylporphyrin/TiO₂ bilayers. *Thin Solid Films* **511-512**, 208–213 (2006).
9. Heeger, A. J. 25th anniversary article: Bulk heterojunction solar cells: understanding the mechanism of operation. *Adv. Mater.* **26**, 10–27 (2014).
10. Lin, Y.-C., Müller, M. & Binder, K. Stability of thin polymer films: influence of solvents. *J. Chem. Phys.* **121**, 3816–3828 (2004).
11. Yang, Y. *et al.* Large [6,6]-phenyl C₆₁ butyric acid methyl (PCBM) hexagonal crystals grown by solvent-vapor annealing. *Mater. Chem. Phys.* **145**, 327–333 (2014).
12. Treossi, E. *et al.* Temperature-enhanced solvent vapor annealing of a C₃ symmetric hexa-peri-hexabenzocoronene: controlling the self-assembly from nano- to macroscale. *Small* **5**, 112–119 (2009).
13. Li, G. *et al.* “Solvent Annealing” effect in polymer solar cells based on poly(3-hexylthiophene) and methanofullerenes. *Adv. Funct. Mater.* **17**, 1636–1644 (2007).

14. Colle, R., Grosso, G., Ronzani, A., Gazzano, M. & Palermo, V. Anisotropic molecular packing of soluble C60 fullerenes in hexagonal nanocrystals obtained by solvent vapor annealing. *Carbon N. Y.* **50**, 1332–1337 (2012).
15. Peumans, P., Uchida, S. & Forrest, S. R. Efficient bulk heterojunction photovoltaic cells using small-molecular-weight organic thin films. *Nature* **425**, 158–162 (2003).
16. Kiel, J. W., Eberle, A. P. R. & Mackay, M. E. Nanoparticle agglomeration in polymer-based solar cells. *Phys. Rev. Lett.* **105**, 168701 (2010).
17. Li, G. *et al.* High-efficiency solution processable polymer photovoltaic cells by self-organization of polymer blends. *Nat. Mater.* **4**, 864–868 (2005).
18. Ogunsipe, A. & Nyokong, T. Effects of substituents and solvents on the photochemical properties of zinc phthalocyanine complexes and their protonated derivatives. *J. Mol. Struct.* **689**, 89–97 (2004).
19. Cid, J.-J. *et al.* Structure-function relationships in unsymmetrical zinc phthalocyanines for dye-sensitized solar cells. *Chemistry* **15**, 5130–5137 (2009).
20. Nemykin, V. N. & Lukyanets, E. A. Synthesis of substituted phthalocyanines. *ARKIVOC* **i**, 136–208 (2010).
21. Thompson, B. C. & Fréchet, J. M. J. Polymer-fullerene composite solar cells. *Angew. Chem. Int. Ed. Engl.* **47**, 58–77 (2008).
22. Kern, W. The Evolution of Silicon Wafer Cleaning Technology. *J. Electrochem. Soc.* **137**, 1887–1892 (1990).
23. Meyerhofer, D. Characteristics of resist films produced by spinning. *J. Appl. Phys.* **49**, 3993–3997 (1978).
24. Bornside, D. E., Macosko, C. W. & Scriven, L. E. Spin coating of a PMMA/chlorobenzene solution. *J. Electrochem. Soc.* **138**, 317–320 (1991).
25. Hu, H. & Larson, R. G. Analysis of the effects of marangoni stresses on the microflow in an evaporating sessile droplet. *Langmuir* **21**, 3972–3980 (2005).
26. Deegan, R. *et al.* Contact line deposits in an evaporating drop. *Phys. Rev. E* **62**, 756–765 (2000).
27. Xu, X., Luo, J. & Guo, D. Radial-velocity profile along the surface of evaporating liquid droplets. *Soft Matter* **8**, 5797–5803 (2012).
28. Esaka, H., Daimon, H., Natsume, Y., Ohsasa, K. & Tamura, M. Growth direction of cellular and dendritic interface in a constrained growth condition. *Mater. Trans.* **43**, 1312–1317 (2002).

29. Mullins, W. W. & Sekerka, R. F. Morphological stability of a particle growing by diffusion or heat flow. *J. Appl. Phys.* **34**, 323–329 (1963).
30. Mullins, W. W. & Sekerka, R. F. Stability of a planar interface during solidification of a dilute binary alloy. *J. Appl. Phys.* **35**, 444–451 (1964).
31. Senthilarasu, S., Hahn, Y. B. & Lee, S.-H. Structural analysis of zinc phthalocyanine (ZnPc) thin films: X-ray diffraction study. *J. Appl. Phys.* **102**, 043512 (2007).
32. Senthilarasu, S. *et al.* Characterization of zinc phthalocyanine (ZnPc) for photovoltaic applications. *Appl. Phys. A Mater. Sci. Process.* **77**, 383–389 (2003).
33. Deegan, R. Pattern formation in drying drops. *Phys. Rev. E* **61**, 475–485 (2000).
34. Anisimov, M. A. *et al.* Effects of resins on aggregation and stability of asphaltenes. *Energy & Fuels* **28**, 6200–6209 (2014).
35. Berne, B. J. & Pecora, R. *Dynamic Light Scattering: With Application to Chemistry, Biology, and Physics*. (Wiley, 1976).
36. Nastishin, Y. *et al.* Pretransitional fluctuations in the isotropic phase of a lyotropic chromonic liquid crystal. *Phys. Rev. E* **70**, 051706 (2004).
37. Israelachvili, J. N. *Intermolecular and Surface Forces*. (Elsevier, 2011).
38. Butt, H.-J., Cappella, B. & Kappl, M. Force measurements with the atomic force microscope: Technique, interpretation and applications. *Surf. Sci. Rep.* **59**, 1–152 (2005).
39. Guo, L. *et al.* Synthesis and spectral properties of soluble trimethylsilyl substituted metal-phthalocyanines. *Dye. Pigment.* **49**, 83–91 (2001).
40. Marchiori, C. F. N. & Koehler, M. Density functional theory study of the dipole across the P3HT : PCBM complex: the role of polarization and charge transfer. *J. Phys. D. Appl. Phys.* **47**, 215104 (2014).
41. Zhang, C., Chen, H., Chen, Y. & Wei, Z. DFT study on methanofullerene derivative [6,6]-Phenyl-C₆₁ butyric acid methyl ester. *Acta Physico-Chimica Sin.* **24**, 1353–1358 (2008).
42. Van Rysselberghe, P. Remarks concerning the Clausius-Mossotti law. *J. Phys. Chem.* **36**, 1152–1155 (1932).
43. Rajesh, K. R. & Menon, C. S. Electrical and optical properties of vacuum deposited ZnPc and CoPc thin films and application of variable range hopping model. **43**, 964–971 (2005).

44. Veldman, D. *et al.* Compositional and electric field dependence of the dissociation of charge transfer excitons in alternating polyfluorene copolymer/fullerene blends. *J. Am. Chem. Soc.* **130**, 7721–7735 (2008).
45. Maennig, B. *et al.* Controlled p-type doping of polycrystalline and amorphous organic layers: Self-consistent description of conductivity and field-effect mobility by a microscopic percolation model. *Phys. Rev. B* **64**, 195208 (2001).
46. Kwaadgras, B. W., Verdult, M., Dijkstra, M. & van Roij, R. Polarizability and alignment of dielectric nanoparticles in an external electric field: bowls, dumbbells, and cuboids. *J. Chem. Phys.* **135**, 134105 (2011).
47. Mitroy, J., Safronova, M. S. & Clark, C. W. Theory and applications of atomic and ionic polarizabilities. *J. Phys. B At. Mol. Opt. Phys.* **43**, 1–38 (2010).
48. Dumas, P., Laboratories, T. B. & Hdl, M. Morphology of hydrogen-terminated Si(111) and Si(100) surfaces upon etching in HF and buffered-HF solutions. **270**, (1992).
49. Farahani, M. A. & Gogolla, T. Spontaneous Raman scattering in optical fibers with modulated probe light for distributed temperature Raman remote sensing. *J. Light. Technol.* **17**, 1379–1391 (1999).
50. Ferraro, J. R., Nakamoto, K. & Brown, C. W. *Introductory Raman Spectroscopy*. *Introd. Raman Spectrosc.* (Elsevier, 2003).
51. Klimov, E., Li, W., Yang, X., Hoffmann, G. G. & Loos, J. Scanning near-field and confocal Raman microscopic investigation of P3HT-PCBM systems for solar cell applications. *Macromolecules* **39**, 4493–4496 (2006).
52. Tackley, D. R., Dent, G. & Smith, W. E. Phthalocyanines: structure and vibrations. *Phys. Chem. Chem. Phys.* **3**, 1419–1426 (2001).
53. Palys, B. J., van Den Ham, D. M. . W., Briels, W. & Feil, D. Resonance Raman spectra of phthalocyanine monolayers on different supports. *J. Raman Spectrosc.* **26**, 63–76 (1995).
54. Tackley, D. R., Dent, G. & Smith, W. E. IR and Raman assignments for zinc phthalocyanine from DFT calculations. *Phys. Chem. Chem. Phys.* **2**, 3949–3955 (2000).
55. Ramachandran, S. & Velraj, G. FT-IR, FT-Raman spectral analysis and density functional theory calculations studies of 3-chloro-2-nitrobenzyl alcohol. *Rom. Journ. Phys.* **57**, 1128–1137 (2012).
56. Raj, A., Varghese, H. T., Granadeiro, C. M., Nogueira, H. I. S. & Panicker, C. Y. IR, Raman and SERS spectra of 2-(methoxycarbonylmethylsulfanyl)-3,5-dinitrobenzene carboxylic acid. *J. Braz. Chem. Soc.* **20**, 549–559 (2009).

57. Jiang, J., Rintoul, L. & Arnold, D. P. Raman spectroscopic characteristics of phthalocyanine and naphthalocyanine in sandwich-type (na) phthalocyaninato and porphyrinato rare earth complexes. *Polyhedron* **19**, 1381–1394 (2000).
58. Temple, P. A. & Hathaway, C. E. Multiphonon Raman Spectrum of Silicon. *Phys. Rev. B* **7**, 3685–3697 (1973).
59. Parker, J. H., W., F. D. & M., A. Raman scattering by Silicon and Germanium. *Phys. Rev.* **155**, 712–714 (1967).
60. Griffiths, P. R. & de Haseth, J. A. *Fourier Transform Infrared Spectrometry*. (John Wiley & Sons, Inc., 2007).
61. Mirabella, F. M. *Internal Reflection Spectroscopy: Theory and Applications*. (Marcel Dekker, 1993).
62. Viana, R. B., da Silva, A. B. F. & Pimentel, A. S. Adsorption of sodium dodecyl sulfate on ge substrate: the effect of a low-polarity solvent. *Int. J. Mol. Sci.* **13**, 7980–7993 (2012).
63. Li, H. & Tripp, C. P. Use of infrared bands of the surfactant headgroup to identify mixed surfactant structures adsorbed on titania. *J. Phys. Chem. B* **108**, 18318–18326 (2004).
64. Al-Hosney, H. a & Grassian, V. H. Water, sulfur dioxide and nitric acid adsorption on calcium carbonate: a transmission and ATR-FTIR study. *Phys. Chem. Chem. Phys.* **7**, 1266–1276 (2005).
65. Müller, M., Kessler, B., Adler, H.-J. & Lunkwitz, K. Reversible switching of protein uptake and release at polyelectrolyte multilayers detected by ATR-FTIR spectroscopy. *Macromol. Symp.* **210**, 157–164 (2004).
66. Milosevic, M. *Internal Reflection and ATR Spectroscopy*. (John Wiley & Sons, Inc., 2012).
67. *Handbook of Surface and Interface Analysis Methods for Problem-Solving, Second Edition*. (CRC Press, 2009).
68. Schnippering, M., Neil, S. R. T., Mackenzie, S. R. & Unwin, P. R. Evanescent wave cavity-based spectroscopic techniques as probes of interfacial processes. *Chem. Soc. Rev.* **40**, 207–220 (2011).
69. El-Nahass, M. M., Afify, H. A., Gadallah, A. –S., Hassanien, A. M. & Atta Khedr, M. Effect of thermal annealing on structural and optical properties of titanyl phthalocyanine thin films. *Mater. Sci. Semicond. Process.* **27**, 254–260 (2014).
70. Collins, R. J. & Fan, H. Y. Infrared lattice absorption bands in Germanium, Silicon, and Diamond. *Phys. Rev.* **93**, 674–678 (1954).

71. Seoudi, R., El-Bahy, G. S. & El Sayed, Z. a. FTIR, TGA and DC electrical conductivity studies of phthalocyanine and its complexes. *J. Mol. Struct.* **753**, 119–126 (2005).
72. Lee, J. U., Kim, Y. D., Jo, J. W., Kim, J. P. & Jo, W. H. Efficiency enhancement of P3HT/PCBM bulk heterojunction solar cells by attaching zinc phthalocyanine to the chain-end of P3HT. *J. Mater. Chem.* **21**, 17209–17218 (2011).
73. Bao, M., Pan, N., Ma, C., Arnold, D. P. & Jiang, J. Infrared spectra of phthalocyanine and naphthalocyanine in sandwich-type (na)phthalocyaninato and porphyrinato rare earth complexes. *Vib. Spectrosc.* **32**, 175–184 (2003).
74. Szybowicz, M. *et al.* Temperature study of Raman, FT-IR and photoluminescence spectra of ZnPc thin layers on Si substrate. *J. Mol. Struct.* **830**, 14–20 (2007).
75. Lambert, J. B., Shurvell, H. F. & Cooks, R. G. *Introduction to Organic Spectroscopy*. (Macmillan, 1987).
76. Reddy, K. R. V. & Keshavayya, J. Synthesis and magnetic, spectral and thermal studies on metal 1,3,8,10,15,17,22,24-Octanitrophthalocyanines. *Turkish J. Chem.* **26**, 573–580 (2002).
77. Coates, J. Interpretation of Infrared Spectra, A Practical Approach. *Encycl. Anal. Chem.* 10815–10837 (2000).
78. Yue, G. *et al.* Flexible dye-sensitized solar cell based on PCBM/P3HT heterojunction. *Chinese Sci. Bull.* **56**, 325–330 (2011).
79. Tlahuice-Flores, A. & Mejía-Rosales, S. Structural and vibrational study of PCBM. *J. Chem. Chem. Eng.* **5**, 1034–1040 (2011).
80. Yoo, S. H., Kum, J. M. & Cho, S. O. Tuning the electronic band structure of PCBM by electron irradiation. *Nanoscale Res. Lett.* **6**, 545 (2011).
81. Gibian, T. G. & McKinney, D. S. Infrared spectra and force constants of chloroform and trichlorosilane. *J. Am. Chem. Soc.* **73**, 1431–1434 (1951).
82. Busch, K. W. *et al.* Wavelength Calibration of a Dispersive Near-Infrared Spectrometer Using Trichloromethane as a Calibration Standard. *Appl. Spectrosc.* **54**, 1321–1326 (2000).
83. Chang, L., Lademann, H. W. A., Bonekamp, J.-B., Meerholz, K. & Moulé, A. J. Effect of trace solvent on the morphology of P3HT:PCBM bulk heterojunction solar cells. *Adv. Funct. Mater.* **21**, 1779–1787 (2011).
84. Kanai, M. *et al.* Scanning tunneling microscopy observation of copper-phthalocyanine molecules on Si(100) and Si(111) surfaces. *Surf. Sci.* **329**, L619–L623 (1995).

85. Myers, D. *Surfaces, Interfaces, and Colloids—Principles and Applications*. (VCH Publishers, 1991).
86. Hu, H. & Larson, R. G. Evaporation of a sessile droplet on a substrate. *J. Phys. Chem. B* **106**, 1334–1344 (2002).
87. Wang, F.-C. & Wu, H.-A. Pinning and depinning mechanism of the contact line during evaporation of nano-droplets sessile on textured surfaces. *Soft Matter* **9**, 5703–5709 (2013).
88. Blake, T. D. The physics of moving wetting lines. *J. Colloid Interface Sci.* **299**, 1–13 (2006).
89. Stauber, J. M., Wilson, S. K., Duffy, B. R. & Sefiane, K. On the lifetimes of evaporating droplets. *J. Fluid Mech.* **744**, R2 (2014).
90. Chen, S., Yuan, X., Fu, B. & Yu, K. Simulation of interfacial Marangoni convection in gas-liquid mass transfer by lattice Boltzmann method. *Front. Chem. Sci. Eng.* **5**, 448–454 (2011).
91. Deegan, R. D., Bakajin, O. & Dupont, T. F. Capillary flow as the cause of ring stains from dried liquid drops. *Nature* **389**, 827–829 (1997).
92. Watts, H. Temperature dependence of the diffusion of carbon tetrachloride, chloroform, and methylene chloride vapors in air by a rate of evaporation method. *Can. J. Chem.* **49**, 67–73 (1971).
93. Nguyen, T. A. H. & Nguyen, A. V. Transient volume of evaporating sessile droplets: $2/3$, $1/1$, or another power law? *Langmuir* **30**, 6544–6547 (2014).
94. Extrand, C. . W. & Moon, S. I. When sessile drops are no longer small: transitions from spherical to fully flattened. *Langmuir* **26**, 11815–11822 (2010).
95. Kopidakis, N. *et al.* Bulk heterojunction organic photovoltaic devices based on phenyl-cored thiophene dendrimers. *Appl. Phys. Lett.* **89**, 103524 (2006).
96. Sun, Y. *et al.* Solution-processed small-molecule solar cells with 6.7% efficiency. *Nat. Mater.* **11**, 44–48 (2012).
97. Paterno', G. *et al.* Micro-focused X-ray diffraction characterization of high- quality [6,6]-phenyl-C61-butyric acid methyl ester single crystals without solvent impurities. *J. Mater. Chem. C* **1**, 5619–5623 (2013).
98. Casalegno, M. *et al.* Electronic Supplementary Information. Solvent-free phenyl-C61-butyric acid methyl ester (PCBM) from clathrates: insights for organic photovoltaics from crystal structures and molecular dynamics. *Chem. Commun.* **49**, 4525–4527 (2013).

99. Mikroyannidis, J. A., Kabanakis, A. N., Sharma, S. S. & Sharma, G. D. A simple and effective modification of PCBM for use as an electron acceptor in efficient bulk heterojunction solar cells. *Adv. Funct. Mater.* **21**, 746–755 (2011).
100. Kobayashi, N. *et al.* Synthesis, spectroscopy, electrochemistry, spectroelectrochemistry, Langmuir-Blodgett film formation, and molecular orbital calculations of planar binuclear phthalocyanines. *J. Am. Chem. Soc.* **116**, 879–890 (1994).
101. Kim, H. *et al.* Electroluminescence in polymer-fullerene photovoltaic cells. *Appl. Phys. Lett.* **86**, 183502 (2005).
102. Powell, C. J. & Jablonski, A. NIST Electron Effective-Absorption-Length Database, Version 1.3, Users' Guide. (2011).
103. Cumpson, P. J. The Thickogram: a method for easy film thickness measurement in XPS. *Surf. Interface Anal.* **29**, 403–406 (2000).
104. Lin, D., Dimitriadis, E. K. & Horkay, F. Robust strategies for automated AFM force curve analysis-I. Non-adhesive indentation of soft, inhomogeneous materials. *J. Biomech. Eng.* **129**, 430–440 (2007).
105. Puttock, M. J., Thwaite, E. G. & National Standard Laboratory (Australia). *Elastic Compression of Spheres and Cylinders at Point and Line Contact*. 64 (Commonwealth Scientific and Industrial Research Organization, 1969).
106. Tsukruk, V. V., Shulha, H. & Zhai, X. Nanoscale stiffness of individual dendritic molecules and their aggregates. *Appl. Phys. Lett.* **82**, 907–909 (2003).
107. Crist, B., Fisher, C. J. & Howard, P. R. Mechanical properties of model polyethylenes: tensile elastic modulus and yield stress. *Macromolecules* **22**, 1709–1718 (1989).
108. Kanari, M., Karino, Y. & Wakamatsu, T. Nanoindentation test for evaluating intermolecular elastic and plastic characteristics of copper phthalocyanine thin films. *Jpn. J. Appl. Phys.* **44**, 8249–8255 (2005).